

**Evaluating the effect of
scale and heterogeneity on the
mechanical behaviour of rock blocks**

Anastasios Stavrou

Submitted in accordance with the requirements for the degree of
Doctor of Philosophy

The University of Leeds
School of Earth and Environment

November 2019

The candidate confirms that the work submitted is his own, except where work which has formed part of jointly authored publications has been included. The contribution of the candidate and the other authors to this work has been explicitly indicated below. The candidate confirms that appropriate credit has been given within the thesis where reference has been made to the work of others.

This thesis is submitted as an alternative style of doctoral thesis including published material alongside a written commentary. This format is appropriate as the material presented in this thesis includes three article manuscripts (i.e. Chapters 2, 3 and 4), each contributing from different perspective knowledge on the mechanical behaviour of rock blocks and their potential contribution on the performance of deep underground openings. These manuscripts are preceded by an appropriate introduction (i.e. Chapter 1) locating the published work within the relevant literature and describing the overall research objectives, the strategy employed and the original contribution to knowledge. Following the included published material, a discussion and conclusion section (i.e. Chapter 5) is provided to bind the manuscripts together into a coherent body of work and to identify directions for future studies.

The material included in Chapter 2 of the thesis has been presented as part of the following publication:

Stavrou, A. and Murphy, W., 2018. Quantifying the effects of scale and heterogeneity on the confined strength of micro-defected rocks. *International Journal of Rock Mechanics and Mining Sciences*, 102, pp.131-143, ISSN 1365-1609, <https://doi.org/10.1016/j.ijrmms.2018.01.019>.

I conducted the literature review, gap analysis, research strategy, numerical modelling, data interpretation and paper preparation (written work and illustrations). William Murphy provided support, guidance and comments, and improved the manuscript.

The material included in Chapter 3 of the thesis has been presented as part of the following publication:

Stavrou, A., Vazaios, I., Murphy, W. and Vlachopoulos, N., 2019. Refined Approaches for Estimating the Strength of Rock Blocks. *Geotechnical and Geological Engineering*, pp.1-31, ISSN 1573-1529, <https://doi.org/10.1007/s10706-019-00989-9>.

I conducted the literature review, gap analysis, research strategy, numerical modelling, data interpretation and paper preparation (written work and illustrations). Ioannis Vazaios assisted on using the software FracMan for fracture generation in UDEC and provided useful comments for the generation of numerical models, the interpretation of the results and the preparation of the manuscript. William Murphy provided support, guidance and comments.

This copy has been supplied on the understanding that it is copyright material and that no quotation from the thesis may be published without proper acknowledgement.

Copyright ©2019 The University of Leeds and Anastasios Stavrou.

The right of Anastasios Stavrou to be identified as Author of this work has been asserted by Anastasios Stavrou in accordance with the Copyright, Designs and Patents Act 1988.

to my girls
Emmanouela
Nefeli & Valeria

Acknowledgements

Being a distance-learning & part-time PhD student, with a full-time job and a young family was not an ideal scenario. This thesis was made possible with the generous support and help of certain people and organisations.

Everything started during the days I was working in URS (now AECOM) at Chesterfield. Mid-late 2014 I had some initial discussions with James Lawrence (then Radioactive Waste Management – RWM) and Bill Murphy (University of Leeds – UoL) for a possible research project involving RWM, UoL and URS. I will always be grateful to James and Bill for their support, time, encouragement and research ideas during these early days.

URS agreed to sponsor my PhD in 2014. This project would have never started without John Holden approving the financial support of this research, both in terms of fees and paid leave. I would always be grateful for the opportunity I was given. I would also like to thank Phil Ward and Adrian Koe for the opportunities in rock engineering projects and especially Ady for looking after my workload and for chasing up to allocate time and additional funding for the PhD. Finally, I would like to thank Peter Skinner, Stephen Beales and Paul Gross for agreeing to support the project.

In 2016 I moved to ARUP in London. This project would have never completed without Paul Morrison agreeing to support financially the project. I would like to thank Hannes Lager, Seth Pollak and Matthew Free for supporting my Invest-in-Arup applications. A special thanks to Hannes for the work flexibility, project opportunities, understanding and interest in my project. Working with Seth in deep rock mechanics projects influenced the last part of this research. A massive thanks to Ioannis Vazaios

for the support, discussions, commitment and positive attitude. I started working with Yannis during the second half of the project and the completion of the project would have been much harder without his help. I would always be grateful for the support I received from ARUP.

I would like to thank my supervisors Bill Murphy and Mark Thomas for the support, advices, comments, useful discussions and the flexibility they gave me to explore my own research paths. I am grateful to Bill for always thinking/monitoring my difficulties to balance the family, work and PhD commitments.

Thanks to my big family and parents Yannis and Maria. Without their support ten years ago to attend a master's course in Leeds University I would not be here today.

Finally, thanks to my wife Emma and my daughters Nefeli and Valeria. For Nefeli I will become a doctor for rocks....keep it for now and I will explain later my little turtle. Emma I am so grateful for encouraging me to keep going and taking most of the house/kids/holidays....responsibilities on your shoulders. Thank you for all the time I took, the long weekends you stayed alone, late evenings and for understanding my excitement, even if you were joking that geology is not a real science. I love you.

Abstract

Rock block strength is a significant factor controlling the rock mass behaviour and the rock-support interactions in fractured rock masses. Especially when the design relies on discontinuum analysis, the adopted block properties are a dominant driver influencing the results. A series of 2D UDEC grain-based models were performed on samples of different sizes and qualities to simulate the results of lab- and block-scale experiments. The effect of pre-existing defects was simulated either in a smeared sense by adjusting the grain micro-properties or by explicitly modelling micro-Discrete Fracture Networks (DFN) that were previously generated within FracMan. Relationships that link the rock block strength with its volume and in-situ heterogeneity were proposed for the estimation of scaled Mohr–Coulomb and Hoek–Brown parameters. The UCS of blocks was expressed as a function of scale, defect intensity, persistence and strength. The quantified scale/condition dependant reduction of block strength was then linked with a block-scale Geological Strength Index parameter named micro GSI (mGSI). Special focus was also given on the selection of appropriate constitutive relationships and discontinuum modelling techniques when simulating tunnel-scale problems. For continuum blocks in-between DFNs the traditional Hoek–Brown approach does not capture realistic behaviours and the modified Damage-Initiation and Spalling-Limit approach is needed to predict the expected damage near the excavation boundaries. When blocks are simulated as a packing of grain elements, considerably reduced damage, stress relaxation and deformation is predicted as the Voronoi skeleton creates a well-interlocked structure that clamps the pre-existing joints. The research highlights that the estimation of representative block properties is of equivalent importance with the selection of appropriate modelling approaches.

Contents

Acknowledgements.....	vii
Abstract.....	ix
Contents.....	xi
List of Figures.....	xv
List of Tables.....	xxiii
Nomenclature	xxv
1. Introduction	1
1.1. Problem Statement	1
1.2. Scale Effects in Rock Mechanics.....	4
1.3. Anticipated Rock Mass Behaviour.....	16
1.4. Numerical Approach	23
1.5. Thesis Structure.....	30
References	31
2. Quantifying the Effects of Scale and Heterogeneity on the Confined Strength of micro-Defected Rocks	39
Abstract	40
2.1. Introduction.....	41
2.2. Rock block scaling effects	42
2.3. Numerical modelling approach.....	45
2.3.1. UDEC micro-mechanical damage model	45
2.3.2. UDEC-DM mechanical behaviour	46
2.4. Rock block scaling methodology.....	49
2.4.1. General approach.....	49
2.4.2. Intact rock macro-mechanical properties.....	50
2.5. UDEC-DM intact rock calibration	52

2.5.1.	Micro-mechanical model description	52
2.5.2.	Calibration procedure.....	54
2.6.	Scaling analysis	59
2.6.1.	Scaling Analysis - Step 1	60
2.6.2.	Scaling Analysis - Step 2	61
2.6.3.	Scaling Analysis - Step 3	64
2.7.	Discussion	69
2.8.	Conclusions	70
	Acknowledgements.....	72
	References	72
3.	Refined Approaches for Estimating the Strength of Rock Blocks	79
	Abstract	80
3.1.	Introduction.....	81
3.2.	Effect of Scale and Defects on UCS.....	83
3.3.	Simulation of Synthetic Rock Block Samples (SRB)	87
3.4.	UDEC Grain-Based Models (GBM)	90
3.4.1.	GBM Mechanical Behaviour.....	90
3.4.2.	Small-scale GBM Intact Rock Calibration.....	92
3.4.3.	Large-scale GBM Intact Rock Calibration.....	95
3.5.	Micro Discrete Fracture Networks (μ DFN).....	97
3.6.	Analysis of Scale Effects	102
3.6.1.	Matrix of Modelling Scenarios.....	102
3.7.	Geometrical Assessment.....	104
3.8.	Predicted Rock Block Strength	106
3.8.1.	Influence of Defect Persistence and Intensity	106
3.8.2.	Influence of Defect Strength	111
3.9.	Predicted Rock Block Young's Modulus	117
3.10.	Observed Failure Modes.....	120
3.11.	Refined approaches for RBS estimation.....	125
3.12.	Discussion	128

3.13.	Conclusions.....	130
	Acknowledgements.....	132
	References	132
4.	Influence of Block Properties and Modelling Techniques on the Predicted Behaviour of Underground Excavations.....	141
	Abstract	142
4.1.	Introduction.....	143
4.2.	Rock Block Parameters	144
	4.2.1. Unconfined Compressive Strength.....	144
	4.2.2. Confined Compressive Strength.....	145
	4.2.2.1. Hoek–Brown Failure Criterion.....	145
	4.2.2.2. Rock Block Scale GSI	147
	4.2.2.3. Modified Hoek–Brown Criteria	149
4.3.	Tunnel Scale Modelling.....	154
	4.3.1. Model Geometry and Boundary Conditions	154
	4.3.2. Modelling Scenarios	156
	4.3.2.1. Case 1: Influence of Selected mGSI	157
	4.3.2.2. Case 2: Influence of Selected Post-Peak Behaviour.....	159
	4.3.2.3. Case 3: Influence of Selected Constitutive Law.....	159
	4.3.2.4. Case 4: Influence of Rock Block Size	173
	4.3.2.5. Case 5: Influence of Modelling Approach.....	175
4.4.	Summary and Conclusions	198
	References	203
5.	Discussion and Conclusions.....	211
5.1.	Thesis Summary.....	211
5.2.	Thesis Contribution	217
5.3.	Future Work.....	218
	References	219

List of Figures

1.1.	Physical-symbolic-statistical representation of scale effects (Cunha, 1990).	5
1.2.	Schematic representation of scale effect on rock properties, where σ_N is the nominal strength of sample with nominal size d_N (Aubertin et al., 2000).	6
1.3.	Schematic representation of samples at different scales (i.e. intact rock, rock block, and rock mass). As specimen size increases then new structural features participate in the progressive larger volumes, leading eventually to different strength reductions and REV sizes. The strength reduces due to intact rock-, rock block- and rock mass-scale heterogeneities at different scales (e.g. micro-, meso- and large-scale defects such as grain boundaries, veins and discontinuities).	7
1.4.	Geometrical limits for the applicability of the Hoek–Brown criterion together with size effects in rock mass characterization (Hoek and Brown, 2018).	9
1.5.	Influence of scale on the three components of shear strength of a rough discontinuity (Bandis et al., 1981).	11
1.6.	Experimental evidence for the scale and stress dependence of peak shear stiffness (Bandis et al., 1983).	11
1.7.	Influence of sample size on intact rock strength (Hoek and Brown, 1980a). ...	12
1.8.	Scale concept used in the MRMR classification system due to the effect of weakening defects at different scales (Jakubec, 2013).	13
1.9.	Strength degradation from intact rock to rock block due to rock block-scale heterogeneities, and from rock block to rock mass due to rock mass-scale heterogeneities as a function of confinement (Bahrani et al., 2018).	14
1.10.	The variability of rock confined strength near excavation boundaries with a lowering of strength as the influence of defects increases (Kaiser et al., 2015).	15
1.11.	Relationship between stable crack length and ratio of applied stresses (Hoek and Bieniawski, 1965).	15
1.12.	Tunnel instability and modes of failure around underground excavations (Hoek et al., 1995), modified by Martin et al. (1999) and Martin et al. (2001).	16

1.13. Matrix of photographic representations for the various tunnel instability failure modes from relevant literature (Hoek et al., 1995; Kaiser et al., 2000; Hoek, 2001; Hoek et al., 2008; Hoek and Brown, 2018).....	19
1.14. Limits of applicability of GSI approach for rock mass strength characterisation in relation to the rock block strength (Kaiser, 2016).	21
1.15. Schematic of DISL model for spalling rocks, showing four zones of distinct rock mass failure mechanisms: no damage, shear failure, spalling, and unravelling. σ_c is the UCS of laboratory samples (Diederichs, 2003). Other rock types yield in shear or show a combined (transitional) behaviour (Perras et al., 2013).....	22
1.16. The difference between discontinuous and continuous materials in a tunnel of similar size (revised by Palmstrom (1995) from Barton (1990).....	24
1.17. Schematic diagram suggesting the range of application of discontinuum modelling (UDEC and 3DEC) in relation to the Q-value (Barton, 1998).	24
1.18. Broad distinction of rock mass types in relation to classification and method of analysis (Bandis et al., 2011).....	25
1.19. Three different underground excavations located in the same jointed rock mass. The CF vary significantly with the tunnel size (Stille and Palmström, 2008). .	26
1.20. Definitions of the EDZ with the same shape and dimension in hard rock under different geological conditions (Shin, 2010).	28
1.21. (a) 3D DFN, (b) the corresponding three-dimensional synthetic rock mass sample, and (c) synthetic rock mass basic components (Mas Ivars et al., 2011).	29
2.1. Scale effect relations for intact rock UCS proposed by Yoshinaka et al. (2008) for sample dimensions 50 x 125 mm. The relation of Hoek and Brown (1980b) is also shown for comparison (after (Pierce et al., 2009)).	45
2.2. Structure, micro-mechanical properties and constitutive behaviour of UDEC-DM model.....	48
2.3. Layout, boundary conditions and monitoring locations (i.e. UDEC history points) of the compression and indirect tensile strength tests.....	54
2.4. Sample No.1: simulated compression tests showing the calibrated stress-strain response and sample damage for different confining pressures.	57
2.5. Sample No.2: simulated compression tests showing the calibrated stress-strain response and sample damage for different confining pressures.	58

-
- 2.6. HB failure envelope and UDEC-DM lab-scale results for samples No.1 (left) and No.2 (right), including the typical failure mechanisms observed during modelling..... 59
 - 2.7. Calibrated stress-strain response of all sample sizes for three different physical conditions (i.e. three different k exponents 0.1, 0.3 and 0.9 in Equation 2.2). . 62
 - 2.8. Examples of macroscopic axial fractures for different sample sizes and conditions during the uniaxial compression tests. 63
 - 2.9. Predicted dimensionless relationships between material macro-cohesion and friction angle values with the specimen equivalent length. 65
 - 2.10. Measured peak strengths for samples No.1 "weak" and No.2 "strong" together with HB envelope fits for different physical conditions and sample sizes. 66
 - 2.11. Predicted relationship between mGSI and the UCS strength ratio $\sigma_c / \sigma_{c,o}$ (above) and percentage adjustment to the HB mi value with respect to the k exponent of the Yoshinaka et al. (2008) relationship (below). 68
 - 3.1. a) Scale effect relations for intact rock UCS proposed by Yoshinaka et al. (2008); b) The maximum and minimum Rock Block Strength (RBS) reductions from the relation of Laubscher and Jakubec (2001) are also shown for comparison; c) Target reduced UCS values for three progressively larger in size numerical samples are shown as green, orange and red symbols respectively; d) The sample height to width ratio is 2.5; (modified after Pierce et al. (2009)). 84
 - 3.2. Rock block strength concept used in the MRMR classification system and strength adjustment factor (modified after Read and Stacey (2009)). 85
 - 3.3. The different components of a Synthetic Rock Block (SRB) model in UDEC: intact Grain-Based Model (GBM) and micro Discrete Fracture Network (μ DFN). 88
 - 3.4. Structure, micro-mechanical properties and constitutive behaviour of UDEC GBM model (Stavrou and Murphy, 2018). 91
 - 3.5. Layout, boundary conditions and monitoring locations (i.e. UDEC history points) of the unconfined compression tests. 93
 - 3.6. Simulated unconfined compression test showing the calibrated stress-strain response and sample damage. 95
 - 3.7. Calibrated stress-strain curves and sample damage for the non-defected numerical samples (the damaged samples shown are not in scale). 96
 - 3.8. Defects at different sampling scales: SEM images of micro-crack distributions in thin sections of (a) Lac du Bonnet granite (Lim et al., 2012), and (b) Wombeyan

marble (Rosengren and Jaeger, 1968). Traces of the micro-cracks were obtained from the image processing package provided in MATLAB for (c) Lac du Bonnet granite, and (d) Wombeyan marble (Vazaios et al., 2018); (e) veins infilled with quartz within sandstone core; (f) defects cemented by gypsum in the rock block scale (Jakubec, 2013).	99
3.9. (a) 3D μ DFN generated in Fracman, (b) defects intersecting a specific plane, (c) traces generated by the defect-plane intersection, and (d) defect traces imported in the UDEC GBM model.	100
3.10. μ DFN mapping along virtual scan-lines to confirm the target P_{10} values.	101
3.11. Matrix of SRB models for 16 μ DFN groups of increasing defect intensity and persistence and 3 specimen sizes (i.e. 100×250 mm, 200×500 mm and 400×1000 mm).	103
3.12. (a) The linear fracture intensity P_{10} expressed as a function of the product between areal fracture intensity P_{21} and defect length L_d . (b) Slope of the best-fit lines in Figure 12a as a function of the defect length L_d . (c) Linear relationship between P_{21} and number of fractures (vertical axis is in a logarithmic scale) for each sample size. Note the significant increase in the slope of the best-fit line for the largest sample. (d) Rate of fracture number (slope of best-fit lines in Figure 3.12c) increases exponentially with sample size.	105
3.13. Normalised UCS values as a function of sample size and P_{10} defect intensity. Also shown for comparison are the Yoshinaka et al. (2008) and Laubscher and Jakubec (2001) strength limits.....	107
3.14. (a) and (b) Normalised UCS values as a function of defect intensity (P_{10} and P_{21}) and defect persistence. Also shown for comparison is the rock block strength reduction for “open” defects proposed by Laubscher and Jakubec (2001). (c) and (d) Normalised UCS values as a function of the “Defect Intensity \times Persistence – (DIP)” factor.	109
3.15. Comparison of predicted UCS results from current study with other numerical investigations examining scaling effects (Elmo and Stead, 2010; Lu, 2014; Hamdi et al., 2015; Gao and Kang, 2016; Vazaios et al., 2018).	111
3.16. Normalised UCS values as a function of sample size and P_{10} defect intensity. Also shown for comparison are the Yoshinaka et al. (Yoshinaka et al., 2008) and Laubscher and Jakubec (Laubscher and Jakubec, 2001) strength limits.	113
3.17. Normalised predicted UCS values as a function of defect intensity (P_{10} and P_{21}) and defect strength. Also shown for comparison are three progressive rock block strength reductions proposed by Laubscher and Jakubec (Laubscher and Jakubec, 2001) for Mohs hardness index 1, 3 and 5.	115

- 3.18. Average normalised UCS values for defect strength 0%, 50% and 100% of the baseline intact rock strength in comparison with rock block strength values predicted by the Laubscher and Jakubec (Laubscher and Jakubec, 2001) method for Mohs hardness index 1, 3 and 5..... 116
- 3.19. Normalised Young's modulus values as a function of the defect intensity (P_{10} and P_{21}) and persistence..... 118
- 3.20. Normalised Modulus Ratio (SRB MR / Lab MR) as a function of the defect intensity (P_{10} and P_{21}), persistence and strength. 119
- 3.21. Normalised Young's modulus vs normalised UCS values. The SRB modulus and strength were normalised with the lab scale properties. 120
- 3.22. Evolution of damage and typical failure modes captured for the intact non-defected (above) and defected (middle and below) SRB samples. The lines with blue colour denote failed pre-existing defects while those with red represent newly generated micro-cracks..... 122
- 3.23. Failure modes for progressively increasing defect intensities and defect persistence. The lines with blue colour denote failed pre-existing defects while those with red represent newly generated micro-cracks. 123
- 3.24. Specimen 100×250 mm for $P_{10}=5$ 1/m and defect length 0.04 m: Typical stress – axial/lateral strain (above), volumetric – axial strain and crack count – lateral strain (below) curves showing the transition in the failure mode as defect strength increases from 0% – 50% – 100% of the baseline intact rock strength..... 125
- 3.25. Proposed diagrams for estimating the Rock Block Strength (RBS) as a function of defect intensity, persistence, and strength..... 127
- 4.1. Quantification of the mGSI (i.e. a block scale GSI) and Rock Block Strength (RBS) as a function of scale, defect intensity, persistence, and strength..... 148
- 4.2. S- or tri-linear shaped failure envelope in principal stress space, showing the range of crack initiation and spalling limit thresholds, and the intact rock and long-term failure envelopes (based on Diederichs (2007))..... 150
- 4.3. (a) Flow chart for estimation of rock block strength for homogenous and heterogenous blocks; and (b) Flow chart for rock mass strength estimation when GSI is not applicable for massive to moderately jointed and/or defected rock. Based on Kaiser et al. (2015) and Kaiser (2016)..... 153
- 4.4. Model layout and detail of DFN used in the analysis..... 155
- 4.5. FracMan DFN model and generated block size distribution..... 156
- 4.6. Influence of mGSI on predicted damage and deformation. 158

4.7. Influence of post-peak properties on predicted damage and deformation.	160
4.8. Influence of post-peak properties on predicted damage and deformation.	161
4.9. Peak and residual envelopes used in the analysis for the CWFS model.	164
4.10. Influence of constitutive law on predicted damage and deformation.	165
4.11. Comparison between the discontinuum CWFS and E-B block models for the progressive development of damage during different relaxation stages.	166
4.12. Ground Reaction Curve showing the progressive development of damage due to the 3D effects (i.e. stress release) of an advancing tunnel face.	168
4.13. Empirical prediction of spall related overbreak depth.	169
4.14. Comparison between the DFN-free continuum CWFS and E-B models for the progressive development of damage during different relaxation stages.	170
4.15. Confinement dependent failure processes at low and high confinements.	171
4.16. Combined GRC and LDP plot together with predicted depth of overbreak. ..	172
4.17. Predicted disturbance with varying joint spacing when using the CWFS (above) and E-B (below) models: a) 5 m; b) 2.5 m; c) 1 m; and d) 0.5 m.	174
4.18. Voronoi block assemblage used for the tunnel-scale analysis.	176
4.19. UDEC GBM used for the UCS testing calibration.	177
4.20. Stress-strain diagrams obtained from UCS tests using the a) Coulomb Slip with residual strength (CSR) model and b) Cohesion-Loss and Friction-Hardening (CLFH) model.	179
4.21. Comparison of predicted rock mass deformation and disturbance for the DFN free continuum E-B and Voronoi CSR models.	180
4.22. Comparison between the DFN-free continuum CWFS and Voronoi CLFH models for the progressive development of damage during tunnelling.	182
4.23. Predicted rock mass displacements for the DFN free continuum CWFS and Voronoi CLFH models.	183
4.24. Principal stress difference around the tunnel at the stage of 100% relaxation for the DFN free continuum CWFS and Voronoi CLFH models.	184
4.25. Tangential stress paths for the roof and side-walls of the circular tunnel: i) elastic and ii) predicted from the continuum CWFS and Voronoi CLFH models.	185
4.26. Comparison between the DFN-free continuum CWFS and the re-calibrated Voronoi CSR models at the stage of 100% relaxation.	187

-
- 4.27. Predicted tensile fracturing at the side-walls of the excavation from the re-calibrated Voronoi CSR model. The figure at the right presents an example from an excavation spalling damage reported by Diederichs et al. (2004). 188
- 4.28. Comparison between the DFN-free continuum CWFS and the calibrated hybrid Voronoi CWFS & CLFH model at the stage of 100% relaxation. 189
- 4.29. Tangential stress paths for the roof and side-walls of the circular tunnel: i) elastic and ii) predicted from the Voronoi CWFS & CLFS and CSR models. 190
- 4.30. Stress paths for the tunnel side-wall from the continuum CWFS and Voronoi models plotted together with the tri-linear envelope of the DISL approach. . 191
- 4.31. Synthetic Rock Mass geometry (i.e. Voronoi models & DFN). 192
- 4.32. Comparison between the discontinuum CWFS and discontinuum Voronoi CSR models for the progressive development of damage. 193
- 4.33. Comparison between the discontinuum CWFS and discontinuum Voronoi CWFS & CLFH models for the progressive development of damage. 194
- 4.34. Comparison between the discontinuum CWFS and discontinuum Voronoi CSR models at the stage of 100% relaxation. 196
- 4.35. Comparison between the discontinuum CWFS and discontinuum Voronoi CWFS & CLFS models at the stage of 100% relaxation. 197

List of Tables

2.1. UDEC Voronoi micro-properties	47
2.2. Lab scale Intact Rock Macro-properties.	52
2.3. Calibrated UDEC Voronoi micro-properties.	56
2.4. Target uniaxial compressive and tensile strength values used for the scaling analysis.....	60
3.1. Target lab-scale macro-mechanical and calibrated micro-mechanical properties.	94
3.2. Calibrated micro-mechanical properties for the large-scale non-defected samples.....	97
3.3. Matrix of modelling scenarios considered to generate SRB models.	103
3.4. Defect interface assigned properties in respect to the calibrated “baseline intact rock strength” micro-mechanical properties for the large-scale non-defected samples.....	112
4.1. Intact rock, rock block and discontinuity properties.....	162
4.2. Hoek–Brown DISL and Mohr–Coulomb CWFS properties.....	163
4.3. Comparison of overbreak depth between empirical and numerical results. ...	171
4.4. UDEC model geometries with varying joint spacing.	173
4.5. Calibrated UDEC Voronoi micro-properties.	177

Nomenclature

List of acronyms

3DEC	Three-Dimensional Distinct Element Code
BB	Barton–Bandis
CD	Crack Damage
CF	Continuity Factor
CGSI	Composite GSI
CI	Crack Initiation
CLFH	Cohesion-Loss and Friction-Hardening
CWFS	Cohesion-Weakening and Friction-Strengthening
DEM	Discrete Element Method
DFN	Discrete Fracture Network
Di	Damage Index
DIP	Defect Intensity \times Persistence
DISL	Damage Initiation and Spalling Limit

EDZ	Excavation Disturbed Zone
FEM	Finite Element Method
GBM	Grain-Based Models
GRC	Ground Reaction Curve
GSI	Geological Strength Index
HB	Hoek–Brown
LDP	Longitudinal Displacement Profile
MRMR	Mining Rock Mass Rating
Q	Tunneling Quality Index
RBS	Rock Block Strength
REV	Representative Elementary Volume
RMR	Rock Mass Rating
SRB	Synthetic Rock Block
SRM	Synthetic Rock Mass
UCS	Unconfined Compressive Strength
UDEC	Universal Distinct Element Code
μ DFN	micro-Discrete Fracture Network

Chapter 1

1. Introduction

1.1. Problem Statement

To ensure the temporary (short-term during construction) and permanent (long-term during operation) stability state of engineering structures built on or within rock masses, it is necessary to:

1. predict the anticipated rock mass behaviour and associated failure modes;
2. define appropriate excavation methods (i.e. drill and blast versus mechanised excavation) and construction sequence stages (i.e. advancement lengths, timing of installations, etc.); and
3. select suitable rock reinforcement and support measures.

The prediction of the anticipated rock mass behaviour prior to the specification of excavation stages and ground support measures is the most important step towards the design of safe and economic underground and surface openings. Lack of capturing the behaviour of the rock mass around excavations could influence a series of design and performance aspects such as:

- technical: rock reinforcement and support measures, excavation methods, construction sequences, excavation geometries and dimensions, etc.;

- commercial: programme, cost, profitability, bill of quantities, excavation / construction / production rates, contractual and risk allocation arrangements, construction contingencies, claims, etc.; and
- health and safety: physical and mental health integrity, hazard identification and risk management plans, safety during construction and operation, safety of property and equipment, accidents, collapses, etc.

Only when the anticipated rock mass behaviour has been properly characterised can become possible to ensure the safe and cost-effective construction of civil and mining related engineering projects (Kaiser, 2016). The realistic prediction of the rock mass behaviour and failure mechanisms is a two-fold problem which relies on the:

1. estimation of representative rock mass properties, structural characteristics and spatial variability in different scales and orientations; and
2. selection of appropriate empirical, analytical and numerical techniques.

It is clear that if a rock mass is poorly characterised during the engineering geological interpretation phase and/or if inappropriate tools are adopted for assessing the stress-deformation response of the rock mass, meaningful understanding of the intrinsic stability and rock-support interactions are lost and hence the predicted rock mass behaviour could bear little or no relationship with reality (Bandis et al., 2011).

Rock mass anisotropy and heterogeneity, scale effects, unforeseen ground conditions, limited ground investigation data, sampling bias and disturbance, time-dependant phenomena and complex coupled thermo-hydro-mechanical-chemical processes, all pose great difficulties for estimating representative properties with reasonable confidence. Consequently, the estimation of rock, joint, and rock mass properties is regarded as a very challenging task that involves high levels of uncertainty and as such requires experience and careful appreciation of all the possible interrelated factors controlling the potential rock mass responses and failure modes.

Rock block strength and deformability are significant factors controlling the rock mass behaviour and the response of the rock support and/or rock reinforcement. The rock blocks (and/or rock bridges) delineated by persistent or non-persistent discontinuities can be influenced by scale effects and the presence of micro- and meso-scale structural defects (Pierce et al., 2009). Such defects impact significantly the mechanical behaviour of blocks and it is therefore critical to account for their weakening effects (Jakubec et al., 2012). Understanding the rock block performance and their contribution to the overall rock mass behaviour is key for selecting appropriate design tools and thus to arrive at the most optimal excavation technique and support measures. Especially when the design relies on discontinuum analysis where rock blocks are modelled explicitly in between discontinuities, accurate rock block properties and appropriate constitutive relations are particularly important for capturing realistic rock mass behaviours and rock-support interactions.

Despite significant advances in rock mechanics research, numerical modelling and design, the role of defects is not typically considered as the principal focus is the assessment and characterisation of large scale discontinuities. Current methodologies to scale and express the unconfined and confined properties of rock blocks according to their size and *in-situ* heterogeneity are either incomplete or not universally accepted.

This research addresses this gap in knowledge by investigating the strength of rock blocks through a series of laboratory simulations at different scales and conditions. Grain-Based Models (GBMs) and Discrete Fracture Networks (DFNs) have been used within the Universal Distinct Element Code (UDEC) (Itasca, 2014) to assess the combined influence of scale and pre-existing defects. A numerical study is finally performed to investigate the impact of scaled rock block properties, constitutive relationships and discontinuum modelling techniques on the behaviour of underground openings excavated in massive to moderately jointed rock masses at depth.

1.2. Scale Effects in Rock Mechanics

In rock engineering, the performance of rock masses is controlled by the condition and structural pattern of discontinuities and the mechanical properties of the rock blocks between the fracture networks. The mechanical properties that are important for design are influenced by the variability/heterogeneity of both the rock material and jointing network, the size of the problem under investigation and the dimension of the samples being tested (either in-situ or in the lab) (Cunha, 1990).

Intact rock and discontinuity properties of standard small-scale specimens are routinely measured in laboratory environments following well established standards and procedures. As a result, a vast amount of published data is available in the literature and several expressions have been proposed to describe their constitutive behaviour. However, these parameters are not representative for the scale of the problem as the laboratory specimens are significantly smaller compared to the rock mass volume affected by the engineering structure (Bandis, 1990). There is a recognised problem associated with extrapolating the results of small-scale tests to the size of specific engineering concern (e.g. slopes, tunnels, foundations, etc.), due to scale effects arising from the different levels of micro/meso/macro structures involved with specimen size and/or the different degrees of geometrical irregularities with joint length.

This challenge in assigning parameters for use in rock engineering design and numerical modelling is made more difficult by the limited availability of large-scale tests and the practical difficulties in attempting to investigate larger rock volumes and discontinuities. Large-scale testing poses major difficulties due to apparatus constraints, sampling limitations, safety hazards, the absence of suitable standards, the uncertainties in interpreting the results and the costly and time-consuming operation of these experiments (DuBois, 1981; Christianson et al., 2006).

Figure 1.1 illustrates that by increasing the specimen size in a discontinuum rock mass, then a progressive denser structural pattern is captured by the different samples (i.e. from intact rock to rock mass), leading eventually to different degrees of heterogeneity and behaviour when subjected to similar test conditions (Cunha, 1990).

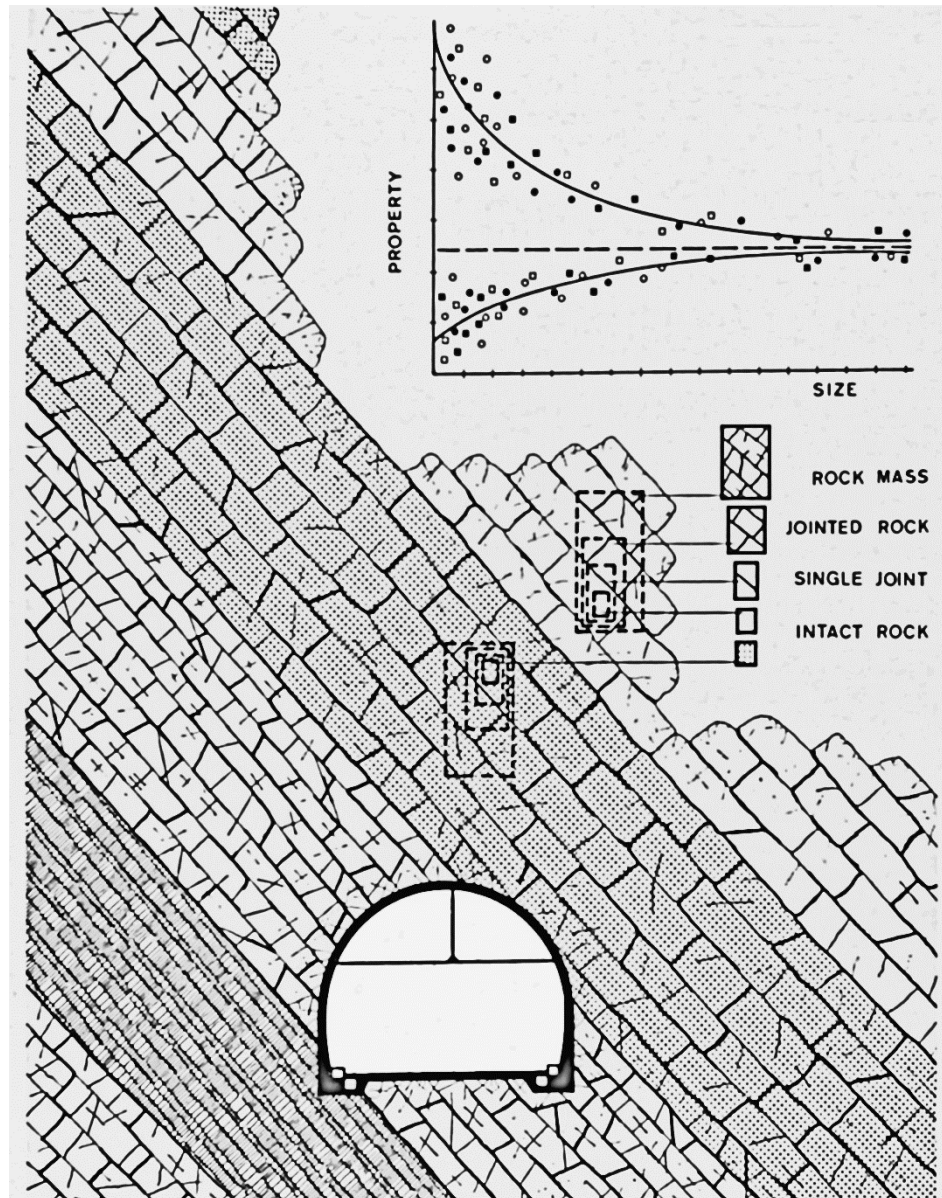


Figure 1.1. Physical-symbolic-statistical representation of scale effects (Cunha, 1990).

The property versus size diagram shown in Figure 1.1 presents in a simple way the concept of the Representative Elementary Volume (REV) and the influence of scale in a given property. The REV is essentially that critical size beyond which the scale effects become much less pronounced and the given property becomes independent of the specimen size and the density of micro- and/or macro-defects. That volume can vary between different rock mass qualities and/or lithologies and different properties could require different REV sizes to reach a minimum asymptotic trend (Cunha, 1990).

The graph in Figure 1.2 shows that for different scales (Figure 1.3), a reference REV could be reached until new types of defects are introduced with increasing specimen dimensions (Aubertin et al., 2000). The intact rock strength decreases as specimen size increases due to grain boundaries inhomogeneities and the presence of micro/meso-scale defects. As specimen size approaches that of the unit block, the effect of scale practically disappears unless macro-scale joints participate in larger volumes where strength reduces further up to that of the rock mass REV.

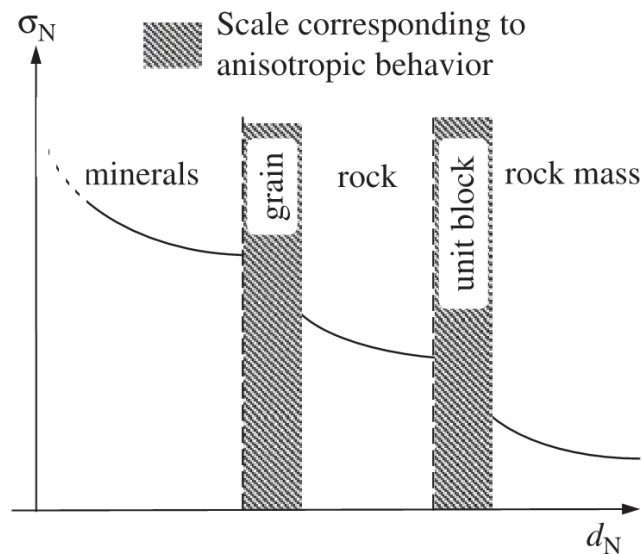


Figure 1.2. Schematic representation of scale effect on rock properties, where σ_N is the nominal strength of sample with nominal size d_N (Aubertin et al., 2000).

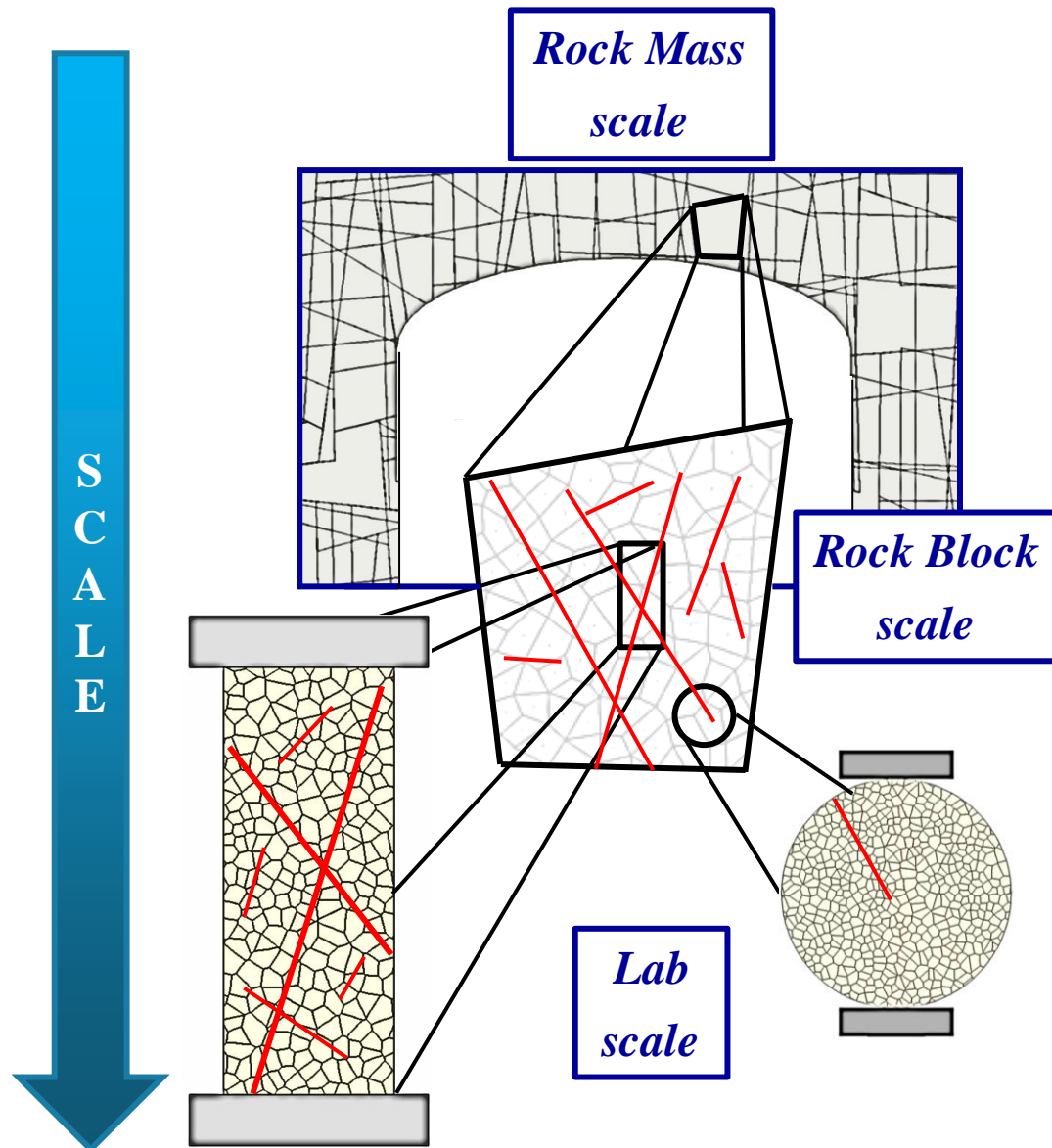


Figure 1.3. Schematic representation of samples at different scales (i.e. laboratory, rock block, and rock mass). As specimen size increases then new structural features participate in the progressive larger volumes, leading eventually to different strength reductions and REV sizes. The strength reduces due to intact rock-, rock block- and rock mass-scale heterogeneities at different scales (e.g. micro-, meso- and large-scale defects such as grain boundaries, veins and discontinuities).

The upscaling to rock mass properties has historically been treated using one or a combination of the following approaches:

1. empirical relationships between lab-scale samples and representative sizes of blocks or discontinuities such as the Hoek–Brown (Hoek and Brown, 1980a) and the Barton–Bandis (Barton and Bandis, 1982) failure criteria;
2. rock mass classification systems such as the Rock Mass Rating (RMR) (Bieniawski, 1976) and Tunneling Quality Index (Q) (Barton et al., 1974);
3. field observations, monitoring and back-analysis; and
4. Synthetic Rock Mass (SRM) modelling techniques (Mas Ivars et al., 2011).

The most well-known failure criterion to estimate the strength of a rock mass as a system was developed by Hoek and Brown (1980a; 1980b). The criterion, despite its major limitations, criticism and the lack of adequate experimental evidences, has been systematically used by the rock engineering community much beyond its initial scope and has been revised many times since 1980, most recently by Hoek and Brown (2018). In its current form, the criterion incorporates the Geological Strength Index (GSI) (Hoek, 1994; Hoek et al., 1995; Hoek and Marinos, 2000; Marinos and Hoek, 2001; Marinos and Carter, 2018) to downgrade the strength and deformation properties of the intact rock to that of the rock mass. In using the criterion, the rock mass is considered to be homogeneous and isotropic in all directions (at least three joints sets) and as a consequence it is not applicable to rock masses in which the behaviour is dominated by preferential structural weaknesses relative to the prescribed loading conditions or when individual rock blocks are more than about $1/10^{\text{th}}$ of the excavation span (Hoek and Brown, 1997). Figure 1.4 presents the limits of applicability of the criterion and the transition from an intact rock specimen to a jointed rock mass. Apart from the geometrical requirements, the Hoek–Brown (HB) criterion is also not applicable in massive to moderately hard jointed rock masses which are subjected to a state of relatively high stress conditions (Kaiser et al., 2011).

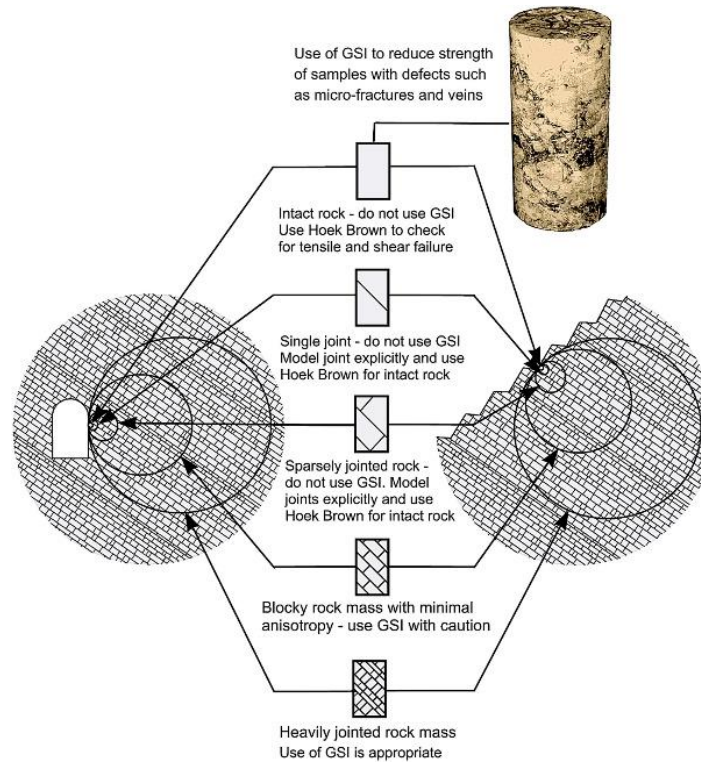


Figure 1.4. Geometrical limits for the applicability of the Hoek–Brown criterion together with size effects in rock mass characterization (Hoek and Brown, 2018).

From design and numerical modelling point of view, the equivalent continuum assumption means that the criterion can be applied only in a continuum numerical analysis (when applicable) or can only describe the homogeneous intact rock pieces of a discontinuum analysis. However, rocks are far much more complex than a continuum medium (both macroscopically and microscopically) and the individual rock blocks of a discontinuum analysis are rarely equivalent to the size of laboratory specimens. Excluding the limited cases where a rock mass can be represented as an equivalent continuum medium (c. 20% of cases) due to the high density or absence of fractures relative to the size of the excavation, it is obvious that the large-scale strength of rock blocks and discontinuities must be treated explicitly in order to evaluate the pragmatic strength and deformability of a rock mass as a system, and to capture the realistic and

essential nature of failure mechanisms (i.e. block detachment or breakage, slip or opening of discontinuities, etc.) and rock support interactions (Barton, 1998; Barla and Barla, 2000; Bandis et al., 2011). The explicit consideration of joints and rock blocks requires knowledge of their field-scale properties and as such a reasoned approach is needed to upscale their parameters from small sample to larger sizes.

For discontinuities, the work of Barton, Bandis and colleagues in the 1970-90's, formed the basis to characterise the scale-dependent strength and deformability properties of rock joints (Barton, 1976; Bandis et al., 1981; Barton and Bandis, 1982; Bandis, 1990). Based on extensive scale-effect experiments and literature review, the authors developed the Barton–Bandis (BB) constitutive law (Barton and Bandis, 1982) that relates the non-linear shear strength and stiffness of joints to the applied stress conditions and also allows for the effects of scale on the strength and roughness of the joint walls. This is shown schematically in Figure 1.5 which presents the influence of scale on the three fundamental components (i.e. an asperity failure, a geometrical and a residual frictional resistance component) of discontinuity shear strength (Bandis et al., 1981). From Figure 1.5, as the joint length (or block size) increases, then larger shear displacements are required to mobilise the ultimate and peak strengths and a reduced asperity strength and dilation are obtained due to size effects. Considering the significant scale effects on the shear strength – shear displacement of joints, then a scale effect on the shear stiffness is also expected. This is shown in Figure 1.6 which summarises shear stiffness data for different scales from the literature for a wide range of discontinuity types and normal stress conditions (Bandis et al., 1983). As can be seen, these data suggest both strong size and normal stress dependency. It is important to be mentioned that scale effects are more pronounced in unaltered rough (or irregular) undulating discontinuities while smooth and planar and/or clay infilled joints tend not to be influenced by size effects for their properties.

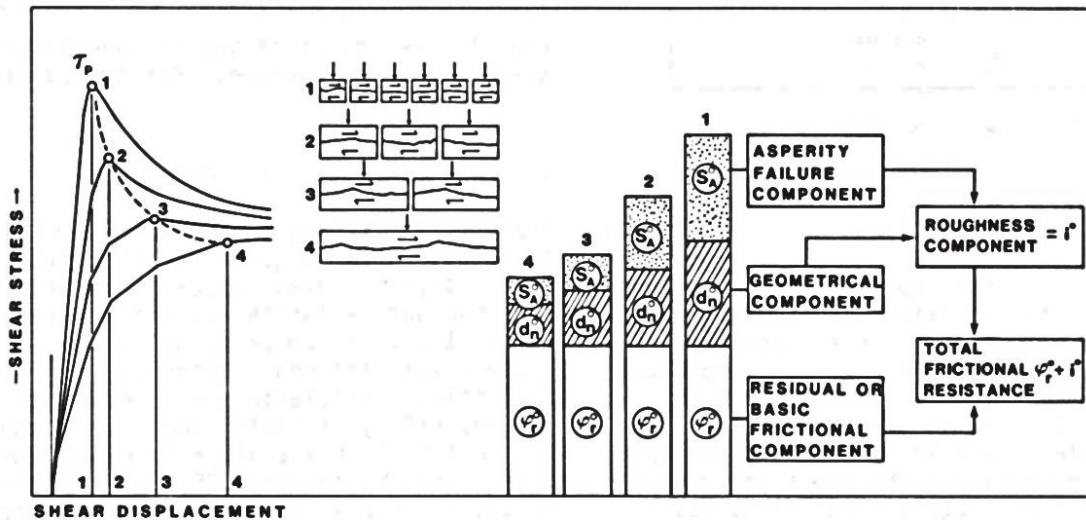


Figure 1.5. Influence of scale on the three components of shear strength of a rough discontinuity (Bandis et al., 1981).

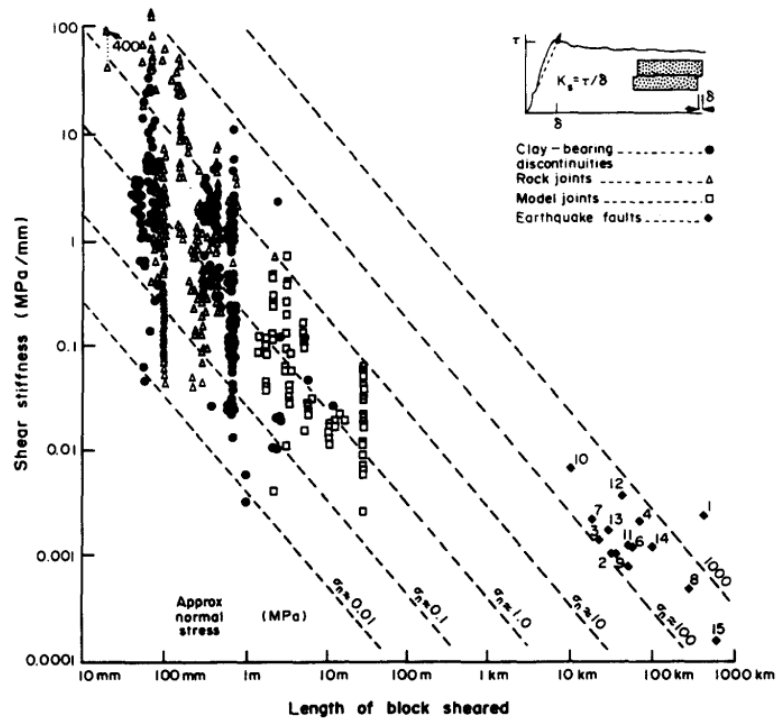


Figure 1.6. Experimental evidence for the scale and stress dependence of peak shear stiffness (Bandis et al., 1983).

For the intact rock, it is well known that the Unconfined Compressive Strength (UCS) and elastic modulus decrease with increasing sample size due to an increased heterogeneity as a function of scale and the greater probability of randomly or preferentially orientated defects to interact with each other and to create through-going failure paths into the larger rock volumes (Bieniawski, 1968; Hoek and Brown, 1997). Figure 1.7 illustrates a widely used graph for hard rocks that shows the influence of specimen size on the strength of the intact rock (Hoek and Brown, 1980b).

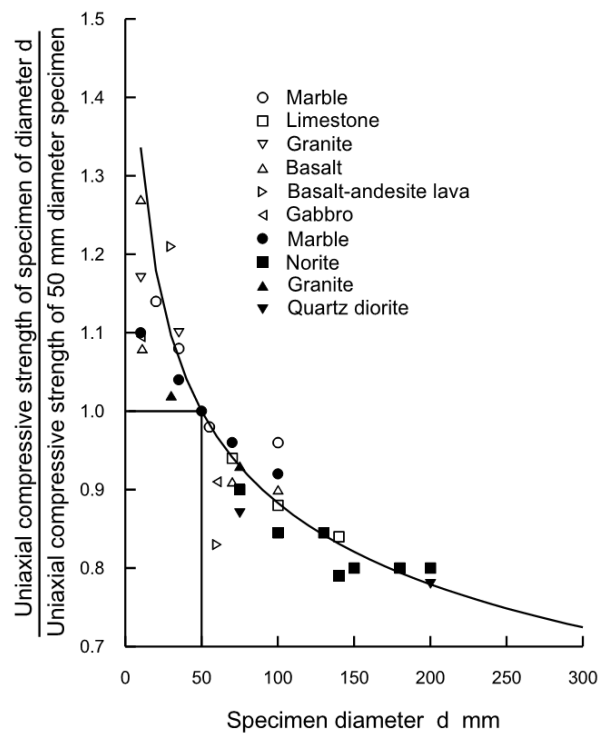


Figure 1.7. Influence of sample size on intact rock strength (Hoek and Brown, 1980b).

The inverse relationship between strength and size is more pronounced in materials associated with brittle behaviour and appears to disappear in comparatively ductile materials. Also, the size effect decreases or even vanishes in high confining pressure conditions as the influence of pre-existing defects is reduced / suppressed (Habib and Vouille, 1966; Tsur-Lavie and Denekamp, 1982; Aubertin et al., 2000).

Although the scale-effect relationship between strength and specimen size has been validated through several laboratory and *in-situ* tests for a wide range of rock types (inter alia: Mogi, 1962; Bieniawski, 1968; Pratt et al., 1972; Medhurst and Brown, 1998), currently there are only limited approaches to predict the size/quality-dependent unconfined Rock Block Strength (RBS) based on qualitative descriptions or quantitative measurements. Since most of the experiments investigating scaling effects were performed under unconfined compression conditions, the existing empirical, statistical and theoretical scale-effect relationships (inter alia: Weibull, 1951; Einstein et al., 1970; Hoek and Brown, 1980b; Carpinteri, 1994; Yoshinaka et al., 2008), are limited to the characterisation of the block UCS by simply fitting the observed strength reduction as a function of size. The only noticeable practical exception that explicitly account for rock block defects was proposed by Laubscher and Jakubec (2001) via the Mining Rock Mass Rating (MRMR) classification system which essentially introduced the concept of the RBS (Figure 1.8). The UCS of rock blocks can be estimated with the MRMR system following a series of adjustments considering the scale of the sample, the frequency of weakening micro/meso defects and their frictional properties.

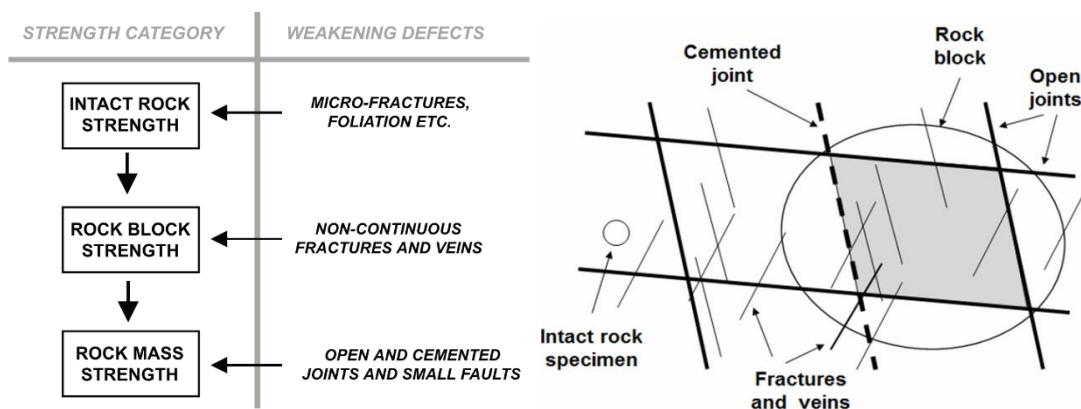


Figure 1.8. Scale concept used in the MRMR classification system due to the effect of weakening defects at different scales (Jakubec, 2013).

In confined conditions, it is again recognised that some form of strength reduction with specimen size and rock block condition exists. As shown in Figure 1.9, the strength of the unit rock block within a rock mass is expected to be in-between the strength of the intact rock (due to block-scale heterogeneities) and that of the rock mass (due to the absence of rock mass-scale heterogeneities) (Bahrani et al., 2018).

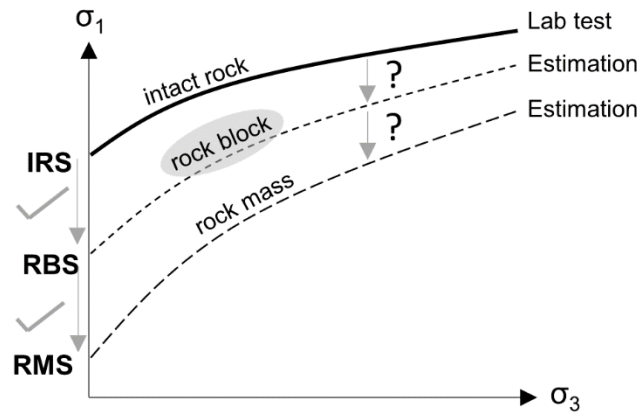


Figure 1.9. Strength degradation from intact rock to rock block due to rock block-scale heterogeneities, and from rock block to rock mass due to rock mass-scale heterogeneities as a function of confinement (Bahrani et al., 2018).

The most common tool for estimating the confined strength of defected rock blocks is the HB failure criterion by downgrading the GSI and/or the intact rock strength. However, in massive to moderately jointed rock masses at high stress environments, certain modifications are required in the HB parameters to capture the observed failures around excavations (Martin et al. 1999; Diederichs 2007). Another option for estimating the confined strength of rock blocks containing defects is the Strength Degradation Approach proposed by Bahrani and Kaiser (2017).

The effects of size and/or block condition are more pronounced at low confining stresses (e.g. near excavation boundaries), where strength is highly variable and failure processes involve the generation of stress-induced tensile cracks along local material heterogeneities and defects such as veins and micro-cracks (Figure 1.10).

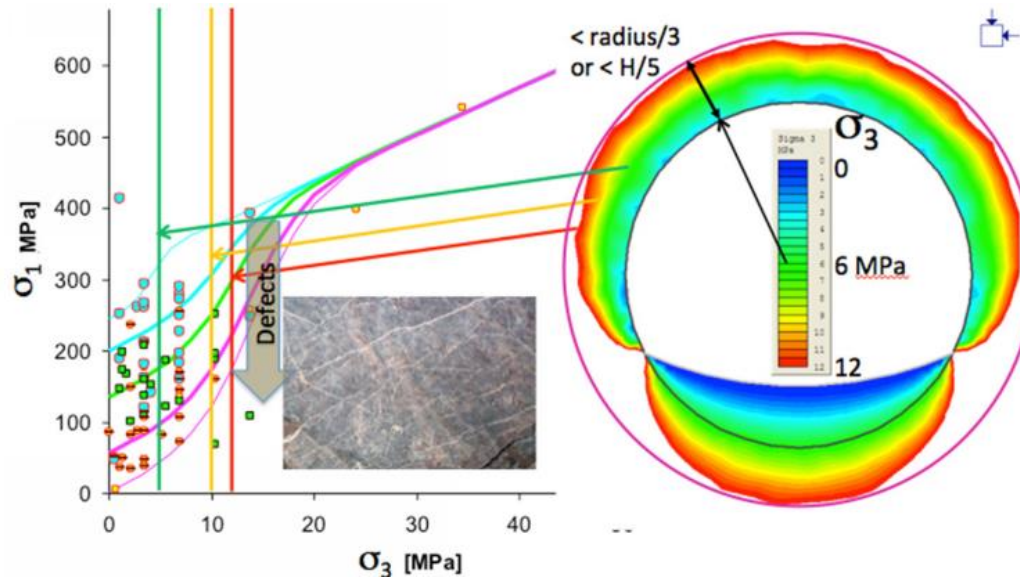


Figure 1.10. The variability of rock confined strength near excavation boundaries with a lowering of strength as the influence of defects increases (Kaiser et al., 2015).

At high confining pressures (i.e. away from the excavation boundaries) the scale effect decreases or even vanishes due to the closure of pre-existing defects and their difficulty to propagate under the influence of elevated stresses, leading eventually to mechanical homogeneity (Barton, 1976; Baecher and Einstein, 1981). This was shown experimentally by Hoek and Bieniawski (1965) who found a strong dependency between the length of the stable propagated cracks and the applied confinement (Figure 1.11).

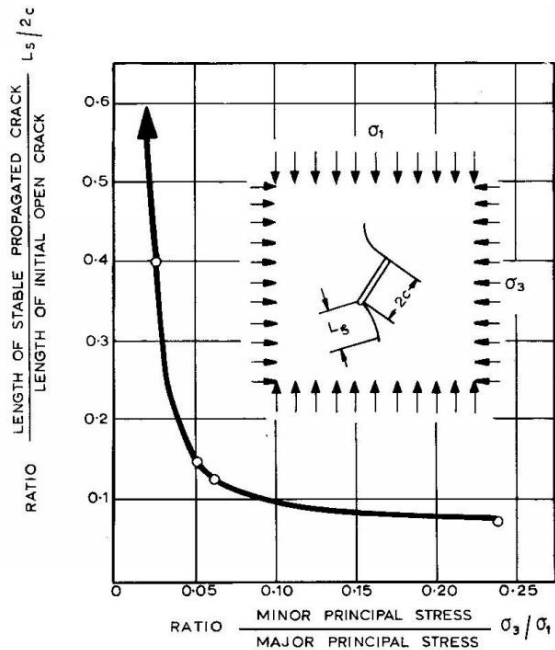


Figure 1.11. Relationship between stable crack length and ratio of applied stresses (Hoek and Bieniawski, 1965).

1.3. Anticipated Rock Mass Behaviour

Hoek et al. (1995) proposed the well-established tunnel instability and modes of failure matrix shown in Figure 1.12 to describe the types of rock mass behaviours commonly anticipated / encountered around underground openings.

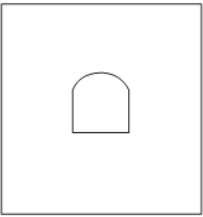
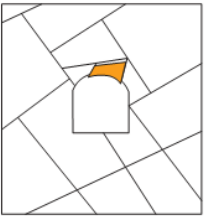
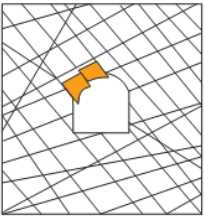
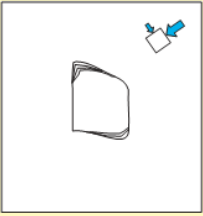
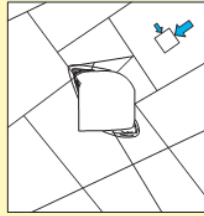
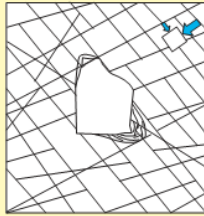
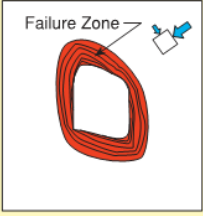
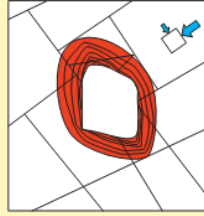
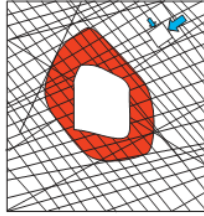
	Massive ($GSI > 75$)	Moderately Fractured ($50 > GSI < 75$)	Highly Fractured ($GSI < 50$)	
Low In-Situ Stress ($\sigma_1 / \sigma_3 > 0.15$)	 <p>Linear elastic response.</p>	 <p>Falling or sliding of blocks and wedges.</p>	 <p>Unravelling of blocks from the excavation surface.</p>	$D_i < 0.4 (\pm 0.1)$
Intermediate In-Situ Stress ($0.15 < \sigma_1 / \sigma_3 < 0.4$)	 <p>Brittle failure adjacent to excavation boundary.</p>	 <p>Localized brittle failure of intact rock and movement of blocks.</p>	 <p>Localized brittle failure of intact rock and unravelling along discontinuities.</p>	$0.4 (\pm 0.1) > D_i < 1.1 (\pm 0.1)$
High In-Situ Stress ($\sigma_1 / \sigma_3 < 0.4$)	 <p>Failure Zone</p> <p>Brittle failure around the excavation.</p>	 <p>Brittle failure of intact rock around the excavation and movement of blocks.</p>	 <p>Squeezing and swelling rocks. Elastic/plastic continuum.</p>	$D_i > 1.1 (\pm 0.1)$

Figure 1.12. Tunnel instability and modes of failure around underground excavations (Hoek et al., 1995), modified by Martin et al. (1999) and Martin et al. (2001).

From the matrix of Figure 1.12, the different instability mechanisms are categorised based on the interrelationship between three factors:

1. the rock mass quality (i.e. blockiness and discontinuity surface condition), expressed as a function of the GSI;
2. the UCS of the intact rock obtained from triaxial compressive testing according to Hoek and Brown (1988);
3. the pre- or post-excavation stress conditions:
 - a. the pre-excavation maximum in-situ stress magnitude at the level of the excavation (left-hand column of matrix in Figure 1.12); and/or
 - b. the post-excavation maximum tangential stress on the boundary of a circular opening (right-hand column of matrix in Figure 1.12);

Depending on the combination of these factors, rock masses around excavations can fail due to three general failure modes (Martin et al., 2003):

1. structurally controlled gravity-driven failures of blocks in low in-situ stress environments or zones of low confinement (e.g. tunnel junctions);
2. stress-induced brittle spalling and slabbing through intact material in highly stressed rock masses (typical in massive to moderate jointed rock masses);
3. a combined stress-induced intact rock fracturing and structurally driven block movement along discontinuities at intermediate stress conditions.

Each of these potential behaviours requires specific design tools, construction methods and support systems. Therefore, lack of understanding the anticipated rock mass behaviour could lead to inappropriate decisions and ineffective designs. From constructability point of view, when moving to the right of the matrix due to decreasing rock mass quality and then downwards due to increasing stress conditions, several problems are anticipated in the form of reduced stand-up times, slower excavation rates, face instability issues, increased convergence and thicker disturbance zones.

Although the structurally controlled failures are typically associated with shallow depths (i.e. low stress levels) and the stress-driven mechanisms are commonly observed at great depths, (i.e. high stress levels), in practise it has been proven that these failure modes can occur essentially at any depth (Martin et al., 2001). For example, in large caverns or in tunnel junctions at great depths, wedge-type failures could dominate the failure processes due to loss of confinement and the presence of unfavourably orientated joint sets. In contrast, the failure of rock masses at shallow depths which are subjected to relatively high locked-in tectonic stresses (e.g. Hawkesbury Sandstone in Sydney), could be driven by stress-induced fracturing rather than gravity driven blocks. Another factor that drives the mobilisation of different failure modes within the same stress and rock mass conditions is the shape and sequencing of the excavations as different excavation geometries will promote different stress paths. In the case of the combined stress-structure failure mode, brittle failure through extensional fracturing needs to occur first within the interlocked rock blocks or the massive rock mass in order to disrupt the continuity of the medium and as such as to create enough kinematic freedom for blocks to rotate and/or slip (Martin et al., 2001). A matrix of photographic representations for the various tunnel instability modes is given in Figure 1.13.

In general, as the stress levels increase (either due to depth or subsequent construction stages), the pre-existing discontinuities become locked and the failure modes become more brittle. At moderate stress magnitudes, only localised stress damage is expected near the excavation boundary but in highly stressed rock masses the stress-induced fracturing involves thick disturbance zones around the whole excavation (Figure 1.12).

This thesis focuses on the yellow highlighted behaviours of Figure 1.12 and more specifically to moderately hard jointed and blocky rock masses at moderate to high stress levels. In these conditions, stress-induced fracturing within the rock blocks is anticipated, combined with structural failures depending on the level of confinement.

	Stress	Low	Moderate	High
Rock Mass Strength	Sheared			
	Blocky			
	Massive			

Figure 1.13. Matrix of photographic representations for the various tunnel instability failure modes from relevant literature (Hoek et al., 1995; Kaiser et al., 2000; Hoek, 2001; Hoek et al., 2008; Hoek and Brown, 2018).

As an attempt to assess the potential for stress-induced brittle failure, Martin et al. (1999) proposed the Damage Index (D_i) shown at the right axis in Figure 1.12, which is the ratio of the maximum tangential stress ($\sigma_{max} = 3 \sigma_1 - \sigma_3$) on the boundary of a circular opening to the laboratory UCS. Compared to only considering the pre-excavation stress magnitudes, the σ_{max} is a better indicator for quantifying the impact of stresses on the anticipated stress-driven instabilities, as considers both the minor and major principal stresses and hence accounts for the stress anisotropy (Kaiser, 2016).

However, considering that the strength of rock blocks is strongly influenced by scaling effects, the intensity of structural micro/meso-defects and the degree of weathering, Kaiser (2016) emphasized that it is essential to establish the rock block strength when using the behavioural matrix of Figure 1.12. Figure 1.14 presents an updated version of Figure 1.12 where the anticipated failure modes are expressed as a function of the block strength and the maximum tangential stresses around the excavation. Given that the rock block strength is one of the predominant factors controlling the behaviour of massive and moderately jointed rock masses (Kaiser et al., 2015), the extent of the disturbed zone around an excavation (Shen and Barton, 1997) and the response of the structural elements used as support (Stavrou et al., 2015), it is clear that it needs to be characterised and estimated as accurately as possible.

Also shown in Figure 1.14, are the limits of the GSI approach applicability. In the cases where tensile fracturing is expected within the rock blocks then the block strength dominates the behaviour (GSI not applicable), while when shear-dominated behaviour occurs then failure modes are driven by block sliding and rotation (GSI applicable) (Kaiser, 2016). When the conventional HB criterion is not applicable, the traditional HB parameters need modifications. Once the rock block strength under unconfined conditions has been defined, then the failure envelope in the principal stress space can be established following the Damage Initiation and Spalling Limit (DISL) approach proposed by Diederichs (2007) or the procedure described by Kaiser (2016).

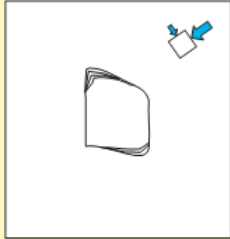
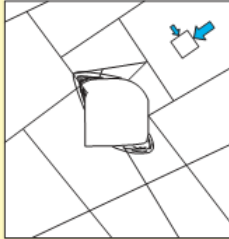
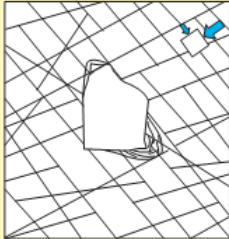
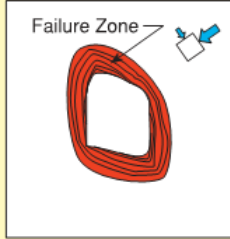

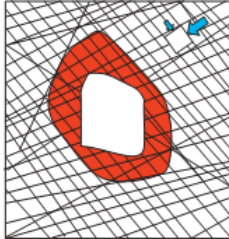
	GSI > 65 GSI not applicable Rock block strength dominates	GSI < 65 GSI applicable Rock block rotation dominates	
Intermediate Induced Stress $0.4 \pm 0.1 < \sigma_{\max} / \sigma_c < 1.15 \pm 0.1$	 <p style="text-align: center;">Brittle failure adjacent to excavation boundary.</p>	 <p style="text-align: center;">Localized brittle failure of intact rock and movement of blocks.</p>	 <p style="text-align: center;">Localized brittle failure of intact rock and unravelling along discontinuities.</p>
High Mining-Induced Stress $\sigma_{\max} / \sigma_c > 1.15 \pm 0.1$	 <p style="text-align: center;">Failure Zone</p> <p style="text-align: center;">Brittle failure around the excavation .</p>	 <p style="text-align: center;">Brittle failure of intact rock around the excavation and movement of blocks.</p>	 <p style="text-align: center;">Squeezing and swelling rocks. Elastic/plastic continuum.</p>

Figure 1.14. Limits of applicability of GSI approach for rock mass strength characterisation in relation to the rock block strength (Kaiser, 2016).

The failure envelopes in these modified versions follow an S- or tri-linear shape to account for the anticipated stress-induced fracturing near the excavation boundaries (Kaiser et al., 2000; Diederichs, 2007). The fundamental difference between the conventional HB (and the equivalent Mohr–Coulomb) strength envelopes and the modified brittle models, is that the latter is not mobilising simultaneously the cohesive and frictional components of strength at low confinements, but allows for significant cohesion loss before activating the frictional strength (Martin, 1997; Carter et al. 2008).

At low confinements, the S-linear envelope strength drops to a lower bound field threshold called the Crack Initiation (CI) (typically approximately 35-55% of UCS), while at higher confining stresses the envelope makes a transition up to the envelope defined by the Crack Damage threshold (CD) (typically approximately 70-90% of UCS). The concept of the S- or tri-linear failure envelopes is shown in Figure 1.15 together with the three anticipated rock mass responses (i.e. no damage, spalling failure and tensile-ravelling failure) commonly observed in massive to moderately jointed rock masses (Diederichs, 2003). This model is typically applicable to hard brittle rocks as other rock types such as weak and soft mudstones or siltstones will fail in shear or will exhibit a combined (transitional) behaviour (Perras et al., 2013).

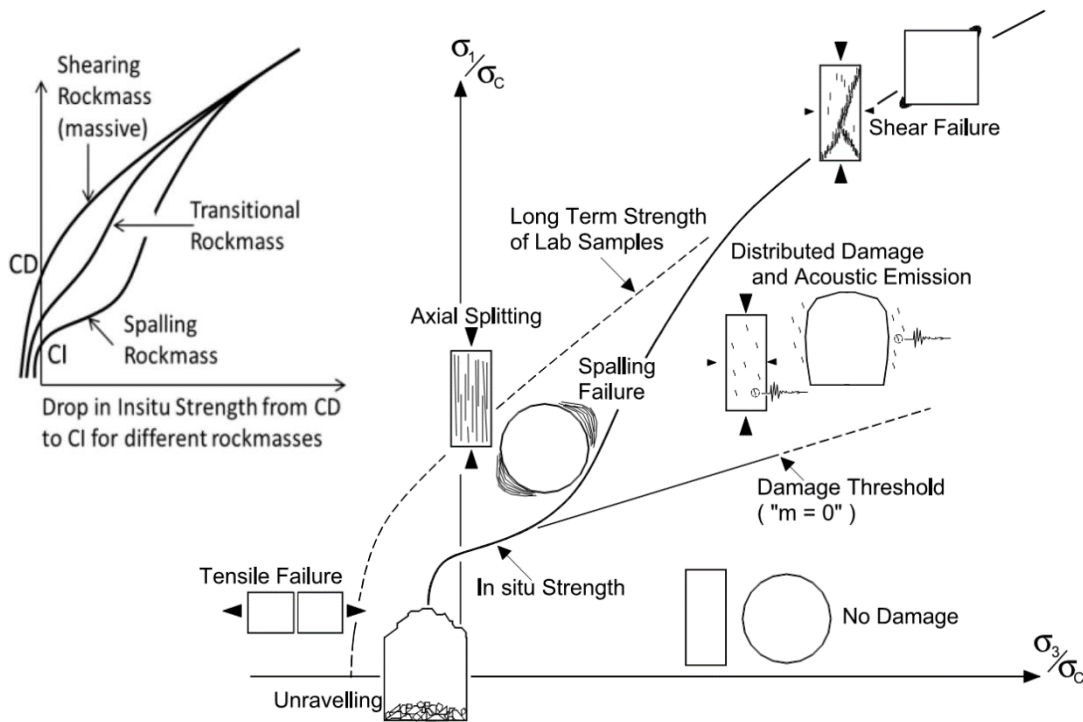


Figure 1.15. Schematic of DISL model for spalling rocks, showing four zones of distinct rock mass failure mechanisms: no damage, shear failure, spalling, and unravelling. σ_c is the UCS of laboratory samples (Diederichs, 2003). Other rock types yield in shear or show a combined (transitional) behaviour (Perras et al., 2013).

1.4. Numerical Approach

The numerical approaches typically adopted to simulate the behaviour of rock masses around underground excavations can generally be divided into three categories: i) continuum modelling; ii) discontinuum or discrete modelling; and iii) hybrid continuum/discrete modelling (Coggan et al., 2012). Coggan et al. (2012) provide a summary for the capabilities, advantages and limitations for each of these methods.

In the continuum approach, the rock mass is represented as an equivalent continuum medium in which isotropic or anisotropic constitutive models are assigned based on the REV concept. In the discontinuum approach, geological structure is modelled explicitly, and the rock mass is represented as an assembly of deformable rock blocks which are separated by discontinuities. The hybrid continuum/discrete approach combines the continuum and discontinuum methods and allows fracturing through intact rock material following fracture mechanics criteria.

The choice between continuum and discontinuum modelling depends on the anticipated failure mechanisms and the condition and geometry of the fracture network in relation to the size of the problem (i.e. tunnel or cavern span, shaft diameter, slope height) under investigation (Figure 1.16). Deere and Miller (1966) suggested that when the discontinuity spacing compared to the tunnel diameter has a ratio approximately between 1/5 and 1/100, then a rock mass can be treated as a discontinuum material. In cases of ratios outside these limits, then a rock mass can be classified as being a continuous medium, though it could behave in an anisotropic manner. Barton (1998) provided the schematic diagram shown in Figure 1.17 in which the selection of appropriate numerical method is based on a range of suggested Q-values (i.e. rock mass quality). According to Figure 1.17, for Q-values between 0.1 and 100 the discontinuum modelling will be more appropriate than the continuum modelling method.

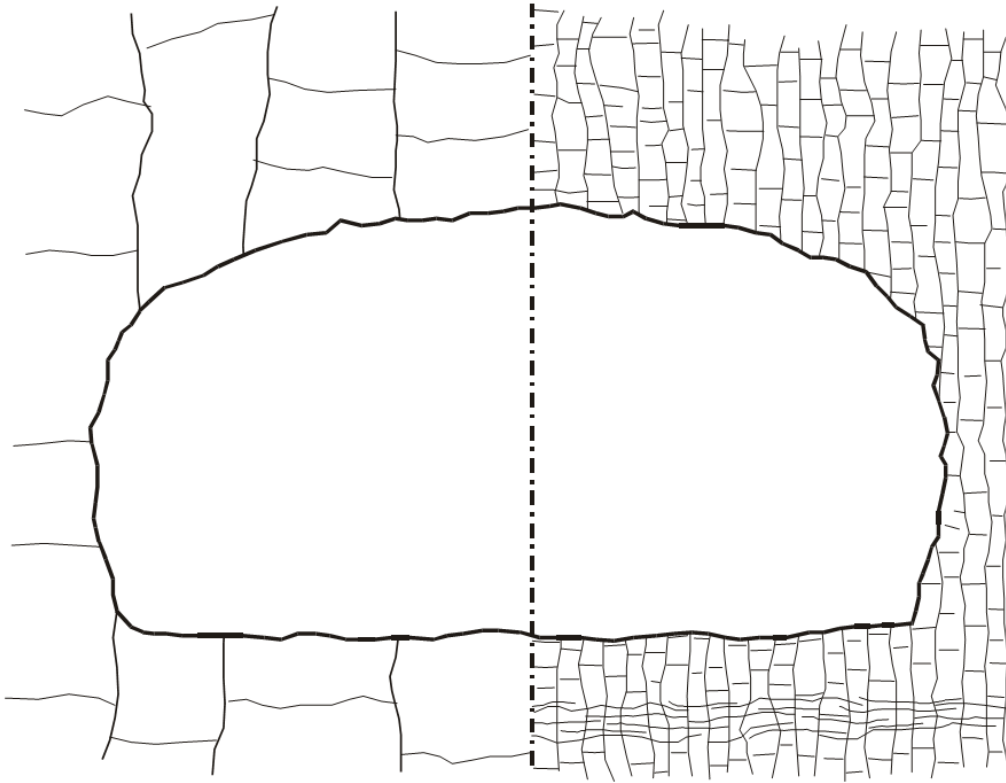


Figure 1.16. The difference between discontinuous and continuous materials in a tunnel of similar size (revised by Palmstrom (1995) from Barton (1990)).

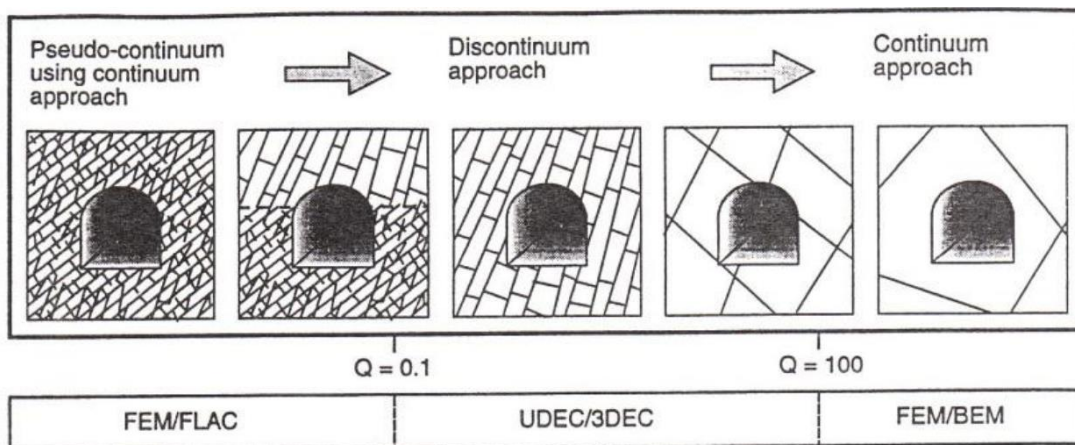


Figure 1.17. Schematic diagram suggesting the range of application of discontinuum modelling (UDEC and 3DEC) in relation to the Q -value (Barton, 1998).

By incorporating the scale of the excavation in relation to the degree of jointing and the most widely used rock mass classification systems (i.e. Q, RMR, GSI), Bandis et al. (2011) defined a broad range of rock mass types and specific rock mass conditions at which each numerical method is applicable (Figure 1.18). According to this work, the discontinuum and equivalent-continuum approaches are applicable to more than 80% and less than 20% of rock masses respectively.

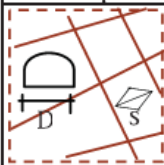
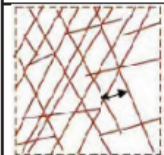

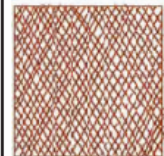
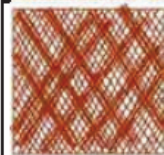
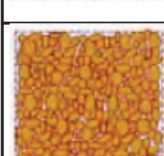
Description of rock mass	Analysis		Classification
 Intact massive $s > 2\text{m}$ $D/s < 5$	Continuum	FEM, BEM	$Q > 1000$ $\text{RMR} > 80$ $\text{GSI} > 80$
 Jointed $s = 0.5 - 2.0\text{m}$ $D/s = 5 - 20$	Discontinuum	DEM	$Q = > 10 - 100$ $\text{RMR} = 61 - 80$ $\text{GSI} = > 40 - 80$ (applicable?)
 Bedded $s = 0.1 - 0.5\text{m}$ $D/s = 20 - 100$			$Q = > 1 - 10$ $\text{RMR} = 41 - 60$ $\text{GSI} = > 30 - 40$ (applicable?)
 Very densely jointed $s = 0.05 - 0.1\text{m}$ $D/s = 100 - 1000$			$Q = 0.1 - 1$ $\text{RMR} = 21 - 40$ $\text{GSI} = > 20 - 30$ (applicable?)
 Tectonically disturbed $s < 0.1\text{m}$ $D/s > 500$	Equiv. Contin.	FEM, FDM	$Q < 0.1$ $\text{RMR} < 21$ $\text{GSI} < 20$
 Rockfill or talus material $d = 0.01 - 0.5\text{m}$ $D/d > 10000$	Continuum	FEM, FDM	$Q < 0.01$ RMR, GSI not applicable

Figure 1.18. Broad distinction of rock mass types in relation to classification and method of analysis (Bandis et al., 2011).

To distinguish between continuous and discontinuous rock masses, Palmstrom (1995) proposed a Continuity Factor (CF) which considers that the problem depends on the relative block size (i.e. tunnel diameter or span / block size). According to this concept, underground excavations of different sizes will behave differently when excavated in the same jointed rock mass (Figure 1.19). For a CF between 3 and 30 (i.e. discontinuous-blocky), the analysis should consider the explicit simulation of discrete blocks, while if CF is less than 6 (i.e. continuous-intact) or greater than 15 (i.e. continuous-bulky) then the overall behaviour should be described as a continuous material. The complex continuous-discontinuous overlapping “grey” zones of the CF imply that good engineering judgment is required in selecting appropriate methods of numerical analysis (Stille and Palmström, 2008).

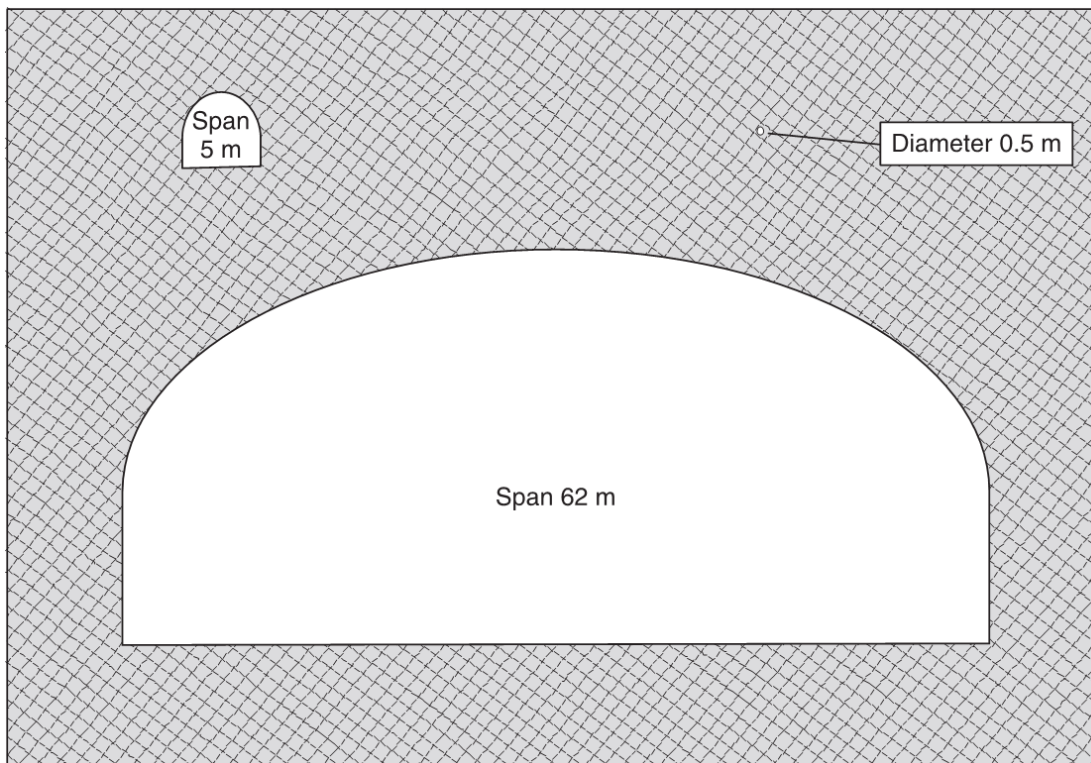


Figure 1.19. Three different underground excavations located in the same jointed rock mass. The CF vary significantly with the tunnel size (Stille and Palmström, 2008).

Shin (2010) considered the nature and extent of the Excavation Disturbance Zones (EDZ) in hard rocks to define suitable techniques for modelling. Depending on the anticipated EDZ characteristics, their behaviour is classified as follows:

- Class-I in massive rock under low in-situ stresses ($\sigma_1 \approx \sigma_3$);
- Class-II in fractured rock under low to medium in-situ stresses ($\sigma_1 > \sigma_3$);
- Class-III in massive rock under relatively high stresses ($\sigma_1 \gg \sigma_3$).

Class-I EDZ is typically analysed using continuum models while Class-II and Class-III EDZs require to capture the block/wedge movement/rotation along pre-existing discontinuities (block model) and/or the extensional damage leading to the generation and development of micro and macro-scale fractures (damage model). Figure 1.20 illustrates the three EDZ zones, together with the different geological conditions and expected rock mass processes and responses (e.g. elastic versus non elastic deformation, deformation of pre-existing or newly generated cracks, etc.) (Shin, 2010).

In general, it is well accepted across the rock engineering community that the discontinuum approach provides the most appropriate modelling technique for simulating the anisotropic and discontinuous nature of most rock mass conditions. In the early years of discontinuum analysis it was not feasible to incorporate all the as-logged/mapped joint data and for computational reasons the modellers were selecting only a limited amount of “critical” joints, typically those which were characterised as more prominent or more systematic. To allow for the weakening effect of the joints not included explicitly in the analysis, equivalent and reduced strength and stiffness parameters were assigned to the solid material (i.e. the “effective” block size) separated by the “critical” joints. Through significant advances in the numerical capabilities and computational power, it has become possible to explicitly represent the “natural” distribution of blocks sizes and/or to use GBMs to capture the fragmentation of rock blocks at the mineral and/or micro-defect level (Fairhurst, 2017).

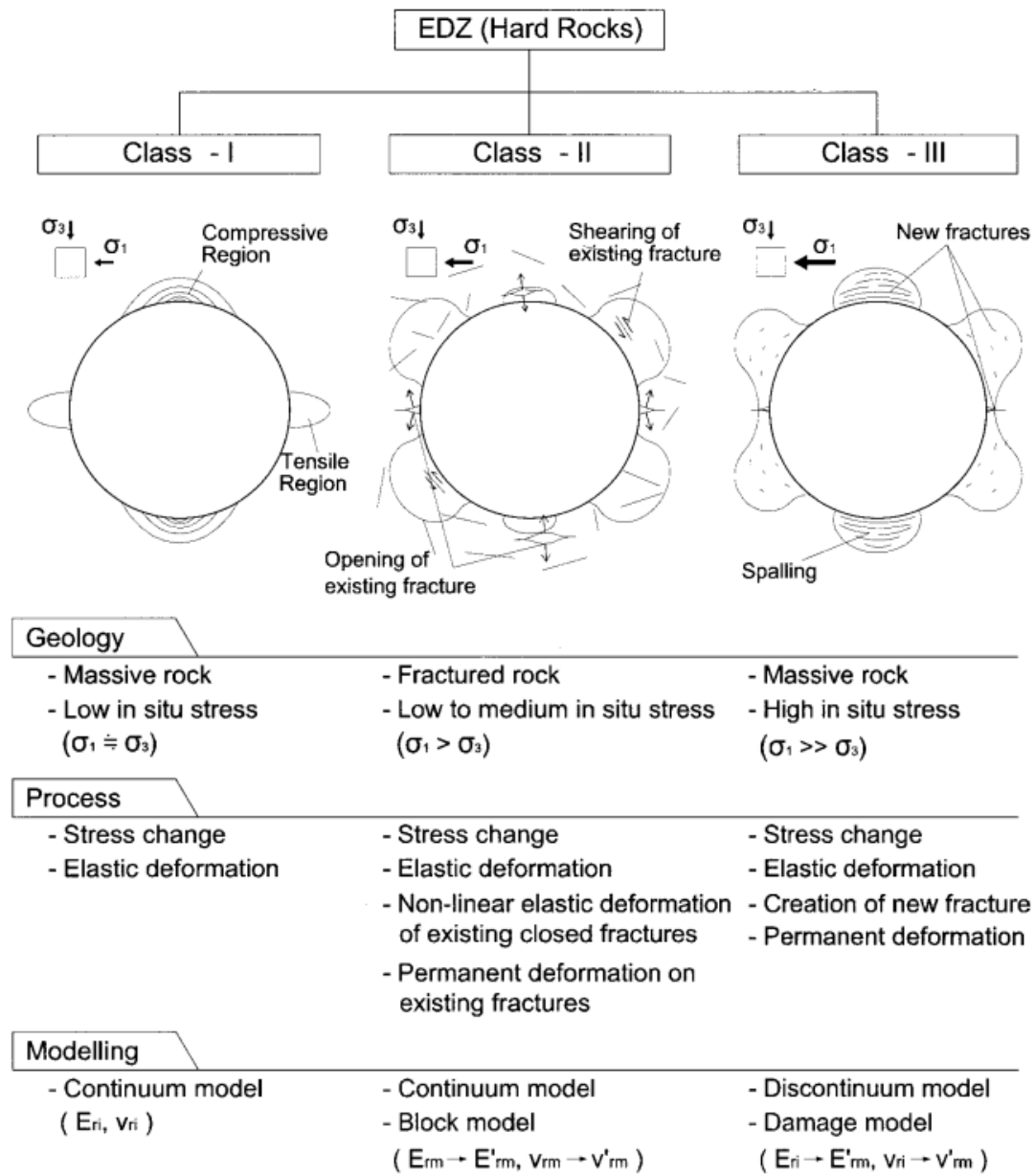


Figure 1.20. Definitions of the EDZ with the same shape and dimension in hard rock under different geological conditions (Shin, 2010).

Of particular importance in the field of discontinuum modelling is the development of the SRM modelling technique (Pierce et al., 2007). In a SRM model, pre-existing joints in the form of DFNs are embedded into a pseudo-continuum intact rock matrix as shown in Figure 1.21. The intact rock material is represented as an assembly of polygonal or spherical elements which are bonded together at their contacts. Depending on the imposed loads the bonds can break, thus allowing to simulate dynamically the fundamental processes of intact rock fracturing and rock mass disintegration (i.e. crack initiation, propagation, interaction and coalescence) (Mas Ivars et al., 2011).

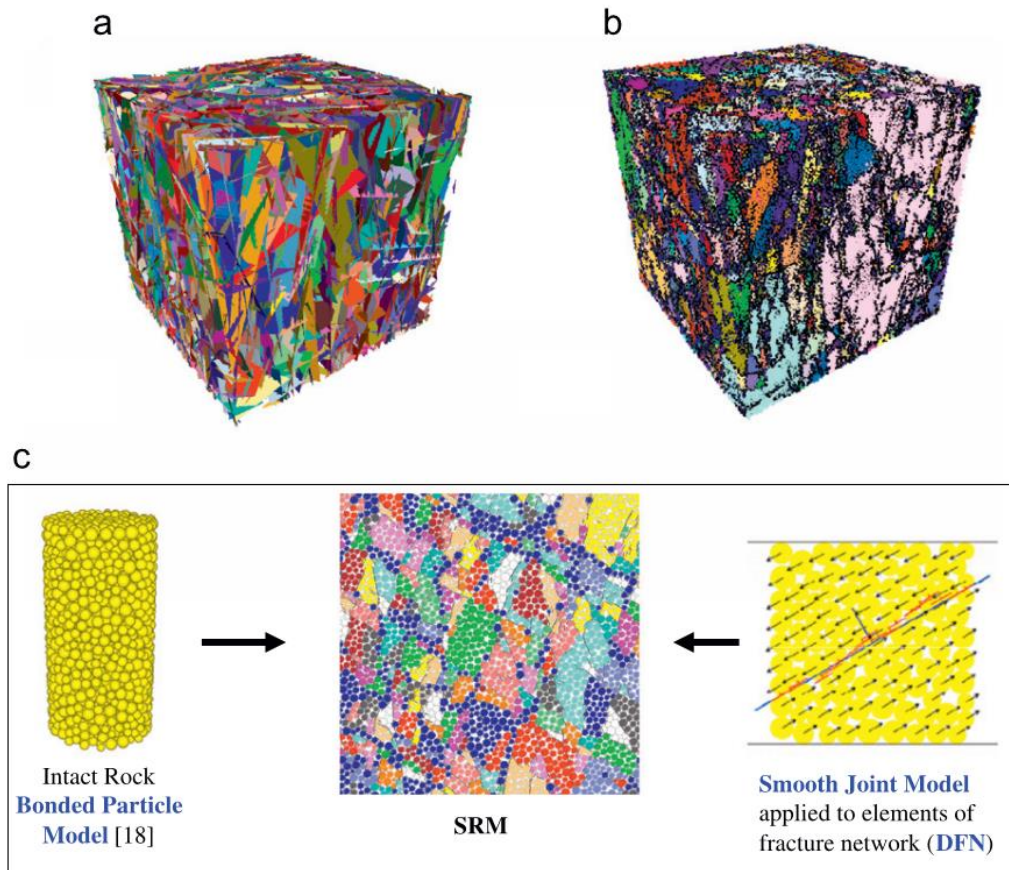


Figure 1.21. (a) 3D DFN, (b) the corresponding three-dimensional synthetic rock mass sample, and (c) synthetic rock mass basic components (Mas Ivars et al., 2011).

1.5. Thesis Structure

The focus of this research was initially to quantify the unconfined and confined strengths of homogenous and heterogenous rock blocks, and subsequently to assess the impact of scaled rock block properties and modelling techniques on the behaviour of underground excavations. This thesis consists of five chapters, as outlined below.

Chapter 2 presents a numerical study that was performed to develop a framework for estimating the confined strength of rock blocks considering scale effects and in-situ heterogeneity. Grain boundary models within UDEC were used to simulate a series of progressively larger in size and degrading in quality numerical specimens under unconfined and confined conditions. Accordingly, relationships that link the rock block strength with its volume and in-situ condition were developed for the preliminary estimation of scaled Mohr–Coulomb and Hoek–Brown parameters.

Chapter 3 presents a numerical study that was performed to develop a practical tool for quantifying the unconfined strength of defected rock blocks. Various DFNs previously generated with FracMan were integrated into UDEC GBMs to assess the strength of defected rock blocks. Several UCS tests were simulated on samples of varying sizes and defect geometries/strengths and refined approaches were proposed for estimating the unconfined strength of rock blocks as a function of specimen size, defect intensity, persistence and strength.

Chapter 4 presents a tunnel-scale numerical study that was performed to investigate the impact of block properties, constitutive relationships and modelling techniques on the behaviour of deep openings in moderately jointed rock masses.

Chapter 5 presents a discussion of the publications included in Chapters 2, 3 and 4 and describes the original contribution to knowledge in the field of engineering rock mechanics. This Chapter also identifies directions for future studies.

References

- Aubertin, M., Li, L. and Simon, R. 2000. A multiaxial stress criterion for short- and long-term strength of isotropic rock media. *International Journal of Rock Mechanics and Mining Sciences*. 37(8), pp.1169–1193.
- Baecher, G.B. and Einstein, H.H., 1981. Size effect in rock testing. *Geophysical Research Letters*, 8(7), pp.671-674.
- Bahrani, N. and Kaiser, P.K. 2017. Estimation of Confined Peak Strength of Crack-Damaged Rocks. *Rock Mechanics and Rock Engineering*. 50(2), pp.309–326.
- Bahrani, N., Kaiser, P.K. and Corkum, A. 2018. Suggested methods for estimation of confined strength of heterogeneous (defected) rocks. *Caving 2018, Vancouver, Canada*.
- Bandis, S.C. 1990. Scale effects in the strength and deformability of rocks and rock joints *In: Proceedings of the 1st International Workshop on Scale Effects in Rock Masses, Loen, Norway. Edited by A. Pinto da Cunha. AA Balkema, Rotterdam., pp.59–76.*
- Bandis, S., Lumsden, A.C. and Barton, N.R. 1981. Experimental studies of scale effects on the shear behaviour of rock joints *In: International journal of rock mechanics and mining sciences & geomechanics abstracts*. Elsevier, pp.1–21.
- Bandis, S.C., Lumsden, A.C. and Barton, N.R. 1983. Fundamentals of rock joint deformation *In: International Journal of Rock Mechanics and Mining Sciences & Geomechanics Abstracts*. Elsevier, pp.249–268.
- Bandis, S.C., Sharp, J.C., Mackean, R.A. and Bacasis, E.A. 2011. Explicit Characterisation and Interactive Analysis for Engineering Design of Rock Caverns *In: Proceedings of the Joint Hong Kong Institute of Engineers – Hong*

- Kong Institute of Planning Conference on Planning and Development of Underground Space.*, pp.133–142.
- Barla, G. and Barla, M. 2000. Continuum and discontinuum modelling in tunnel engineering. *Rudarsko-Geolosko-Naftni Zbornik*. 12(1), p.45.
- Barton, N. 1976. The shear strength of rock and rock joints. *International Journal of Rock Mechanics and Mining Sciences & Geomechanics Abstracts*. 13(9), pp.255–279.
- Barton, N. 1990. Scale effects or sampling bias? *In: Int. Workshop on Scale Effects in Rock Masses*. Balkema, Rotterdam, pp.31–55.
- Barton, N. 1998. Quantitative description of rock masses for the design of NMT reinforcement *In: Keynote Lecture, Int. Conf. on Hydro Power Development in Himalayas, Shimla, India, Balkema, Rotterdam*.
- Barton, N., Lien, R. and Lunde, J. 1974. Engineering classification of rock masses for the design of tunnel support. *Rock mechanics*, 6(4), pp.189-236.
- Barton, N. and Bandis, S. 1982. Effects Of Block Size On The Shear Behavior Of Jointed Rock *In: The 23rd U.S Symposium on Rock Mechanics (USRMS)*., pp.739–760.
- Bieniawski, Z.T. 1968. Propagation of brittle fracture in rock *In: the 10th US Symposium on Rock Mechanics (USRMS)*. American Rock Mechanics Association.
- Bieniawski, Z.T. 1976. Rock mass classification in rock engineering applications. *In Proceedings of a Symposium on Exploration for Rock Engineering, 1976* (Vol. 12, pp. 97–106).
- Carpinteri, A. 1994. Fractal nature of material microstructure and size effects on apparent mechanical properties. *Mechanics of Materials*. 18(2), pp.89–101.

- Carter, T.G., Diederichs, M.S. and Carvalho, J.L. 2008. Application of modified Hoek–Brown transition relationships for assessing strength and post yield behaviour at both ends of the rock competence scale. *Journal of the Southern African Institute of Mining and Metallurgy*. 108(6), pp.325–338.
- Christianson, M., Board, M. and Rigby, D. 2006. UDEC simulation of triaxial testing of lithophysal tuff In: *The 41st U.S. Symposium on Rock Mechanics (USRMS)*. American Rock Mechanics Association.
- Coggan, J., Gao, F., Stead, D. and Elmo, D. 2012. Numerical modelling of the effects of weak immediate roof lithology on coal mine roadway stability. *International Journal of Coal Geology*. 90, pp.100–109.
- Cunha, A.P. 1990. Scale effects in rock mechanics In: *Proceedings of the 1st International Workshop on Scale Effects in Rock Masses, Loen, Norway*. Edited by A. Pinto da Cunha. AA Balkema, Rotterdam., pp.3–27.
- Deere, D.U. and Miller, R.P. 1966. *Engineering classification and index properties for intact rock*. Illinois Univ At Urbana Dept Of Civil Engineering.
- Diederichs, M.S. 2003. Manuel rocha medal recipient rock fracture and collapse under low confinement conditions. *Rock Mechanics and Rock Engineering*. 36(5), pp.339–381.
- Diederichs, M.S. 2007. The 2003 Canadian Geotechnical Colloquium: Mechanistic interpretation and practical application of damage and spalling prediction criteria for deep tunnelling. *Canadian Geotechnical Journal*. 44(9), pp.1082–1116.
- DuBois, A. 1981. Factors in the design and manufacture of large high pressure and high temperature triaxial cells. *Geophysical Research Letters*. 8(7), pp.683–686.
- Einstein, H.H., Baecher, G.B. and Hirschfeld, R.C. 1970. The effect of size on strength of a brittle rock. *International Society of Rock Mechanics, Proceedings*. 1(1–19).

- Fairhurst, C., 2017. Some challenges of deep mining. *Engineering*, 3(4), pp.527–537.
- Habib, P. and Vouille, G. 1966. Sur la disparition de l'effet d'échelle aux hautes pressions. *Comptes Rendus Acad. Sc. Paris*. 626, pp.715–717.
- Hoek, E. 1994. Strength of rock and rock masses. *ISRM News Journal*. 2(2), pp.4–16.
- Hoek, E. 2001. Big tunnels in bad rock. *Journal of Geotechnical and Geoenvironmental Engineering*. 127(9), pp.726–740.
- Hoek, E. and Bieniawski, Z.T. 1965. Brittle fracture propagation in rock under compression. *International Journal of Fracture Mechanics*. 1(3), pp.137–155.
- Hoek, E. and Brown, T. 1980a. Empirical strength criterion for rock masses. *Journal of Geotechnical and Geoenvironmental Engineering*. 106(ASCE 15715).
- Hoek, E. and Brown, T. 1980b. *Underground Excavations in Rock*. Institution of Mining and Metallurgy, London.
- Hoek, E., Kaiser, P. and Bawden, W. 1995. *Support of Underground Excavation in Hard Rock*.
- Hoek, E. and Brown, E.T. 1997. Practical estimates of rock mass strength. *International Journal of Rock Mechanics and Mining Sciences*. 34(8), pp.1165–1186.
- Hoek, E. and Marinos, P. 2000. Predicting tunnel squeezing problems in weak heterogeneous rock masses. *Tunnels and Tunnelling International*. 32(11), pp.45–51.
- Hoek, E., Carranza-Torres, C. and Diederichs, M. 2008. The 2008 Kersten Lecture Integration of geotechnical and structural design in tunneling.
- Hoek, E. and Brown, E.T. 2018. The Hoek–Brown failure criterion and GSI – 2018 edition. *Journal of Rock Mechanics and Geotechnical Engineering*, 11(3),

pp.445–463.

Itasca. 2014. Universal Distinct Element Code (UDEC) Version 6.0. Itasca Consulting Group, Minneapolis, Minnesota.

Jakubec, J. 2013. Role of defects in rock mass classification. *Australian Centre for Geomechanics.*, pp.1–8.

Jakubec, J., Board, M., Campbell, R., Pierce, M. and Zaro, D. 2012. Rock mass strength estimate—Chuquicamata case study *In: MassMin 2012*. Sudbury, Canada: Canadian Institute of Mining, Metallurgy and Petroleum (CIM).

Kaiser, P.K. 2016. *Ground Support for Constructability of Deep Underground Excavations: Challenge of Managing Highly Stressed Ground in Civil and Mining Projects*. ITA/AITES.

Kaiser, P.K., Diederichs, M.S., Martin, C.D., Sharp, J. and Steiner, W. 2000. Underground works in hard rock tunnelling and mining *In: ISRM International Symposium*. International Society for Rock Mechanics and Rock Engineering.

Kaiser, P.K., Kim, B., Bewick, R.P. and Valley, B. 2011. Rock mass strength at depth and implications for pillar design. *Mining Technology*. 120(3), pp.170–179.

Kaiser, P.K., Amann, F. and Bewick, R.P. 2015. Overcoming challenges of rock mass characterization for underground construction in deep mines *In: 13th ISRM International Congress of Rock Mechanics*. International Society for Rock Mechanics.

Laubscher, D.H. and Jakubec, J., 2001. The MRMR rock mass classification for jointed rock masses. *Underground Mining Methods: Engineering Fundamentals and International Case Studies*, WA Hustrulid and RL Bullock (eds) Society of Mining Metallurgy and Exploration, SMME, pp.475-481.

Marinos, P. and Hoek, E. 2001. Estimating the geotechnical properties of

- heterogeneous rock masses such as flysch. *Bulletin of Engineering Geology and the Environment*. 60(2), pp.85–92.
- Marinos, V. and Carter, T.G. 2018. Maintaining geological reality in application of GSI for design of engineering structures in rock. *Engineering geology*. 239, pp.282–297.
- Martin, C.D. 1997. Seventeenth Canadian geotechnical colloquium: the effect of cohesion loss and stress path on brittle rock strength. *Canadian Geotechnical Journal*. 34(5), pp.698–725.
- Martin, C.D., Kaiser, P.K. and McCreath, D.R. 1999. Hoek–Brown parameters for predicting the depth of brittle failure around tunnels. *Canadian Geotechnical Journal*. 36(1), pp.136–151.
- Martin, C.D., Christiansson, R. and Söderhäll, J. 2001. *Rock stability considerations for siting and constructing a KBS-3 repository. Based on experiences from Aespoe HRL, AECL's URL, tunnelling and mining*. Swedish Nuclear Fuel and Waste Management Co.
- Martin, C.D., Kaiser, P.K. and Christiansson, R., 2003. Stress, instability and design of underground excavations. *International Journal of Rock Mechanics and Mining Sciences*. 40(7-8), pp.1027–1047.
- Mas Ivars, D., Pierce, M.E., Darcel, C., Reyes-Montes, J., Potyondy, D.O., Paul Young, R. and Cundall, P.A. 2011. The synthetic rock mass approach for jointed rock mass modelling. *International Journal of Rock Mechanics and Mining Sciences*. 48(2), pp.219–244.
- Medhurst, T.P. and Brown, E.T., 1998. A study of the mechanical behaviour of coal for pillar design. *International Journal of Rock Mechanics and Mining Sciences*, 35(8), pp.1087–1105.

- Mogi, K. 1962. The influence of the dimensions of specimens on the fracture strength of rocks. *Bulletin Earthquake Research Institute*. 40(1962), pp.175–185
- Palmstrom, A. 1995. RMI—a rock mass characterization system for rock engineering purposes [Ph. D. Thesis]. *University of Oslo, Denmark*.
- Perras, M.A., Ghazvinian, E., Diederichs, M.S. and Lam, T. 2013. Queenston Formation: tunnel back analysis and forward shaft prediction *In: 47th US Rock Mechanics/Geomechanics Symposium*. American Rock Mechanics Association.
- Pierce, M., Cundall, P., Potyondy, D. and Mas Ivars, D. 2007. A synthetic rock mass model for jointed rock *In: Rock Mechanics: Meeting Society's Challenges and Demands, 1st Canada-US Rock Mechanics Symposium, Vancouver.*, pp.341–349.
- Pierce, M., Gaida, M. and DeGagne, D. 2009. Estimation of rock block strength *In: RockEng09 (Proceedings, 3rd CANUS Rock Mechanics Symposium, Toronto*.
- Pratt, H.R., Black, A.D., Brown, W.S. and Brace, W.F. 1972. The effect of specimen size on the mechanical properties of unjointed diorite. In *International Journal of Rock Mechanics and Mining Sciences & Geomechanics Abstracts* (Vol. 9, No. 4, pp. 513–516). Pergamon.
- Shin, S.W. 2010. *Excavation disturbed zone in Lac du Bonnet granite*. PhD thesis, Edmonton, Canada: University of Alberta, 224p.
- Shen, B. and Barton, N., 1997. The disturbed zone around tunnels in jointed rock masses. *International Journal of Rock Mechanics and Mining Sciences*, 34(1), pp.117–126.
- Stavrou, A., Murphy, W. and Lawrence, J.A., 2015, January. Evaluating the influence of block size in cable bolt performance. In *ISRM Regional Symposium-EUROCK 2015*. International Society for Rock Mechanics and Rock Engineering.

- Stille, H. and Palmström, A. 2008. Ground behaviour and rock mass composition in underground excavations. *Tunnelling and Underground Space Technology*. 23(1), pp.46–64.
- Tsur-Lavie, Y. and Denekamp, S.A. 1982. Comparison of size effect for different types of strength tests. *Rock Mechanics*. 15(4), pp.243–254.
- Weibull, W. 1951. A statistical distribution function of wide applicability. *Journal of Applied Mechanics*. 18, pp.293–297.
- Yoshinaka, R., Osada, M., Park, H., Sasaki, T. and Sasaki, K. 2008. Practical determination of mechanical design parameters of intact rock considering scale effect. *Engineering Geology*. 96(3–4), pp.173–186.

Chapter 2

Quantifying the Effects of Scale and Heterogeneity on the Confined Strength of micro-Defected Rocks

A. Stavrou^{1,2} and W. Murphy²

¹ Arup | Geotechnics, 13 Fitzroy Street London W1T 4BQ United Kingdom.

² School of Earth and Environment, University of Leeds, Leeds. LS2 9JT.

Citation: **Stavrou**, A. and Murphy, W., 2018. Quantifying the effects of scale and heterogeneity on the confined strength of micro-defected rocks. *International Journal of Rock Mechanics and Mining Sciences*, 102, pp.131-143, ISSN 1365-1609, <https://doi.org/10.1016/j.ijrmms.2018.01.019>.

Abstract

A numerical study was performed to develop a framework for estimating the confined strength of rock blocks considering scale effects and in-situ heterogeneity (i.e. intensity of structural microdefects and degree of weathering). Grain boundary models using the Voronoi tessellation scheme within UDEC have been used to simulate the results of small (lab) and large (field) scale compression (unconfined and triaxial) and indirect tensile (Brazilian) tests on a series of progressively larger in size and degrading in quality numerical specimens. Accordingly, relationships that link rock block strength with its volume and in-situ condition were developed for the preliminary estimation of scaled Mohr–Coulomb and Hoek–Brown parameters. The results from the scaling analysis generally suggest that cohesion decreases with both increasing scale and degrading sample condition in a manner similar to the scale/condition dependant reduction of uniaxial compressive strength (UCS), while the friction angle shows only minor variation with no apparent trend. The measured peak confined strength values were also fitted to the Generalized Hoek–Brown criterion and a new block-scale Geological Strength Index parameter is introduced named micro GSI (mGSI) which was also linked to the scale/condition dependant reduction of UCS. By using the proposed linear and non-linear approaches, once the UCS reduction due to scaling effects is known, the confined strength of rock blocks could be then defined and can be used to carry out preliminary rock engineering calculations and to run discontinuum numerical models in which rock blocks are simulated explicitly.

Keywords: rock block, scale effect, heterogeneity, confined strength, UDEC Voronoi

2.1. Introduction

In rock engineering the performance of a jointed rock mass and the interactions with rock reinforcement elements are controlled by the strength and structural pattern of discontinuities and the strength of rock blocks between the fracture networks. There is a recognised problem associated with upscaling the results of small-scale tests on both rock joints and rock blocks. This challenge in assigning parameters for use in rock engineering design and numerical modelling is made more difficult by the limited availability of large-scale tests and the practical difficulties in attempting to investigate the confined strength of larger rock block volumes. Therefore, this has historically been treated by using empirical relationships between lab scale samples and representative sizes of blocks or discontinuities, field observations and more recently by sophisticated synthetic rock mass modelling techniques (Mas Ivars et al., 2011).

If we exclude the cases where a rock mass can be represented as an equivalent continuum medium (c. 20% of cases) due to the high density or absence of fractures relative to the size of the excavation, it is clear that rock blocks and joints must be treated explicitly and a reasoned attempt to upscale their strength from small sample to field scale is required (Bandis et al., 2011).

While there are upscaling relationships for rock joints (e.g. Barton and Bandis, 1982), the options available to scale the strength of rock blocks are more limited (see Bahrani and Kaiser, 2016). Generic relationships that correlate the confined strength of rock blocks according to their size and *in-situ* condition are not comprehensively available in the technical literature, due to challenges associated with performing large-scale triaxial compression tests on large scale rock block volumes. For that reason, a series of small and large-scale micromechanical numerical simulations of standard tests (i.e. uniaxial/triaxial compression and indirect tensile strength) have been conducted

within UDEC to establish a methodology for estimating the confined strength of rock blocks based on their volume and *in-situ* condition (i.e. degree of heterogeneity and alteration). Accordingly, relationships that link rock block strength with its volume and *in-situ* condition were developed for the preliminary estimation of scaled Mohr–Coulomb and Hoek–Brown parameters for use in discontinuum numerical modelling and rock engineering design calculations.

Given that the block scaling effects and the variable strength of defected and non-defected rock blocks is one of the predominant factors controlling rock mass behaviour (Kaiser et al., 2015), the extent of the disturbed zone around an excavation (Shen and Barton, 1997) and the response of the structural elements used as support (Stavrou et al., 2015), the overall aim of this paper is to contribute towards a more precise prediction of rock mass strength.

2.2. Rock block scaling effects

It has been proven experimentally that the uniaxial compressive strength (UCS) of intact rock decreases with increasing sample size (Cunha, 1990). This has been attributed to the increased heterogeneity in rock as a function of volume and the greater probability of microdefects to allow unstable crack propagation (Hoek and Brown, 1997). This argument coincides with the statistical theory of Weibull (Weibull, 1951) which ascribes failure to the increased population of randomly distributed structural flaws. In contrast, some other researchers (Einstein et al., 1970) have linked the complex size-dependent strength reduction to the combined effect of increased volume and the elevated strain energy that is stored in larger samples. Finally, Carpinteri (1994) proposed that strength size effects are related to the geometrical multifractality of the fracture surfaces. Regardless of which model is accepted, the fact that larger rock blocks have observably smaller strengths than a smaller block in the same material has

been established, although some exceptions have also been reported (Darlington et al., 2011). The inverse relationship between strength and size is more pronounced in materials associated with brittle behaviour and appears to disappear in comparatively ductile materials. Equally in higher confining pressure tests the block size effect decrease or even vanish (Tsur-Lavie and Denekamp, 1982; Aubertin et al., 2000). This is likely to be an effect of closure of defects that control strength at low confining pressures.

The scale-effect relationship between strength and specimen size has been validated through laboratory and *in-situ* tests for a wide range of lithological formations and several empirical and theoretical expressions have been proposed in the past in order to quantify this relationship (inter alia: Mogi, 1962; Bieniawski, 1968a; Pratt et al., 1972; Medhurst and Brown, 1998).

The majority of experiments investigating scaling effects were performed under unconfined compression conditions, therefore existing scale-effect relationships are limited to the prediction of the UCS. The most widely utilised size-effect relationship was proposed by Hoek and Brown (1980b), who compiled and analysed published laboratory test data and suggested a power law function as follows:

$$\sigma_{cd} = \sigma_{c.50} \left(\frac{d}{50} \right)^{-0.18} \quad 2.1$$

where $\sigma_{c.50}$ is the UCS of a 50 mm diameter cylindrical sample and σ_{cd} is the UCS of a specimen with a diameter d between 10 and 200 mm.

The dataset used by Hoek and Brown (1980b) illustrates that the rock strength reduction due to scale effects is limited by an asymptotic constant value of approximately 0.8. However, these data represent homogeneous samples and in this respect, Equation 2.1 is likely to over-predict the strength of samples which contain

microdefects or influenced by weathering (Pierce et al., 2009; Martin et al., 2011). In addition, Equation 2.1 is applicable only for samples with diameter less than 200 mm and is only representative of medium to very strong rocks (UCS between 25-250 MPa).

In the absence of an universal strength-size law that has the ability to incorporate the variability of the *in-situ* block conditions (e.g. lithology, intensity of structural microdefects and degree of weathering) over a wide range of unjointed specimen sizes and shapes, Yoshinaka et al. (2008) derived an expression that utilises an equivalent length, $d_e = V^{1/3}$, and an exponent, $k = 3/m$, as follows:

$$\frac{\sigma_c}{\sigma_{c,0}} = \left(\frac{d_e}{d_{e0}} \right)^{-k} \quad 2.2$$

where m is a material constant and $d_{e0} = 62.6$ mm is the equivalent length of a specimen with a diameter of 50 mm and a ratio length to diameter equal to 2.5.

This expression follows the general form of the Hoek and Brown's equation but is using a variable exponent k and an equivalent length in order to capture the strength-scale effects for a wide range of lithologies, conditions and specimen geometries. Based on data from both laboratory and in-situ experiments, it was suggested that the exponent k varies substantially with rock type, strength and material micro-structural heterogeneity and lies between 0.1-0.3 for homogeneous strong rocks with UCS between 25-250 MPa; between 0.3-0.9 for highly weathered and/or severely microflawed rocks and between 0.0-0.5 for weak rocks with a UCS between 0.5-25 MPa (Figure 2.1).

From the graph shown in Figure 2.1, an equivalent length (≈ 200 - 250 mm) can be reached beyond which the scale effects become much less pronounced and the strength becomes independent of the specimen size and the density of defects. That critical size, is commonly referred as Representative Elementary Volume (REV) and

is the minimum volume needed to evaluate the scale effects on intact rock strength (Cunha, 1990). The strength of a material with dimensions equal to the REV can have a minimum asymptotic value as low as about 20% of the strength measured at standard small-scale laboratory specimens.

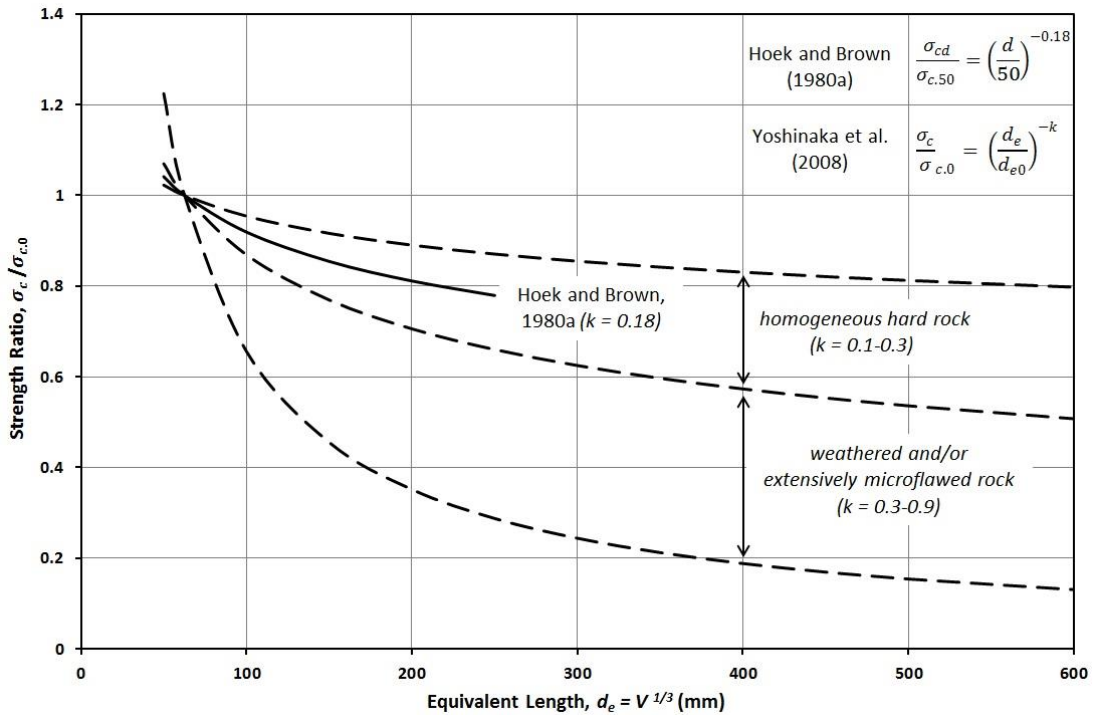


Figure 2.1. Scale effect relations for intact rock UCS proposed by Yoshinaka et al. (2008) for sample dimensions 50 x 125 mm. The relation of Hoek and Brown (1980b) is also shown for comparison; after Pierce et al. (2009).

2.3. Numerical modelling approach

2.3.1. UDEC micro-mechanical damage model

In order to develop a relationship between block size, rock *in-situ* conditions and strength, a numerical scaling approach was followed by using the Universal Distinct Element Code (UDEC) version 6.0 available from Itasca Consulting Group, Inc.

Typically, a rock block in UDEC is represented as a continuous deformable medium that indirectly mimics damage according to a chosen constitutive law. However, by using the Voronoi Tessellation Generator, a rock block can be represented as a packing of randomly-sized rigid or deformable polygonal sub-blocks which are bonded together at their contacts (Lin et al., 2007; Gao and Stead, 2014). The UDEC Voronoi model is often referred as UDEC Damage Model (DM) or Grain based Model (GBM) and represents a valuable numerical tool to build the micro-structure of rock and thus to investigate the fundamental mechanisms of progressive damage (Shin et al., 2007; Lorig et al., 2009). Based on this capability, the UDEC-DM is classified as a direct modelling technique in which the randomly-sized cemented polygons are linked to the grain-interface or grain cementation properties of crystalline and sedimentary rocks (Potyondy and Cundall, 2004; Kazerani and Zhao, 2010). The major advantage of the GBM direct logic against the indirect continuum modelling approach is the explicit generation and propagation of both micro-fractures and macro-fractures and that relatively simple constitutive behaviour can closely resemble naturally occurring failure processes by avoiding the application of complex constitutive laws (Lan et al., 2010).

2.3.2. UDEC-DM mechanical behaviour

In a UDEC-DM the rock material is treated as an assembly of glued structural units interacting at their boundaries (Kazerani and Zhao, 2010). These polygons can be assumed to represent mineral grains while their boundaries can be considered as flaws. Pre-existing cracks can also be incorporated either by the assignment of specific properties across the Voronoi grains or by the generation of micro-joints within the Voronoi skeleton (Lu et al., 2013; Gao and Stead, 2014). Because it is known that the size and size distribution of grains and flaws influence strength (Fredrich et al., 1990), it is critical that the model resolution is sufficient enough to replicate the material

behaviour and the anticipated failure mechanisms (Potyondy and Cundall, 2004; Christianson et al., 2006; Lin et al., 2007). The mechanical behaviour of a UDEC Voronoi model is therefore governed by the grain-cement micro-properties and the packing arrangement of the grains. The Voronoi micro-mechanical properties (see Table 2.1) refer to the deformability properties of the Voronoi sub-blocks together with the strength and stiffness parameters of the contacts that separate them.

Table 2.1. UDEC Voronoi micro-properties

Young's Modulus	E_m	Voronoi block elastic properties
Poisson's Ratio	ν_m	
Normal Stiffness	k_n	Voronoi contact elastic properties
Shear Stiffness	k_s	
Cohesion*	c_m	Voronoi contact strength properties
Friction Angle*	φ_m	
Tensile Strength*	t_m	
*both peak and residual properties		

The Voronoi sub-blocks are assumed to represent an equivalent elastic continuum which is sub-divided with triangular shaped finite difference zones. As a result, plastic deformation and slip or separations (i.e. damage) are confined only along the boundaries between the micro-blocks, which represent the location of potential failure paths (i.e. fractures). The Voronoi contact behaviour will obey a linearly elastic-perfectly plastic model. The deformability of the contacts in the normal and shear directions is represented by normal (k_n) and shear (k_s) stiffnesses respectively. The shear strength of the Voronoi joints follows the MC plasticity criterion, by a combination of contact cohesion (c_m) and friction angle (φ_m), and the tensile yield is evaluated based on a limiting tensile strength (t_m). Once a force exceeds either in shear or in tension the strength of a contact, a displacement-softening procedure is followed and the shear/tensile strengths decrease to a residual value (Kazerani et al., 2011). Figure 2.2 illustrates the UDEC Voronoi assembly micro-properties and constitutive contact behaviour.

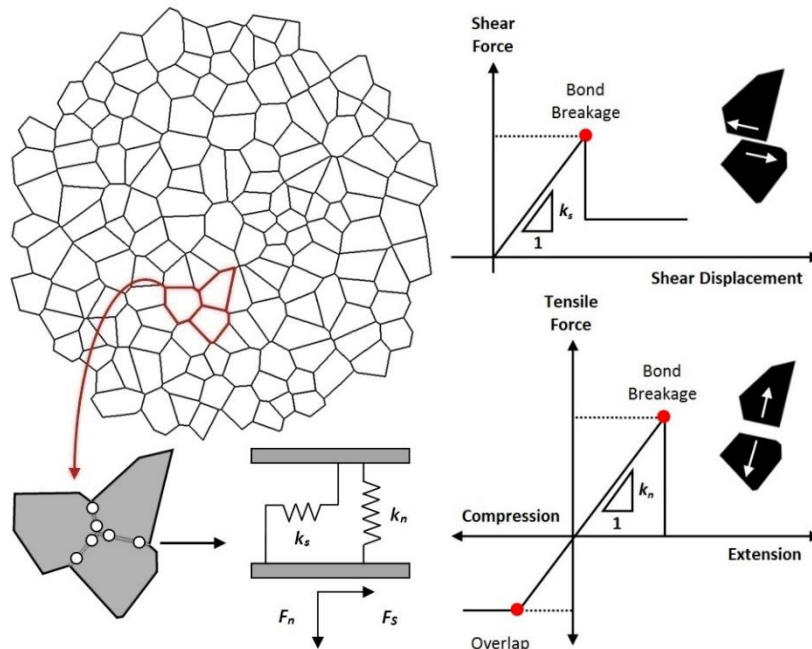


Figure 2.2. Structure, micro-mechanical properties and constitutive behaviour of UDEC-DM model.

When a perturbation is induced by the application of a load, a series of mechanical interactions occur between the Voronoi sub-blocks which lead in the development and transmission of contact forces, the generation of complex heterogeneous stresses and eventually the motion and disturbance of the system. If the induced contact forces acting on and along between grain boundaries exceed their tensile or shear strength, the bond between the grains break and a compression-induced tensile or sliding crack is initiated (Lin et al., 2007). Redistribution of forces may then trigger stress localisations and adjacent joint breakage which, in turn, can induce microcrack propagation, interaction and the eventual generation of macroscopic failure bands (Potyondy and Cundall, 2004). In this way, the GBM model allows the realistic fracturing of the intact rock by following the widely accepted gradual failure processes and replicates realistically the fundamental role of micro-scale tensile or extensional damage in the development of macro-fractures (Lan et al., 2010).

2.4. Rock block scaling methodology

2.4.1. General approach

Several numerical investigations have been conducted to study the influence of scaling effects on defected and non-defected rock blocks (Christianson et al., 2006; Pierce et al., 2009; Lan et al., 2010; Zhang et al., 2011; Martin et al., 2011; Mas Ivars et al., 2011; Vallejos et al., 2013; Gao et al., 2014; Gao and Kang, 2016; Bahrani and Kaiser, 2016). A series of progressively larger micro-mechanical models were generated in UDEC and then, a series of simulated uniaxial, triaxial and indirect tensile (Brazilian) compression tests were conducted to replicate the results of small (lab) and large (field) scale testing and subsequently to determine the relationship between size, quality and strength mechanical properties (both equivalent MC and HB).

The strength scaling analysis followed three steps:

Step 1: Estimation of typical laboratory scale macro-mechanical properties to be used as target values for the calibration of laboratory scale UDEC-DMs.

Step 2: Generation of standard laboratory size samples and simulation of standard laboratory scale tests. At this stage, the micro-mechanical properties of the GBM were calibrated via parametric analysis against the target macro-properties determined in the previous step.

Step 3: Large size UDEC-DMs were created for the simulation of large-scale testing. The micro-properties of the large GBM were initially calibrated to match a set of target uniaxial and tensile strength properties that were obtained by scaling down the strength properties of the intact rock samples considering the relation proposed by Yoshinaka et al. (2008). Then, a series of large triaxial tests were performed to calculate the scaled MC and HB failure parameters.

2.4.2. Intact rock macro-mechanical properties

Two unconfined compressive strength values; 25 and 200 MPa, were selected to characterise the strength of two laboratory scale samples. These two end members cover the range of rock materials found by Yoshinaka et al. (2008) and others to be severely influenced by strong strength-scaling effects. Their macro-strength failure envelopes were determined by fitting the HB failure surface over a limited range of confining pressures (i.e. $0 \leq \sigma'_3 \leq \text{UCS}/10$). The generalised HB failure criterion (Hoek et al., 2002) is described by:

$$\sigma'_1 = \sigma'_3 + \sigma_{ci} \left(m_i \frac{\sigma'_3}{\sigma_{ci}} + s \right)^a \quad 2.3$$

where σ'_1 and σ'_3 are the major and minor effective principal stresses at failure, σ_{ci} is the UCS of the intact rock and m_i and s are material constants, where $s = 1$ and $a = 0.5$ for intact rock. The failure envelopes were constructed by using the σ_{ci} values of 25 and 200 MPa and by assuming a HB constant m_i equal to 10 and 30 respectively.

Equivalent MC angles of friction (φ) and cohesive strengths (c) were estimated by fitting a mean straight line to the non-linear curve defined by Equation 2.3. A secant envelope was defined by the peak strength σ_f and for confinements in the range P_0 (0 MPa) to P_1 ($\sigma'_3 = \text{UCS}/10$) via:

$$N_\varphi = \frac{\sigma_f(P_1) - \sigma_f(P_0)}{P_1 - P_0} \quad 2.4$$

while the friction angle (φ) and cohesion (c) were obtained using (Potyondy and Cundall, 2004):

$$\varphi = \sin^{-1} \left(\frac{N_\varphi - 1}{N_\varphi + 1} \right) \quad 2.5$$

$$c = \frac{\sigma_{ci}}{2\sqrt{N_\varphi}} \quad 2.6$$

The tensile strength σ_t was determined by using a relationship between the tension cutoff (defined by the ratio $\sigma_{ci}/|\sigma_t|$) and the HB parameter m_i as follows (Hoek and Martin, 2014):

$$\frac{\sigma_{ci}}{|\sigma_t|} = 8.62 + 0.7m_i \quad 2.7$$

Finally, a Poisson's ratio, ν_i , equal to 0.25 was assumed for both samples and the associated intact rock Young's modulus values, E_i , were derived based on the following empirical relationship (Hoek and Diederichs, 2006):

$$E_i = MR \sigma_{ci} \quad 2.8$$

where MR is the modulus ratio, assumed to be equal to 400.

Table 2.2 lists the intact rock macro-mechanical properties of both samples No.1 and No.2 (hereafter referred to as "weak" and "strong" samples) respectively. Although strength scale effects for samples with UCS less than 25 MPa have been generally found to be insignificant, the behaviour of the chosen samples can be extrapolated to lower strength categories only in the case were significant evidence of scale effects have been found for the rocks under consideration.

Table 2.2. Lab scale Intact Rock Macro-properties.

Property		Unit	Sample	
			No.1 "weak"	No.2 "strong"
UCS	σ_{ci}	MPa	25	200
Modulus Ratio	MR	-	400	400
Young's Modulus	E_i	GPa	10	80
Poisson's ratio	ν_i	-	0.25	0.25
HB Constants	m_i	-	10	30
	s	-	1	1
	a	-	0.5	0.5
Secant Slope	N_φ	-	5.1	11.0
Cohesion	c	MPa	5.5	30.2
Friction Angle	φ	°	42.4	56.4
Tensile Strength	σ_t	MPa	1.6	6.8

2.5. UDEC-DM intact rock calibration

2.5.1. Micro-mechanical model description

A rectangular 50 x 125 mm and a circular 50 mm in diameter samples (Figure 2.3) were generated in UDEC to simulate laboratory scale compression (uniaxial and triaxial) and tension (Brazilian) experiments. The grain edge length and size distribution were chosen to ensure that the Voronoi block mosaic does not control the formation and accumulation of macro-fractures (Gao and Stead, 2014). The samples were discretised into a large number of random polygons with an average edge length equal to 3 mm to avoid geometry and grain size testing constraints (Brown, 1981). The Voronoi tessellation was developed with a relatively non-uniform grain size distribution to mimic the internal micro-structural heterogeneity that is typically observed in real rocks (Lan et al., 2010).

All model simulations include two steel platens at the top and bottom of the samples. A constant velocity was applied in the y-direction at the upper platen while the lower platen was fixed in both the x- and y-directions. An axial loading velocity of 0.01 ms^{-1} (i.e. loading rate) was applied to the top platen in both the compression and tension tests. The loading rate was selected to ensure that the samples remain in a quasi-static state (Kazerani and Zhao, 2010). In the case of the triaxial tests, stresses were applied isotropically to the lateral boundaries and static equilibrium was reached prior to axial loading.

For all the simulated compression tests, the axial stress was continuously recorded by the sum of the reaction forces along the contact between the sample and the top loading platen. The axial and lateral strains were monitored at several locations across the middle one-third of the specimens (Figure 2.3) and then built-in FISH functions were used to calculate average strain values.

For the tension tests, the axial stress was defined by considering sum of the reaction forces that generated along an artificial joint in the middle of the upper platen. The peak axial stress was measured indirectly via:

$$\sigma_t = \frac{P_{max}}{\pi R t} \quad 2.9$$

where P_{max} is the maximum force recorded on the platen, R and t symbolise the radius and thickness of the disk specimen, where $t=1$ for a 2D analysis.

In all models, when a force violates the strength of a contact segment (either in shear or tension), an internal plasticity flag is set to declare the irreversible plastic state of the contact, the cohesive and tensile strengths are eliminated to zero (instantaneous softening) and the friction angle is softened to a residual value.

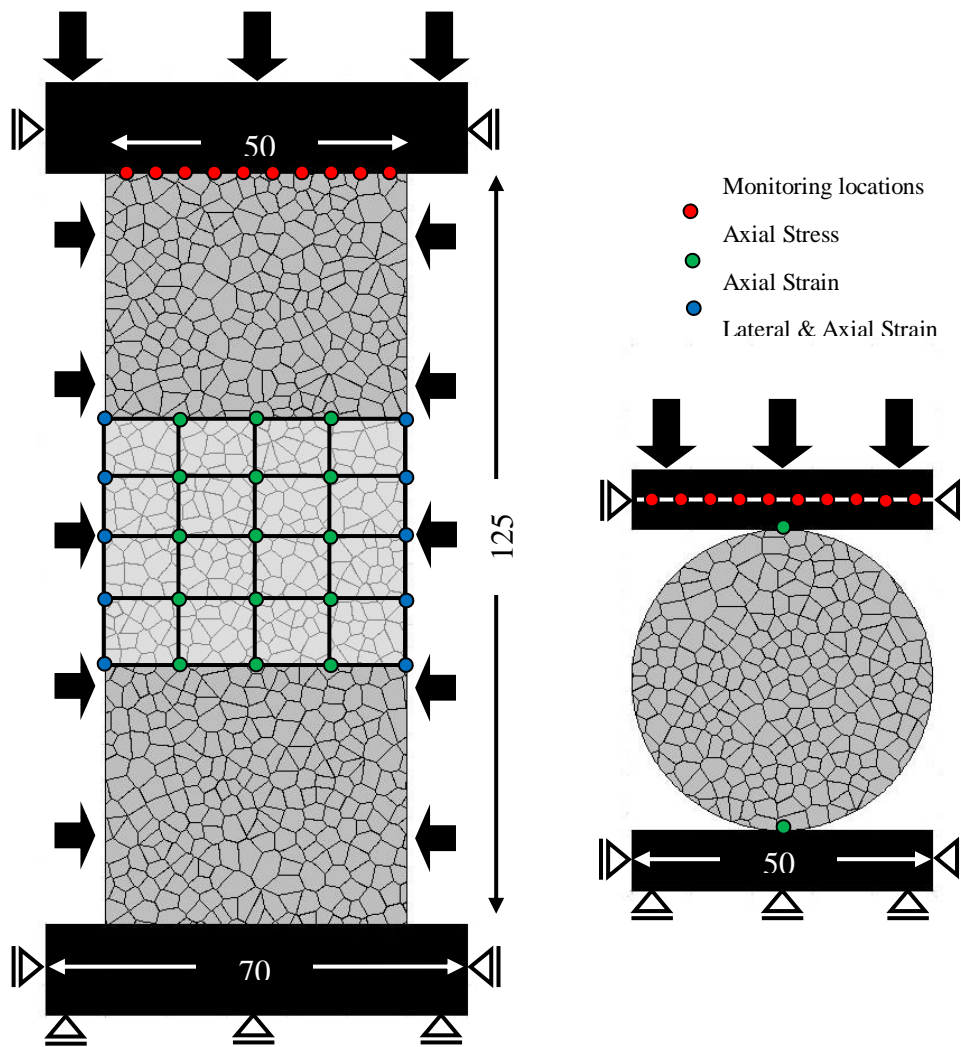


Figure 2.3. Layout, boundary conditions and monitoring locations (i.e. UDEC history points) of the compression and indirect tensile strength tests.

2.5.2. Calibration procedure

The micro-parameters controlling the elasticity (i.e. E_m , ν_m , k_n and k_s) and strength (i.e. c_m , ϕ_m and t_m) behaviour of the micro-block assembly were estimated following a multi-stage parametric analysis in which the model response was calibrated against the deformability (i.e. E_i , ν_i) and strength (i.e. c , ϕ and σ_t) macro-mechanical

properties shown in Table 2.2. The trial-and-error calibration process followed the procedures outlined by Christianson et al. (2006), Kazerani and Zhao (2010) and by Gao and Stead (2014). In summary, the following steps were followed:

Calibration - Step 1: The macro-mechanical Young's Modulus (E_i) and Poisson's ratio (ν_i) were calibrated by running a series of unconfined compression test simulations. The Young's Modulus and Poisson's ratio of the grains were initially defined to be equal to the macro-properties of the intact rock (i.e. $E_i = E_m$ and $\nu_i = \nu_m$). The macro-Poisson's ratio (ν_i) was then calibrated by varying the contact stiffness ratio k_s/k_n . Once the contact stiffness ratio was set, both the normal stiffness (k_n) and block deformability (E_m) were altered to fit the macro-Young's Modulus (E_i). In this process, the normal stiffness (k_n) of the contacts was set to a factor times the deformability of the block zones using the following expression (Itasca, 2014):

$$k_n = n \left[\frac{K_m + (4/3) G_m}{\Delta Z_{min}} \right], 1 \leq n \leq 10 \quad 2.10$$

where K_m and G_m are the bulk and shear stiffnesses of the Voronoi blocks respectively, and ΔZ_{min} is the smallest width of the zone adjoining the contact in the normal direction.

Calibration - Step 2: The material tensile strength (σ_t) was calibrated by running a series of Brazilian disk tests with varying contact micro-tensile strength (t_m).

Calibration - Step 3: The material micro-cohesion (c_m) and -friction angle (φ_m) values were calibrated by running a series of triaxial compression tests with increasing confining pressures in the range $0 \leq \sigma'_3 \leq UCS/10$. The macro-cohesion (c) was calibrated by adjusting the Voronoi contact micro-cohesion and then the macro-friction angle was (φ) calibrated by rescaling the Voronoi contact micro-friction angle.

The micro-properties produced by the described calibration process are listed in Table 2.3. By using the calibrated properties shown in Table 2.3, a perfect agreement was found to the macro-strength and -stiffness values shown in Table 2.2.

Table 2.3. Calibrated UDEC Voronoi micro-properties.

Property	Unit	Sample		
		No.1 "weak"	No.2 "strong"	
Voronoi Block Elastic Properties				
Young's Modulus	E_m	GPa	7.0	58.0
Poisson's Ratio	ν_m	-	0.25	0.25
Bulk Modulus	K_m	GPa	4.7	38.7
Shear Modulus	G_m	GPa	2.8	23.2
Voronoi Contact Elastic Properties				
Normal Stiffness	k_n	GPa/m	5500	46400
Shear Stiffness	k_s	GPa/m	4125	32480
Stiffness Ratio	k_s/k_n	-	0.75	0.70
Voronoi Contact Strength Properties				
Cohesion	c_m	MPa	7.2	50.7
Friction Angle	ϕ_m	°	44.0	52.0
Tensile Strength	t_m	MPa	2.3	7.5
Residual Cohesion	c_{mr}	MPa	0.0	0.0
Residual Friction Angle	ϕ_{mr}	°	15.0	15.0
Residual Tensile Strength	t_{mr}	MPa	0.0	0.0

Figure 2.4 and Figure 2.5 provide the stress-strain response of the calibrated models and present the sample damage for different confinement pressures. The white voids within the numerical samples represent macro-fractures which were formed as a result of grain de-bonding and micro-crack coalescence.

The UDEC grain-based models clearly capture the fundamental behaviours of rocks in compression tests and prove they are capable of replicating the expected significant rock strengthening as a function of confinement and the transition from brittle to ductile behaviour from low to high confining pressures. For both the unconfined and triaxial compression tests, the stress-strain response of the samples shows an initial linear elastic trend up to a peak stress value. The post-peak failure response of the specimens in uniaxial compression generally exhibits a rapid loss of

strength while the stress-strain curves of the confined specimens pass progressively from a strain-softening to a strain-hardening behaviour with higher ductility as confining pressure increases. At low or no confinement, the samples fails mainly due to axial splitting whereas at higher confining pressures a transition in the failure mode is observed and the models capture the development of typical macroscopic shear fractures and/or conjugate damage zones.

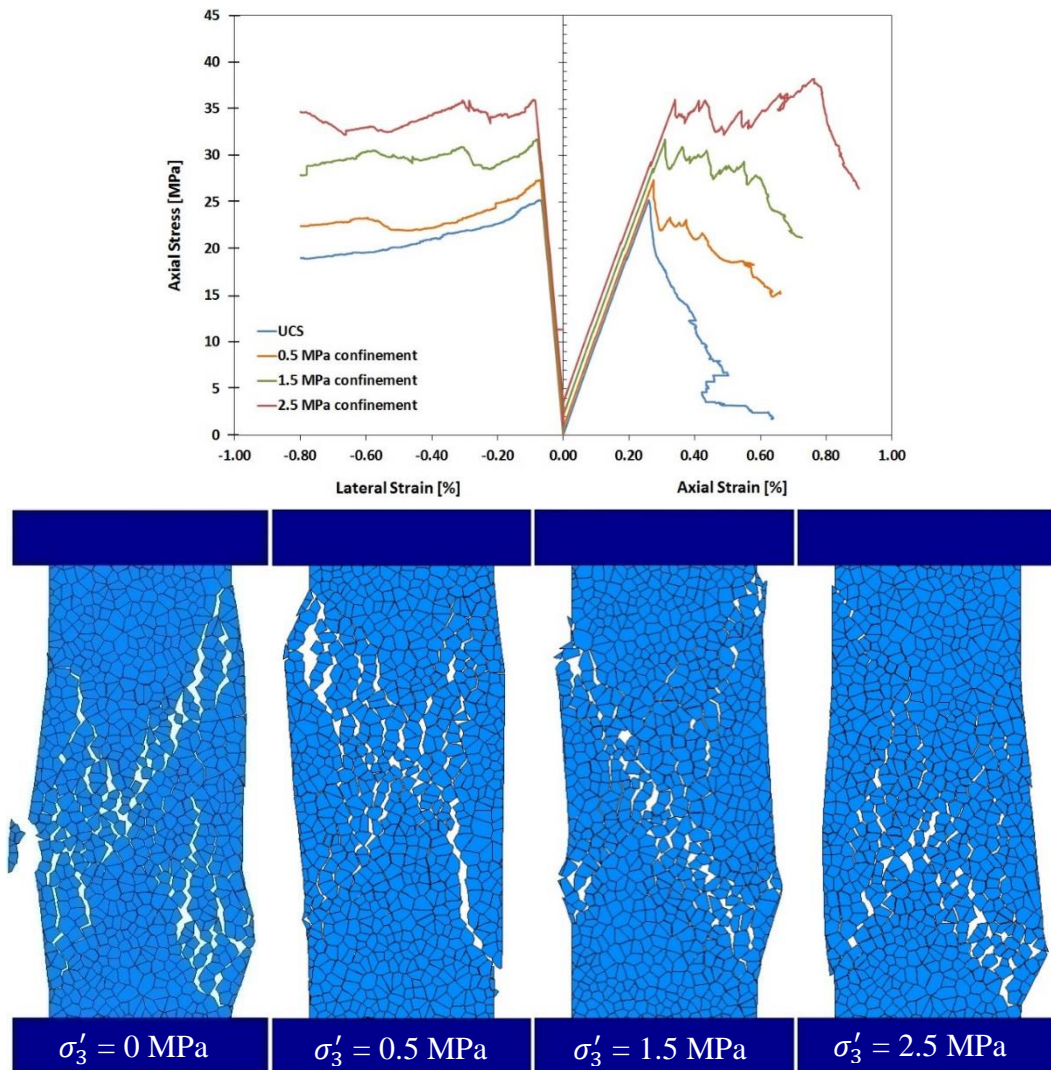


Figure 2.4. Sample No.1: simulated compression tests showing the calibrated stress-strain response and sample damage for different confining pressures.

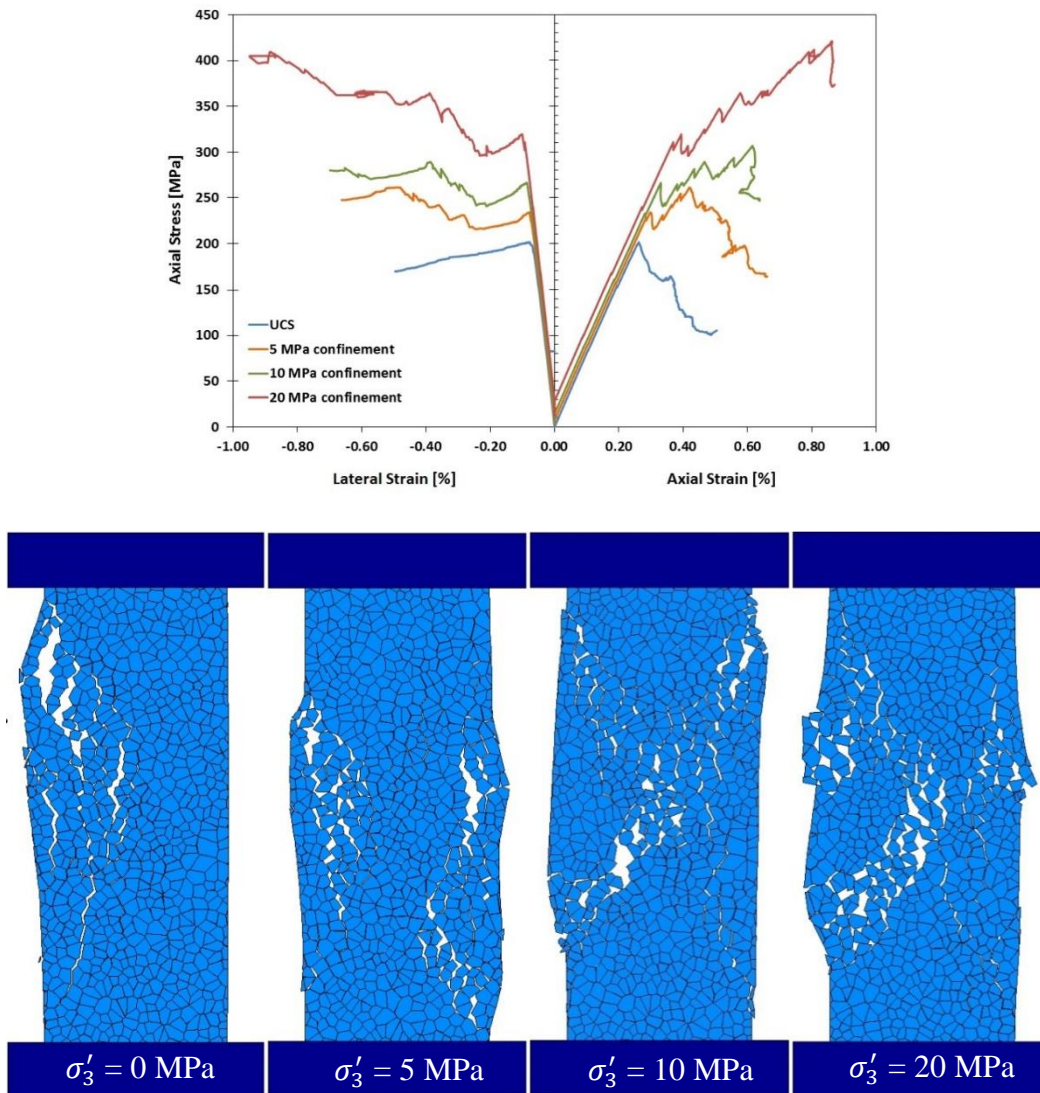


Figure 2.5. Sample No.2: simulated compression tests showing the calibrated stress-strain response and sample damage for different confining pressures.

To examine the repeatability of the target values by using the calibrated micro-parameters, four different Voronoi tessellations were generated for each model and all tests were repeated following identical procedures and boundary conditions. Figure 2.6 show the results in a principal stress space (i.e. σ'_1 vs. σ'_3) and compare the peak stress values calculated from all the analyses with the empirical HB failure envelopes defined

by Equation 2.3. Considering that the grain size distribution has been kept constant, it appears that numerical samples of similar “heterogeneity” produce similar results and influenced by identical failure mechanisms (i.e. extensional microcracking due to tensile stress concentrations along the grain boundaries). The relationship between the GBM results and the HB envelope clearly indicates a very good fit and gives confidence that the UDEC-DM approach is the appropriate tool to simulate realistically large-scale uniaxial/triaxial compression and tensile tests for the needs of the scaling analysis presented in the following section.

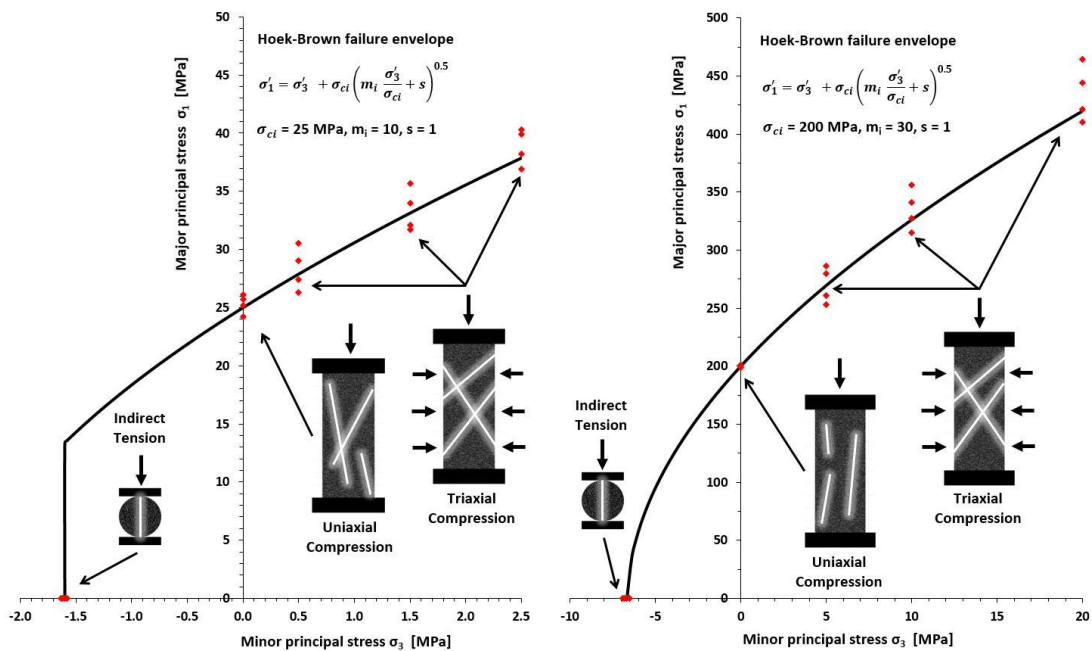


Figure 2.6. HB failure envelope and UDEC-DM lab-scale results for samples No.1 (left) and No.2 (right), including the typical failure mechanisms observed during modelling.

2.6. Scaling analysis

The numerical modelling scaling analysis procedure included three distinct steps.

2.6.1. Scaling Analysis - Step 1

Three progressively larger samples were chosen to be simulated in compression and indirect tension tests. These samples were 100 x 250 mm, 200 x 500 mm and 400 x 1000 mm for the compression and 100 x 100 mm, 200 x 200 mm and 400 x 400 mm for the Brazilian disk tests. The mathematical function proposed by Yoshinaka et al. (2008) was adopted to predict their reduced UCS values under three different conditions (i.e. three different k exponents 0.1, 0.3 and 0.9 in Equation 2.2) based on increased likelihood of structural microdefect intensity and/or degree of weathering. Scaled tensile strength values were assumed to obey again on the Yoshinaka et al. (2008) function whereas the macro-stiffness values were assumed to be the same for all models because deformation modulus is relatively scale independent (Pratt et al., 1972; Hudson et al., 1972; Jackson and Lau, 1990; Martin et al., 2011). The estimated scaled uniaxial and tensile strength properties were utilised as target values that were calibrated for step 2. Table 2.4 shows the target reduced uniaxial compressive and tensile strength values of the three progressively larger samples as a function of the exponent k and the equivalent sample length (d_e).

Table 2.4. Target uniaxial compressive and tensile strength values used for the scaling analysis.

Test	width mm	height mm	volume mm ³	d_e mm	No of blocks	Sample No.1			Sample No.2			
						k			k			
						0.1	0.3	0.9	0.1	0.3	0.9	
Uniaxial Compression	50	125	2.5E05	62.6	761	σ_{ci} MPa	25.0	25.0	25.0	200.0	200.0	200.0
	100	250	2.0E06	125.2	2912		23.3	20.3	13.4	186.6	162.5	107.2
	200	500	1.6E07	250.4	11373		21.8	16.5	7.2	174.1	132.0	57.4
	400	1000	1.3E08	500.9	44971		20.3	13.4	3.8	162.5	107.2	30.8
Brazilian	50	50	4.9E04	36.6	256	σ_t MPa	1.6	1.6	1.6	6.8	6.8	6.8
	100	100	3.9E05	73.2	926		1.5	1.3	0.9	6.3	5.5	3.6
	200	200	3.1E06	146.5	3578		1.4	1.1	0.5	5.9	4.5	2.0
	400	400	2.5E07	292.9	14173		1.3	0.9	0.2	5.5	3.6	1.0

2.6.2. Scaling Analysis - Step 2

Three progressively larger UDEC Voronoi samples were generated by keeping the same grain size distribution characteristics. Subsequently, several uniaxial compression and Brazilian test simulations were run for each sample size to calibrate the models. During the new calibration process, the initial calibrated Voronoi contact micro-strength properties (i.e. Table 2.3: c_m , ϕ_m and t_m of models No.1 and No.2) were systematically downgraded to reach the target macro-strength values shown in Table 2.4 following a strength reduction approach.

The different calibrated reduced properties represent indirectly the progressive elevated disturbance of the large samples, as inferred by the variability of the exponent k in Equation 2.2. In general, it is considered impractical to attempt modelling explicitly the effect of pre-existing micro-structural heterogeneities (e.g. pores, flaws, cavities, fissures, veins, micro-cracks) in UDEC as long as the overall mechanical response of the models is in agreement with the overall material behaviour of the disturbed samples. Figure 2.7 shows the calibrated stress-strain curves for the experimental simulations while Figure 2.8 shows examples of the failure geometries indicated in test simulations. Regardless of the size and the quality of the samples, it was shown that extensional fracturing dominates the failure process under unconfined conditions with the formation of macro-cracks parallel to the direction of loading. It should also be noted that for the models that were allowed to run for a sufficient large number of numerical cycles, shear localization was also observed, and a mixed axial splitting / shear banding type of failure was captured at the final stage of the analysis.

As previously, in order to verify that the reduced micro-strength properties can reproduce the target macro-strength values, the tests were repeated under different Voronoi tessellations apart from the 400 x 1000 mm compression and 400 x 400 mm tension tests which proved to be excessively large and computationally demanding. It

should be noted that the $k = 0.9$ case of the 400 x 1000 mm size models was not calibrated as was regarded to give unrealistically low strength values that can be explained only by the presence of critical orientated macro-planes of weakness (Martin et al., 2011; Wasantha et al., 2015).

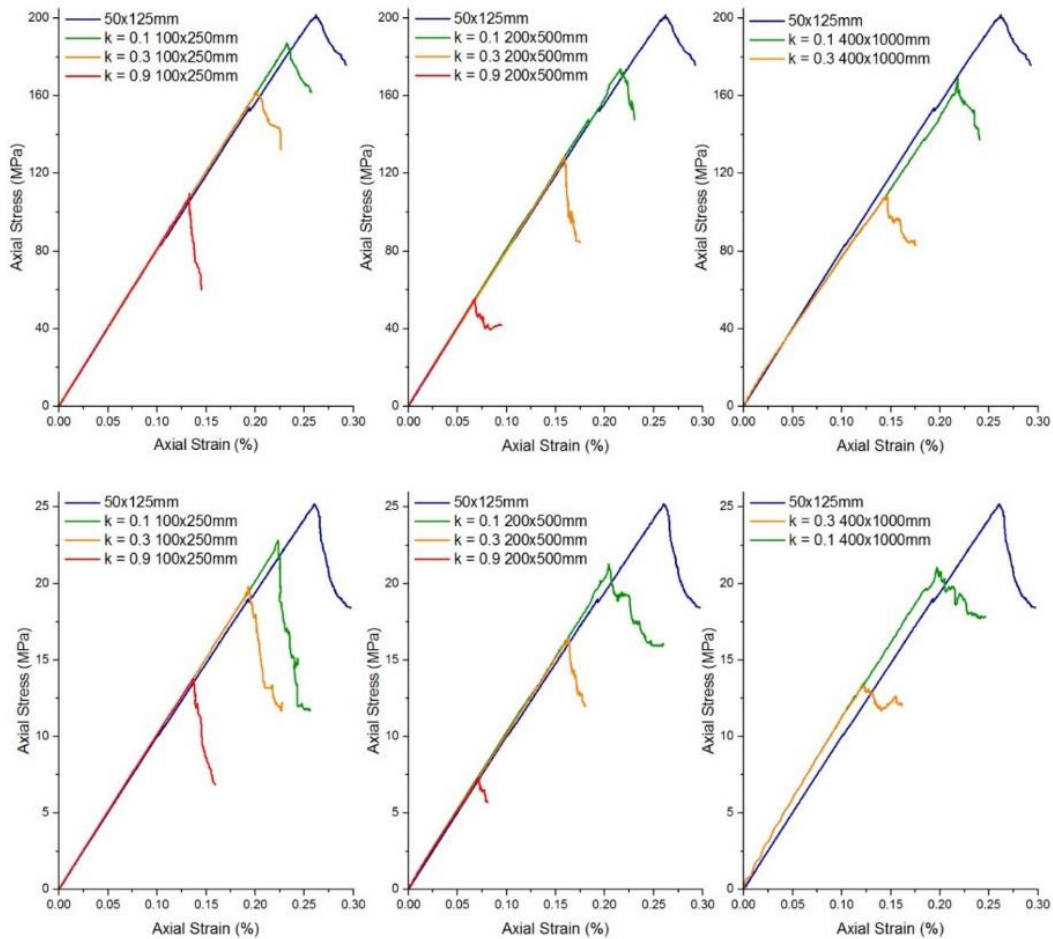


Figure 2.7. Calibrated stress-strain response of all sample sizes for three different physical conditions (i.e. three different k exponents 0.1, 0.3 and 0.9 in Equation 2.2).

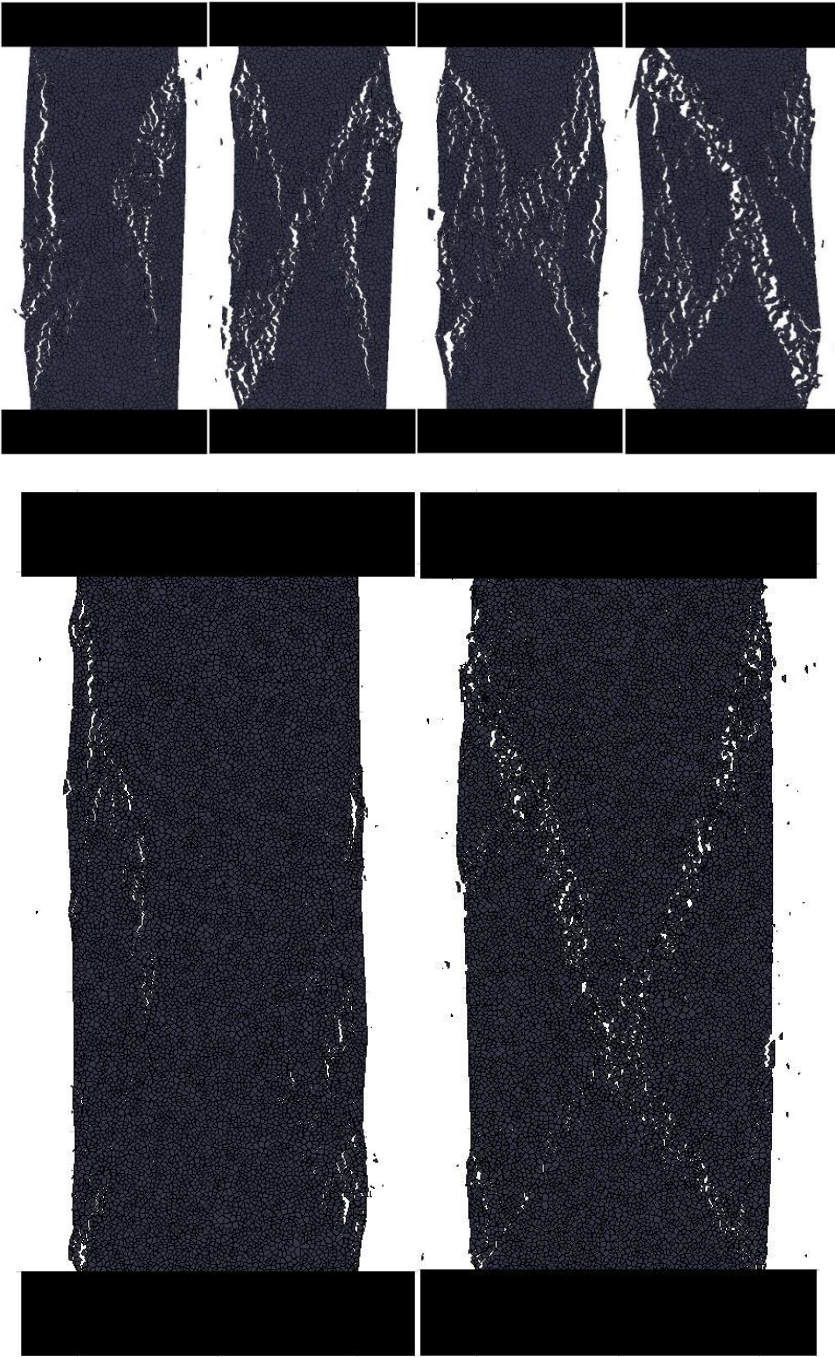


Figure 2.8. Examples of macroscopic axial fractures for different sample sizes and conditions during the uniaxial compression tests.

2.6.3. Scaling Analysis - Step 3

Once, the micro-strength properties were calibrated to match the reduced target unconfined macro-strength values (see Table 2.4 and Figure 2.7), a series of large-scale triaxial tests were performed in the 3rd step to predict scaled linear (MC) and non-linear (HB) failure envelopes. These steps allowed a methodology for estimating scaled rock block failure properties based on their volume and *in-situ* condition to be established. The confining pressures used in these analyses were in the range of $0 \leq \sigma'_3 \leq \text{UCS}/10$ and identical with those used for the calibration of the lab-scale rock samples.

The increase of sample size and disturbance reveals a strong size/condition effect to the predicted confined peak strengths values. A review of the data suggests that the rate of confined strength decrease reduces with increasing confinement and increases with sample disturbance and size. Similarly to the lab-scale samples, macro-fracturing tends to be almost parallel with the loading direction (i.e. axial-splitting) at low confining pressures, while as confinement increases the failure modes are dominated by the formation of macroscopic shear and conjugate zones. Hence, it is once again verified that under different confining pressures, the triggered failure mechanisms are independent from the scale of the sample.

Figure 2.9 exhibits the predicted scaled relationship between the predicted macro-cohesion and friction angle values in respect to the specimen equivalent length (d_e). The scaling analysis results of both samples generally suggest that material macro-cohesion decreases with both increasing scale and degrading sample condition up to an asymptotic value while the macro-friction angle appears relatively insensitive. This behaviour is consistent with experimental findings given by Il'Nitskaya (1969), Pratt (1974), Tani (2001) and Liu (2009). These findings suggest that all samples have experienced the weakening of their cohesive component prior to the mobilisation of the frictional strength and that their behaviour can be captured within a Mohr–Coulomb

linear logic only by a cohesion-weakening-friction-strengthening constitutive model. A review of the scale/condition dependant reduction of UCS and material cohesion shown in Figure 2.1 and Figure 2.9 respectively, reveals a similarity in the non-linear decrease of these properties and therefore suggests that Equation 2.2 can be transformed as follows:

$$\frac{c_c}{c_{c,0}} = \left(\frac{d_e}{d_{e0}} \right)^{-k} \quad 2.11$$

where $c_{c,0}$ is the cohesion of a standard laboratory size sample and c_c is the cohesion of specimens with equivalent length d_e .

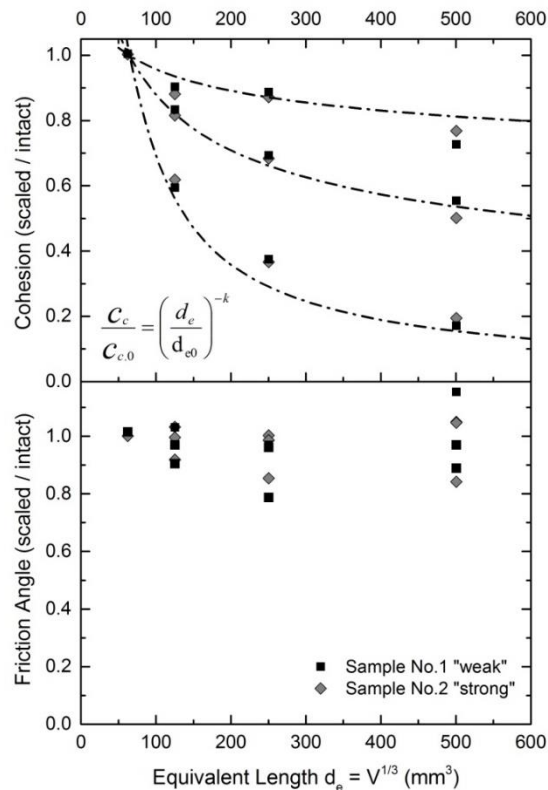


Figure 2.9. Predicted dimensionless relationships between material macro-cohesion and friction angle values with the specimen equivalent length.

Based on this observation, it means that once the UCS reduction due to scaling effects has been determined and the cohesion and friction angle of the lab-scale sample have been estimated, the block-scale cohesion can be predicted using Equation 2.11 while the friction is suggested to remain unchanged or altered up to $\pm 20\%$ of the original value since exhibits no clear increasing or decreasing trends.

To fit non-linear failure envelopes, all scaling analysis results were plotted in a principal stress space according to the numerical sample sizes (Figure 2.10). The recorded peak strength values for both the "weak" and "strong" samples display a clear pattern at each confining pressure and a consistent rock strengthening with increasing confinement, regardless of the specimen's condition or size. These results again indicate that the friction angle of large samples remains relatively unchanged while the cohesion is influenced by marked scaling and quality effects.

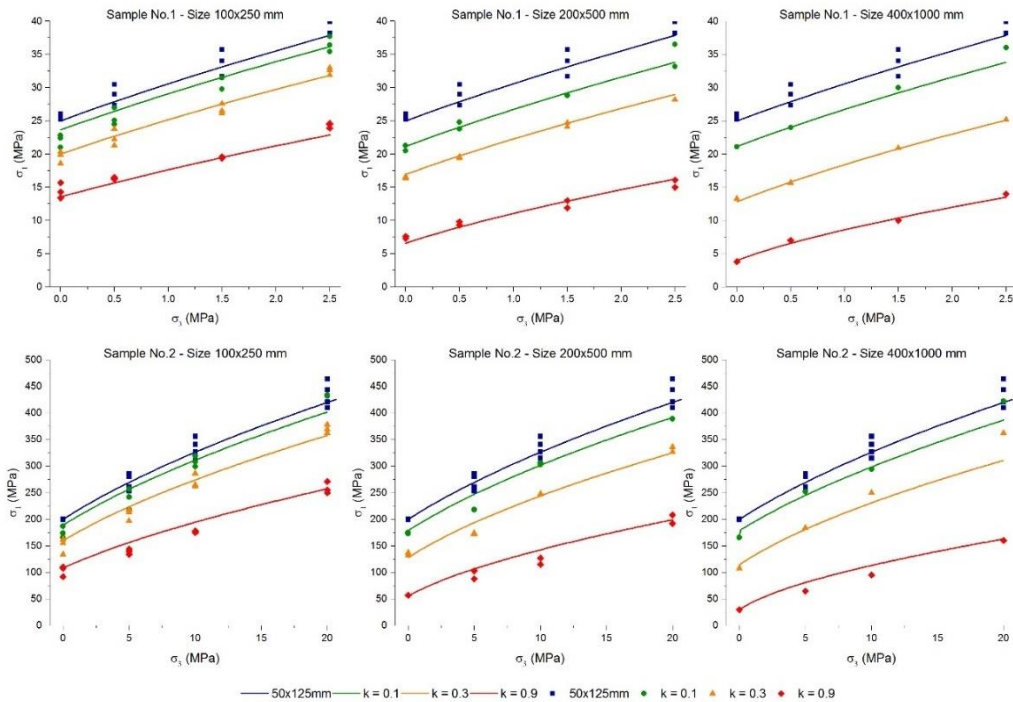


Figure 2.10. Measured peak strengths for samples No.1 "weak" and No.2 "strong" together with HB envelope fits for different physical conditions and sample sizes.

To derive scaled strength failure envelopes, a non-linear curve fitting process was followed using the Generalized Hoek–Brown criterion and the Geological Strength Index (GSI) (Hoek, 1994; Hoek et al., 2002). In this process, the HB constant m_i is systematically reduced with respect to the exponent k of the Yoshinaka et al. (2008) relationship, following the percentages shown in Figure 2.11. In essence, the GSI system is utilised as a rock block (instead of rock mass) scaling parameter to reduce the strength of the intact rock and establish a best-fit to the dataset. However, the derived GSI values could easily be linked with the internal condition (e.g. micro-heterogeneity, weathering, etc.) of the large-scale block volumes and therefore the back-calculated GSI values can be regarded to have a real physical meaning to the rock block strength reduction. For this reason, to avoid confusion with terminology, a new block-scale GSI parameter is introduced, named micro Geological Strength Index (mGSI), which can be used to predict the in-situ peak confined strength of field-scale rock blocks. The mGSI replaces the traditional GSI parameter in the HB expressions and reflects the elevated rock block disturbance with increasing scale, intensity of structural microdefects and degree of weathering.

Figure 2.11 shows the calibrated mGSI values against the reduced UCS of the large-scale samples, as were defined by using the function proposed by Yoshinaka et al. (2008), normalised by their unconfined intact rock strength. The characteristic lab-scale UCS is advisable to be estimated from a sufficiently large number of experiments to capture strength variability as a result of localised features, damage during coring and to overcome sampling bias. The corresponding relationship to account for the strength loss as a function of block volume and/or quality can be described by a power-law expression, and is given by:

$$mGSI = 100 \left(\frac{\sigma_c}{\sigma_{c,0}} \right)^{0.21} \quad 2.12$$

From Figure 2.11 (or Equation 2.12), once the reduced UCS of the field-scale blocks is known, a mGSI value between 100 and 65 could be found and the *in-situ* confined strength of the blocks could be then estimated using the Generalized HB strength criterion. In the absence of large-scale unconfined strength tests, the user needs to decide based on geological descriptions and engineering judgment how much to reduce the UCS value of the large-scale blocks or to use the Yoshinaka et al. (2008) scaling approach.

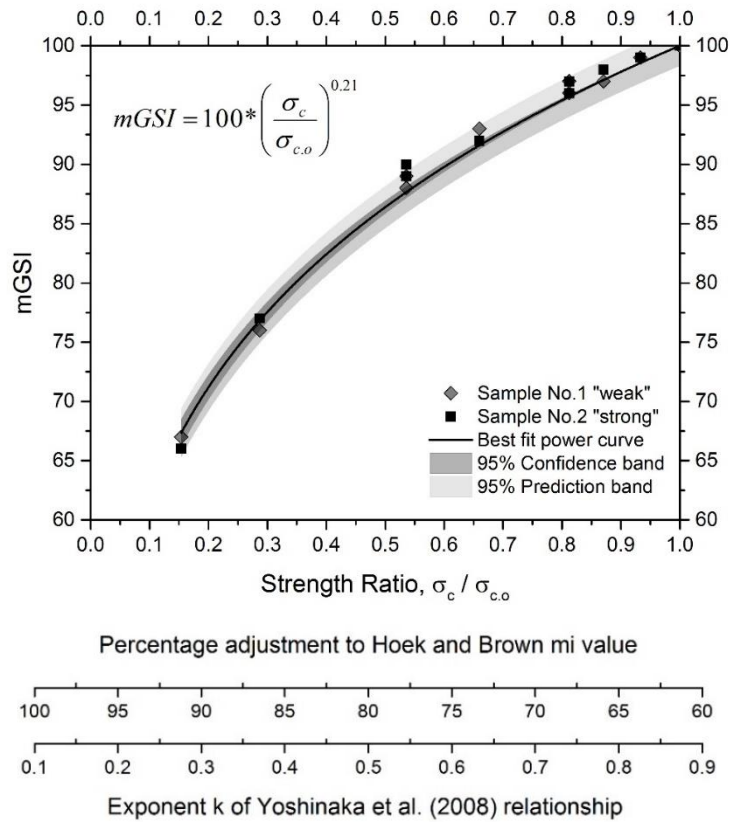


Figure 2.11. Predicted relationship between mGSI and the UCS strength ratio $\sigma_c / \sigma_{c,o}$ (above) and percentage adjustment to the HB m_i value with respect to the k exponent of the Yoshinaka et al. (2008) relationship (below).

Hence, by using the proposed linear and non-linear approaches given with Equation 2.11 (or Figure 2.9) and Equation 2.12 (or Figure 2.11) respectively, a unique

set of strength parameters that describe the *in-situ* strength of rock blocks could be defined, that can be used to carry out preliminary rock engineering calculations and especially to run discontinuum numerical models where rock block strength is an essential parameter of the analysis.

2.7. Discussion

This study examined the effect of size and heterogeneity on the confined strength of rock specimens. A series of compression and Brazilian tests were run in UDEC at progressively larger in size and degrading in quality grain-based models in order to develop a framework for estimating the confined strength of rock blocks considering scale effects and *in-situ* heterogeneity (i.e. intensity of micro- and meso-defects).

The results reveal that macro-cohesion is strongly influenced by both size and condition effects while the macro-friction angle shows only minor variation with no apparent trend. A comparison between the predicted cohesion and the scaled UCS values clearly demonstrates a similarity between their behaviours and appears safe to conclude that there is an inter-dependency between them. To our view, this is linked with the concept of cohesion loss and the delayed friction mobilization. Similarly to the UCS, above a critical volume the cohesion of the rock blocks becomes size-invariant and approaches a constant value. Consequently, knowledge of the scale/condition related UCS reduction can be used as a guide to define the variability of the material cohesion in larger block volumes while the friction angles in suggested to remain relatively unchanged.

Analysis of the large-scale triaxial tests data shows that there is a systematic block strength reduction with increasing specimen volume and decreasing rock quality. The HB approach was adopted to estimate the reduced peak confined strength and a new mGSI parameter is proposed to be used in the HB expressions to fit non-linear

failure envelopes with a reasonable success. The predicted range of the mGSI (i.e. 100-65) describes the *in-situ* block-scale condition of individual rock pieces but further research is required to rationalise the mGSI in terms of geological characterisations or other approaches. A simple non-linear curve was fitted to approximate the relationship between mGSI and the normalised UCS strength reduction. By using this relationship, the confined strength of blocks can be estimated provided that the UCS strength ratio $\sigma_c / \sigma_{c,o}$ is known. Although appears tempting to reverse this expression (Equation 2.12 or Figure 2.11) and back-estimate the strength reduction of the rock blocks based on known mGSI values, the development of a qualitative or quantitative approach similar to the known published GSI charts is not feasible at this stage and further research is required to establish a correlation between strength, mGSI, size and the internal *in-situ* condition of the rock blocks. Despite of these difficulties, it is to be expected that the increase in the intensity of structural microdefects and/or the degree of weathering (i.e. increase of exponent k in Equation 2.2) will cause a reduction in the mGSI values which in turn will reduce the confined strength of the blocks under consideration.

When applying the mGSI, a rock block is assumed as an equivalent isotropic medium and is not affected by preferential anisotropy or planes of weakness. In the case of critically orientated structural features, a modified HB criterion such the one proposed by Saroglou and Tsiambaos (Saroglou and Tsiambaos, 2008) should be used and then a scaling analysis could be performed to examine the effect of rock anisotropy in larger rock blocks.

2.8. Conclusions

Rock block strength is a significant factor controlling rock mass behaviour (i.e. deformations, failure modes, etc.) and rock-support/reinforcement interactions. Hence, a high degree of accuracy and experience is required in the estimation of rock block

properties, especially when running discontinuum numerical models where rock masses are simulated as a system of rock blocks which are separated by persistent or non-persistent fracture networks.

It is well known that the lab-scale unconfined compressive strength reduces with increasing sample size and that is influenced by material quality and the presence of flaws, cavities, fissures, veins, healed joints and micro-cracks. However, because of many uncertainties and the practical difficulties in performing large-scale triaxial compression tests, generic relationships that correlate the confined strength of rock blocks with their size and condition, even in a qualitative sense, are very difficult to be established and only few studies have investigated this subject (e.g. Medhurst and Brown, 1998).

Sophisticated numerical modelling has allowed to overcome some of the practical limitations and is seen as the most effective tool for assessing the *in-situ* confined strength of rock blocks. Accordingly, a scaling analysis was performed in UDEC and based on our findings, relationships that link rock block strength with its volume and condition are proposed for the preliminary estimation of scaled Mohr–Coulomb and Hoek–Brown parameters.

The proposed predictive approaches are by no means intended to replace large scale laboratory and *in-situ* testing programs but aims to provide the engineer and numerical analyst with a practical design tool for the preliminary estimation of size/condition related rock block strength parameters that can be used in rock mechanics numerical modelling and design. The proposed strength relationships overcome important practical difficulties and considered as very friendly tools to describe the inverse confined strength relationship as a function of scale and material quality. While limitations exist, the methodology outlined, and the results obtained are considered as a significant step towards the development of a rigorous approach for

estimating the confined strength of blocks and a basis for overcoming the challenge of assigning realistic parameters for blocks in discontinuum models which so far is a matter of speculation.

Acknowledgements

The authors would like to thank ARUP and AECOM for financially supporting this research. Harry Saroglou and Fuqiang Gao are gratefully acknowledged for discussion and advice on matters pertaining to block scaling effects and micromechanical modelling using UDEC.

References

- Aubertin, M., Li, L. and Simon, R. 2000. A multiaxial stress criterion for short- and long-term strength of isotropic rock media. *International Journal of Rock Mechanics and Mining Sciences*. 37(8), pp.1169–1193.
- Bahrani, N. and Kaiser, P.K. 2016. Numerical investigation of the influence of specimen size on the unconfined strength of defected rocks. *Computers and Geotechnics*. 77, pp.56–67.
- Bahrani, N. and Kaiser, P.K. 2016. Strength Degradation Approach (SDA) for Estimation of Confined Strength of Micro-Defected Rocks *In: 50th US Rock Mechanics / Geomechanics Symposium*. American Rock Mechanics Association.
- Bandis, S.C., Sharp, J.C., Mackean, R.A. and Bacasis, E.A. 2011. Explicit Characterisation and Interactive Analysis for Engineering Design of Rock Caverns *In: Proceedings of the Joint Hong Kong Institute of Engineers – Hong Kong Institute of Planning Conference on Planning and Development of Underground Space.*, pp.133–142.

- Barton, N. and Bandis, S. 1982. Effects Of Block Size On The Shear Behavior Of Jointed Rock *In: The 23rd U.S Symposium on Rock Mechanics (USRMS)*., pp.739–760.
- Bieniawski, Z.T. 1968. The Effect Of Specimen Size On Compressive Strength Of Coal. *International Journal of Rock Mechanics and Mining Sciences*. 5(ii), pp.325–335.
- Brown, E.T. 1981. Rock characterisation, testing and monitoring. ISRM suggested methods: Oxford: Pergamon Press, 1981, 211P. *International Journal of Rock Mechanics and Mining Sciences & Geomechanics Abstracts*. 18(6), p.109.
- Carpinteri, A. 1994. Fractal nature of material microstructure and size effects on apparent mechanical properties. *Mechanics of Materials*. 18(2), pp.89–101.
- Christianson, M., Board, M. and Rigby, D. 2006. UDEC simulation of triaxial testing of lithophysal tuff *In: The 41st U.S. Symposium on Rock Mechanics*.
- Cunha, A.P. 1990. Scale effects in rock mechanics *In: Proceedings of the 1st International Workshop on Scale Effects in Rock Masses, Loen, Norway. Edited by A. Pinto da Cunha. AA Balkema, Rotterdam.*, pp.3–27.
- Darlington, W.J., Ranjith, P.G. and Choi, S.K. 2011. The Effect of Specimen Size on Strength and Other Properties in Laboratory Testing of Rock and Rock-Like Cementitious Brittle Materials. *Rock Mechanics and Rock Engineering*. 44(5), p.513.
- Einstein, H.H., Baecher, G.B. and Hirschfeld, R.C. 1970. The effect of size on strength of a brittle rock. *International Society of Rock Mechanics, Proceedings*. 1(1–19).
- Fredrich, J.T., Evans, B. and Wong, T.-F. 1990. Effect of grain size on brittle and semibrittle strength: Implications for micromechanical modelling of failure in compression. *Journal of Geophysical Research*. 95(B7), p.10907.

- Gao, F., Stead, D. and Kang, H. 2014. Numerical investigation of the scale effect and anisotropy in the strength and deformability of coal. *International Journal of Coal Geology*. 136, pp.25–37.
- Gao, F.Q. and Kang, H.P. 2016. Effects of pre-existing discontinuities on the residual strength of rock mass - Insight from a discrete element method simulation. *Journal of Structural Geology*. 85, pp.40–50.
- Gao, F.Q. and Stead, D. 2014. The application of a modified Voronoi logic to brittle fracture modelling at the laboratory and field scale. *International Journal of Rock Mechanics and Mining Sciences*. 68, pp.1–14.
- Hoek, E. 1994. Strength of rock and rock masses. *ISRM News Journal*. 2(2), pp.4–16.
- Hoek, E. and Brown, E.T. 1997. Practical estimates of rock mass strength. *International Journal of Rock Mechanics and Mining Sciences*. 34(8), pp.1165–1186.
- Hoek, E. and Brown, T. 1980b. *Underground Excavations in Rock*. Institution of Mining and Metallurgy, London.
- Hoek, E., Carranza, C. and Corkum, B. 2002. Hoek–Brown failure criterion – 2002 edition. *Narms-Tac.*, pp.267–273.
- Hoek, E. and Diederichs, M. 2006. Empirical Estimation of Rock Mass Modulus. *International Journal of Rock Mechanics and Mining Sciences*. 43(2), pp.203–215.
- Hoek, E. and Martin, C.D. 2014. Fracture initiation and propagation in intact rock - A review. *Journal of Rock Mechanics and Geotechnical Engineering*. 6(4), pp.287–300.
- Hudson, J.A., Brown, E.T. and Fairhurst, C. 1972. Shape of the complete stress-strain curve for rock *In: Stability of Rock Slopes*. ASCE, pp.773–795.

- Itasca. 2014. Universal Distinct Element Code (UDEC) Version 6.0. Itasca Consulting Group, Minneapolis, Minnesota.
- Il'nitskaya, E.I. 1969. Effect of Rock-Specimen Size on Mechanical Properties in Shear Tests. *by Protodyakonov, Koifman and others. Israel Program for Scientific Translations, Jerusalem.*, pp.57–63.
- Jackson, R. and Lau, J.S.O. 1990. The effect of specimen size on the laboratory mechanical properties of Lac du Bonnet grey granite *In: Proceedings of the 1st International Workshop on Scale Effects in Rock Masses, Loen, Norway. Edited by A. Pinto da Cunha. AA Balkema, Rotterdam.*, pp.165–174.
- Kaiser, P.K., Amann, F. and Bewick, R.P. 2015. Overcoming challenges of rock mass characterization for underground construction in deep mines *In: 13th ISRM International Congress of Rock Mechanics. International Society for Rock Mechanics.*
- Kazerani, T., Yang, Z.Y. and Zhao, J. 2011. A Discrete Element Model for Predicting Shear Strength and Degradation of Rock Joint by Using Compressive and Tensile Test Data. *Rock Mechanics and Rock Engineering.*, pp.695–709.
- Kazerani, T. and Zhao, J. 2010. Micromechanical parameters in bonded particle method for modelling of brittle material failure. *International Journal for Numerical and Analytical Methods in Geomechanics.* 34(18), pp.1877–1895.
- Lan, H., Martin, C.D. and Hu, B. 2010. Effect of heterogeneity of brittle rock on micromechanical extensile behavior during compression loading. *Journal of Geophysical Research.* 115(B1), p.B01202.
- Lin, M., Kicker, D., Damjanac, B., Board, M. and Karakouzian, M. 2007. Mechanical degradation of emplacement drifts at Yucca Mountain—A modeling case study—Part I: Nonlithophysal rock. *International Journal of Rock Mechanics*

- and Mining Sciences*. 44(3), pp.351–367.
- Liu, S.G., Chi, Y., Wang, S., LIU, H. and SHI, A. 2009. Size effect on shear strength of basalt rock mass with columnar joints. *J Eng Geol*. 17(3), pp.367–370.
- Lorig, L.J., Watson, A.D., Martin, C.D. and Moore, D.P. 2009. Rockslide run-out prediction from distinct element analysis. *Geomechanics and Geoengineering*. 4(1), pp.17–25.
- Lu, Y., Martin, C.D. and Lan, H. 2013. Strength of Intact Rock Containing Flaws *In: 47th US Rock Mechanics/Geomechanics Symposium*. American Rock Mechanics Association.
- Martin, C.D., Lu, Y. and Lan, H. 2011. Scale Effects in a Synthetic Rock Mass *In: 12th International Congress on Rock Mechanics of the International Society for Rock Mechanics*. International Society for Rock Mechanics, pp.473–478.
- Mas Ivars, D., Pierce, M.E., Darcel, C., Reyes-Montes, J., Potyondy, D.O., Paul Young, R. and Cundall, P.A. 2011. The synthetic rock mass approach for jointed rock mass modelling. *International Journal of Rock Mechanics and Mining Sciences*. 48(2), pp.219–244.
- Medhurst, T.P. and Brown, E.T. 1998. A study of the mechanical behaviour of coal for pillar design. *International Journal of Rock Mechanics and Mining Sciences*. 35(8), pp.1087–1105.
- Mogi, K. 1962. The influence of the dimensions of specimens on the fracture strength of rocks: Comparison between the strength of rock specimens and that of the earth's crust.
- Pierce, M., Gaida, M. and DeGagne, D. 2009. Estimation of rock block strength *In: RockEng09 (Proceedings, 3rd CANUS Rock Mechanics Symposium, Toronto)*.
- Potyondy, D.O. and Cundall, P.A. 2004. A bonded-particle model for rock.

- International Journal of Rock Mechanics and Mining Sciences*. 41(8), pp.1329–1364.
- Pratt, H.R., Black, A.D. and Brace, W.F. 1974. Friction and deformation of jointed quartz diorite. *Proc. 3rd Congr. ISRM, Denver, II-A*. 306310.
- Pratt, H.R., Black, A.D., Brown, W.S. and Brace, W.F. 1972. The effect of specimen size on the mechanical properties of unjointed diorite. *International Journal of Rock Mechanics and Mining Sciences and*. 9(4), pp.513–516.
- Saroglou, H. and Tsiambaos, G. 2008. A modified Hoek–Brown failure criterion for anisotropic intact rock. *International Journal of Rock Mechanics and Mining Sciences*. 45(2), pp.223–234.
- Shen, B. and Barton, N. 1997. The disturbed zone around tunnels in jointed rock masses. *International Journal of Rock Mechanics and Mining Sciences*. 34(1), pp.117–125.
- Shin, S.W., Martin, C.D., Park, E.S. and Christiansson, R. 2007. Methodology for estimation of excavation damaged zone around tunnels in hard rock *In: 1st Canada-US Rock Mechanics Symposium*. American Rock Mechanics Association.
- Stavrou, A., Murphy, W. and Lawrence, J.A. 2015. Evaluating the influence of block size in cable bolt performance *In: ISRM Regional Symposium-EUROCK 2015*. International Society for Rock Mechanics.
- Tani, K. 2001. Scale effect on shear strength of sedimentary soft rocks observed in triaxial compression test (influence of potential joints) *In: 36th National Conference of the Japanese Geotechnical Society.*, pp.597–598.
- Tsur-Lavie, Y. and Denekamp, S.A. 1982. Comparison of size effect for different types of strength tests. *Rock Mechanics*. 15(4), pp.243–254.

- Vallejos, J.A., Brzovic, A., Lopez, C., Bouzeran, L. and Ivars, D.M. 2013. Application of the Synthetic Rock Mass approach to characterize rock mass behavior at the El Teniente Mine, Chile *In: FLAC/DEM Symposium, Minneapolis*.
- Wasantha, P.L.P., Ranjith, P.G., Zhang, Q.B. and Xu, T. 2015. Do joint geometrical properties influence the fracturing behaviour of jointed rock? An investigation through joint orientation. *Geomechanics and Geophysics for Geo-Energy and Geo-Resources*. 1(1), pp.3–14.
- Weibull, W. 1951. A statistical distribution function of wide applicability. *Journal of Applied Mechanics*. 18, pp.293–297.
- Yoshinaka, R., Osada, M., Park, H., Sasaki, T. and Sasaki, K. 2008. Practical determination of mechanical design parameters of intact rock considering scale effect. *Engineering Geology*. 96(3–4), pp.173–186.
- Zhang, Q., Zhu, H., Zhang, L. and Ding, X. 2011. Study of scale effect on intact rock strength using particle flow modeling. *International Journal of Rock Mechanics and Mining Sciences*. 48(8), pp.1320–1328.

Chapter 3

Refined Approaches for Estimating the Strength of Rock Blocks

A. Stavrou^{1,2}, I. Vazaios¹, W. Murphy² and N. Vlachopoulos³

¹ *Arup, 13 Fitzroy Street London W1T 4BQ United Kingdom.*

² *School of Earth and Environment, University of Leeds, Leeds. LS2 9JT.*

³ *Department of Civil Engineering, Royal Military College of Canada, Kingston, Canada, K7K 7B4.*

Citation: **Stavrou, A., Vazaios, I., Murphy, W. and Vlachopoulos, N., 2019.** Refined Approaches for Estimating the Strength of Rock Blocks. *Geotechnical and Geological Engineering*, pp.1-31, ISSN 1573-1529, <https://doi.org/10.1007/s10706-019-00989-9>.

Abstract

Micro-discrete fracture networks (μ DFNs) have been integrated into grain-based models (GBMs) within the numerical software UDEC to assess rock block strength through a series of Unconfined Compressive Strength (UCS) tests of progressively larger in size numerical specimens. GBMs were generated by utilizing a Voronoi tessellation scheme to capture the crack evolution processes within the intact rock material, and μ DFNs were separately created and embedded into the GBMs to simulate the effect of pre-existing defects. Various μ DFNs realisations were generated stochastically within the software FracMan to assess the combined impact of defect intensity, persistence, strength and specimen size. The resulting synthetic rock block (SRB) models were used to assess the “flawed” material strength at block scale through a rigorous sensitivity numerical analysis. The acquired results predict a progressive strength reduction with decreasing intact rock quality and certain trends are captured when rock block strength is expressed as a function of a newly proposed “Defect Intensity \times Persistence” (DIP) factor. This allowed us to standardise the data along specific strength reduction envelopes and to propose generic relationships that cover a wide range of defect geometrical combinations, defect strengths and sample sizes. Accordingly, an attempt is undertaken to refine two existing empirical approaches that consider the effect of scale and micro-defects explicitly for predicting the UCS of rock blocks.

Keywords: Rock block strength, scale effect, pre-existing defects, synthetic rock block, UDEC, FracMan

3.1. Introduction

Understanding the strength and deformability of rock blocks and their contribution to the overall rock mass behaviour is key for the rock engineering design of underground and surface excavations in civil and mining engineering projects (Stavrou and Murphy, 2018). Rock blocks are volumes of macroscopically unjointed intact rock material that are delineated by persistent or non-persistent discontinuities. Their various shapes and sizes are determined by the spatial geometrical arrangement of the fracture network (i.e. intensity, persistence, spacing, termination, sequence of fracturing), which in turn depends on the rock type, the evolution of the stress regime, and the conditions under which these discontinuities were developed (Palmstrom, 2005).

Depending on the geological history, chemical processes and conditions (i.e. temperatures, pressures, stresses, tectonism) to which the rock material has been subjected, some rock blocks may have developed heterogeneities and/or preferential anisotropy while some other may be relatively homogeneous and isotropic. Heterogeneity is typically expressed by the presence of micro and meso-scale structural features (hereafter referred as “defects”) and/or elevated degrees of weathering. On the other hand, defects in homogeneous rocks are very sparse or even absent.

Rock block defects govern the physical, mechanical, dynamic, thermal and hydraulic properties of rock blocks and thus influence the overall behaviour of the rock mass. Depending on their geometrical (i.e. persistence, orientation and frequency) and mechanical characteristics (i.e. open, cement filled), such defects could significantly accelerate the rock failure processes and reduce the strength of the rock blocks (Laubscher and Jakubec, 2001). However, due to the practical challenges in evaluating the impact of these defects on the rock block and rock mass strength, the role of micro

and meso-scale defects (e.g. grain boundaries, cavities, fissures, veins and open or healed micro-cracks, etc.) is not typically considered in design, with the principal focus mainly being on the assessment of large scale structures (e.g. joints, bedding, faults, etc.).

It is widely recognised that the Unconfined Compressive Strength (UCS) of intact rock decreases with increasing scale due to an increased inherent heterogeneity as a function of volume and the greater probability of randomly and/or critically orientated defects to create failure paths within larger rock volumes (Tsur-Lavie and Denekamp, 1982; Hoek and Brown, 1997). In confined conditions, it is again recognised that some form of strength reduction with specimen size exists. Previous work by Stavrou and Murphy (2018) examined the combined effect of size and heterogeneity on the confined strength of rock blocks. According to this work, provided that the UCS reduction due to scaling effects is known, the confined strength of rock blocks could be determined by using the linear and non-linear scaling relationships proposed by the authors. This is particularly important in discontinuum numerical modelling where rock blocks are simulated explicitly and represent an essential element of the analysis. Hence, it appears that knowledge of the scale/condition related UCS reduction of rock blocks is key to characterise accurately the behaviour of the rock mass and the rock -support interactions during excavation.

In this study, a series of simulated laboratory tests are performed on samples of varying sizes and defect intensities to examine the combined influence of sample scale and pre-existing defects on the UCS of rock blocks. As part of the modelling process, Discrete Fracture Networks (DFNs) have been embedded into Grain-Based Models (GBMs) within the Universal Distinct Element Code (UDEC) (Itasca, 2014) to capture both the fracturing of the intact material and the effect of pre-existing defects. Following the initial calibration of a lab-scale intact (non-defected) rock sample, randomly distributed defects of increased frequency, persistence and strength are

integrated in a series of progressively larger in size samples to generate synthetic rock specimens. The results from these experiments are compared with previous studies and the predicted UCS values are analysed in terms of sample size, defect density, persistence and strength.

3.2. Effect of Scale and Defects on UCS

The inverse relationship between the UCS and specimen size has been validated through laboratory and *in-situ* test campaigns for a wide range of lithologies and rock conditions (Mogi, 1962; Bieniawski, 1968b; Pratt et al., 1972; Hoek and Brown, 1980b) although some exceptions have also been reported in the literature (Pells, 2004). The scale beyond which strength becomes independent of the specimen size and/or the density of defects is known as the Representative Elementary Volume (REV) and is considered to be the minimum volume of rock needed to evaluate scale effects and to achieve repeatability of tests results (Cunha, 1990).

To capture the variability of the *in-situ* rock block conditions (e.g. lithology, intensity of micro-defects and degree of weathering) for a wide range of rock block volumes, Yoshinaka et al. (2008) adopted Weibull's statistical theory (Weibull, 1939; Weibull, 1951) and proposed a power law relationship that predicts the reduction of UCS with specimen size as follows:

$$\frac{\sigma_c}{\sigma_{c,0}} = \left(\frac{d_e}{d_{e0}} \right)^{-k} \quad 3.1$$

where σ_c and $\sigma_{c,0}$ are the UCS of large and lab-scale specimens respectively, d_e and d_{e0} are their equivalent lengths expressed as a function of their volume (i.e. $d_e = V^{1/3}$ and $d_{e0} = V_0^{1/3}$) and the exponent $k = 3/m$ where m is a material constant called the coefficient of uniformity.

The exponent k varies substantially with rock type, strength and material micro-structural heterogeneity and lies between 0.1 – 0.3 for homogeneous strong rocks with UCS between 25 – 250 MPa; between 0.3 – 0.9 for highly weathered and/or severely defected rocks and between 0.0 – 0.5 for weak rocks with a UCS between 0.5 – 25 MPa (Figure 3.1). Ideally, to define the exponent k , a series of large UCS tests are required to capture the variability of strength with size. Apart from the case studies summarised by Yoshinaka et al. (2008) to fit the exponent k , other examples include the works by Pierce et al. (2009), Smith and Habte (2011) and Vallejos et al. (2016).

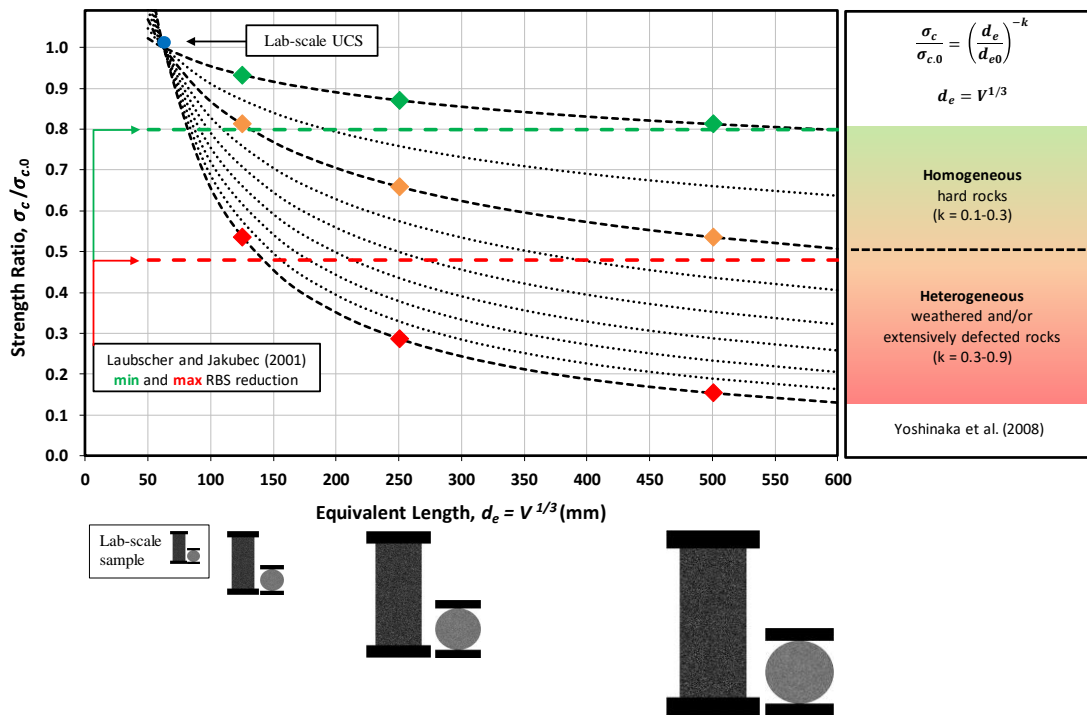


Figure 3.1. a) Scale effect relations for intact rock UCS proposed by Yoshinaka et al. (2008); b) The maximum and minimum Rock Block Strength (RBS) reductions from the relation of Laubscher and Jakubec (2001) are also shown for comparison; c) Target reduced UCS values for three progressively larger in size numerical samples are shown as green, orange and red symbols respectively; d) The sample height to width ratio is 2.5; modified after Pierce et al. (2009).

Although several empirical, statistical and theoretical models have been proposed to describe the scale effects on strength (inter alia: Weibull, 1951; Einstein et al., 1970; Hoek and Brown, 1980; Carpinteri, 1994), relatively little research has been carried out to develop a practical tool from which practitioners would be able to predict the size/quality-dependent Rock Block Strength (RBS) based on qualitative descriptions or quantitative measurements. The only noticeable exception that explicitly account for rock block defects was proposed by Laubscher and Jakubec (2001) via the Mining Rock Mass Rating (MRMR) classification system which essentially introduced the rock block strength concept (Figure 3.2).

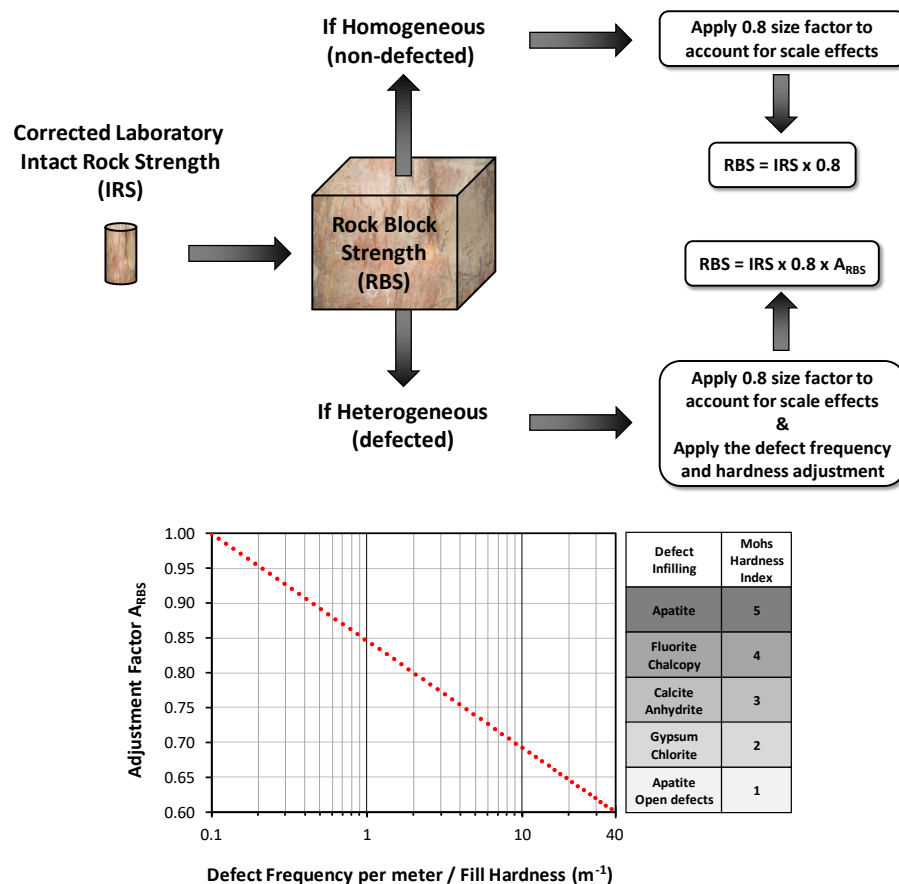


Figure 3.2. Rock block strength concept used in the MRMR classification system and strength adjustment factor; modified after Read and Stacey (2009).

The MRMR system expresses the RBS of homogenous rock blocks as a function of a size-corrected Intact Rock Strength (IRS) that is 80% of a corrected UCS obtained from laboratory scale samples (Figure 3.2). This RBS reduction was adopted from earlier work conducted by Hoek and Brown (1980b) who demonstrated that the UCS reduction due to scale effects in homogenous hard rocks is limited by an asymptotic constant value of approximately 0.8. For heterogeneous rock blocks, the MRMR system reduces the RBS up to 60% by applying a second adjustment that considers the frequency of defects and their frictional properties (i.e. infill hardness) (Figure 3.2). The maximum combined RBS reduction considering both the 80% size-effect factor and the 60% defect frequency/hardness adjustment is therefore 48% of the laboratory derived UCS.

Both the relations of Yoshinaka et al. (2008) and Laubscher and Jakubec (2001) are plotted in Figure 3.1 for comparison. As can be observed, the RBS reductions derived from the Laubscher and Jakubec (2001) approach lie approximately between the asymptotes for $k = 0.1$ and 0.3 of the Yoshinaka et al. (2008) scaling relationship. For weathered and/or extensively defected rocks, Yoshinaka et al. (2008) proposed RBS reductions that can drop the lab UCS up to 80% and as such their relation offers more aggressive strength reductions than the approach proposed by Laubscher and Jakubec (2001). Although the comparison suggests that the Laubscher and Jakubec (2001) relation is likely to overpredict the strength of heavily defected rock blocks, Yoshinaka et al. (2008) do not provide any guidelines for selecting the exponent k in their expression. For that reason the Laubscher and Jakubec (2001) methodology remains the only attractive way to estimate the rock block strength based on field measurements (i.e. micro-fracture frequency and mineral infill strength).

An alternative approach to quantify the effect of scale and defects on UCS was proposed by Pierce et al. (2009) who demonstrated how Synthetic Rock Mass (SRM) modelling techniques could be used to supplement existing empirical relationships,

such as those described by Laubscher and Jakubec (2001) and Yoshinaka et al. (2008). Their work employed a SRM scaling study to assess the impact of defect strength on RBS and related the exponent k of the Yoshinaka et al. (2008) relation to the strength of persistent veins. Their results were very promising and essentially, Pierce et al. (2009) opened the Pandora's box for further SRM studies so that the influence of defect strength, frequency and persistence could be quantified to assess RBS over a wide range of scales and conditions. Following Pierce et al. (2009) recommendations, in this study various μ DFN geometries have been embedded into different GBM sizes, to better understand the strength reduction of rock blocks as a function of scale, defect geometry (i.e. intensity, persistence) and defect strength. Based on our numerical findings, guidelines for estimating the strength of defected rock blocks are proposed in an attempt to refine the existing empirical relationships.

3.3. Simulation of Synthetic Rock Block Samples (SRB)

A hybrid modelling approach was employed to create Synthetic Rock Block (SRB) samples to investigate the combined effect of size and pre-existing micro-defects on the strength and deformability properties of rock blocks. A SRB model is created by coupling previously generated μ DFN geometries within the GBM structure and as such it allows the simulation of pre-existing defects within the intact rock matrix. The major advantage of a SRB model is the capability of modelling the fundamental fracturing processes of intact rock (i.e. crack initiation, propagation and coalescence) without resorting to complicated constitutive behaviour. The logic is identical with the Synthetic Rock Mass (SRM) modelling approach (Pierce et al., 2007; Mas Ivars et al., 2007) with the only difference being the scale of interest.

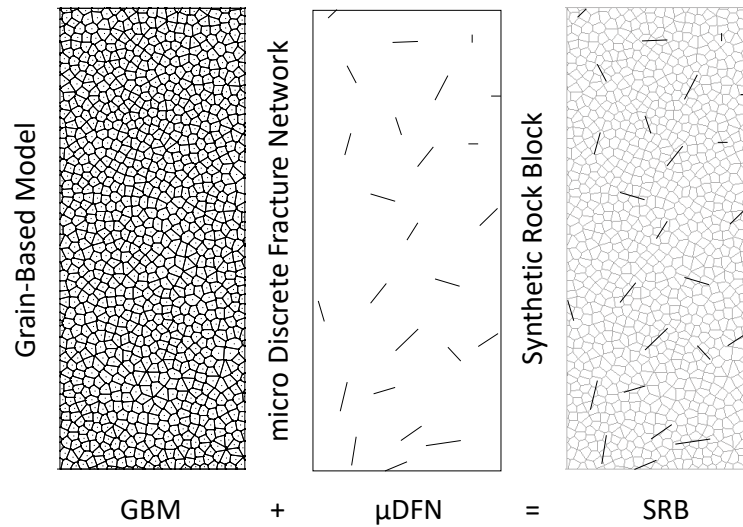


Figure 3.3. The different components of a Synthetic Rock Block (SRB) model in UDEC: intact Grain-Based Model (GBM) and micro Discrete Fracture Network (μ DFN).

Previous numerical investigations on simulated unconfined compression tests have demonstrated the importance of scale and pre-existing defects on the strength, and the resulting failure modes.

Pierce et al. (2009) used the SRM modelling technique within the Particle Flow Code (PFC) to examine the effect of scale on the RBS of extensively defected quartzite from the Bingham Canyon Mine. With progressively increasing sample sizes and decreasing relative vein strengths, it was observed that RBS falls up to 40% of the mean laboratory UCS following a power-law trend similar in form to the relation proposed by Yoshinaka et al. (2008).

Zhang et al. (2011) undertook a numerical study in PFC3D to investigate the dependence of specimen size on the UCS of the Yamaguchi marble. In this PFC modelling, it was shown that to capture realistic scale effects on the UCS, the size and number of random pre-existing micro-fractures needs to increase faster than the specimen size considering an exponential expression derived using the fractal theory.

Jakubec et al. (2012) used the SRM approach within PFC to better understand the influence of defects on rock mass strength at the Chuquicamata Mine in Chile. A series of simulated micro-defected samples were tested in unconfined compression and it was revealed that UCS reduces asymptotically as the defect shear strength decreases and the sample size increases. From the acquired results it was concluded that RBS lies approximately between 40% and 45% of the laboratory UCS values and corresponds well with the RBS estimates given by the Laubscher and Jakubec approach (Laubscher and Jakubec, 2001).

Bahrani and Kaiser (2016) coupled GBMs with DFNs using PFC to investigate the influence of specimen size on the strength of non-defected and defected rocks. The UCS of the defected samples showed that it may decrease or increase with increasing specimen size depending on the orientation of defects.

Although some other numerical studies did not include the scale effect in terms of specimen size, the influence of size was considered indirectly by simulating pre-existing defects of different intensities within single laboratory or rock block scale samples.

Damjanac et al. (2007) tested in UDEC and PFC large-size GBMs of the Lithophysal Tuff to supplement existing laboratory data and to investigate the variability of mechanical properties as a function of lithophysal porosity. Material heterogeneity was represented explicitly within the models in the form of lithophysal cavities and a strength-deformability decreasing effect was captured with increased porosity due to an increasing tendency for axial splitting.

Lu (2014) developed GBMs in UDEC to investigate the effect of scale and defect intensity distribution on the UCS of flawed rocks. The obtained results demonstrated that for a constant micro-crack density and different flaw lengths the UCS decreases with increasing specimen size up to constant value. Furthermore, GBMs of randomly

distributed defects showed a strong correlation between UCS and defect intensity with the reduction of strength also depending on the defect persistence relative to the sample size.

Hamdi et al. (2015) examined the effect of stress-induced micro-cracks on the strength of the Lac du Bonnet granite by using the combined finite-discrete element method (FDEM) within the ELFEN software package. Standard laboratory size samples of varying micro-crack intensities were tested under unconfined and confined compression, and indirect tension (Brazilian test). Their numerical results revealed the strength degradation due to the increase in micro-crack intensity, with its impact becoming less severe as confining stresses increase.

Gao and Kang (2016) used the UDEC Trigon approach to investigate under confined and unconfined conditions the impact of pre-existing discontinuities on large scale coal samples. A significant reduction in the peak strength was observed as DFN intensity was increased. Their results also demonstrated that DFN intensity has little impact on the residual strength and that with increasing confinement, both the peak and residual strengths tend to increase but with the latter at a significantly higher increasing rate.

From all the aforementioned numerical studies, it has been generally shown that UCS decreases as sample size and/or defect intensity increase, with other factors such as defect orientation, persistence and strength being equally important.

3.4. UDEC Grain-Based Models (GBM)

3.4.1. GBM Mechanical Behaviour

In a UDEC GBM, a rock specimen is treated as a packing of randomly-sized deformable grains which are bonded together along their boundaries (Figure 3.4). The

mechanical behaviour of a GBM is controlled by the grain-to-grain interface micro-properties and the geometrical arrangement of the Voronoi blocks (i.e. size and size distribution). The micro-mechanical properties refer to the deformability properties of the grains together with the strength and stiffness parameters of the contact interfaces that separate them. Once the contact strength is exceeded either in shear or in tension, the bond between the grains breaks and a compression-induced, tensile or sliding crack is initiated (Figure 3.4). During this process, the cohesive and tensile strengths are reduced to zero (instantaneous softening) and the friction angle decreases to a residual value. As a technique, the micro-mechanical modelling represents a valuable numerical tool to build the micro-structure of rocks and hence to study the mechanisms of crack generation, progressive fracture propagation and intact rock disaggregation (Gao et al., 2014).

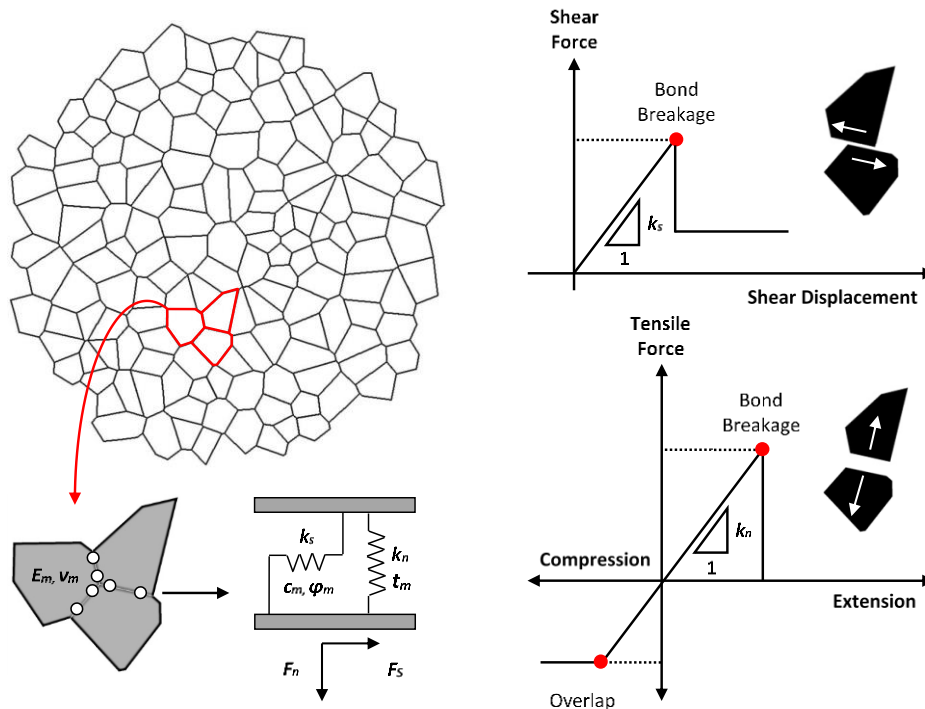


Figure 3.4. Structure, micro-mechanical properties and constitutive behaviour of UDEC GBM model (Stavrou and Murphy, 2018).

3.4.2. Small-scale GBM Intact Rock Calibration

A rectangular 50×125 mm sample and a circular 50 mm in diameter sample were initially generated to simulate laboratory scale compression (unconfined and confined) and indirect tension (Brazilian) experiments. The average edge length of the Voronoi blocks was specified equal to 5 mm and a relatively non-uniform grain size distribution was built to mimic the internal micro-structural heterogeneity of real rocks. Visual inspection of the samples suggests that the ratio largest grain size - specimen diameter is at least 10:1. This grain size was chosen to ensure the numerical efficiency of the larger numerical samples that would be used later in the scaling analysis. For all the simulated compression tests, a constant velocity of 0.005 m/s (i.e. loading rate) was applied in the y-direction at both the upper and lower platens of the sample, and a servo-control function was used to control the progressive response of the samples during failure. Figure 3.5 illustrates the boundary conditions and the stress/strain monitoring locations (i.e. history points) used at the unconfined compression tests.

A set of typical lab-scale macro-mechanical parameters were defined to be used as target values for the calibration of the lab-scale GBMs. The calibration process followed the procedures outlined by Kazerani and Zhao (2010) and by Gao and Stead (2014). For this study a baseline UCS of 50 MPa was selected to describe the lab-scale intact rock strength. Table 3.1 lists the target intact rock macro-mechanical and the calibrated micro-mechanical properties respectively, while Figure 3.6 illustrates the calibrated stress-strain response for the unconfined compression test and the associated sample damage. Initially the specimen behaves elastically and then, after the peak load has been reached, the specimen experiences a rapid loss of strength and fails due to axial splitting and accumulation / interaction of micro-tensile fracturing.

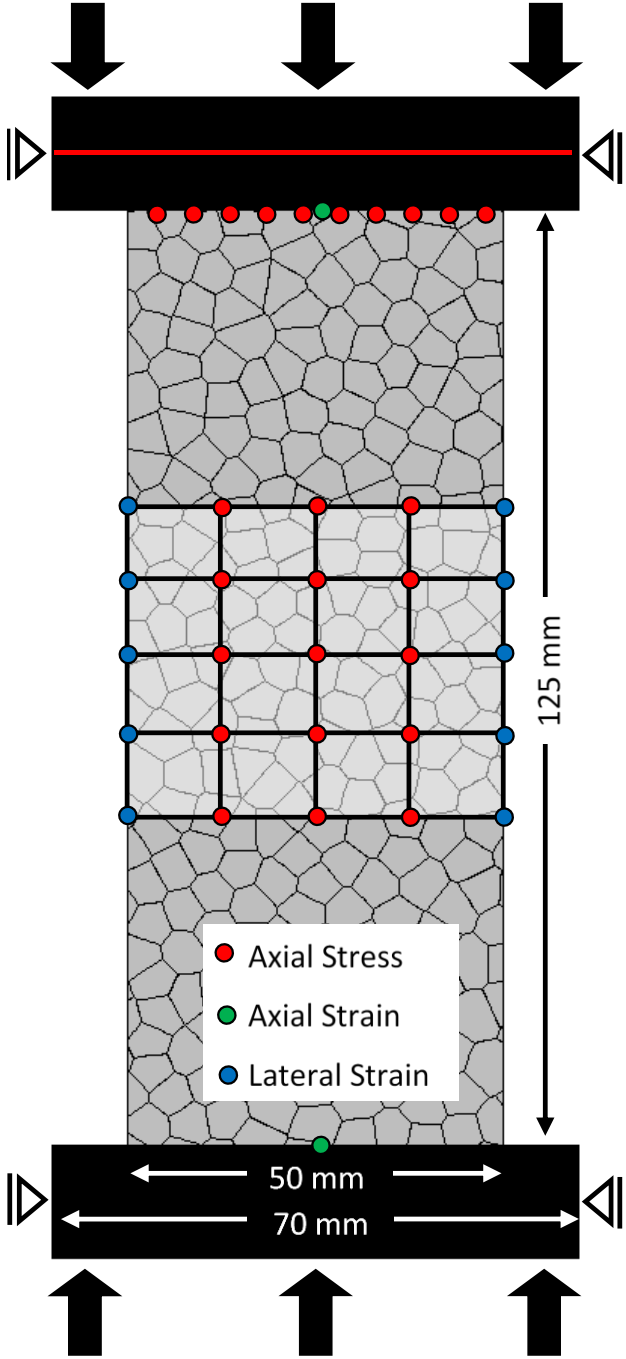


Figure 3.5. Layout, boundary conditions and monitoring locations (i.e. UDEC history points) of the unconfined compression tests.

Table 3.1. Target lab-scale macro-mechanical and calibrated micro-mechanical properties.

Property		Unit	Value
Target macro-mechanical properties			
UCS	σ_i	MPa	50
Modulus Ratio	MR	-	400
Young's Modulus	E_i	GPa	20
Poisson's ratio	ν_i	-	0.25
HB Constants	m_i	-	15
	s	-	1
	a	-	0.5
Secant Slope	N_φ	-	6.8
Cohesion	c	MPa	9.6
Friction Angle	φ	°	48.1
Tensile Strength	σ_t	MPa	3.3
Calibrated SRB micro-mechanical properties			
Grain Young's Modulus	E_m	GPa	26.0
Grain Poisson's Ratio	ν_m	-	0.25
Contact Normal Stiffness	k_n	GPa/m	15600
Contact Shear Stiffness	k_s	GPa/m	14040
Contact Stiffness Ratio	k_s/k_n	-	0.9
Contact Cohesion	c_m	MPa	11.5
Contact Friction Angle	φ_m	°	48.1
Contact Tensile Strength	t_m	MPa	3.3
Residual Cohesion	c_{mr}	MPa	0.0
Residual Friction Angle	φ_{mr}	°	25
Residual Tensile Strength	t_{mr}	MPa	0.0

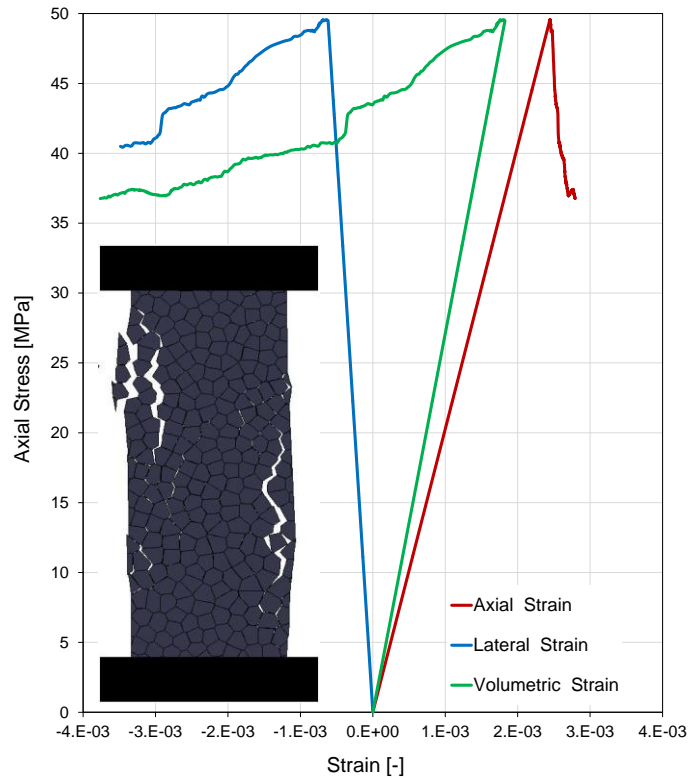


Figure 3.6. Simulated unconfined compression test showing the calibrated stress-strain response and sample damage.

3.4.3. Large-scale GBM Intact Rock Calibration

To investigate the effect of size, three progressively larger in size samples with diameters of 100, 200 and 400 mm and a height-to-width ratio of 2.5 were generated in UDEC. All models have a similar mean grain size (i.e. 5 mm) and size distribution as the lab scale specimens. Initially, the previously calibrated intact rock micro-mechanical properties were adopted and a strength degradation approach was followed to re-calibrate the samples and to capture the expected size-dependant RBS reduction for homogenous and non-defected rocks suggested by Laubscher and Jakubec (2001) and Yoshinaka et al. (2008). The micro-strength properties of the 400×1000 mm sample were adjusted considering the Laubscher and Jakubec 80% size factor to derive

a target UCS value equal to 40 MPa (i.e. 80% of the baseline UCS of 50 MPa). Since this strength reduction coincides well with the least strength decrease proposed by the Yoshinaka et al. (2008) relation for large samples, the 200×500 mm and 100×250 mm samples were calibrated to follow the asymptote for an exponent $k = 0.1$. Table 3.2 presents the calibrated micro-mechanical properties for the non-defected large samples.

Figure 3.7 shows the target reduced UCS values together with the generated stress-strain responses and associated failure modes. Regardless of the size it is observed that all specimens fail under similar failure patterns, which is the initiation, propagation and coalescence of axial micro-tension cracks parallel to the loading direction followed by macroscopic fracture zones.

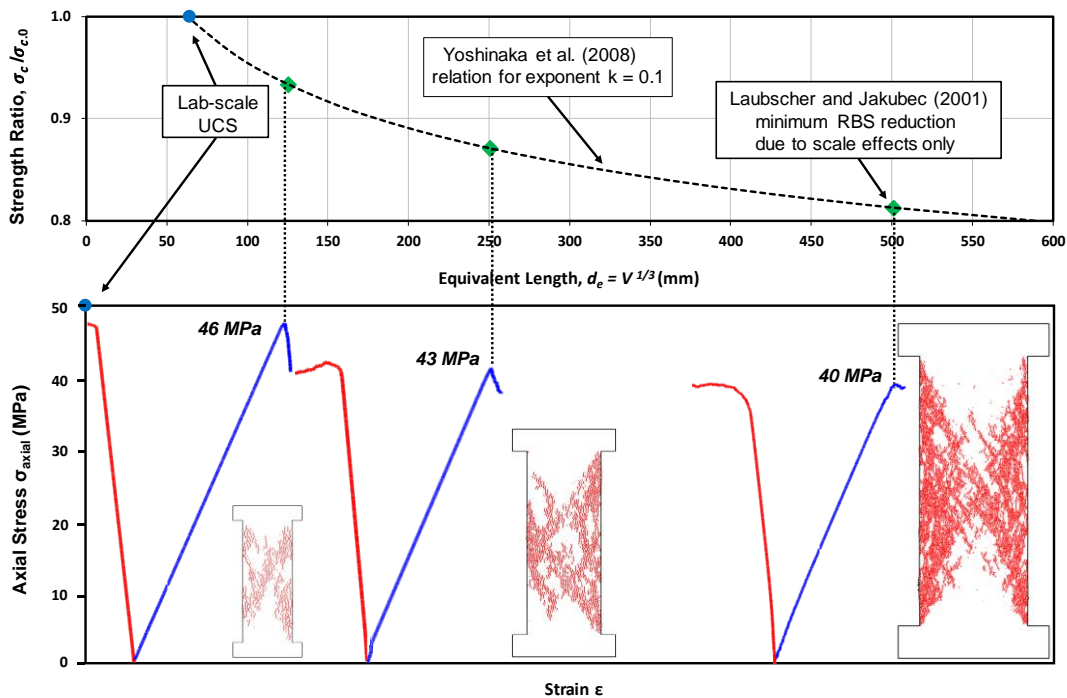


Figure 3.7. Calibrated stress-strain curves and sample damage for the non-defected numerical samples (the damaged samples shown are not in scale).

Table 3.2. Calibrated micro-mechanical properties for the large-scale non-defected samples.

Property	Unit	Sample size (mm)			
		50x125	100x250	200x500	400x1000
Target UCS strength	MPa	50.0	46.4	43.1	40.0
Contact Cohesion	MPa	11.5	11.3	10.7	9.4
Contact Friction Angle	°	48.1	47.5	46.2	42.4
Contact Tensile Strength	MPa	3.3	3.3	3.3	3.3

3.5. Micro Discrete Fracture Networks (μ DFN)

Once the UCS of the homogenous samples was calibrated, a series of unconfined compression tests were run by integrating the μ DFN geometries. DFN modelling has become a powerful tool over the years to realistically capture the influence of discontinuity geometry within fractured rocks for a wide variety of projects. Treated as discrete features, fractures and the overall joint geometry are simulated by using random variables of the joint geometrical features such as location, size and orientation. These random variables are usually assigned a probability distribution in order to determine their numerical value and generate the geometry (Xu and Dowd., 2010). The stochastic modelling of fracture network geometries and its implementation into geological and rock engineering projects has been studied by various researchers (Baecher, 1983; Dershowitz and Einstein, 1988; Davy et al., 2013; Vazaios et al., 2017, 2018) mostly focusing on meso- and large-scale discontinuity features and their influence at a rock mass scale. In such cases, DFN models are generated based on discontinuity data collected in the field by either employing conventional mapping

techniques (e.g. scanlines, convex or circular mapping windows etc.) or remote sensing approaches (e.g. photogrammetry, laser scanning etc.) by using 3D geometrical models of the exposed rock mass.

Although meso and large scale DFN geometries have been adopted in various studies to assess the jointed material mechanical properties at a rock mass scale, at a rock block scale those meso and large-scale rock mass structures are not valid to be used. Therefore, there is the requirement to differentiate the stochastic nature of micro/meso-scale defects from larger scale discontinuities (Hamdi et al., 2015).

The micro Discrete Fracture Network geometries (herein called μ DFN) (Hamdi et al., 2015) introduced in this study refer to the rock heterogeneity at very small scales which can include geometrical features like grain boundaries, fissures, veins and micro-cracks. Micro-cracks present within a macroscopically “intact” rock block can be “healed” and “cemented” with a material weaker or stronger than the host rock, or can be open defects due to the geological history of the medium. This micro-structure can be identified during mapping or core logging if macroscopically visible, or in the laboratory by employing imaging techniques including the image analysis of thin sections (Lim et al., 2012), processing with CAD software (Turichshev and Hadjigeorgiou, 2017), X-Ray CT imaging (Nasseri et al., 2009) etc. (Figure 3.8). In this way, the micro-crack orientation and intensity (persistence and density) can be evaluated quantitatively and serve as input parameters for the generation of the μ DFN geometrical models. This approach can assist in considering site specific conditions and tie the numerical results to a specific rock mass, which is however, out of the scope of this study.

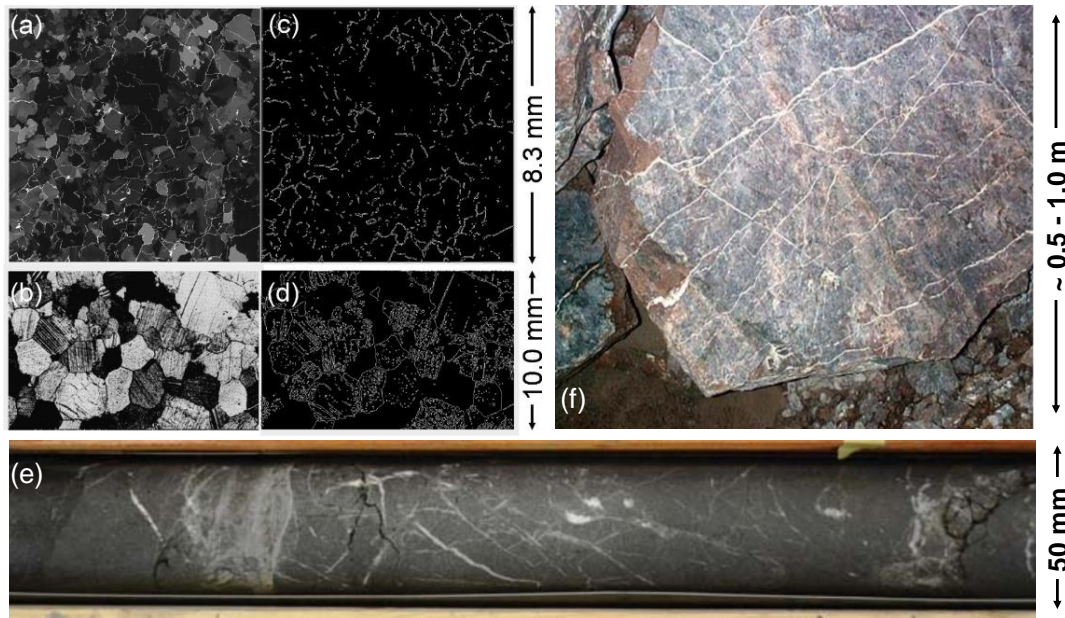


Figure 3.8. Defects at different sampling scales: SEM images of micro-crack distributions in thin sections of (a) Lac du Bonnet granite (Lim et al., 2012), and (b) Wombeyan marble (Rosengren and Jaeger., 1968). Traces of the micro-cracks were obtained from the image processing package provided in MATLAB for (c) Lac du Bonnet granite, and (d) Wombeyan marble (Vazaios et al., 2018); (e) veins infilled with quartz within sandstone core; (f) defects cemented by gypsum in the rock block scale (Jakubec, 2013).

Regarding the determination of size and location of the simulated joints, it is common practice to use one of the intensity measures proposed by Dershowitz and Herda (1992) either in one dimension (linear – P_{10}), two dimensions (areal – P_{21}) or three dimensions (volumetric – P_{32}), since these measures allow for the quantification of fracture frequency and size. Based on the dimension of the sampling region and the dimension of the joint feature, these measures have been proven particularly useful in providing quantifiable means of joint geometry assessment, and in this study both the P_{10} (measured as the numbers of fractures per unit length of scan line or borehole core) and P_{21} (measured as the ratio of the sum of the fracture trace lengths to the sampling area) are used to determine the crack system geometry within the rock specimens.

More specifically, various target fracture frequency P_{10} values were specified for different crack persistence lengths and specimen sizes. The generation of the μ DFN geometries was conducted following a fracture frequency (i.e. fracture per meter) logic to allow a direct comparison with the work of Laubscher and Jakubec (2001), which currently is the only practical tool for quantifying the effect of pre-existing fractures on the strength of rock blocks. The defect geometrical models were mainly generated by using the DFN generator Fracman (Dershowitz et al., 2014) (Figure 3.9), and the models created by Stavrou and Vazaios (2018) were additionally used to enhance the obtained results.

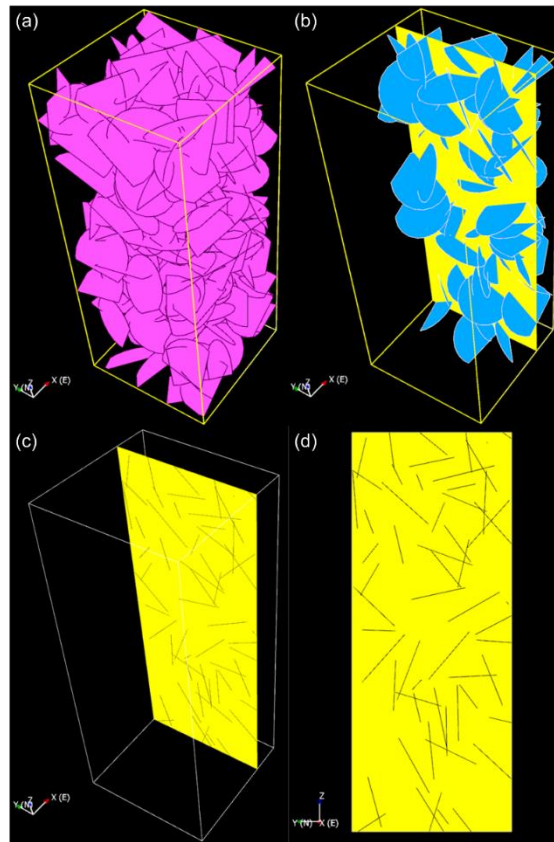


Figure 3.9. (a) 3D μ DFN generated in Fracman, (b) defects intersecting a specific plane, (c) traces generated by the defect-plane intersection, and (d) defect traces imported in the UDEC GBM model.

For the DFN generated, the fracture intensity P_{10} was used as the primary target parameter by applying the Baecher model for non-persistent discontinuities. The assigned P_{10} value was verified by introducing “virtual” scanlines within the numerical model, as illustrated in Figure 3.10. The defects were sampled along those scanlines and the average value of P_{10} was compared to the one used as input to ensure that the model complies with it. Once P_{10} was in agreement with the targeted value, the μ DFN geometry was introduced into the large-scale calibrated UDEC GBM models. To minimize the creation of preferential planes of weakness and the potential for anisotropic behaviour, the pre-existing defects were assigned an arbitrary orientation between 0^0 and 90^0 with a uniform probability distribution.

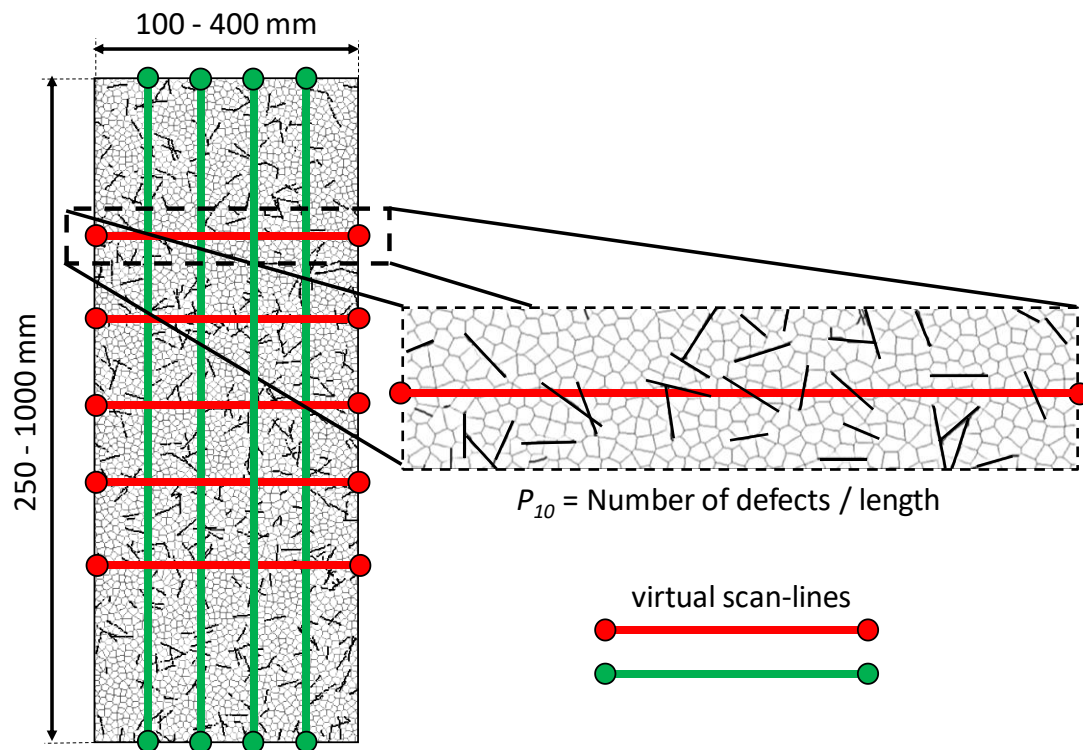


Figure 3.10. μ DFN mapping along virtual scan-lines to confirm the target P_{10} values.

3.6. Analysis of Scale Effects

3.6.1. Matrix of Modelling Scenarios

To investigate scale effects on the strength of defected samples, the current study considers two cases of numerical simulations:

Case 1: Various geometries of randomly distributed “open” defects were embedded into the large-scale calibrated intact GBMs to assess the combined impact of defect intensity, persistence and specimen size. In the adopted approach, the number of defects is proportional to the volume of the specimens. The generated cracks in this case 1 were modelled as “open defects” and assumed to be purely frictional (i.e. zero cohesion and tensile strength), with the friction angle and stiffness values being identical to those of the calibrated intact GBMs (see Table 3.1).

Case 2: Further analysis was undertaken by strengthening the defects for some of the previously generated SRB models to assess the combined impact of defect strength, intensity, persistence and specimen size. A parametric analysis was employed where defect strength (i.e. cohesion and tensile strength) was increased by 50% and 100% in respect to the baseline intact rock strength and these results were compared with the predicted UCS values for defect strength of 0% (“open” defects).

For the purposes of this study, 16 μ DFN groups of increasing fracture intensity and persistence were incorporated within the previously calibrated large-scale intact GBMs (Table 3.3). For each μ DFN group and sample size, 2 to 3 different μ DFN realizations were generated by using identical geometric input parameters to examine the repeatability of the results. Table 3.3 presents the matrix of modelling scenarios and Figure 3.11 illustrates examples of the different generated SRB models.

Table 3.3. Matrix of modelling scenarios considered to generate SRB models.

Width	Height	Area	Volume	de	~No of blocks	P10 cases				Persistence cases			
mm	mm	mm ²	mm ³	mm	-	defects / m				m			
50	125	6.25E+03	2.5E+05	63	300	-				-			
100	250	2.50E+04	2.0E+06	125	1100	5	10	20	40	0.01	0.02	0.04	0.10
200	500	1.00E+05	1.6E+07	250	4100								
400	1000	4.00E+05	1.3E+08	501	16200								
Case 1						√	√	√	√	√	√	√	√
Case 2						√	√	√	√	√	-	√	-

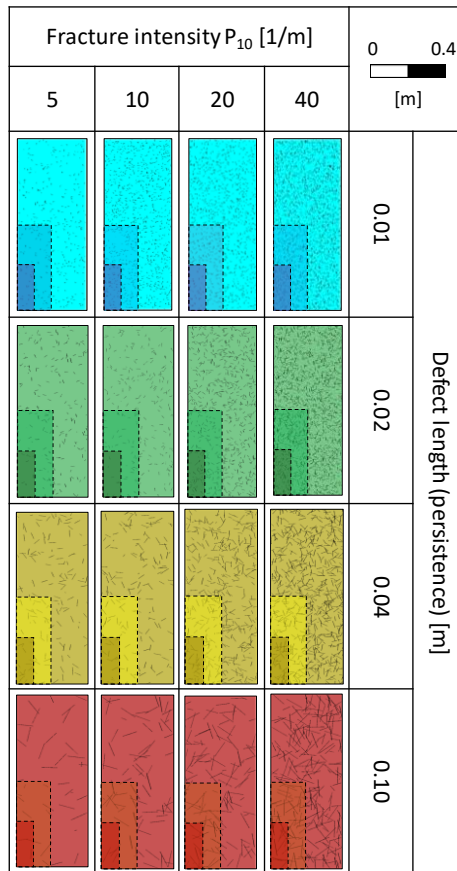


Figure 3.11. Matrix of SRB models for 16 μ DFN groups of increasing defect intensity and persistence and 3 specimen sizes (i.e. 100×250 mm, 200×500 mm and 400×1000 mm).

3.7. Geometrical Assessment

Prior to the mechanical property evaluation of the various samples, a rigorous geometrical assessment of the generated μ DFNs was conducted. The first step in this procedure involved the investigation of the relationship between the lineal fracture intensity P_{10} , serving as an input parameter, and the measured areal fracture intensity P_{21} depending on the utilized defect length L_d . By plotting P_{10} as a function of the product between P_{21} and the defect persistence L_d (Figure 3.12a), it can be observed that a linear relationship can be acquired with the slope of the best-fit line varying depending on the defect length. Further analysis of the obtained results reveals that the slope values can be expressed as a power-law function of the defect length (i.e. defect persistence), as observed in Figure 3.12b. By coupling those two plots it becomes evident that if the defect persistence is known and either P_{10} or P_{21} is available, the third quantity can be directly back-calculated.

Additionally, the number of defects for each of the investigated DFN geometries was evaluated for each specimen size. From Figure 3.12c, it can be observed that for a specific specimen size the number of defects in the model increases in an approximately non-linear fashion as the areal fracture intensity P_{21} increases. Furthermore, the acquired results demonstrate that this increase in the defect number with increasing P_{21} depends on the specimen size (Figure 3.12d). More specifically, in the smaller samples the increase in the defect number occurs at a lower rate than in the larger specimens. The relationship between the defect number increase rate and the sample size can be described by an exponential curve (Figure 3.12d), and this observation is in agreement with the argument made by Hoek and Brown (1997) that larger rock block volumes are more likely to be influenced by an increased population of defects. Additionally, it becomes evident that this rate is influenced by the defect persistence with smaller defect lengths producing higher rates with increasing sample

size. On the contrary, as the defect persistence increases the defect number increase rate decreases.

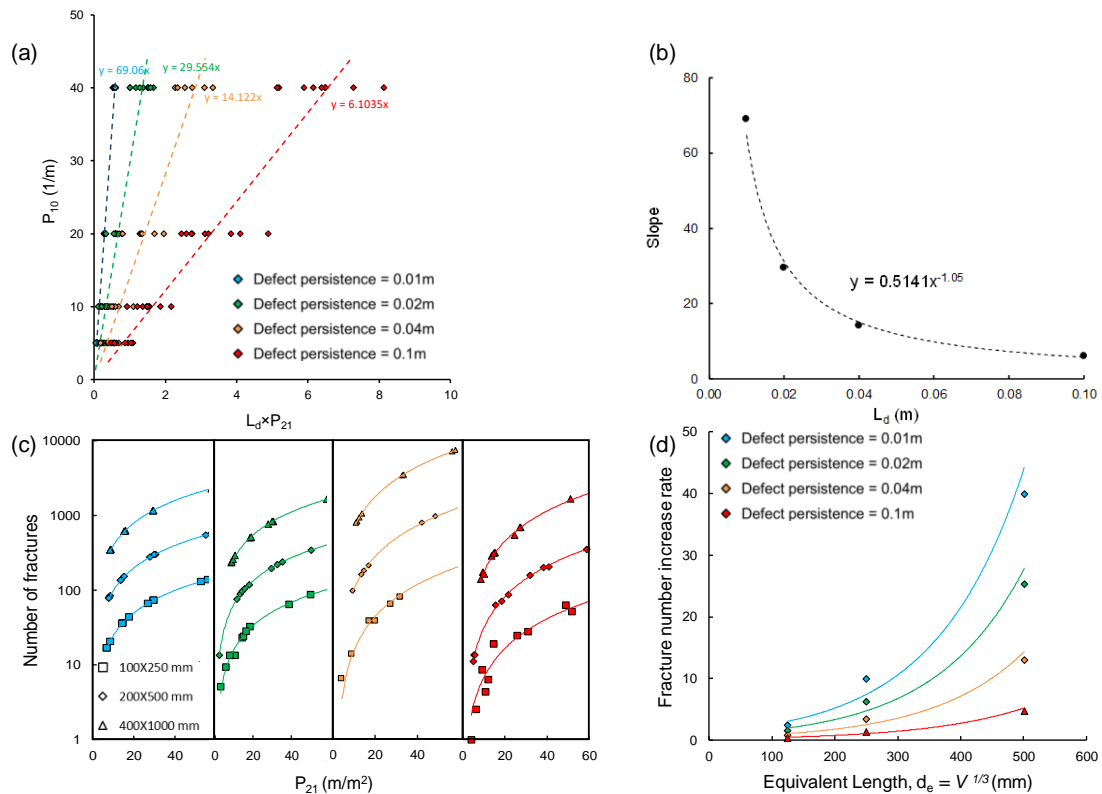


Figure 3.12. (a) The linear fracture intensity P_{10} expressed as a function of the product between areal fracture intensity P_{21} and defect length L_d . (b) Slope of the best-fit lines in Figure 12a as a function of the defect length L_d . (c) Linear relationship between P_{21} and number of fractures (vertical axis is in a logarithmic scale) for each sample size. Note the significant increase in the slope of the best-fit line for the largest sample. (d) Rate of fracture number (slope of best-fit lines in Figure 3.12c) increases exponentially with sample size.

3.8. Predicted Rock Block Strength

3.8.1. Influence of Defect Persistence and Intensity

The results from the scaling analysis generally suggest that the UCS of rock blocks is strongly influenced by the presence of “open” pre-existing defects. Figure 3.13 exhibits the predicted UCS values in respect to the sample equivalent length (d_e) and μ DFN intensity P_{10} . The predicted UCS values from the SRB experiments have been normalised to the intact lab UCS of 50 MPa. As can be seen, substantial reductions in strength are recorded as defect intensity and persistence increase. The results of the samples with persistence equal to 0.1 m were not included in Figure 3.13 as strength dropped rapidly at about 10 – 20% of the intact rock UCS and then remained constant. The effect of specimen size is particularly important at low fracture frequencies (due to the greater areal size of solid intact rock bridges in between the micro-defects) and becomes less significant for higher defect intensities and defect trace lengths (continuities). This behaviour indicates that REV has been achieved for the highly defected samples even from the relatively smaller samples (i.e. 100 × 250 mm) while larger samples seem to be required to achieve a constant response for the less broken micro-defected samples. For the specimens with large defect persistence (i.e. 0.04 m and 0.1 m), an increase of strength with scale was also observed due to an increased contribution of the intact rock bridges within the samples and because at smaller scales the large defects reduce significantly the loading capacity of the specimen.

Figure 3.13 also shows the Yoshinaka et al. (2008) and Laubscher and Jakubec (2001) strength limits. From these graphs it appears that the maximum RBS reduction derived by the Laubscher and Jakubec (2001) relationship (i.e. 48% of the baseline UCS), corresponds reasonably well with the strengths of the large samples with defect persistence of 0.01 m, possibly suggesting that this method describes successfully the behaviour of rock blocks influenced by micro-heterogeneities in the grain scale.

However, the UCS of specimens with persistence 0.02 m, 0.04 m and 0.1 m respectively is underestimated by Laubscher and Jakubec (2001) but further testing is required to validate this observation. On the other hand, the scale effect asymptotes proposed by Yoshinaka et al. (2008) allow for more dramatic strength reductions which in turn are more consistent with the predicted UCS values from the SRB modelling. For low fracture frequencies (i.e. $P_{10} = 5 - 10$ 1/m) where the effect of specimen size appears important, the decreasing trend of UCS is similar in shape to the Yoshinaka et al. (2008) relations while for higher defect intensities (i.e. $P_{10} = 20 - 40$ 1/m) and defect continuities where strength drops rapidly and then reaches a constant value, an adjustment appears to be needed to capture the observed behaviour.

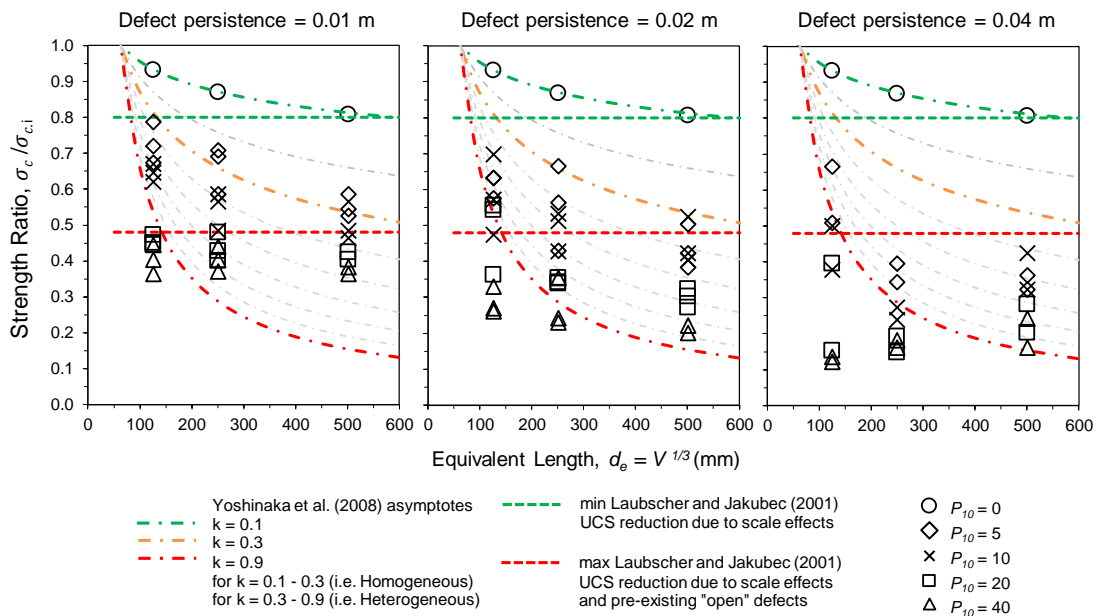


Figure 3.13. Normalised UCS values as a function of sample size and P_{10} defect intensity. Also shown for comparison are the Yoshinaka et al. (2008) and Laubscher and Jakubec (2001) strength limits.

The results from the SRB scaling simulations were also plotted as a function of the μ DFN P_{10} and P_{21} defect intensities (Figure 3.14). As expected, the reduction of UCS is more profound as defect frequency increases and defects persist. From a P_{10} perspective (Figure 3.14a), the inverse relationship between strength and defect frequency is not unique as four different envelopes delineate the strength decrease as a function of the four different defect lengths of 0.01 m, 0.02 m, 0.04 m and 0.1 m. A similar trend is also revealed when the data are plotted as a function of the P_{21} intensity (Figure 3.14b). Both Figure 3.14a and Figure 3.14b diagrams also reveal that the decay of strength follows a power-law trend and that beyond a certain defect intensity RBS remains relatively constant. However, it is important to note that the rate of strength reduction increases with an increase on defect persistence, meaning that strength reaches a constant behaviour at smaller fracture intensities as micro-defect length increases. From Figure 3.14a and Figure 3.14b it is also clear that, regardless of using the P_{10} or P_{21} μ DFN intensities, a systematic strength loss is observed for defect persistence of 0.01 m, 0.02 m and 0.04 m while for defect persistence of 0.1 m the magnitude of strength reduction has been reduced remarkably, suggesting that strength approaches a horizontal asymptote corresponding to a minimum strength in rock block scale. Because of this progressive strength reduction, when the defect intensities for each case are combined with the defect persistence (i.e. P_{10} or $P_{21} \times$ Persistence), a very good clustering of the obtained values is observed in the data set and a unique solution appears to exist when the UCS ratio is plotted against the “Defect Intensity \times Persistence – (DIP)” factor (Figure 3.14c and Figure 3.14d). The general trend of the data shown in Figure 3.14c and Figure 3.14d is encouraging and suggests that the combination of defect intensity with defect persistence is adequate to express the strength of rock blocks under different geometrical scenarios and defect arrangements.

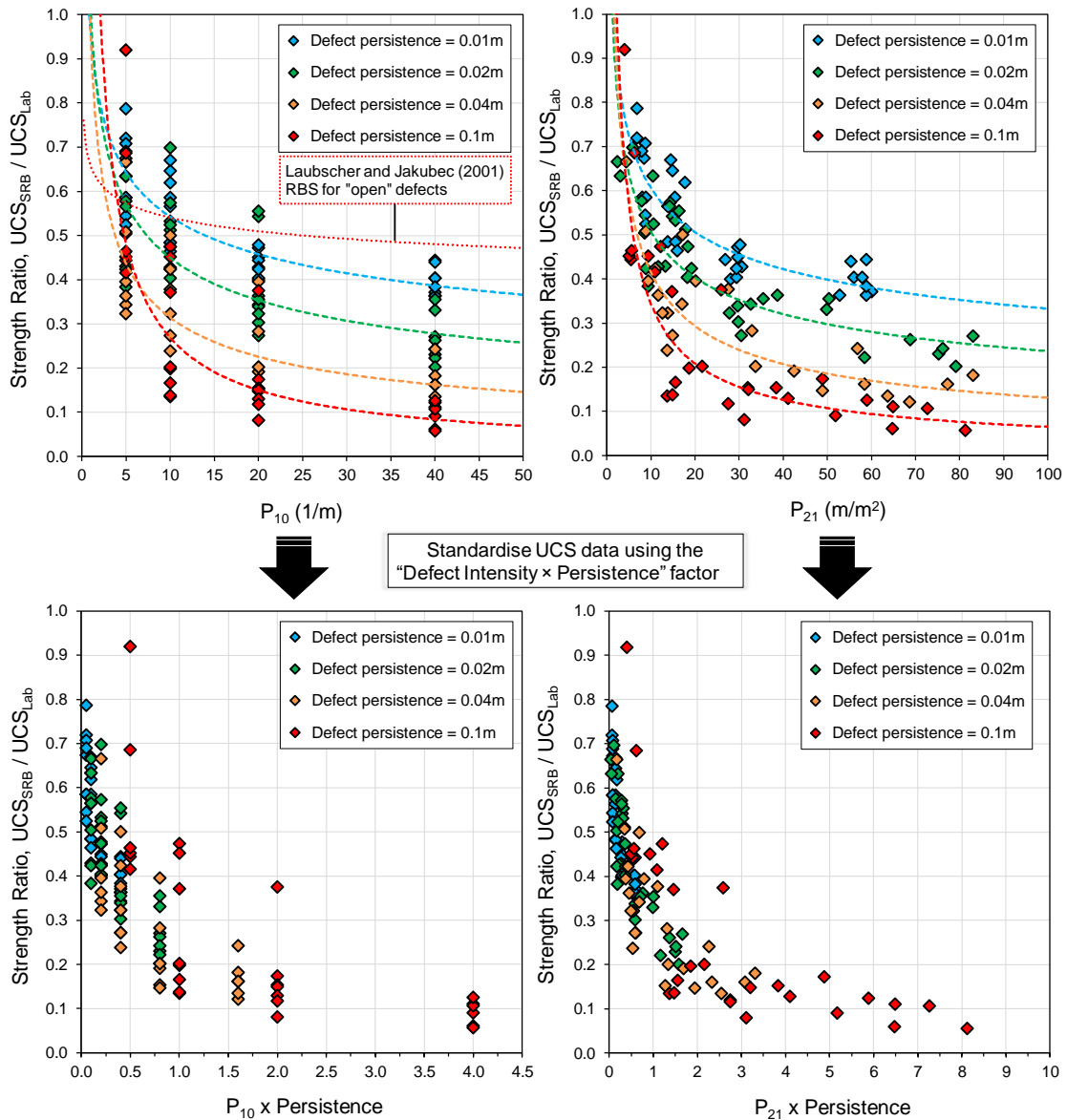


Figure 3.14. (a) and (b) Normalised UCS values as a function of defect intensity (P_{10} and P_{21}) and defect persistence. Also shown for comparison is the rock block strength reduction for “open” defects proposed by Laubscher and Jakubec (2001). (c) and (d) Normalised UCS values as a function of the “Defect Intensity \times Persistence – (DIP)” factor.

In Figure 3.15, the predicted UCS values from the current study (Figure 3.14) were plotted together with results from other numerical investigations for comparison. All studies, show a systematic decrease in the UCS with increasing degree of microfracturing, but the shape / rate of the strength reduction illustrates clear discrepancies. The data of this study are in perfect agreement with Gao and Kang (2016), partially in agreement with Lu (2014) for large P_{2l} values, but differed from the findings of Hamdi et al. (2015). Lu (2014) and Hamdi et al. (2015) considered in their studies small laboratory scale samples with crack lengths 15 ± 1 mm and less than 1 mm respectively while Gao and Kang (2016) simulated larger block volumes (i.e. 300×600 mm) with defect persistence of 60 ± 20 mm. The Hamdi et al. (2015) work considers heterogeneities in the grain scale, the influence of which has already been accounted in our study by adopting the Laubscher and Jakubec (2001) 80% size factor (i.e. 80% of the baseline intact UCS). The good agreement with the results from Lu (2014) for large P_{2l} intensities and the identical results of Gao and Kang (2016) indicate again that variations in specimen size and defect length have a clear impact on the strength of rock blocks, the rate of strength loss and the resulting REVs. This observation is further supported in Figure 3.15 by including two rock mass scale SRM studies (Elmo and Stead, 2010; Vazaios et al., 2018) which demonstrate even more dramatic strength decrease rates, as expected, hence validating the general trend of strength reduction from small to large rock volumes with increasing defect populations and defect persistence.

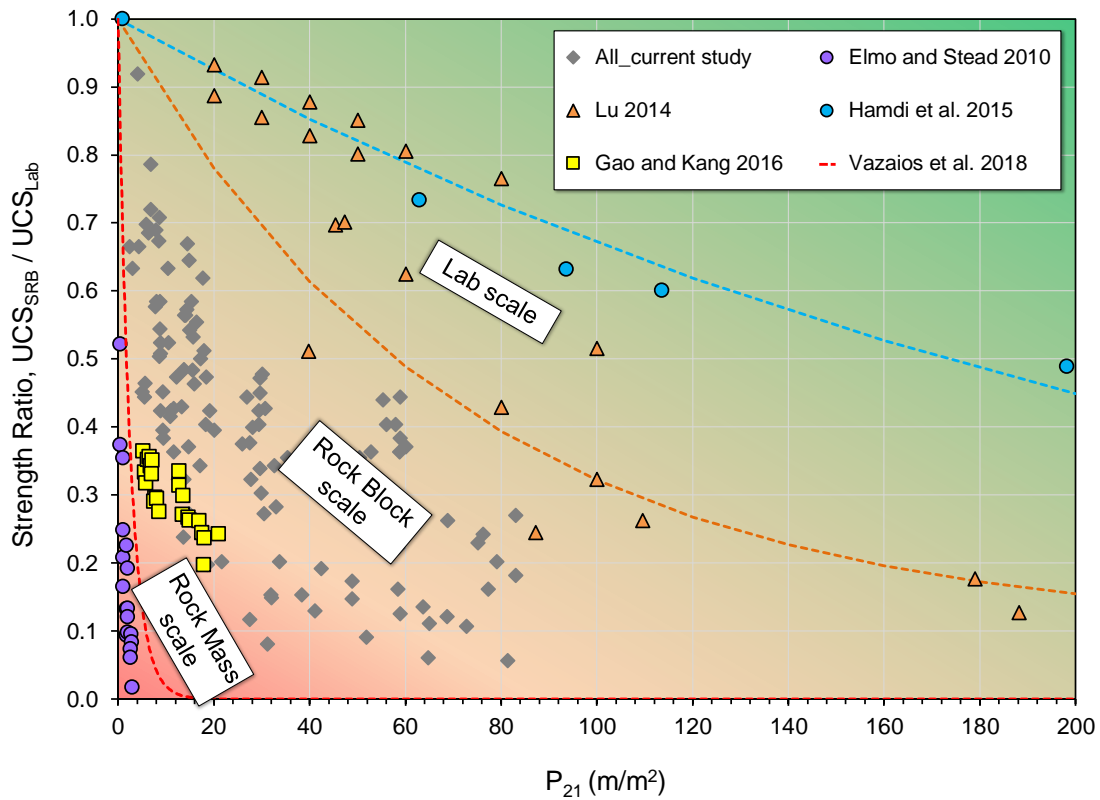


Figure 3.15. Comparison of predicted UCS results from current study with other numerical investigations examining scaling effects (Elmo and Stead, 2010; Lu, 2014; Hamdi et al., 2015; Gao and Kang, 2016; Vazaios et al., 2018).

3.8.2. Influence of Defect Strength

The analyses conducted in the previous section for the “open” defects demonstrated the significant effect of defect intensity and persistence on the strength of rock blocks. Further numerical simulations were undertaken to assess the impact of defect strength for the previously generated SRB models with micro-defect persistence values of 0.01 m and 0.04 m respectively. A parametric analysis was employed in which defect strength (i.e. cohesion and tension) was increased by 50% and 100% in respect to the size-corrected Voronoi interface strengths for the non-defect samples shown in Table 3.2 (hereafter referred as “baseline intact rock strength”) while the

stiffness values were assigned to be equal to the intact rock interface contacts. Figure 3.16 exhibits the predicted UCS values in respect to the sample equivalent length (d_e), the μ DFN intensity P_{10} and the defect strength. These findings are in agreement with similar studies conducted by Pierce et al. (2009) and Jakubec et al. (2012) who used the SRM method to study the combined effect of micro-defect strength and size on the UCS of rock blocks. The variation of UCS for the SRB samples with defect lengths of 0.01 m coincides reasonably well with the Yoshinaka et al. (2008) asymptotes but a less good fit is found for the samples with defect persistence of 0.04 m. This is because the behaviour of the samples is not driven by the intact rock material in between the defects and the UCS reaches rapidly a constant strength even from the smaller samples. Nevertheless, these results suggest that in the case of non-highly persistent micro-defects, the exponent k in the Yoshinaka et al. (2008) relationship could be expressed in terms of sample size and defect intensity P_{10} .

Table 3.4. Defect interface assigned properties in respect to the calibrated “baseline intact rock strength” micro-mechanical properties for the large-scale non-defected samples.

			Sample Size (mm)								
			100x250			200x500			400x1000		
Defect Properties			0%	50%	100%	0%	50%	100%	0%	50%	100%
Cohesion	c_d	MPa	0	5.65	11.3	0	5.35	10.7	0	4.7	9.4
Friction Angle	φ_d	[o]	47.5	47.5	47.5	46.2	46.2	46.2	42.4	42.4	42.4
Tensile Strength	t_d	MPa	0	1.65	3.3	0	1.65	3.3	0	1.65	3.3
notes	1	The 0% defect strength properties refer to the “open defects” modelled in section 4.3.1.									
	2	The 100% defect strength properties are equal to the size-corrected Voronoi interface strength properties for non-defected samples shown in Table 3.2.									

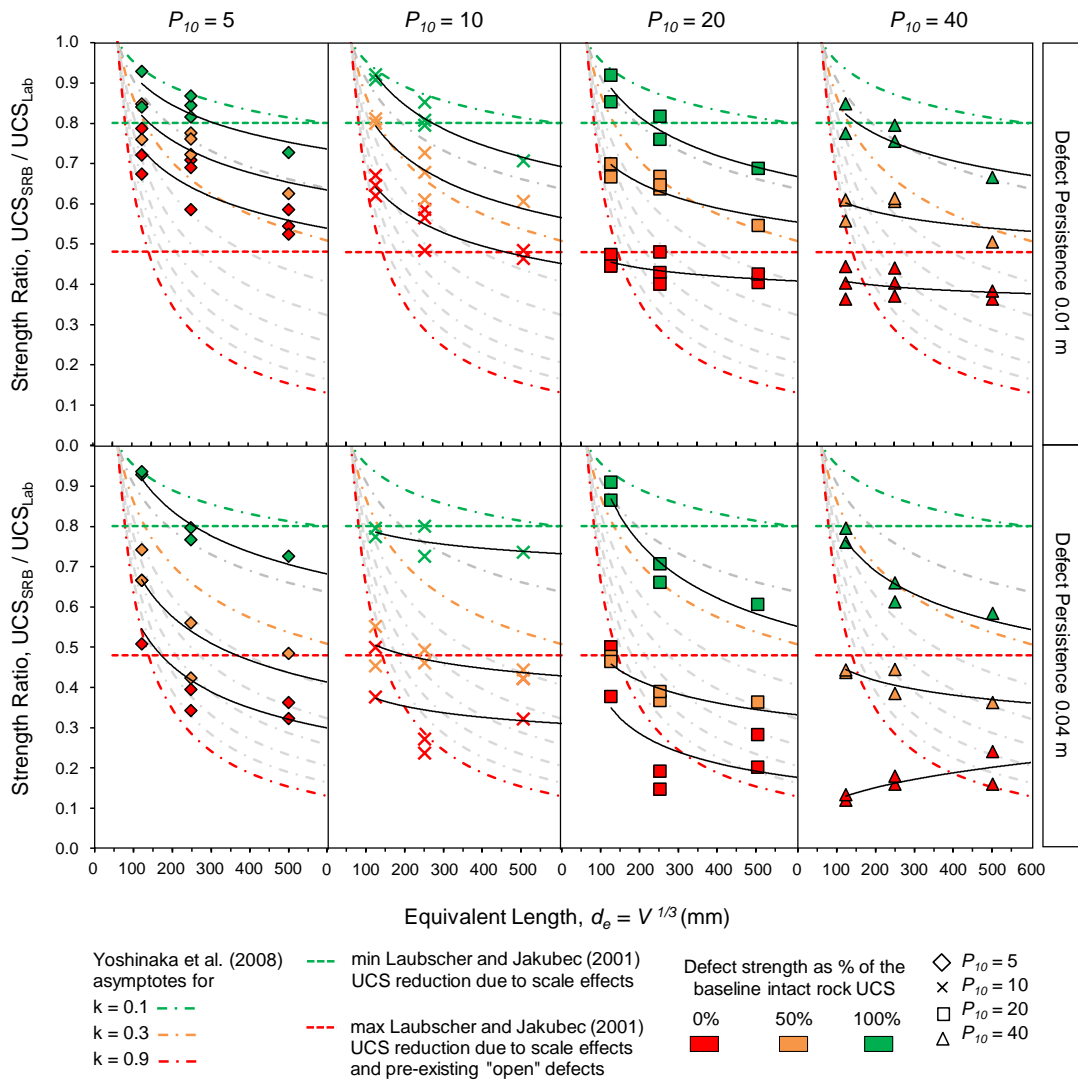


Figure 3.16. Normalised UCS values as a function of sample size and P_{10} defect intensity. Also shown for comparison are the Yoshinaka et al. (2008) and Laubscher and Jakubec (2001) strength limits.

All results were also plotted together with the predicted UCS values for defect strength of 0% (“open” defects) as a function of the P_{10} and P_{21} defect intensities and are illustrated in Figure 3.17. The progressive increase in defect strength from 0% to 100% of the baseline intact rock strength improves significantly the UCS of the simulated samples as the micro-cracks are “locked” and their effect becomes less important (for the 50% defect strength) or even vanish (for the 100% defect strength). As can be seen in Figure 3.17, the rate of gain in UCS for the SRB samples with defect persistence of 0.04 m is faster than the strengthening rate of samples with persistence of 0.01 m, meaning that the shear strength of defects overrides the effect of persistence as defect strength increases. This is more obvious at the scenario with defect strength equal to 100% of the baseline UCS where the strength of both samples has approached the scaled non-defected intact rock condition (i.e. 80% of the lab scale UCS) and the effect of persistence has essentially disappeared.

Figure 3.17 also includes the Laubscher and Jakubec (2001) relations for three different defect strengths ranging in the Mohs hardness index from 1 (“open” defects) to 5 (e.g. apatite and quartz). These limits define the lower and upper bounds for the defect frictional properties given in the MRMR system (Laubscher and Jakubec, 2001). The Laubscher and Jakubec (2001) curves appear relative insensitive to the defect strength as the UCS increases by only 7 – 8% when defect strength increases from 1 to 5 for the complete range of micro-crack frequencies. On the other hand, the peak strengths attained by the SRB modelling suggests an increase in between 20% – 40% and 35% – 65% for the defect lengths 0.01 m and 0.04 m respectively.

This observation is schematically illustrated in Figure 3.18. However, a direct comparison between our findings and the Laubscher and Jakubec (2001) method is not possible at this stage.

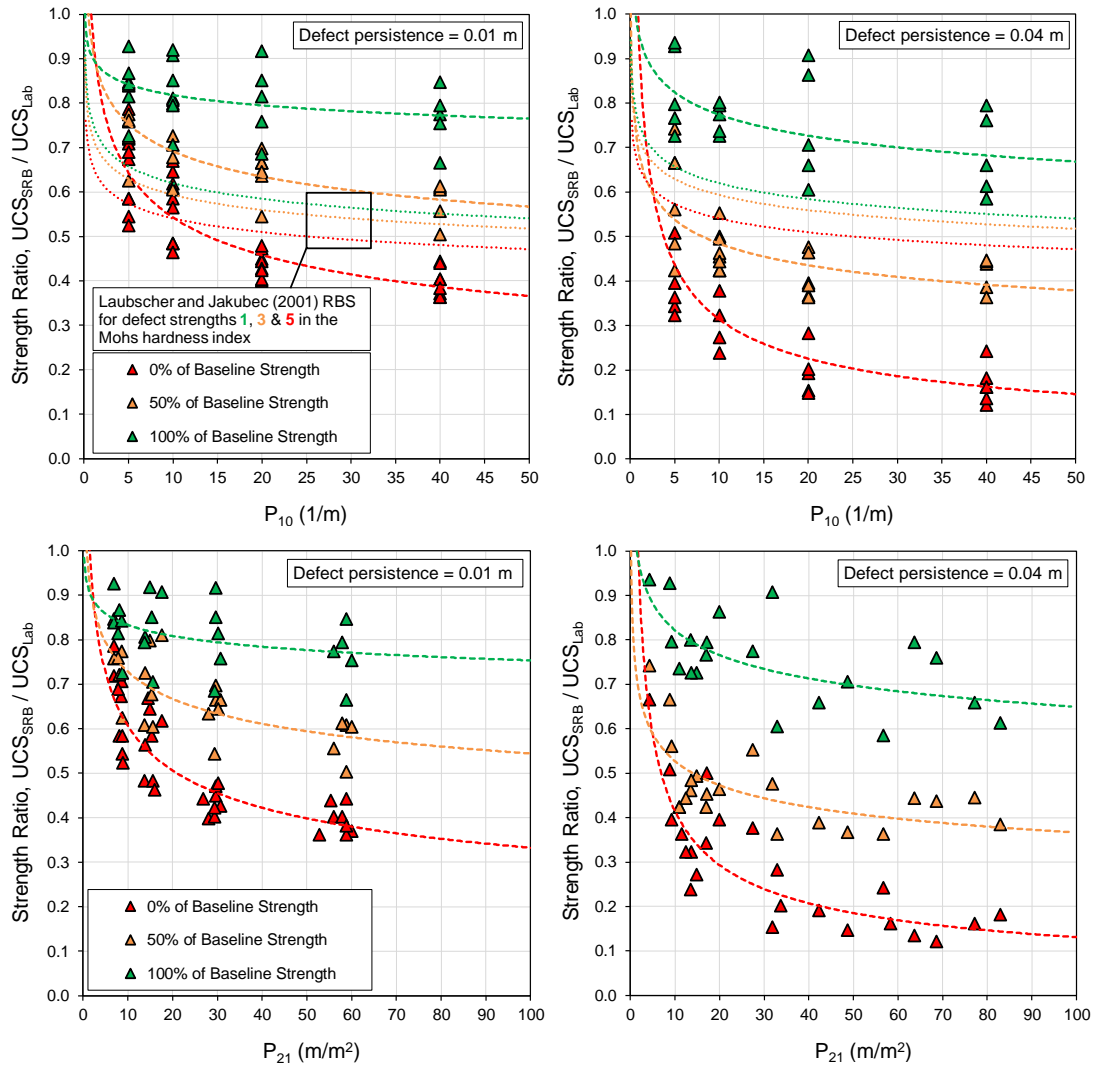


Figure 3.17. Normalised predicted UCS values as a function of defect intensity (P_{10} and P_{21}) and defect strength. Also shown for comparison are three progressive rock block strength reductions proposed by Laubscher and Jakubec (2001) for Mohs hardness index 1, 3 and 5.

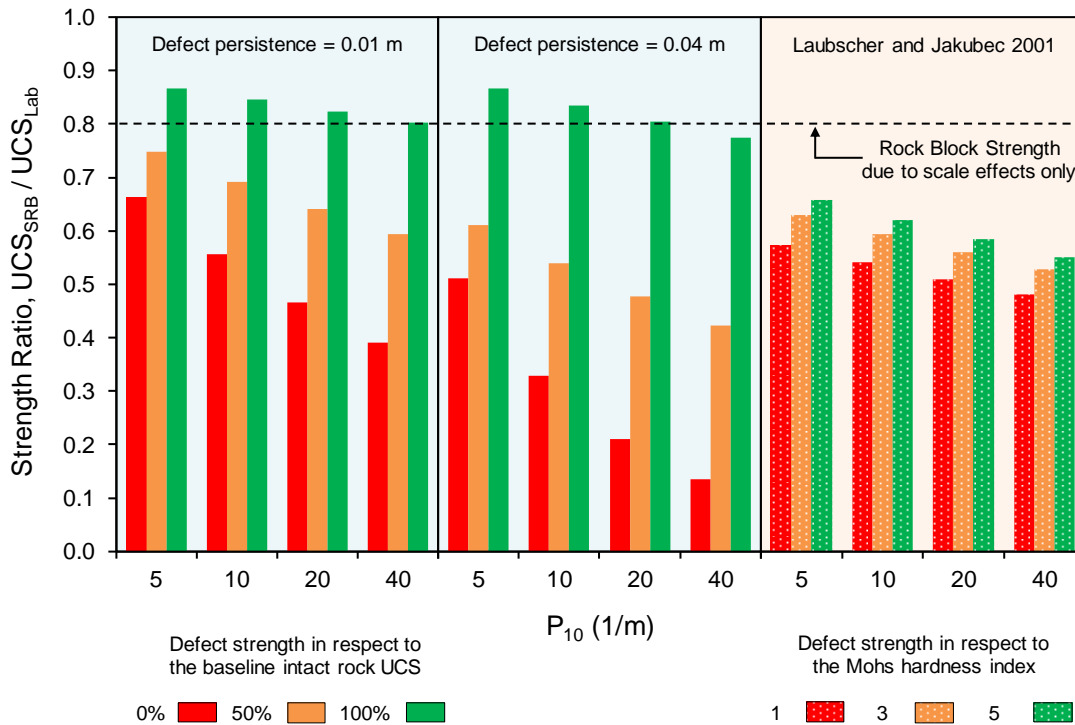


Figure 3.18. Average normalised UCS values for defect strength 0%, 50% and 100% of the baseline intact rock strength in comparison with rock block strength values predicted by the Laubscher and Jakubec (2001) method for Mohs hardness index 1, 3 and 5.

Turichshev and Hadjigeorgiou (2017) demonstrated in their study that the peak strength of laboratory scale defected samples is strongly influenced by the vein mineralogy and thickness. For specimens with high volumetric content of “hard” minerals (i.e. Mohs hardness index > 4) the authors found that the resulted strengths are higher by approximately 25% from specimens with high content of “soft” minerals (i.e. Mohs hardness index < 4). These findings agree quite well with the UCS predictions from the SRB modelling performed in the current study. On the contrary, from an extensive laboratory dataset of different types of heterogenous rock samples with vein infilling ranging in Mohs hardness scale from 2 to 4, Bewick et al. (2019) found that vein hardness played relatively minor role on the resulting UCS values

supporting the nomogram developed by Laubscher and Jakubec (2001). Although there is limited data available, the studies from Turichshev and Hadjigeorgiou (2017) and Bewick et al. (2019) possibly support the existence of a mineral hardness threshold of 4 that has been previously suggested by Brzovic and Villaescusa (2007). Regardless of these findings, as has been highlighted by Jakubec and Esterhuizen (2007), the proposed Mohs hardness scale for estimating the defect infill strength is only an empirical approach, and an effort should be made to better understand the strength contribution of these defects by means of laboratory experiments (e.g. Day et al., 2017) and/or SRM modelling (e.g. Pierce et al., 2009).

3.9. Predicted Rock Block Young's Modulus

From the conducted UCS experiments in UDEC, the Young's modulus at 50% of peak strength was also obtained to examine the effect of the pre-existing defects on the deformability of the synthetic models. Figure 3.19 demonstrates the predicted Young's modulus values from the SRB samples normalised in respect to the intact rock modulus of 20 GPa and Figure 3.20 illustrates the resultant Modulus Ratio (MR) (i.e. Young's modulus / UCS) from the SRB analyses normalised with the intact rock MR (i.e. 20 GPa / 50 MPa = 400).

For a defect persistence of 0.01 m and 0.02 m, the obtained modulus is relatively insensitive to the size and the presence of the pre-existing cracks while for a defect persistence of 0.04 m and 0.1 m, significant reduction is observed due to the reduced influence of intact rock bridges in between adjacent defects. In general, the deformation modulus appears to experience less pronounced scale effects in comparison with the predicted UCS values, but both properties follow a similar power-law function. The fact that the deformation modulus and strength follow a different scale effect response is further supported in Figure 3.20 which clearly shows an increase in MR with increasing defect length and then a progressive decrease with increasing defect

strength. This is because strength experiences more aggressive reductions than the modulus of elasticity and because the rate of modulus improvement is faster than the rate of strength increase when defect strength increase from 0% to 100% of the baseline intact rock strength.

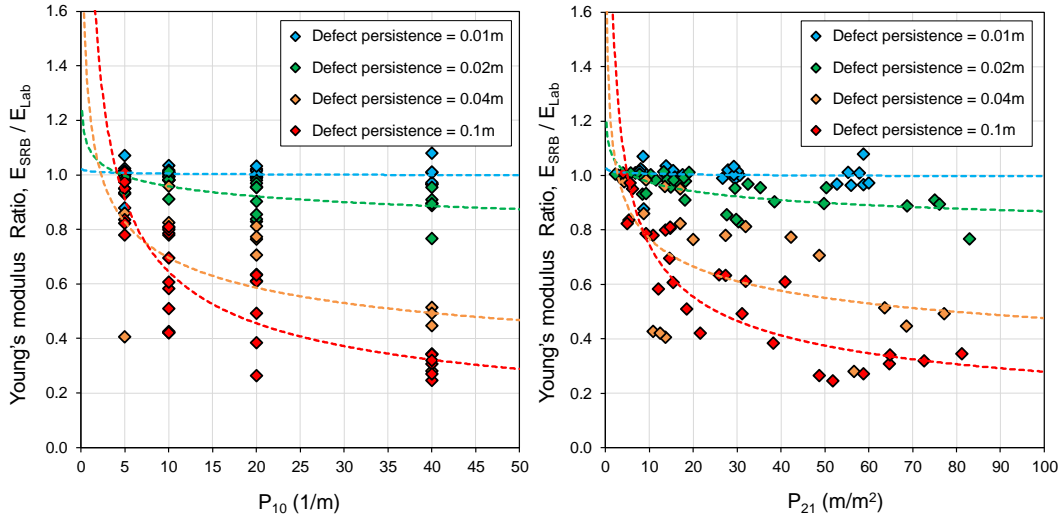


Figure 3.19. Normalised Young's modulus values as a function of the defect intensity (P_{10} and P_{21}) and persistence.

To investigate a possible correlation between strength and stiffness, the predicted normalised UCS values from all cases were plotted against the associated normalised Young's modulus values (Figure 3.21). Both parameters were normalised in respect to the lab scale strength and modulus respectively. As it can be observed, for UCS reductions up to 40%, the elastic modulus remains essentially unchanged (i.e. Zone 1) and then for greater strength reductions, the Young's modulus departs from the intact rock behaviour and decreases rapidly as strength drops with decreasing intact rock quality (i.e. Zone 2).

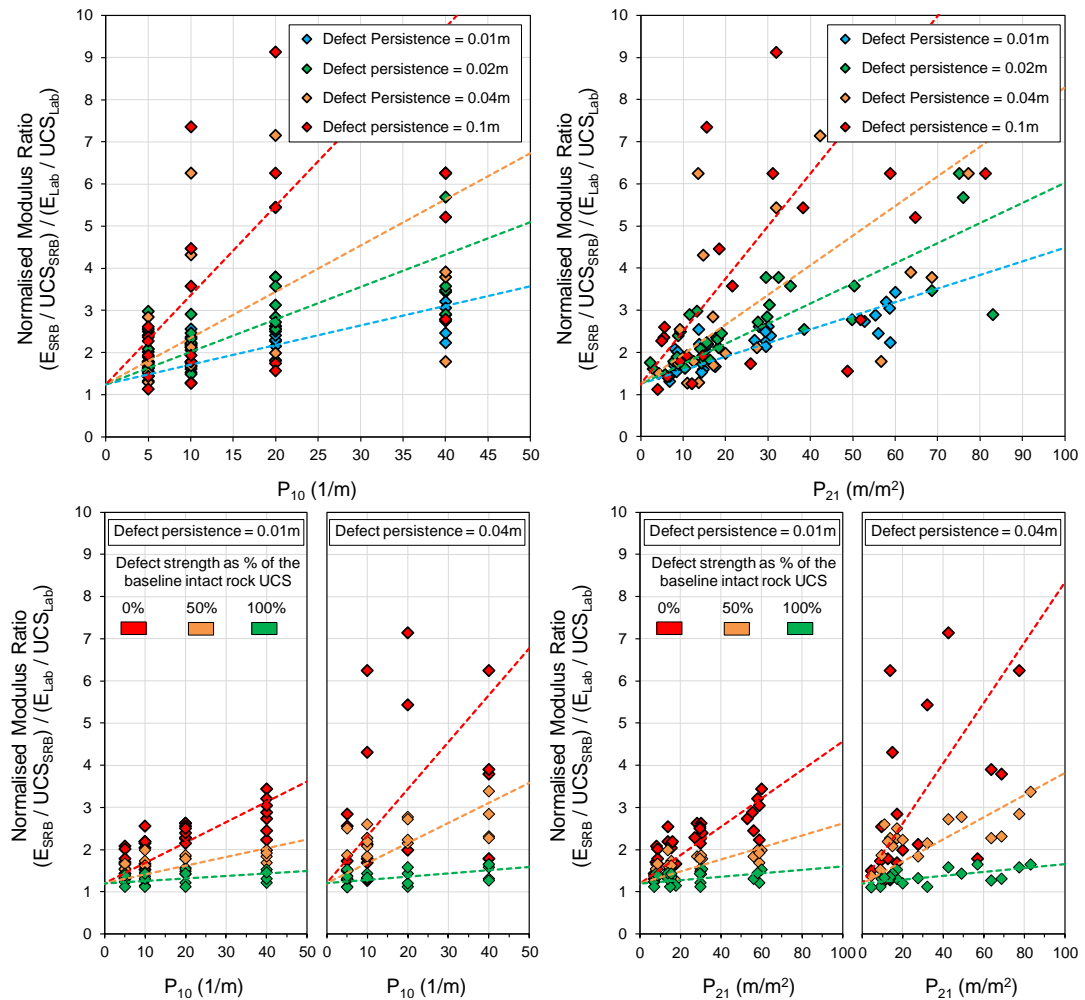


Figure 3.20. Normalised Modulus Ratio (SRB MR / Lab MR) as a function of the defect intensity (P_{10} and P_{21}), persistence and strength.

Based on laboratory studies investigating scaling effects in block size, no major influence on the elastic modulus has been found as specimen size increases (Singh and Huck, 1972; Pratt et al., 1972; Price, 1986; Jackson and Lau, 1990). The deformation modulus from these studies appear to remain relatively unaffected or to decrease up to 15% with changes in sample size. Although limited experimental data is available, the range of observed moduli from the SRB analysis results are consistent with the general admission that the Young's modulus is relatively independent of sample size.

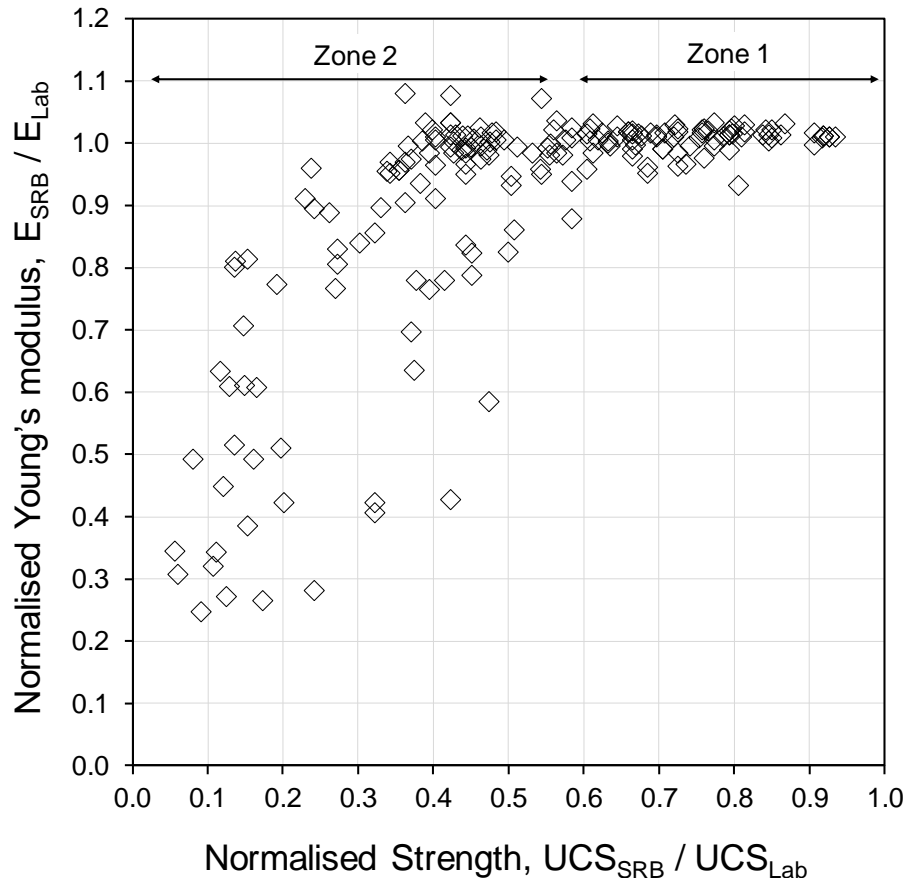


Figure 3.21. Normalised Young's modulus vs normalised UCS values. The SRB modulus and strength were normalised with the lab scale properties.

3.10. Observed Failure Modes

The SRB simulations replicated successfully the failure processes that are typically observed in actual laboratory experiments under unconfined conditions (i.e. crack initiation followed by crack propagation and coalescence resulting in unstable extensional fracturing parallel to the direction of loading). However, the presence of cohesionless pre-existing defects triggered distinctly different failure modes in comparison with the non-defected samples. Figure 3.22 illustrates the transition from an intact rock fracturing driven failure mechanism to a structurally controlled

dominated damage. As observed, for the specimens containing defects, wing cracks are generated at the tips of the pre-existing flaws due to localised stress concentrations leading to unstable micro-fracturing and the formation of macroscopic bands. In contrast, for the non-defected specimens, failure typically initiates from the edges of the samples due to extensional microfracturing and then propagates inwards forming a double pyramid failure shape.

The contribution of the wing cracks in the overall strength reduction appears to increase as defect persistence increases due to the interaction of neighbouring defect tips which tend to attract each other. Regardless of the size and orientation of the pre-existing defects, wing cracks propagate simultaneously from the upper and lower tips due to micro-tensile fracturing parallel to the direction of loading. Figure 3.23 summarises the typical failure modes observed for increasing defect intensity and persistence. For specimens with low fracture intensities, tensile localisation and splitting along the “grains” dominate the failure process, while for a higher degree of fracturing, crack propagation is significantly prohibited, and sample damage is clearly dependent on the failure of the pre-existing defects. From Figure 3.23 it can be inferred that samples with smaller intact rock bridges are more likely to fail at lower stress magnitudes, with the extent of reduction being closely dependent on the persistence of pre-existing defects.

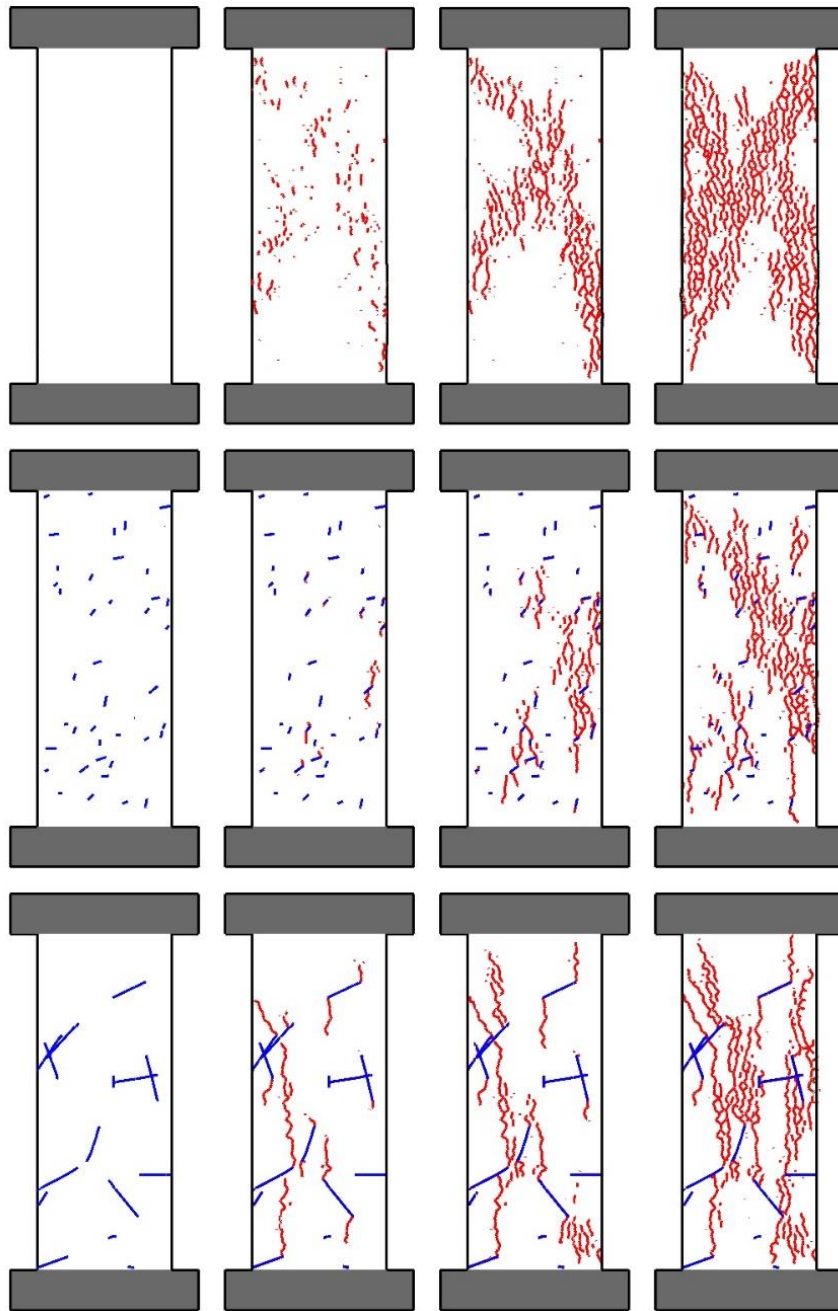


Figure 3.22. Evolution of damage and typical failure modes captured for the intact non-defected (above) and defected (middle and below) SRB samples. The lines with blue colour denote failed pre-existing defects while those with red represent newly generated micro-cracks.

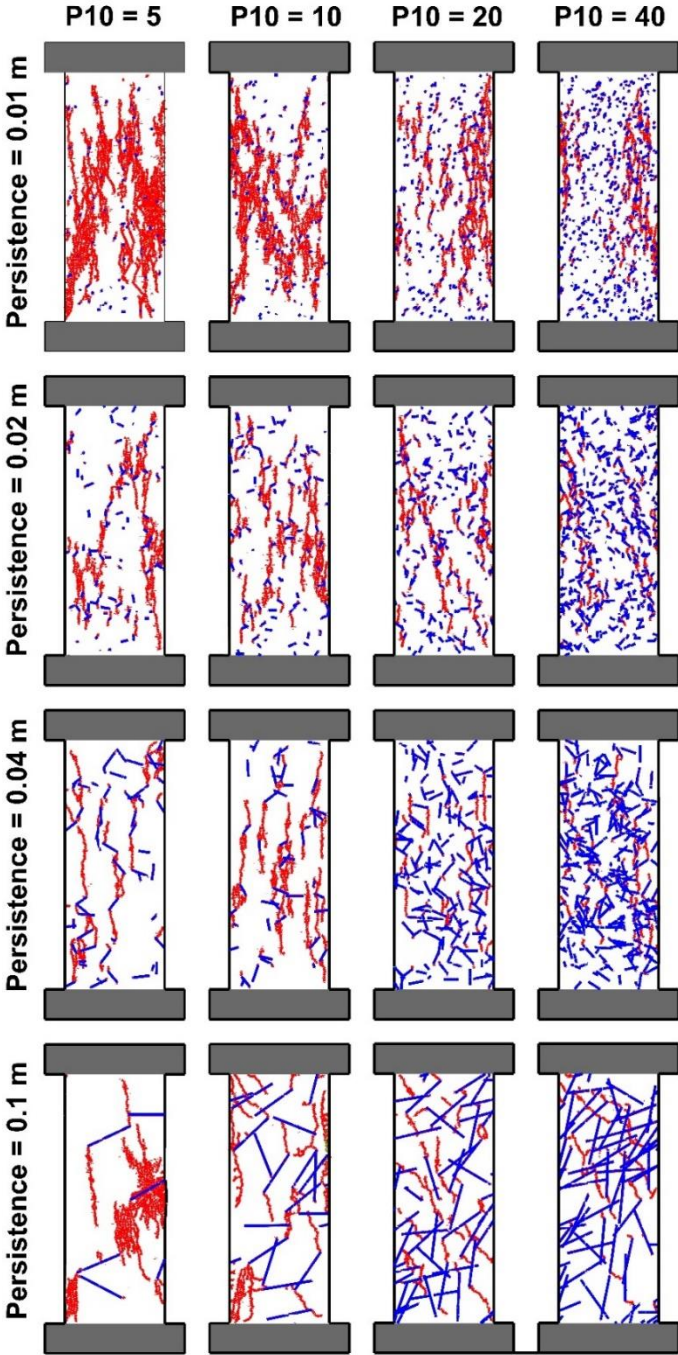


Figure 3.23. Failure modes for progressively increasing defect intensities and defect persistence. The lines with blue colour denote failed pre-existing defects while those with red represent newly generated micro-cracks.

Regarding the response of the samples as defect strength increases from 0% to 50% and then 100% of the baseline intact rock strength, defect strength is proven to be a dominant factor controlling the failure mode of the SRB samples. In Figure 3.24, initially it can be observed that as the pre-existing defect strength increases from 0% (purely frictional defects) to 100% (defects with cohesion and tensile strength equal to Voronoi block interfaces) a progressive increase in the specimen strength to that of the intact sample is achieved, as expected. By examining the lateral and volumetric strain curves, this increase in material strength can be directly related to the strain capacity of the sample which also increases by improving the defect condition. More specifically, for the case of 0% defect strength, both the lateral and volumetric strains follow a stepped path due to the stress localization at the defect tips, promoting the creation of wing cracks, and subsequently the fracturing of intact rock bridges before the complete failure of the sample. This is confirmed by the crack monitoring scheme employed. From it, it becomes evident that as rock bridges fail a temporary stable condition is achieved before the next rock bridge breaks as indicated by the crack number remaining constant for a short period of time (short plateaus appearing in the broken contact curve). By increasing the defect strength to 50%, a partially similar response can be observed. However, as a result of the increased defect strength, pre-existing discontinuities become harder to fail, stress localization at the defect tips is reduced, and new cracks involve both the generation of wing cracks at the defect tips and axial cracks initiating at the Voronoi block edges within the intact parts of the sample. For the case where Voronoi and defect strength interfaces are the same, the sample response is not governed by the failure of rock bridges. On the contrary, cracks forming parallel to the load direction (axial cracks) start appearing in the specimen until they reach a critical density and the specimen fails having distinct shear bands (Figure 3.24). This transition of the generated new cracks from wing to axial fractures results in an increased strain capacity of the sample (the sample can contract more) before

failing, and a more abrupt (brittle) failure occurs. On the contrary, for lower defect strengths this occurs in a more gradual, progressive fashion as described above due to the distinct rock bridges breaking.

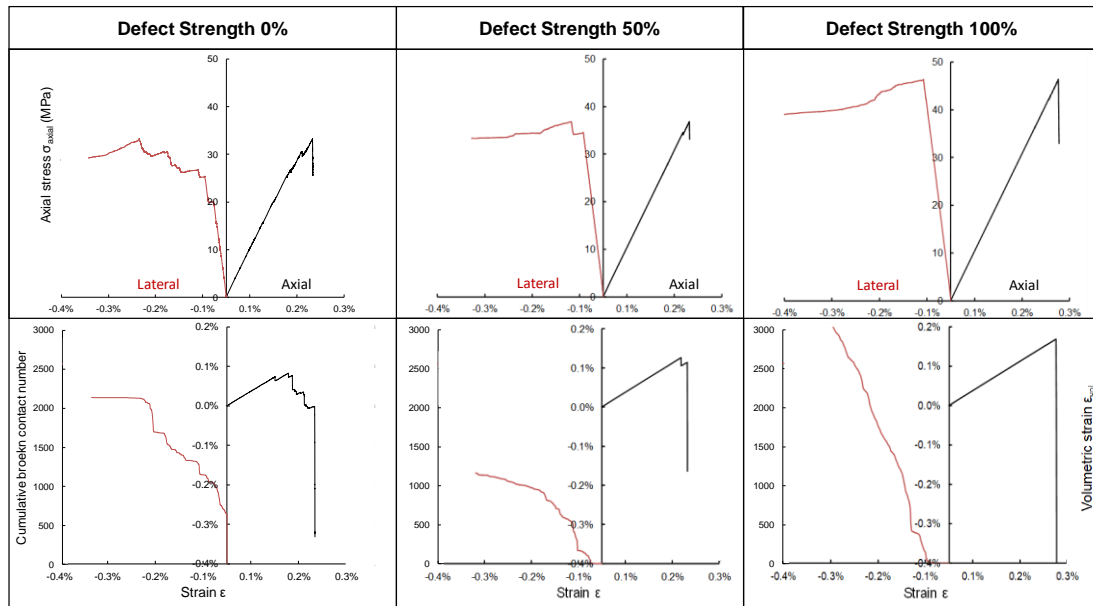


Figure 3.24. Specimen 100×250 mm for $P_{10}=5$ 1/m and defect length 0.04 m: Typical stress – axial/lateral strain (above), volumetric – axial strain and crack count – lateral strain (below) curves showing the transition in the failure mode as defect strength increases from 0% – 50% – 100% of the baseline intact rock strength.

3.11. Refined approaches for RBS estimation

The results of the SRB numerical study are encouraging as certain trends were observed in the UCS reduction in respect to the sample size, defect intensity, persistence and strength. Based on our findings, we attempt to extend the empirical relationships given by Laubscher and Jakubec (2001) and Yoshinaka et al. (2008), and modified correlations are proposed for estimating the strength of defected rock blocks.

The empirical relation of Laubscher and Jakubec (2001) (Figure 3.2) considers the influence of specimen scale, and the impact of defect frequency together with the

defect infill hardness. Extending this logic, Figure 3.25 presents a series of charts that express rock block strength as function of sample size, defect intensity, defect persistence and defect strength. In these charts, the fracture intensity (either P_{10} or P_{21}) from the various modelling scenarios has been combined with the persistence of each case (i.e. the DIP factor) to standardise the data variability into one unique solution and to allow for flexibility in the UCS predictions over a wide range of defect geometries and defect strengths. The same inverse strength relationships are presented into three different diagrams to magnify specific defect geometrical regions which otherwise would have been difficult to visualise if they were plotted by the same chart.

The proposed charts incorporate all the essential factors controlling the unconfined strength of rock blocks. Defect strength can be assessed by empirical approaches such as drop testing of the core during logging or by the hammer blow test. Core breaks along pre-existing defects during drilling can also provide an indication about the nature of the micro-defects and their possible contribution to rock block strength. Classification of failure modes (e.g. “intact”, “structural”, “combined” failure types) from UCS and triaxial lab testing has also been proven as an effective method to estimate the shear strength of specific defects from samples that have failed along pre-existing planes of weakness (Bewick et al., 2019). Furthermore, back-analysis of laboratory experiments using synthetic rock block samples can be used to derive site-specific correlations and to investigate the mobilised shear strength of individual defects (Turichshev and Hadjigeorgiou, 2017). By calibrating the micro-properties of non-defected and defected specimens it should be possible to derive the defect strength reduction as a function of the baseline intact rock grain-to-grain strength.

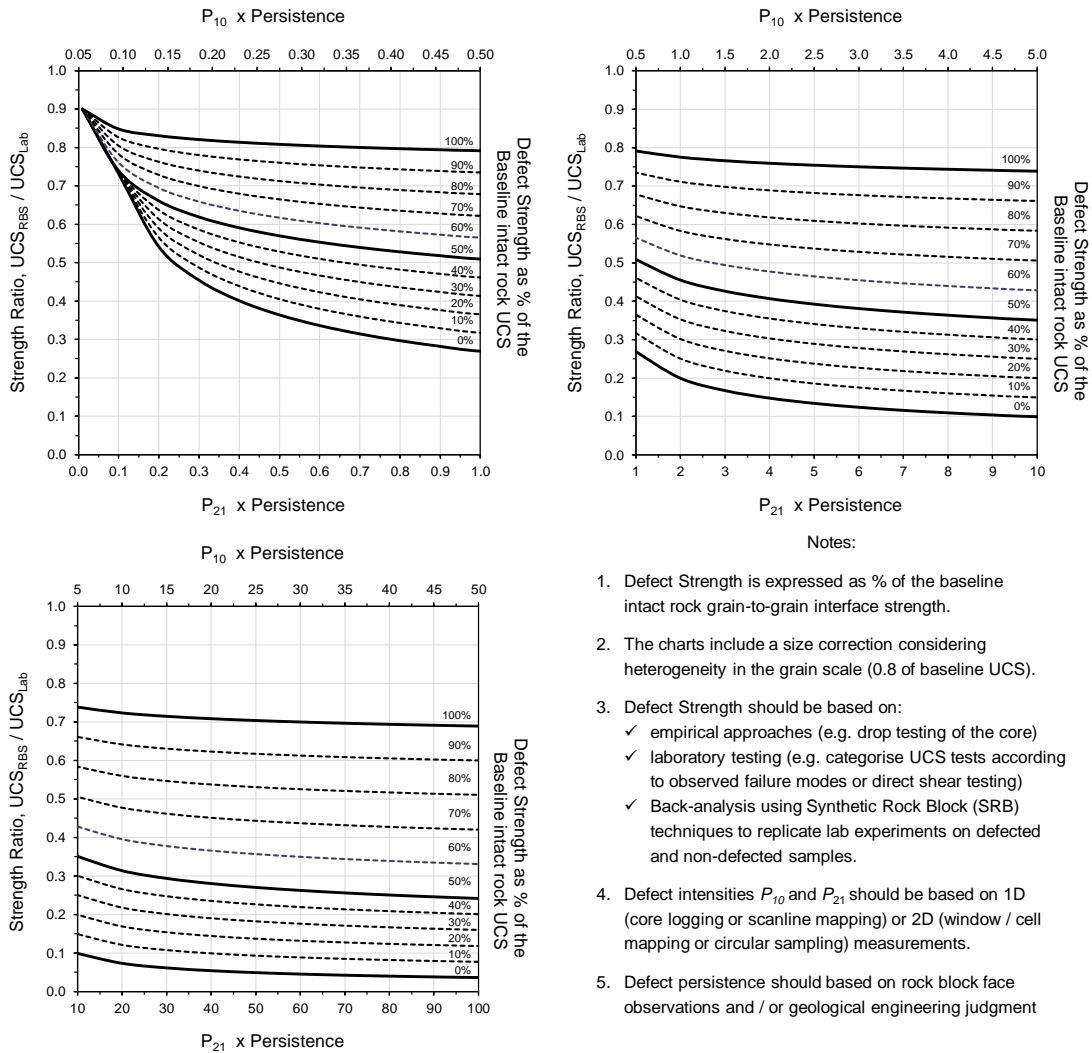


Figure 3.25. Proposed diagrams for estimating the Rock Block Strength (RBS) as a function of defect intensity, persistence, and strength.

In terms of the geometrical inputs, defect intensity could be derived via logging explicitly the micro-defects that occur along cores / scan-lines (1D observation), by sampling rock surface exposures (2D observation) or by using imaging techniques (e.g. Lidar or photogrammetry). Quantification of the defect length can be challenging due to the three-dimensional character of the defects and restrictions in mapping the internal

structure of rock blocks. Nevertheless, trace lengths measured as part of rock face mapping investigations can provide a reasonable approximation for the persistence. In case of micro-defects macroscopically not visible by naked eye, then very small persistence values should be used but it should be reminded that the charts already contain a size correction allowance considering heterogeneity in the grain scale (i.e. contrasts in the geometrical or mechanical properties of grains).

In regard to the empirical scaling relationship from Yoshinaka et al. (2008), although it allows for a wide range of UCS predictions, the results from our numerical study found poor correlations between size, defect geometries and strength. As a consequence, a calibration of the exponent k was not attempted, although theoretically it can be back-calculated using the diagram shown in Figure 3.25.

3.12. Discussion

It is widely recognised that the UCS of intact rock decreases with increasing scale and/or increasing micro-defect intensity due to size effects and the reduced intact rock bridges in between the defects (e.g. grain boundaries, cavities, fissures, veins and open or healed micro-cracks, etc.). However, apart from two empirical approaches (Laubscher and Jakubec 2001; Yoshinaka et al. 2008) that consider the effect of scale and micro-defects to evaluate the strength of rock blocks, the available guidelines are limited, and more rigorous methodologies are required to obtain representative rock block strength parameters. Yoshinaka et al. (2008) proposed a scaling relationship that can capture the inverse relationship of strength for a wide range of the *in-situ* rock block conditions but the authors do not provide guidelines on how to apply their methodology based on qualitative or quantitative approaches. On the other hand, the empirical methodology of Laubscher and Jakubec (2001) provides a clear pathway on

how to assess rock block strength based on size and defect conditions adjustments but their relation offers predictions for a limited range of strength reductions.

In this context, a numerical study was performed to examine the combined effect of sample size and defect conditions (i.e. intensity, persistence and strength) on the strength of rock blocks. Several UCS tests were conducted on synthetic rock block samples of varying sizes and defect geometries/strengths as an attempt to develop a framework for assessing the strength of defected rock blocks. The results from these experiments were compared with previous studies and the existing empirical relationships, and refined approaches are proposed for estimating the unconfined strength of rock blocks as a function of specimen size, defect intensity, persistence and strength.

The predicted UCS values were found to be strongly influenced by both size and defect condition effects while the Young's modulus appeared to be less sensitive. Nevertheless, both properties appear to follow a power-law distribution that eventually reaches a plateau for large samples sizes and/or closely spaced defects and/or highly persistent defects. Analysis of the large-scale UCS tests revealed that there is a systematic and progressive strength reduction with decreasing intact rock quality in terms of defect intensity, persistence and strength. When the fracture intensity (either P_{10} or P_{21}) from the various modelling scenarios was combined with the persistence of each case, all data followed certain paths for the analysed defect strengths. This allowed us to standardise the data along specific strength reduction envelopes and to propose generic predictive diagrams that cover a wide range of defect geometrical combinations and strengths. The use of the "Defect Intensity \times Persistence" or DIP factor is likely to be transferable to larger scales and rock mass classifications systems that currently consider only the blockiness of rock masses and not the effect of non-persistent discontinuities.

Currently, defect strength is expressed as a percentage of the intact size-corrected grain-to-grain strengths and although further research is required to rationalise this parameter, the use of synthetic rock block modelling techniques can be used to define lower and upper bounds. Despite of these difficulties, it is to be expected that strong defects can result in blocks behaving essentially as an intact material while weaker defects can cause dramatic strength reductions and changes on the failure modes. In addition, defect micro-persistence is unlikely to be constant for a given rock type and an effort should be made to derive an equivalent defect length from the anticipated size distributions. Since micro-defect populations are typically developed at similar conditions and possibly simultaneously with the large-scale discontinuities, analysis of the macro-fracture patterns can also be used as an indicator for the geometrical assessment of defects.

It is important to mention that careful consideration is required to establish characteristic lab-scale intact rock strengths when using the proposed approaches as underestimation or overestimation of the baseline UCS will influence the predictions for rock block strength. Sampling bias in favour of the better quality sections of core may result in overestimating the intact rock strength while material disturbance due to drilling/handling damage or stress relief and micro-cracking are the most common reasons to underpredict strength. To overcome these uncertainties, it is suggested to narrow the large scatter of results by classifying the UCS test data based on the observed failure methods (i.e. homogeneous versus heterogeneous samples) and by performing statistical analysis to assess the variability of the data for each group.

3.13. Conclusions

Rock block strength is a significant factor controlling the rock mass behaviour (i.e. deformations, failure modes, fragmentation, stand-up time, etc.) and the response

of the structural elements used as rock support and rock reinforcement. For massive to moderately jointed rock masses with incomplete discontinuities and/or high degree of interlock between the rock blocks, rock mass failure cannot occur without fracturing through rock blocks. Hence, it is vital to assess the strength of blocks as accurately as possible.

Especially when the design relies on discontinuum analysis where rock blocks are modelled explicitly as equivalent continuum materials in between discontinuities, rock block properties are a dominant driver influencing the results and the specification of reinforcement solutions and construction stages.

Several case-studies have highlighted the importance of considering the effect of pre-existing defects within the rock material but typically, the role of defects is neglected when evaluating the strength of rock blocks and rock masses. This can lead to misleading evaluations and implications on i) health and safety issues (e.g. instabilities, injuries/fatalities); ii) a sequence of design decisions (e.g. support measures, construction methods and sequence); and iii) project economics (e.g. delays, loss of production and claims).

In the current study, an extensive numerical analysis was performed using synthetic specimens composed by micro-mechanical elements and discrete fracture networks and relationships that link the UCS of rock blocks with its size and the geometrical arrangement and strength of defects were developed. Previous work by Stavrou and Murphy (2018) proposed linear and non-linear scaling relationships for estimating the confined strength of rock blocks, provided that the UCS reduction due to scaling effects is known. The combination of the current work (for estimating the unconfined strength of rock blocks) and the previous work by Stavrou and Murphy (2018) (for estimating the confined strength of rock blocks) offers the full suite of

relationships needed to determine a complete set of design properties at a rock block scale.

Although further research is required to validate the proposed approaches against actual laboratory experiments or in-situ monitoring data and back-analysis, the results showed how the impact of the pre-existing cracks can be quantified to relate the strength of rock blocks with specific measurable quantities. The study is therefore highlighting the strong potential of using synthetic rock mass modelling techniques to develop quantitative guidelines, to refine empirical relationships and to update rock mass classification systems.

Acknowledgements

The authors would like to thank ARUP for financially supporting this research. We would also like to thank Dr. Mark S. Diederichs for his guidance and meaningful discussions and James Woodman for matters concerning numerical modelling.

References

- Aubertin, M., Li, L. and Simon, R. 2000. A multiaxial stress criterion for short- and long-term strength of isotropic rock media. *International Journal of Rock Mechanics and Mining Sciences*. 37(8), pp.1169–1193.
- Baecher, G.B. 1983. Statistical analysis of rock mass fracturing. *Journal of the International Association for Mathematical Geology*. 15(2), pp.329–348.
- Bahrani, N. and Kaiser, P.K. 2016. Numerical investigation of the influence of specimen size on the unconfined strength of defected rocks. *Computers and Geotechnics*. 77, pp.56–67.

- Bewick, R.P., Kaiser, P.K. and Amann, F. 2019. Strength of massive to moderately jointed hard rock masses. *Journal of Rock Mechanics and Geotechnical Engineering*, 11(3), pp.562-575.
- Bieniawski, Z.T. 1968. The Effect Of Specimen Size On Compressive Strength Of Coal. *International Journal of Rock Mechanics and Mining Sciences*. 5(ii), pp.325–335.
- Brzovic, A. and Villaescusa, E. 2007. Rock mass characterization and assessment of block-forming geological discontinuities during caving of primary copper ore at the El Teniente mine, Chile. *International Journal of Rock Mechanics and Mining Sciences*. 44(4), pp.565–583.
- Carpinteri, A. 1994. Fractal nature of material microstructure and size effects on apparent mechanical properties. *Mechanics of Materials*. 18(2), pp.89–101.
- Cunha, A.P. da (Antonio) 1990. Scale effects in rock masses : proceedings of the first International Workshop on Scale Effects in Rock Masses, Loen, Norway, 7-8 June 1990 / edited by A. Pinto da Cunha In: A. P. da (Antonio) Cunha and I. C. on S. E. in R. Mechanics, eds. Rotterdam: Published for the ISRM Commission on Scale Effects in Rock Mechanics by A.A. Balkema.
- Damjanac, B., Board, M., Lin, M., Kicker, D. and Leem, J. 2007. Mechanical degradation of emplacement drifts at Yucca Mountain—A modeling case study: Part II: Lithophysal rock. *International Journal of Rock Mechanics and Mining Sciences*. 44(3), pp.368–399.
- Davy, P., Le Goc, R. and Darcel, C. 2013. A model of fracture nucleation, growth and arrest, and consequences for fracture density and scaling. *Journal of Geophysical Research: Solid Earth*. 118(4), pp.1393–1407.

- Day, J.J., Diederichs, M.S. and Hutchinson, D.J. 2017. New direct shear testing protocols and analyses for fractures and healed intrablock rockmass discontinuities. *Engineering Geology*. 229, pp.53–72.
- Dershowitz, W., Lee, G., Geier, J., Foxford, T., LaPointe, P. and Thomas, A. 2014. FracMan Version 7.4—Interactive Discrete Feature Data Analysis, Geometric Modeling, and Exploration Simulation: User Documentation.
- Dershowitz, W.S. and Einstein, H.H. 1988. Characterizing rock joint geometry with joint system models. *Rock Mechanics and Rock Engineering*. 21(1), pp.21–51.
- Dershowitz, W.S. and Herda, H.H. 1992. Interpretation of fracture spacing and intensity *In: Rock Mechanics*.
- Einstein, H.H., Baecher, G.B. and Hirschfeld, R.C. 1970. The effect of size on strength of a brittle rock. *International Society of Rock Mechanics, Proceedings*. 1(1–19).
- Elmo, D. and Stead, D. 2010. An integrated numerical modelling—discrete fracture network approach applied to the characterisation of rock mass strength of naturally fractured pillars. *Rock Mechanics and Rock Engineering*. 43(1), pp.3–19.
- Farahmand, K., Vazaios, I., Diederichs, M.S. and Vlachopoulos, N. 2018. Investigating the scale-dependency of the geometrical and mechanical properties of a moderately jointed rock using a synthetic rock mass (SRM) approach. *Computers and Geotechnics*. 95, pp.162–179.
- Gao, F., Stead, D. and Kang, H. 2014. Numerical investigation of the scale effect and anisotropy in the strength and deformability of coal. *International Journal of Coal Geology*. 136, pp.25–37.

- Gao, F.Q. and Kang, H.P. 2016. Effects of pre-existing discontinuities on the residual strength of rock mass - Insight from a discrete element method simulation. *Journal of Structural Geology*. 85, pp.40–50.
- Gao, F.Q. and Stead, D. 2014. The application of a modified Voronoi logic to brittle fracture modelling at the laboratory and field scale. *International Journal of Rock Mechanics and Mining Sciences*. 68, pp.1–14.
- Hamdi, P., Stead, D. and Elmo, D. 2015. Characterizing the influence of stress-induced microcracks on the laboratory strength and fracture development in brittle rocks using a finite-discrete element method-micro discrete fracture network FDEM- μ DFN approach. *Journal of Rock Mechanics and Geotechnical Engineering*, 7(6), pp.609-625.
- Hoek, E. and Brown, E.T. 1997. Practical estimates of rock mass strength. *International Journal of Rock Mechanics and Mining Sciences*. 34(8), pp.1165–1186.
- Hoek, E. and Brown, T. 1980. *Underground Excavations in Rock* [Online]. Taylor & Francis. Available from: <https://books.google.co.uk/books?id=XeGKeYa8d30C>.
- Itasca. 2014. Universal Distinct Element Code (UDEC) Version 6.0. Itasca Consulting Group, Minneapolis, Minnesota.
- Jackson, R. and Lau, J.S.O. 1990. The effect of specimen size on the laboratory mechanical properties of Lac du Bonnet grey granite *In: Proceedings of the 1st International Workshop on Scale Effects in Rock Masses, Loen, Norway. Edited by A. Pinto da Cunha. AA Balkema, Rotterdam.*, pp.165–174.
- Jakubec, J. 2013. Role of defects in rock mass classification. *Australian Centre for Geomechanics.*, pp.1–8.

- Jakubec, J., Board, M., Campbell, R., Pierce, M. and Zaro, D. 2012. Rock mass strength estimate—Chuquicamata case study *In: MassMin 2012*. Sudbury, Canada: Canadian Institute of Mining, Metallurgy and Petroleum (CIM).
- Jakubec, J. and Esterhuizen, G.S. 2007. Use of the mining rock mass rating (MRMR) classification: industry experience *In: Proceedings International Workshop on Rock Mass Classification in Underground Mining*, C. Mark, R. Pakalnis, RJ Tuchman (eds), Vancouver, BC, Canada, National Institute for Occupational Safety and Health Information Circular (IC)., pp.413–421.
- Kazerani, T. and Zhao, J. 2010. Micromechanical parameters in bonded particle method for modelling of brittle material failure. *International Journal for Numerical and Analytical Methods in Geomechanics*. 34(18), pp.1877–1895.
- Laubscher, D.H. and Jakubec, J. 2001. The MRMR rock mass classification for jointed rock masses. *Underground Mining Methods: Engineering Fundamentals and International Case Studies*, WA Hustrulid and RL Bullock (eds) Society of Mining Metallurgy and Exploration, SMME., pp.475–481.
- Lim, S.S., Martin, C.D. and Åkesson, U. 2012. In-situ stress and microcracking in granite cores with depth. *Engineering geology*. 147, pp.1–13.
- Lu, Y. 2014. Estimating Rock Strength of Moderately Fractured EDZ in Hard Rock Tunnels: Äspö Hard Rock Laboratory. PhD Thesis, University of Alberta.
- Mas Ivars, D., Deisman, N., Pierce, M. and Fairhurst, C. 2007. *The Synthetic Rock Mass Approach – A Step Forward in the Characterization of Jointed Rock Masses*. In *11th ISRM Congress*. International Society for Rock Mechanics and Rock Engineering.
- Mogi, K. 1962. The influence of the dimensions of specimens on the fracture strength of rocks: Comparison between the strength of rock specimens and that of the

- earth's crust. Bulletin of the Earthquake Research Institute, University of Tokyo. 1962 Aug 15;40(1):175-85.
- Nasseri, M.H.B., Young, R.P., Rezanezhad, F. and Cho, S.H. 2009. Application of 3D X-ray CT scanning techniques to evaluate fracture damage zone in anisotropic granitic rock *In: 3rd US-Canada rock mechanics symposium. Toronto, Canada.*, pp.55–56.
- Palmstrom, A. 2005. Measurements of and correlations between block size and rock quality designation (RQD). *Tunnelling and Underground Space Technology*, 20(4), pp.362-377.
- Pells, P.J.N. 2004. On the absence of size effects for substance strength of Hawkesbury Sandstone. *Australian Geomechanics*. 39, pp.79–83.
- Pierce, M., Cundall, P., Potyondy, D. and Mas Ivars, D. 2007. A synthetic rock mass model for jointed rock *In: Rock Mechanics: Meeting Society's Challenges and Demands, 1st Canada-US Rock Mechanics Symposium, Vancouver.*, pp.341–349.
- Pierce, M., Gaida, M. and DeGagne, D. 2009. Estimation of rock block strength *In: RockEng09 (Proceedings, 3rd CANUS Rock Mechanics Symposium, Toronto.*
- Pratt, H.R., Black, A.D., Brown, W.S. and Brace, W.F. 1972. The effect of specimen size on the mechanical properties of unjointed diorite. *International Journal of Rock Mechanics and Mining Sciences and*. 9(4), pp.513–516.
- Price, R.H. 1986. *Effects of sample size on the mechanical behavior of Topopah Spring tuff*. Sandia National Labs.
- Read, J. and Stacey, P. 2009. *Guidelines for open pit slope design*. CSIRO publishing.
- Rosengren, K.J. and Jaeger, J.C. 1968. The mechanical properties of an interlocked low-porosity aggregate. *Geotechnique*. 18(3), pp.317–326.

- Singh, M.M. and Huck, P.J. 1972. Large scale triaxial tests on rock *In: The 14th US Symposium on Rock Mechanics (USRMS)*. American Rock Mechanics Association, pp. 35-60.
- Smith, A. and Habte, M. 2011. A large-scale unconfined compressive strength test for determination of rock mass parameters in tunnel design *In: 14th Australasian Tunnelling Conference 2011: Development of Underground Space*. Engineers Australia and Australasian Institute of Mining and Metallurgy, p.435.
- Stavrou, A. and Murphy, W. 2018. Quantifying the effects of scale and heterogeneity on the confined strength of micro-defected rocks. *International Journal of Rock Mechanics and Mining Sciences*. 102, pp.131–143.
- Stavrou, A. and Vazaios, I. 2018. Investigating the effect of size and pre-existing microdefects on the strength and deformability of rock blocks *In: 2nd International Discrete Fracture Network Engineering Conference*. American Rock Mechanics Association.
- Tsur-Lavie, Y. and Denekamp, S.A. 1982. Comparison of size effect for different types of strength tests. *Rock Mechanics*. 15(4), pp.243–254.
- Turichshev, A. and Hadjigeorgiou, J. 2017. Quantifying the effects of vein mineralogy, thickness, and orientation on the strength of intact veined rock. *Engineering Geology*, 226, pp.199-207.
- Vallejos, J.A., Suzuki, K., Brzovic, A. and Ivars, D.M. 2016. Application of synthetic rock mass modeling to veined core-size samples. *International Journal of Rock Mechanics and Mining Sciences*. 81, pp.47–61.
- Vazaios, I., Farahmand, K., Vlachopoulos, N. and Diederichs, M.S. 2018. Effects of confinement on rock mass modulus: A synthetic rock mass modelling (SRM)

study. *Journal of Rock Mechanics and Geotechnical Engineering*. 10(3), pp.436–456.

Vazaios, I., Vlachopoulos, N. and Diederichs, M.S. 2017. Integration of lidar-based structural input and discrete fracture network generation for underground applications. *Geotechnical and Geological Engineering*. 35(5), pp.2227–2251.

Weibull, W. 1951. A statistical distribution function of wide applicability. *Journal of applied mechanics*. 18, pp.293–297.

Weibull, W. 1939. *A statistical theory of the strength of materials*. Generalstabens litografiska anstalts förlag.

Xu, C. and Dowd, P. 2010. A new computer code for discrete fracture network modelling. *Computers and Geosciences*, 36(3), pp.292-301.

Yoshinaka, R., Osada, M., Park, H., Sasaki, T. and Sasaki, K. 2008. Practical determination of mechanical design parameters of intact rock considering scale effect. *Engineering Geology*. 96(3–4), pp.173–186.

Zhang, Q., Zhu, H., Zhang, L. and Ding, X. 2011. Study of scale effect on intact rock strength using particle flow modeling. *International Journal of Rock Mechanics and Mining Sciences*. 48(8), pp.1320–1328.

Chapter 4

Influence of Block Properties and Modelling Techniques on the Predicted Behaviour of Underground Excavations

Abstract

In this paper the available tools and theoretical background for estimating the unconfined and confined properties of rock blocks are examined. Special attention was given to the selection of appropriate constitutive relationships and discontinuum modelling techniques for the analysis of such materials. A series of continuum, discontinuum and Voronoi models were run in UDEC for a circular excavation at a prescribed depth of 1000 m. For the discontinuum models, a DFN was embedded into the rock matrix to represent a rock mass with a GSI of 60 ± 5 . Block strength was shown to be an important factor in discontinuum modelling. As block strength reduces then the extent of damage and rock mass deformation increase. Therefore, careful block characterisation is needed as rather small mGSI (i.e. a block scale GSI) reduction steps lead to dramatic reductions in the unconfined and confined properties of blocks. When blocks are simulated as continuum material in between the joints, the traditional Hoek–Brown approach overestimates the in-situ strength of blocks and thus the disturbed zone and magnitude of displacements are underestimated. While, the application of the modified Damage-Initiation and Spalling-Limit approach captures the expected low confinement zone near the excavation boundaries due to extensional fracturing. When blocks are simulated as a packing of Voronoi elements, it is shown that significant effort is required to calibrate the Voronoi micro-properties for tunnel-scale problems. The results show that the Voronoi models predicted a considerably reduced damage, stress relaxation and deformation when combined with the pre-existing discontinuities. The Voronoi skeleton is believed to provide a more realistic rock mass behaviour by creating a well-interlocked structure that clamps the pre-existing joints, allowing in this way the stress-induced slabbing type of failure to dominate the behaviour of the model before the activation of any kinematic instabilities.

4.1. Introduction

In underground environments, depending on the in-situ stress conditions, the strength of the intact rock material and the degree/quality of fracturing, rock masses can fail due to: i) structurally controlled processes; ii) stress driven fracturing through intact material; and iii) a combined stress-structure failure mode (Martin et al., 2003). In moderately jointed and blocky rock masses, Rock Block Strength (RBS) is therefore a significant factor controlling the rock mass behaviour and the response of the structural elements used as rock support and rock reinforcement (Kaiser, 2016).

From a numerical modelling perspective, it has long been recognised that discontinuum modelling and the explicit consideration of rock blocks and discontinuities provide the most appropriate and reliable technique for capturing the behaviour of the anisotropic discontinuum medium and the interactive response of the engineering structure (Bandis et al., 2011). An essential aspect in discontinuum modelling is to recognise that the strength and stiffness of both the blocks and joints are influenced by scale effects, and that certain allowances are required for upscaling the results of small scale tests to larger block volumes.

Currently there is no widely accepted approach for obtaining representative parameters of rock blocks containing defects for use in discontinuum analysis. Such defects impact significantly the mechanical behaviour of heterogeneous rock blocks, and it is therefore critical to account for their weakening effect on the overall rock mass behaviour (Pierce et al., 2009; Jakubec et al., 2012). In this context, this section provides a brief review on the available tools for estimating the properties of defected and non-defected rock blocks, and then investigates the impact of scaled rock block properties and modelling techniques on the behaviour of underground openings excavated in moderately jointed rock masses via a series of numerical simulations.

4.2. Rock Block Parameters

4.2.1. Unconfined Compressive Strength

The Unconfined Compressive Strength (UCS) is known to reduce with size due to an increased heterogeneity as a function of scale and the greater probability of defects to create through-going failure paths (Hoek and Brown, 1997). The inverse relationship between UCS and specimen size has been expressed by several empirical, analytical and theoretical relationships (inter alia: Weibull, 1951; Einstein et al., 1970; Hoek and Brown, 1980b; Carpinteri, 1994; Yoshinaka et al., 2008). However, relatively little research has been carried out to develop practical tools for obtaining estimates of the RBS based on qualitative descriptions or quantitative measurements.

The only noticeable approach that explicitly accounts for rock block defects is the Mining Rock Mass Rating (MRMR) classification system. The RBS can be estimated with the MRMR system following a series of adjustments considering the scale of the sample, the frequency of defects and their frictional properties (Laubscher and Jakubec, 2001).

To understand better the combined impact of defect geometry (i.e. intensity and persistence), defect strength and specimen size on the UCS of rock blocks, Stavrou et al. (2019) performed a numerical investigation using the Universal Distinct Element Code (UDEC) (Itasca, 2014) and the software FracMan (Dershowitz et al., 2014). Various micro-Discrete Fracture Networks (μ DFN) were embedded into Grain-Based Models (GBM) to simulate UCS tests on large-scale Synthetic Rock Block (SRB) samples. The results revealed a systematic strength reduction as defect intensity and persistence increase and as defect strength decrease. This allowed the development of refined charts that follow the MRMR logic. In these charts, RBS is expressed as a function of defect intensity, persistence, strength and specimen size (Figure 4.1).

4.2.2. Confined Compressive Strength

In confined conditions, it is again recognised that some form of strength reduction with size and rock block condition exists. The effects of size and/or block condition are more pronounced at low confining stresses (e.g. near excavation boundaries), whereas at high confining pressures (e.g. away from excavation boundaries) the scale effect decreases or even vanishes (Baecher and Einstein, 1981). This has been attributed to the closure of pre-existing defects and their difficulty in propagating under the influence of elevated confining stresses, leading eventually to mechanical homogeneity (Hoek and Bieniawski, 1965).

4.2.2.1. Hoek–Brown Failure Criterion

The most common tool for estimating the confined strength of rock blocks is the nonlinear Hoek–Brown failure criterion and the Geological Strength Index (GSI).

For intact rock strength, the Hoek–Brown criterion takes the following form (Hoek and Brown, 1980a; Hoek and Brown, 1980b):

$$\sigma_1 = \sigma_3 + \sigma_{ci} \left(m_i \frac{\sigma_3}{\sigma_{ci}} + 1 \right)^{0.5} \quad 4.1$$

where σ_1 and σ_3 are the major and minor principal stresses, respectively; σ_{ci} is the unconfined compressive strength; and m_i is a material constant for the intact rock.

For estimating the rock mass strength, Hoek (1994) and Hoek et al. (1995) introduced the “generalised” Hoek–Brown criterion which is expressed as follows:

$$\sigma_1 = \sigma_3 + \sigma_{ci} \left(m_b \frac{\sigma_3}{\sigma_{ci}} + s \right)^a \quad 4.2$$

where m_b , s , and a are scaling constants that can be related to GSI as follows:

$$m_b = m_i \exp\left(\frac{GSI - 100}{28 - 14D}\right) \quad 4.3$$

$$s = \exp\left(\frac{GSI - 100}{9 - 3D}\right) \quad 4.4$$

$$a = \frac{1}{2} + \frac{1}{6} \left(e^{-\frac{GSI}{15}} - e^{-\frac{20}{3}} \right) \quad 4.5$$

where D is a factor that is based upon the degree of rock mass disturbance.

The UCS is estimated by setting $\sigma_3 = 0$ in Equation 4.2:

$$\sigma_c = \sigma_{ci} s^a \quad 4.6$$

while the tensile strength is estimated by setting $\sigma_1 = \sigma_3 = \sigma_t$ in Equation 4.2:

$$\sigma_t = -\frac{s \sigma_{ci}}{m_b} \quad 4.7$$

For design purposes practitioners use the Hoek–Brown criterion to derive rock block properties with one of the following approaches:

1. by initially estimating tunnel-scale (continuum) properties and then subsequently, 1-2 m³ block scale (discontinuum) properties are derived with “improved” GSI values (typically as much as 10 to 20);
2. by reducing the intact rock GSI (i.e. 100) to account for the effect of defects that are anticipated to be encountered within the 1-2 m³ rock block scale;
3. by decreasing the intact rock unconfined strength in the Hoek–Brown equations considering scaling effects, micro-heterogeneity and/or material anisotropy in the rock block scale; and
4. by using a combination of the above.

While, in principle, the properties of a rock block should lie in between that of the rock mass and the intact rock, several inaccuracies could arise such as:

- under/over-estimation of the rock mass (i.e. tunnel scale) related GSI will undoubtedly lead to a substantially inaccurate rock block GSI;
- misleading appreciation of intact rock contribution to the overall rock block and therefore rock mass performance;
- omission to recognise the role of micro- and meso-scale defects;
- usage of optimistic or conservative scale relationships beyond the boundaries of the block Representative Elementary Volume (REV); and
- incorrect failure modes due to limitations of the GSI approach.

4.2.2.2. Rock Block Scale GSI

Day et al. (2012), considering the significant influence of intrablock structure proposed a modified GSI system (i.e. CGSI) to provide an improved estimate of strength for rock masses containing multiple structures at different scales. In light of the work of Day et al. (2012), Hoek and Brown (2018) also recognised that size effects and defects in rock block scale should be kept in mind when choosing the “intact rock” properties (i.e. m_i and UCS) in the Hoek–Brown criterion expressions.

Stavrou and Murphy (2018) run in UDEC a series of laboratory tests on progressively larger in size and degrading in quality samples to investigate the confined strength of rock blocks. The measured peak confined strength values from the large-scale triaxial tests were fitted to the Hoek–Brown criterion and a block-scale GSI parameter was introduced, named micro Geological Strength Index (mGSI) to reflect the effect of elevated block-scale heterogeneity on the confined strength. The relationship to account for the strength loss as a function of block volume and/or quality was described by a power-law expression as follows:

$$mGSI = 100 \left(\frac{\sigma_c}{\sigma_{c,0}} \right)^{0.21} \tag{4.8}$$

where σ_c and $\sigma_{c,0}$ are the UCS of large (block) and small (lab) scale specimens respectively and mGSI is the block scale GSI. It should be mentioned that RBS estimates from Equation 4.8 are in strong agreement with the UCS values calculated by the traditional Hoek–Brown criterion.

The combination of the predictive diagrams for RBS given by Stavrou et al. (2019) with the mGSI-strength relationship of Stavrou and Murphy (2018), allows to quantify the mGSI with specimen size, intensity and quality of defects (Figure 4.1).

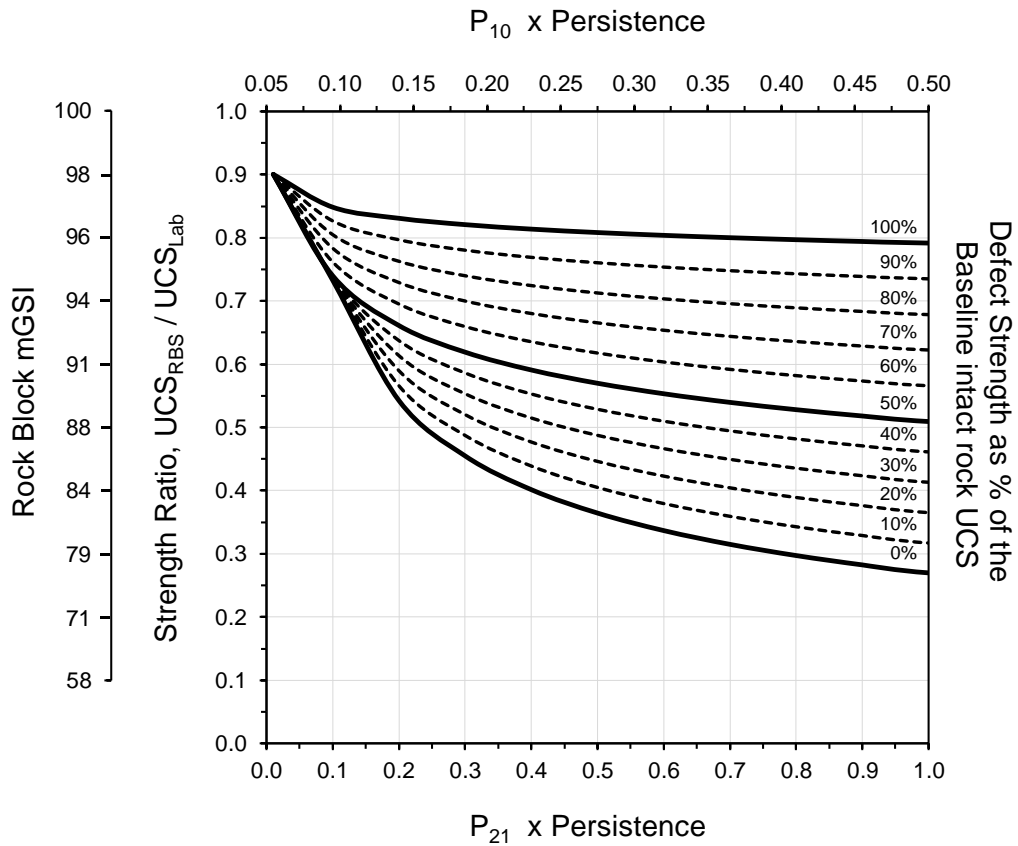


Figure 4.1. Quantification of the mGSI (i.e. a block scale GSI) and Rock Block Strength (RBS) as a function of scale, defect intensity, persistence, and strength.

From Figure 4.1, once the RBS has been estimated based on the field condition of the blocks or large-scale UCS tests, then a mGSI value between 100 and 65 could be found to estimate the in-situ confined strength. Typically, in the selection of GSI values it is strongly recommended to give a range of values (i.e. $\pm 5-10$) rather than trying to be too precise (Marinos and Carter, 2018). However, RBS drops rather aggressively for small mGSI reduction steps which suggests that careful consideration must be given in assigning representative mGSI ranges for design. Therefore, narrower ranges are recommended for the characterisation of rock material in the block scale (in contrast to the wider GSI ranges typically given at rock mass scale).

4.2.2.3. Modified Hoek–Brown Criteria

In order to use the Hoek–Brown criterion in massive to moderately jointed rock masses ($GSI \geq 65$) at high stress environments where brittle damage dominates the failure processes, it has been shown that certain modifications are required in the Hoek–Brown parameters to capture the observed failures around tunnels and shafts (Martin et al., 1996; Martin et al., 1999; Diederichs, 2007; Carter et al., 2008; Vazaios et al., 2017; Vlachopoulos and Vazaios, 2018). The failure envelopes in these modified versions follow an S- or tri-linear shape to account for the anticipated stress-induced extensile fracturing near the excavation boundaries (Kaiser et al., 2000; Diederichs, 2007; Kaiser and Kim, 2015) (Figure 4.2).

Logically therefore, at low confinement levels (i.e. near excavation boundaries) where σ_3 is typically less than $UCS/10$: i) rock fails due to axial splitting (i.e. fractures parallel to the maximum compressive stresses); ii) the Crack Initiation (CI is typically $\approx 30 - 50\%$ of the intact UCS) threshold controls the long-term in-situ strength and depends on the density of internal flaws and heterogeneity; and iii) the cohesive and frictional strengths of the rock material cannot be mobilised instantaneously and simultaneously, as significant damage (i.e. loss of cohesion) is required to activate the

frictional strength. In this respect, the cohesive and mobilized frictional strengths control the pre-peak and post-peak (i.e. residual) behaviours respectively, and thus the role of friction in crack initiation and propagation is essentially limited (Martin, 1997; Diederichs, 2007; Carter et al., 2008).

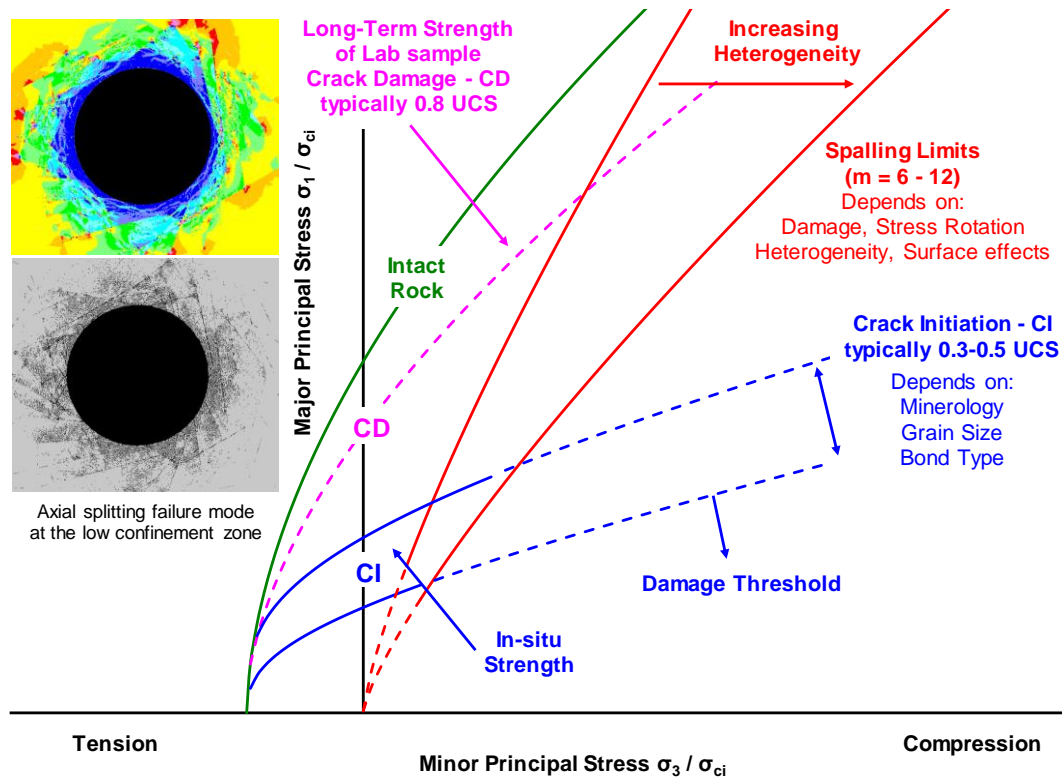


Figure 4.2. S- or tri-linear shaped failure envelope in principal stress space, showing the range of crack initiation and spalling limit thresholds, and the intact rock and long-term failure envelopes; based on Diederichs (2007).

At higher confinements (i.e. away from excavation boundaries, pillars cores, etc.), however: i) rock mass dilation and tensile fracturing are inhibited; ii) shear rupture through intact rock dominates the failure behaviour; iii) the Crack Damage (CD is typically $\approx 70 - 90\%$ UCS) threshold controls the long-term in-situ strength; and iv) both cohesion and friction contribute to the peak strength (i.e. instantaneous and simultaneous mobilisation) (Kaiser et al., 2000).

The axial-splitting and shear rupture failure modes occur either side of the “spalling limit”, which represents the transition between low and high confinement zones and typically ranges between σ_1 / σ_3 ratios of 10 – 20 at the intersection with the CI threshold (Kaiser et al., 2000; Diederichs, 2007; Bewick et al., 2019) (Figure 4.2).

To apply the complete S-shaped envelopes in numerical models using conventional tools, Diederichs (2007) proposed the Damage Initiation and Spalling Limit (DISL) approach. This is a strain softening – hardening modification of the Hoek–Brown criterion where a “peak envelope” is described by:

$$a_p = 0.25 \quad 4.9$$

$$s_p = \left(\frac{CI}{UCS} \right)^{\frac{1}{a_p}} \quad 4.10$$

$$m_p = s_p \left(\frac{UCS}{|T|} \right) \quad 4.11$$

where T is the lab scale true tensile strength (i.e. Direct Tensile Strength - DTS), and a “residual envelope” is described by:

$$a_r = 0.75 \quad 4.12$$

$$s_r = 0.0001 \quad 4.13$$

$$m_r = 6 - 12 \quad 4.14$$

In these formulations, the “peak envelope” specifies the CI threshold while the “residual envelope” the spalling limit. This behaviour can also be approximated using the Mohr–Coulomb criterion by fitting linear envelopes to the peak and residual failure envelopes. This approach is known as the Cohesion-Weakening and Friction-

Strengthening (CWFS) model (Hajiabdolmajid et al., 2002), and is based on the concept of progressive cohesion loss and delayed frictional mobilisation (Martin and Chandler, 1994). The transition from the peak cohesion to a residual value and the delayed mobilisation of the frictional strength is typically undertaken at two different plastic strain limits, to describe the accumulated damage (i.e. gradual cohesion loss) due to tensile fracturing and the delayed interaction (i.e. friction mobilisation) between newly generated rock fragments. These plastic strain limits can be approximated by:

$$\varepsilon_{pf} = \frac{2 CI}{E_b} \quad 4.15$$

$$\varepsilon_{pc} = \frac{CI}{E_b} \quad 4.16$$

where ε_{pc} is the plastic shear strain required to reduce the peak cohesion to its residual value, ε_{pf} is the plastic shear strain required for full friction mobilisation, and E_b is the intact rock block deformation modulus (Oliveira and Diederichs, 2017).

Kaiser et al. (2015) and Kaiser (2016), provided the guidelines shown in Figure 4.3 to establish the tri-linear strength envelopes for non-defected and defected rock masses at low and high confinements. To account for scale effects and block heterogeneity, the intact rock UCS in the failure envelopes is replaced by the σ'_{ci} and σ_{bl} strengths. The σ'_{ci} represents the strength of blocks influenced by scale effects only (i.e. homogenous) while the σ_{bl} is the strength of blocks containing defects (heterogenous). The Hoek–Brown strength envelope is represented using the so-called brittle strength parameters: $m = 0$, $s = 0.11-0.25$ and $a = 0.5$ (Martin et al., 1999). Essentially, for the low confinement zone, the envelopes delineated by the Kaiser (2016) procedure are “equivalent” to the Diederichs (2007) “peak envelopes” as soon as the Hoek–Brown “s” constant is calibrated to match the target CI threshold.

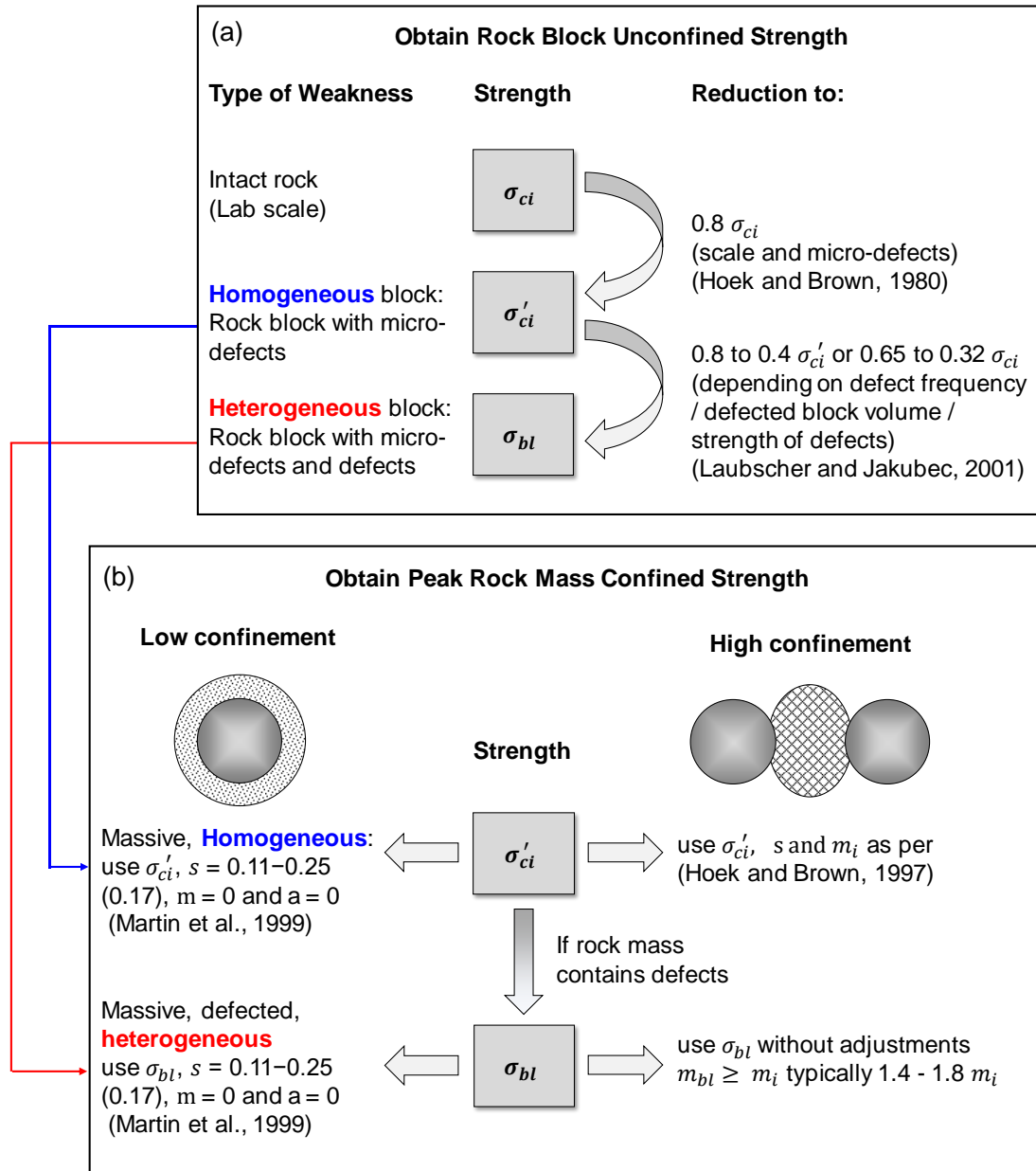


Figure 4.3. (a) Flow chart for estimation of rock block strength for homogenous and heterogenous blocks; and (b) Flow chart for rock mass strength estimation when GSI is not applicable for massive to moderately jointed and/or defected rock. Based on Kaiser et al. (2015) and Kaiser (2016).

4.3. Tunnel Scale Modelling

A series of tunnel scale numerical models were run to assess the impact of scaled rock blocks properties and modelling approaches on the intrinsic behaviour (unsupported) of underground excavations hosted in moderately jointed/blocky rock masses. The modelling cases considered are as follows:

- Case 1 investigates the influence of scaled rock block properties;
- Case 2 examines the impact of selecting different post-peak models;
- Case 3 investigates the influence of the chosen constitutive laws;
- Case 4 considers the effect of rock block size;
- Case 5 compares two discontinuum modelling techniques for the analysis of rock blocks, i.e. continuum blocks vs. blocks represented as GBM.

4.3.1. Model Geometry and Boundary Conditions

All UDEC models include a circular 5 m in diameter tunnel and have a rectangular geometry with outer boundaries 50 m long. A Discrete Fracture Network (DFN) was restricted within a 20×20 m region at the centre of the model to represent the fracturing pattern of a rock mass with a GSI of 60 ± 5 (Figure 4.4). The boundaries of the DFN region were chosen to be sufficiently far away from the excavation so as not to be influenced by rock mass deformations and stress rearrangements.

The vertical and lower horizontal boundaries of the models were fixed in the x- and y-directions to prevent movements and rotations along these directions while a stress boundary condition was applied along the top of the model to achieve the desired simulated depth. An unsupported full-face tunnel was modelled in all cases by gradually reducing the boundary forces on the interior of the excavation to simulate the 3D effects of an advancing tunnel face and the anticipated rock mass relaxation.

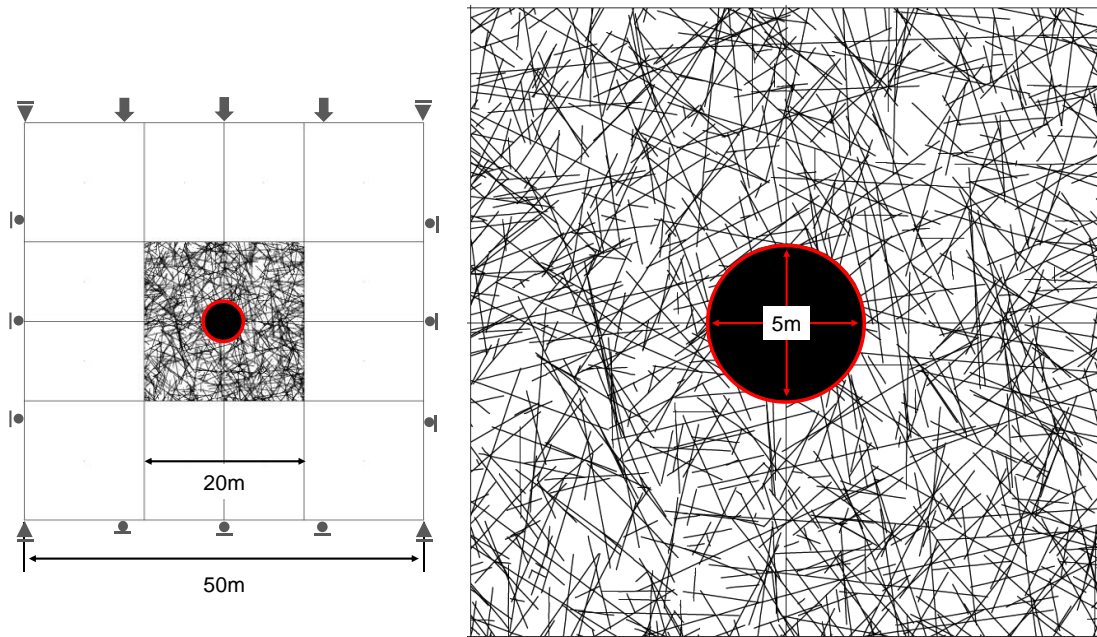


Figure 4.4. Model layout and detail of DFN used in the analysis.

The DFN was generated using the software FracMan (Dershowitz et al., 2014) by assigning a target volumetric intensity, P_{32} (i.e. total fracture area/unit volume [m^2/m^3]). The target discontinuity system was built considering the quantified GSI chart developed by Schlotfeldt and Carter (2018), in which GSI and thus degree of blockiness are linked among other with the block volume and the P_{32} intensity. Considering an average joint surface quality in the RMR (Bieniawski, 1989) or Q-system (Barton et al., 1974) scale, a target P_{32} of 8 was defined from the GSI chart, which corresponds to a rock mass with a GSI of 60 ± 5 , an RQD of 90% and for an approximate average block volume of 0.1 m^3 . To minimize the creation of preferential planes of weakness, the pre-existing defects were assigned with an arbitrary orientation between 0° and 90° and with a uniform probability distribution. Figure 4.5 presents the cumulative size distribution of blocks generated in UDEC, following the deletion of incomplete joints that were imported from FracMan.

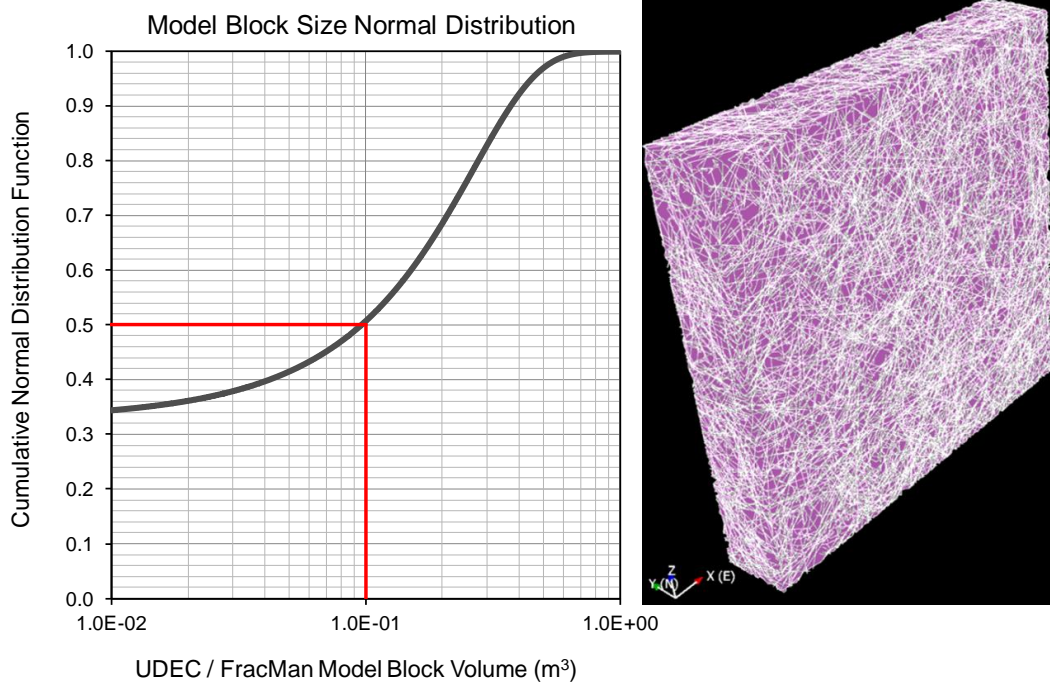


Figure 4.5. FracMan DFN model and generated block size distribution.

4.3.2. Modelling Scenarios

The discontinuum modelling was undertaken using UDEC v.6.0 (Itasca, 2014). The matrix of modelling scenarios investigates the effect of rock block properties, block constitutive relations and modelling techniques on the behaviour of unsupported circular tunnels at depth.

The evaluation and comparison of the numerical results is performed in terms of the observed failure mechanisms, the nature (i.e. size and shape) of the Excavation Disturbance Zone (EDZ) and the predicted rock mass displacements. The extent of the damage is assessed based on the UDEC plastic indicators. If the tunnel induced stresses satisfy the selected failure criterion then the zone elements could fail in either shear or tension. It should be noted that in this study, both the regions of “yielded in past” and “at yield surface” indicators are considered for the detection of a failure mechanism.

4.3.2.1. Case 1: Influence of Selected mGSI

Three progressively reduced rock block strength values of 80, 50 and 20% in respect to the baseline intact UCS were defined as target values to reflect three different rock block conditions (i.e. from homogenous to highly weathered and/or severely microflawed rock blocks). The target RBS values were back-calculated using the Hoek–Brown criterion (Hoek and Brown, 2018) by reducing the mGSI. Table 4.1 lists the material properties used in the analyses. In this case the blocks were assumed to follow an Elastic-Plastic behaviour. The analysis was undertaken for a tunnel 1000 m below ground level and for two different stress scenarios (i.e. horizontal to vertical stress ratio - Sh / Sv): i) $Sh / Sv = 1$; and ii) $Sh / Sv = 0.5$.

The disturbed zones triggered by the excavations and the predicted displacements are shown in Figure 4.6. As can be seen, there are significant differences between the models and the analysis highlights the significant effect in adopting reduced RBS in discontinuum modelling. The extent of block failure has increased by a factor of 2 when RBS drops from 80% to 20% and the number of failed zones increases by a factor of greater than 4. In the $Sh / Sv = 0.5$ condition and for RBS equal to 20%, several block detachments were observed from the wall and the roof of the tunnel. The distribution of movement appears to change dramatically around the excavation as more than 40% deformation was recorded for the models with the lower RBS. The results reveal that by only reducing the mGSI from 96 (80% RBS) to 70 (20% RBS), then significant different conclusions could be made for the overall rock mass behaviours, which in turn could influence specific design elements and decisions (e.g. support type, excavation methods). It is clear that if rock block strength is poorly characterised during the engineering geological interpretation phase, meaningful understanding of the intrinsic stability and rock-support interactions could be lost, leading into optimistic (and possible unsafe) or conservative (and very costly) designs.

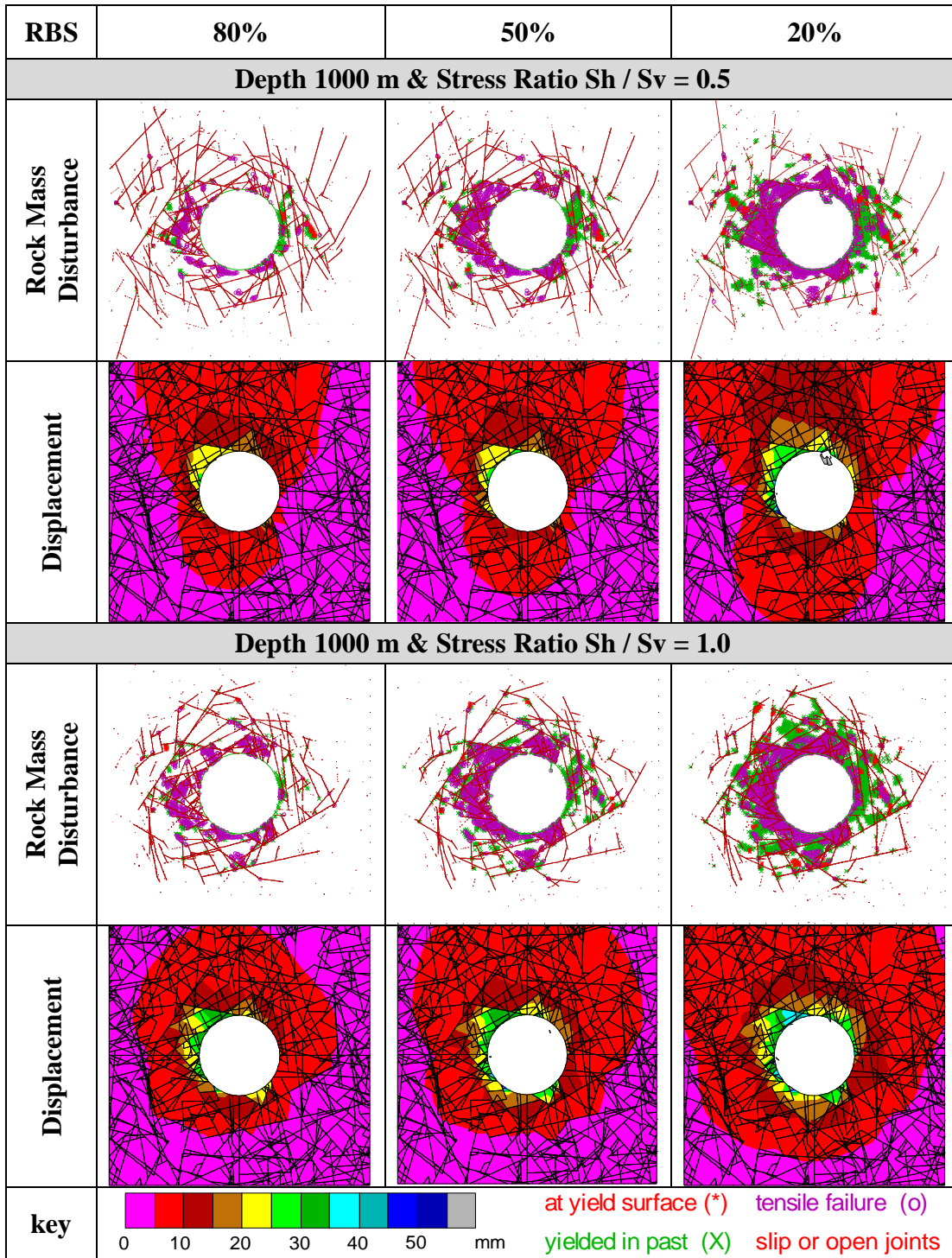


Figure 4.6. Influence of mGSI on predicted damage and deformation.

4.3.2.2. Case 2: Influence of Selected Post-Peak Behaviour

The Elastic-Plastic (E-P) models for the 80 and 20% RBS of the previous case were re-run for comparison by also assuming an Elastic-Brittle (E-B) and a Strain-Softening (S-S) behaviour in the post-peak phase. The residual properties for the E-B and S-S methods were estimated using a residual mGSI (Cai et al., 2007) and the critical plastic strain was specified using the relationship given by Brown (2003). The material properties for the post-peak behaviour are shown in Table 4.1.

The predicted disturbed zones and displacements are illustrated in Figure 4.7 and Figure 4.8. The analysis suggests that for the strength-stress ratios considered, the post-peak properties in rock block scale have very little influence in the overall rock mass response around the tunnel. Regardless of softening the strength to a residual state or keeping it constant after rock block failure, no significant differences can be observed in-between the scenarios analysed. In all cases the number of failed zones and extent of disturbance are very similar, and the predicted displacements are almost identical. The influence of post-peak properties is re-examined in Case 3.

4.3.2.3. Case 3: Influence of Selected Constitutive Law

For this case the confined strength of the rock blocks with RBS equal to 80% of the baseline intact UCS is represented by using the DISL approach to capture the potential brittle behaviour of the rock material. Equivalent Mohr–Coulomb linear parameters were fitted to the composite DISL criterion in order to use the CWFS model. Table 4.2 lists the properties used in the analysis and Figure 4.9 illustrates the associated peak and residual envelopes.

The results from the Case 3 models are summarised in Figure 4.10 and are compared with the traditional Hoek–Brown Elastic-Brittle models presented in Case 2 in terms of damage and rock mass deformations (Figure 4.7).

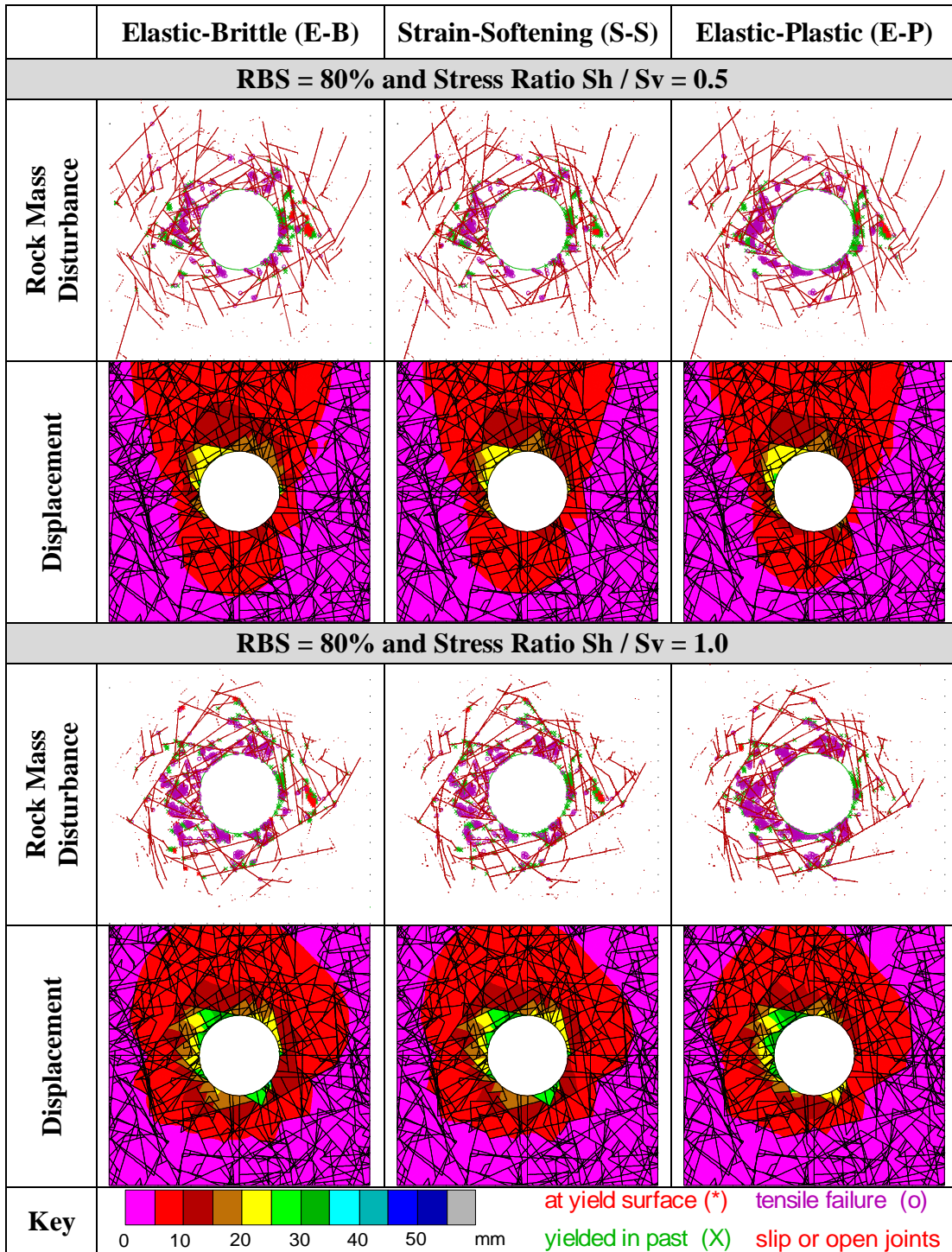


Figure 4.7. Influence of post-peak properties on predicted damage and deformation.

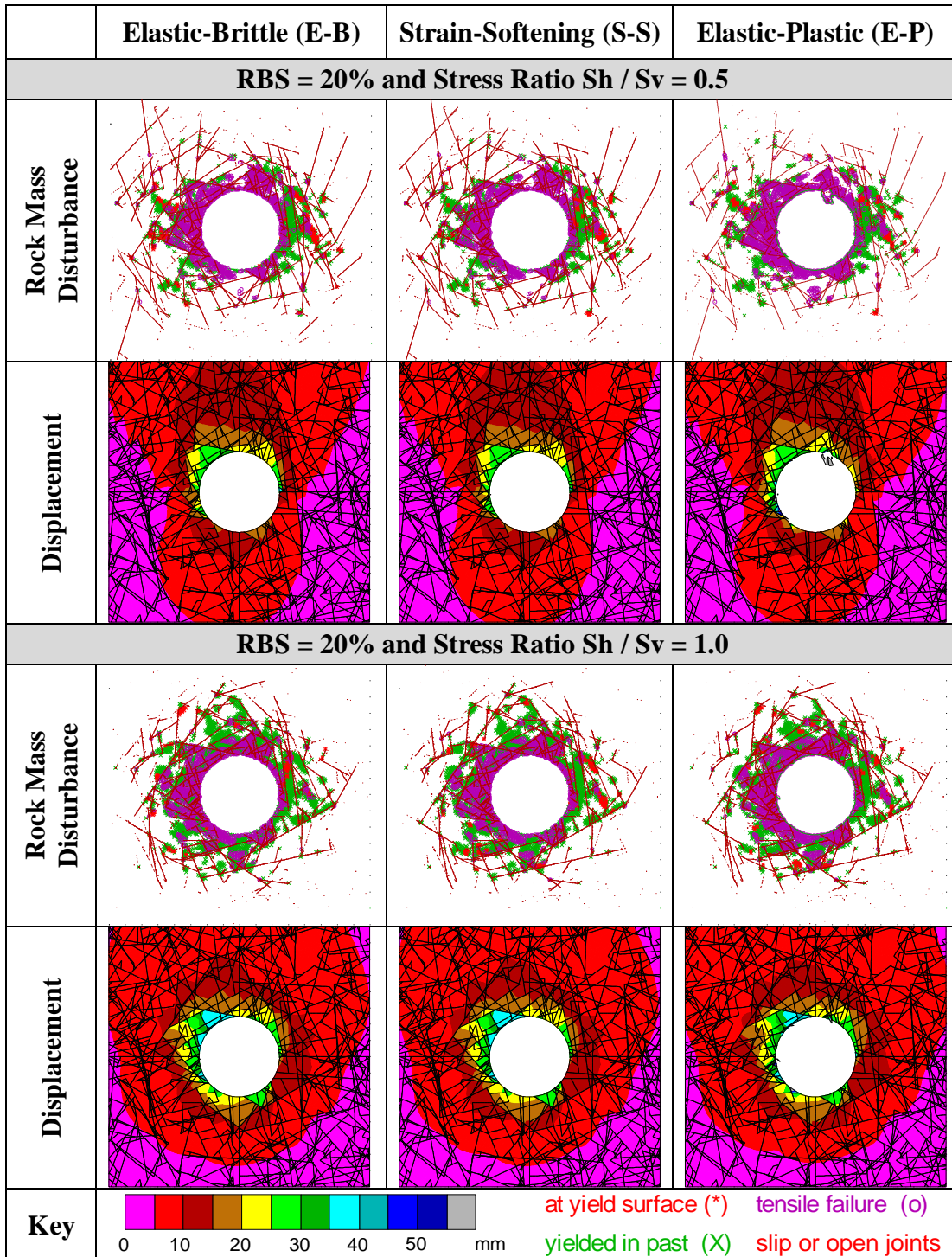


Figure 4.8. Influence of post-peak properties on predicted damage and deformation.

Table 4.1. Intact rock, rock block and discontinuity properties.


	Parameter	symbol	unit	Decreasing Rock Block Condition			
							
Peak	micro Geological Strength Index	mGSI	-	100	96	88	71
	Unconfined Compressive Strength	UCS	MPa	50.0	40.0	25.0	10.0
	Rock Block UCS / Intact UCS	-	%	100	80	50	20
	Tensile Strength	σ_t	MPa	3.3	2.47	1.31	0.37
	Hoek–Brown constants	mb	-	15.000	13.003	9.633	5.325
		s	-	1.000	0.641	0.252	0.040
		a	-	0.500	0.500	0.500	0.501
	Young’s Modulus	E	GPa	20.00	19.67	18.90	15.02
	Cohesion	c	MPa	7.9	6.4	4.2	2.4
	Friction Angle	ϕ	°	52.3	52.1	51.0	47.6
Dilation Angle	ψ	°	19.2	17.9	14.7	6.9	
Post-Peak	Brittle-Plastic	Cohesion	c_r	MPa	0.0		
		Friction Angle	ϕ_r	°	34.2		
		Dilation Angle	ψ	°	0.0		
		Tensile strength	σ_{tr}	MPa	0.0		
	Strain-Softening	Cohesion	c_r	MPa	1.0		
		Friction Angle	ϕ_r	°	34.2		
		Dilation Angle	ψ	°	0.0		
		Tensile strength	σ_{tr}	MPa	0.01		
	Elastic-Plastic	Cohesion	c_r	MPa	6.4	4.2	2.4
		Friction Angle	ϕ_r	°	52.1	51.0	47.6
		Dilation Angle	ψ	°	0.0		
		Tensile strength	σ_{tr}	MPa	2.47	1.31	0.37
Discontinuity	Cohesion	c_d	MPa	0.35			
	Friction Angle	ϕ_d	°	35			
	Normal Stiffness	kn	MPa/m	15000			
	Shear Stiffness	ks	MPa/m	1500			

Table 4.2. Hoek–Brown DISL and Mohr–Coulomb CWFS properties.

	Parameter	symbol	unit	RBS = 80% of intact UCS
	Unconfined Compressive Strength	UCS	MPa	40.0
Peak	Crack Initiation Ratio	CIR	-	0.5
	Crack Initiation	CI	MPa	20.0
	Hoek–Brown Peak constants for the DISL model	a_p	-	0.25
		s_p	-	0.063
		m_p	-	1.014
Residual	Hoek–Brown Residual constants for the DISL model	a_r	-	0.75
		s_r	-	0.001
		m_r	-	12
Peak	Mohr–Coulomb Peak properties for the CWFS model	c_p	MPa	7.5
		ϕ_p	°	18.9
		σ_{tp}	MPa	2.47
		ψ_p	°	17.6
Residual	Mohr–Coulomb Residual properties for the CWFS model	c_p	MPa	0.1
		ϕ_p	°	61
		σ_{tp}	MPa	0.01
		ψ_p	°	3.5
Plastic Strain	Cohesion loss	ϵ_{pc}	-	0.002
	Friction mobilisation	ϵ_{pf}	-	0.004

The traditional modelling approaches appear to underestimate the EDZ and rock mass deformation. For both stress conditions, the CWFS model captures an increased brittle failure as the failed zones have increased by a factor of 4. Although, it was generally anticipated that the CWFS model will trigger more damage, the presence of pre-existing fractures seems to magnify the extent of brittle failure due to local stress concentrations across discontinuities. Significant shear displacements along joints could result in more severe stress-induced fracturing than expected, which in turn could give rise to enough kinematic freedom so block/wedge movements can occur.

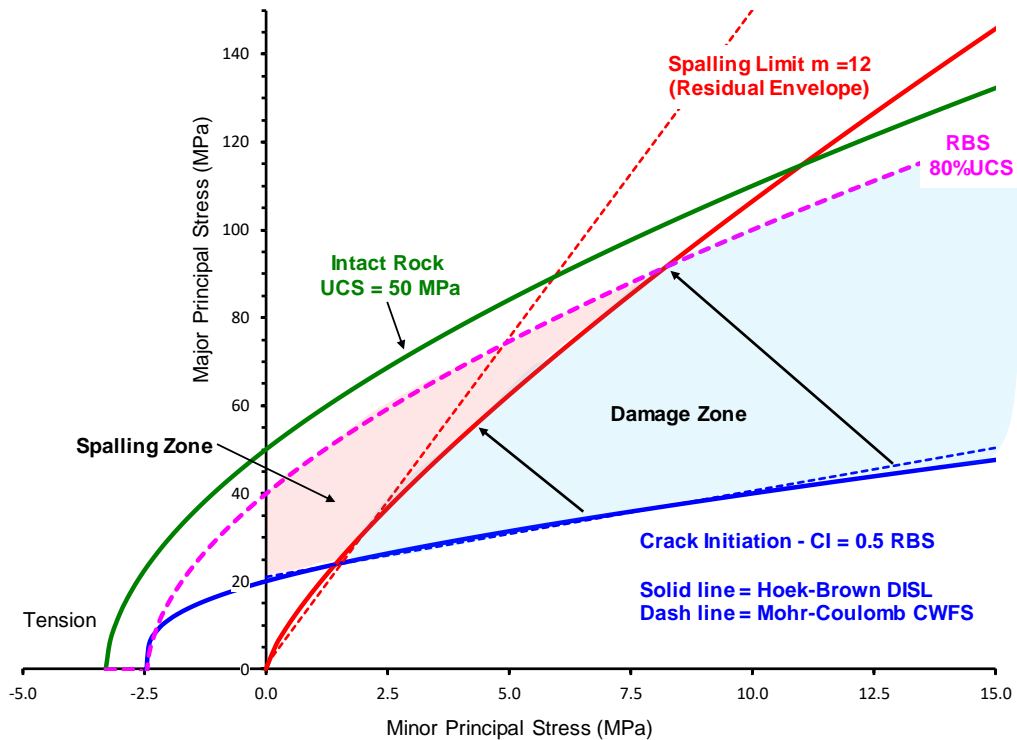


Figure 4.9. Peak and residual envelopes used in the analysis for the CWFS model.

The predicted EDZs were also extracted at intermediate relaxation steps to allow the further comparison between the different modelling approaches. The aim was to examine the progressive evolution of damage around the excavation while the tunnel face is advancing. This comparison was undertaken only for the $S_h / S_v = 0.5$ stress condition. Figure 4.11 presents the evolution of damage for four relaxation (or deconfinement) stages: 20, 40, 60 and 80% decrease of the pre-mining stress state. As can be seen from Figure 4.11, at 20% relaxation both models show an elastic behaviour as no fracturing has occurred yet. The magnitude of the maximum tangential stresses at this stage has not reached the crack initiation stress threshold and as such the CWFS model is still in a pre-peak state. As further relaxation is allowed with the advancement of the tunnel face, the CWFS model captures the formation of a v-shaped notch type of failure parallel to the minor principal stresses. In contrary, the E-B UDEC model is not

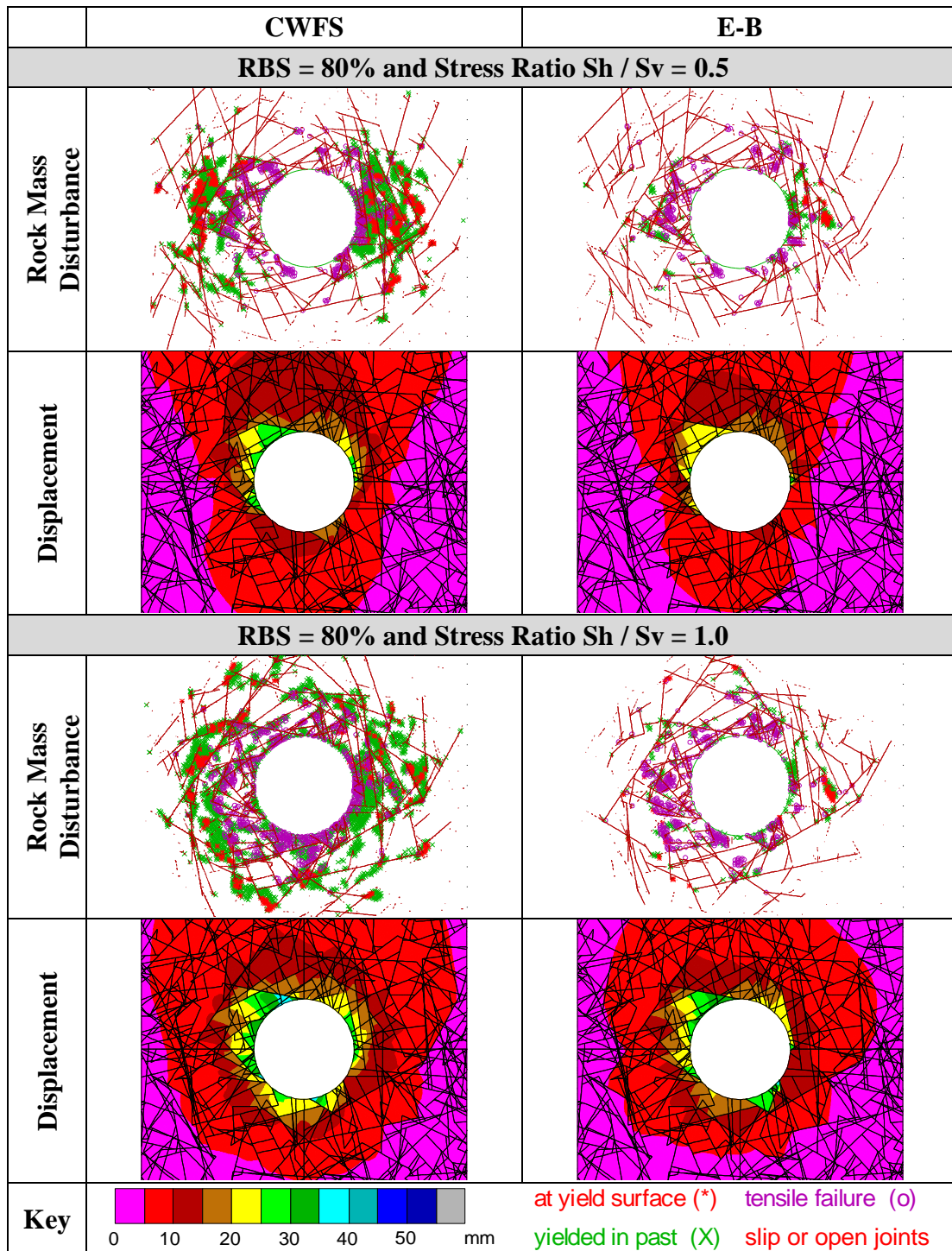


Figure 4.10. Influence of constitutive law on predicted damage and deformation.

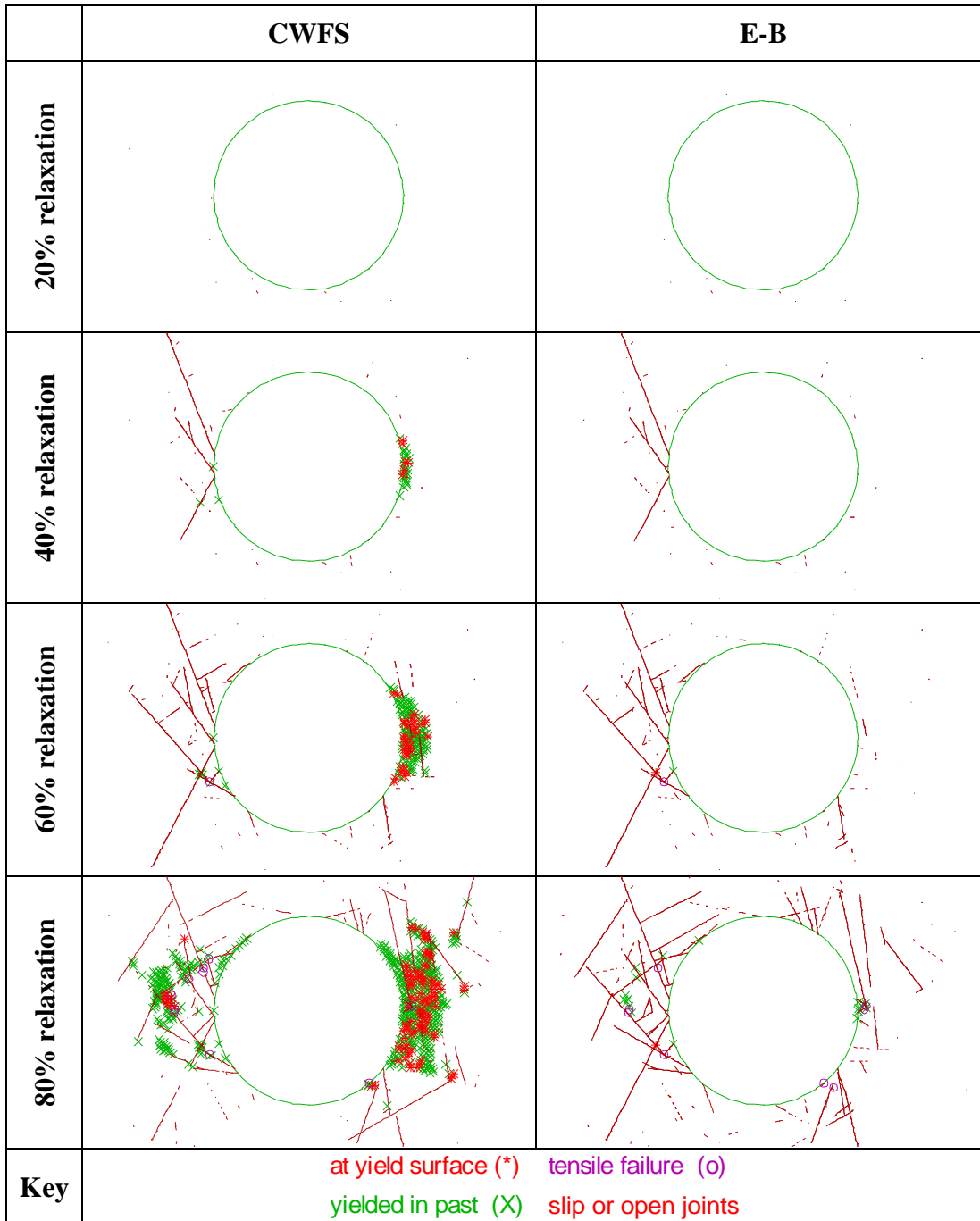


Figure 4.11. Comparison between the discontinuum CWFS and E-B block models for the progressive development of damage during different relaxation stages.

capturing the formation of the damage zone as essentially the rock blocks around the excavation have remained under an elastic condition up to 80% relaxation and the disturbed zone is only controlled by the opening or slip of individual discontinuities. Thus, the traditional Hoek–Brown criterion is not able to capture the failure mode in a realistic manner even when an E-B model is chosen to describe the post-peak behaviour of the rock material. This is because the reaction of a brittle rock mass cannot be captured by conventional shear failure criteria, which overestimate the actual in-situ strength of the rock blocks and as such underestimate the extent of damage.

Of interest from the comparison at different relaxation steps is that the extensive block damage at the CWFS approach mainly occurs at the right-hand side of the tunnel where the rock mass is relatively more massive compared to the left-hand side which is more broken, and/or the joints have unfavourable orientation. As it can be observed from Figure 4.11, at the more fractured left-hand side of the tunnel both the CWFS and E-B models predict very similar EDZ patterns up to the 60% relaxation, while for the 80 and 100% relaxation stages the CWFS model obtains a much wider damage profile.

The plot shown in Figure 4.12 was constructed from the results of the CWFS model to study the development of damage in relation to the tunnel convergence during the advancing tunnel face. This plot is generally known as the Ground Reaction Curve (GRC) and is typically used, together with support reaction curves and Longitudinal Displacement Profiles (LDP), to define support requirements and guidelines for the distance of support installation behind the tunnel face. Essentially, this GRC suggests that at 20% relaxation the tunnel face provides adequate internal support pressures that withstand the formation of spalling failure. However, close behind the face at 40% relaxation this apparent support pressure decreases rapidly, and the plastic indicators show that spalling initiation is likely to occur near the face while the excavation is under progress. This behaviour is very important for the selection of appropriate support measures, the time of installation and the safety of personnel and equipment.

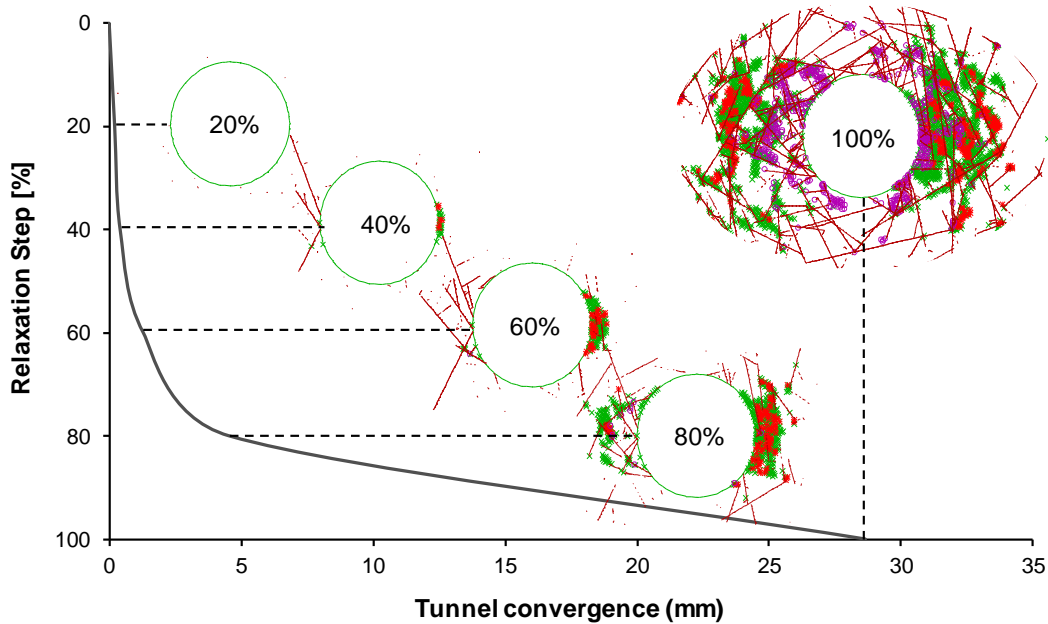


Figure 4.12. Ground Reaction Curve showing the progressive development of damage due to the 3D effects (i.e. stress release) of an advancing tunnel face.

The notable differences between the different modelling approaches are in general agreement with findings from other studies (e.g. Hajiabdolmajid et al., 2002; Vlachopoulos and Vazaios, 2018). Hajiabdolmajid et al. (2002) demonstrated that to predict the extent of the damage around deep underground openings in massive hard rocks, then the concept of the CWFS model needs to be employed. The mobilisation of peak and residual strength parameters at different plastic strain limits in the CWFS models captured successfully the depth and shape of the observed damage zone. On the other hand, the conventional E-P and E-B models underestimated significantly the extent of failure and overestimated the lateral depth of failure in the extensile region (Hajiabdolmajid et al., 2002).

Although the CWFS concept is generally adopted in continuum models, the current study shows that it also plays an important role when describing the brittle behaviour of continuum rock blocks in between joints in discontinuum models.

To isolate the influence of the constitutive law from the behaviour of the DFN, fracture-free continuum models were run by adopting the properties shown in Table 4.1 and Table 4.2 for the E-B and CWFS models respectively.

Figure 4.14 presents the results from the fracture free continuum models at different relaxation stages. The Elastic-Brittle model fails to capture the anticipated damage and underestimates significantly the extent of fracturing as the criterion allows the rock mass to withstand higher compressive stresses. On the other hand, the CWFS assumption resembles successfully the damage profile (i.e. shape and depth) that was expected for the stress conditions investigated. This is confirmed by employing the following empirical solution for spall prediction (Diederichs et al., 2010):

$$\frac{r}{a} = 0.5 \left(\frac{\sigma_{max}}{CI} + 1 \right) \quad 4.17$$

where $\sigma_{max} = 3\sigma_1 - \sigma_3$ (i.e. maximum tangential stresses), r is the overbreak extent from the tunnel centre, and a is the tunnel radius (Figure 4.13).

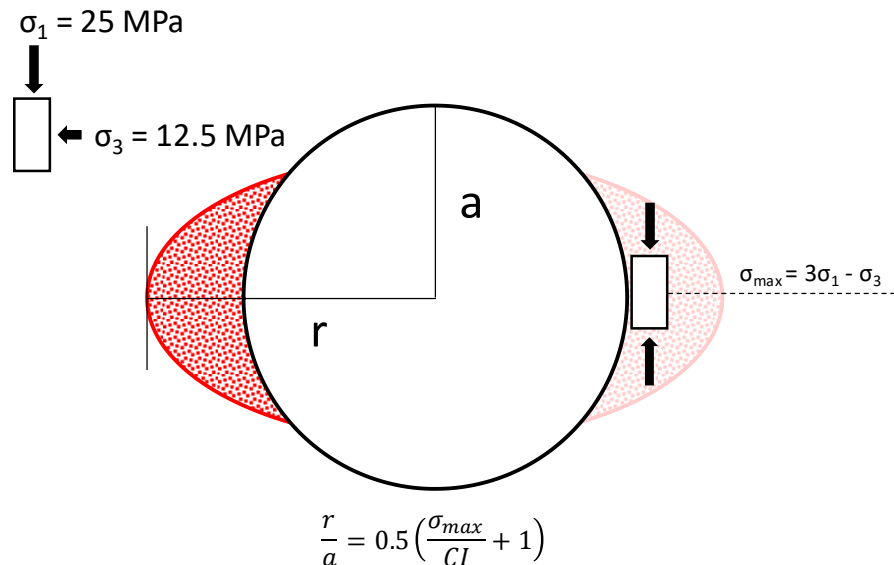


Figure 4.13. Empirical prediction of spall related overbreak depth.

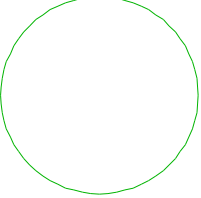
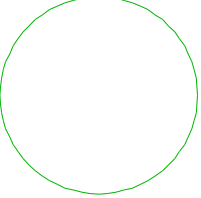
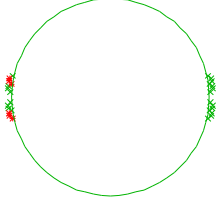
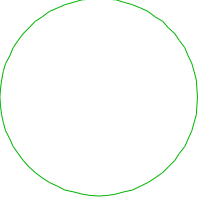
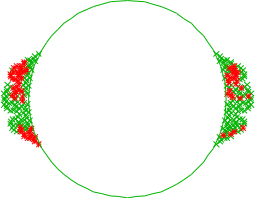
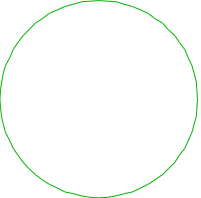
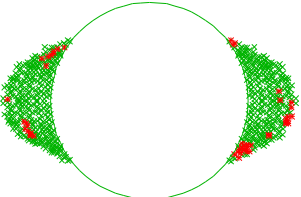
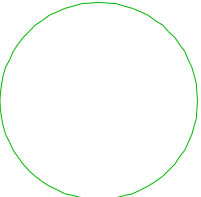
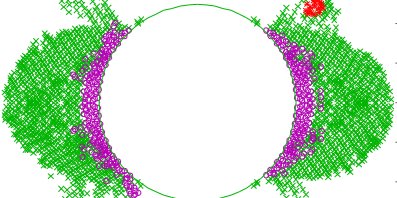
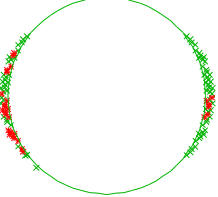
	CWFS	E-B
20% relaxation		
40% relaxation		
60% relaxation		
80% relaxation		
100% relaxation		

Figure 4.14. Comparison between the DFN-free continuum CWFS and E-B models for the progressive development of damage during different relaxation stages.

The empirical estimated overbreak depths are compared with the numerical predictions of the CWFS model for different relaxation steps. Table 4.3 shows that both approaches are in very good agreement, validating the applicability of the CWFS (or DISL) approach in capturing the real brittle response of the rock mass.

Table 4.3. Comparison of overbreak depth between empirical and numerical results.

Relaxation Stage (%)	σ_{\max} (MPa)	r/a	Overbreak depth – Empirical (m)	Overbreak depth – Numerical (m)
0	0	0.5	n/a	n/a
20	13	0.8	n/a	n/a
40	25	1.1	2.8	2.7
60	38	1.4	3.6	3.3
80	50	1.8	4.4	3.9
100	63	2.1	5.2	5.0

In terms of failure modes, the behaviour near the excavation differs substantially from that away from the opening. At a close distance of about 0.5 m from the tunnel contour where the confinement is very low, the rock mass fails due to stress-induced extensile fracturing (i.e. spalling). In contrary, away from the excavation at a distance between 0.5-3 m where the confinement is high, the shear rupture through intact rock dominates the failure behaviour of the rock mass (Figure 4.15).

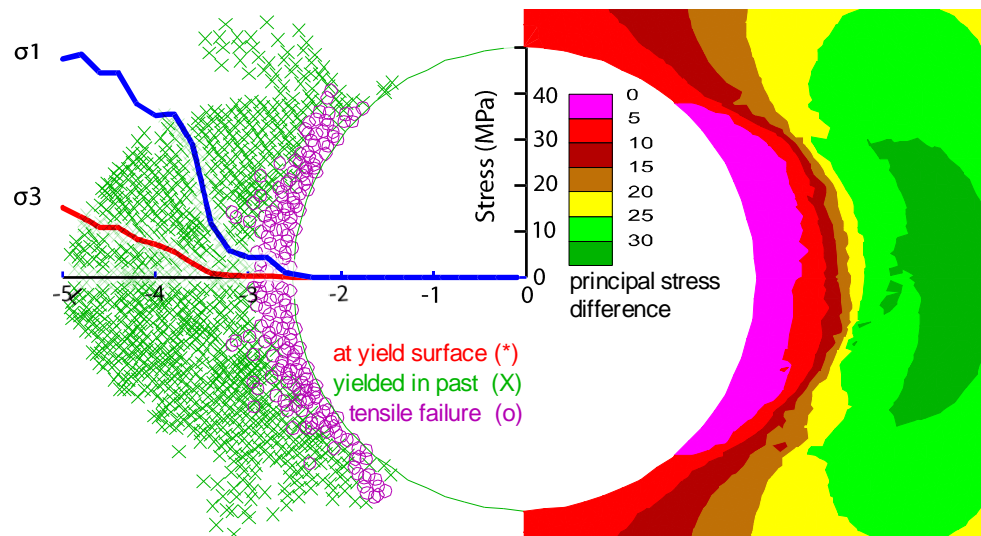


Figure 4.15. Confinement dependent failure processes at low and high confinements.

A significant aspect of a rock reinforcement/support design is the time of installation. If the system is installed too early, then the tunnel induced loads may exceed the capacity of the structural elements while if it is installed too late, then the rock mass may have already experienced irreversible damage and relaxation. Figure 4.16 illustrates a combined GRC and LDP plot together with the predicted depth of overbreak. In this case the LDP was constructed based on the analytical solutions proposed by Vlachopoulos and Diederichs (2009).

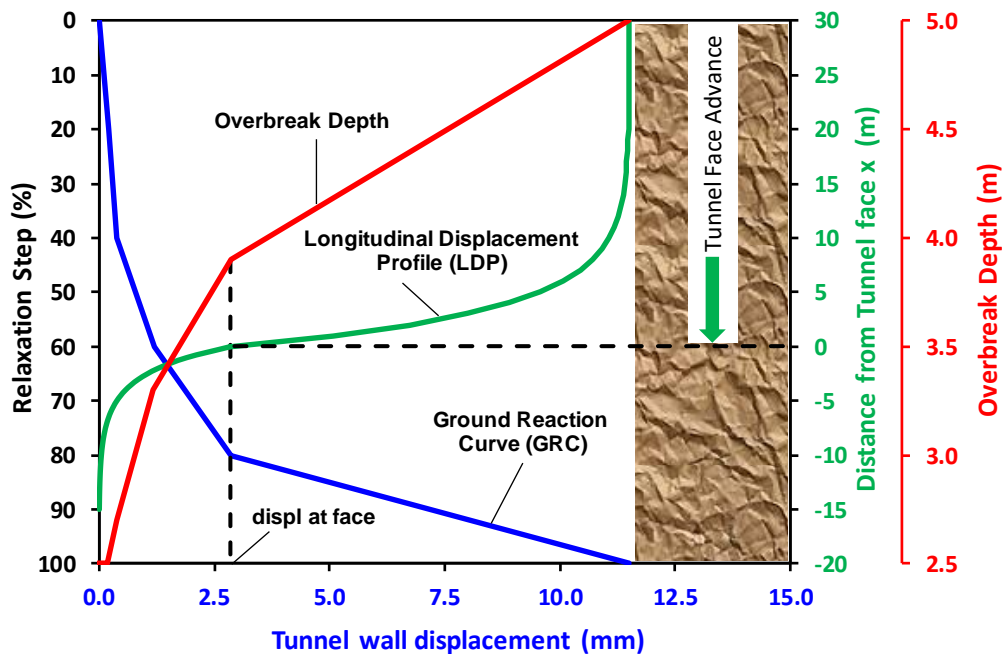


Figure 4.16. Combined GRC and LDP plot together with predicted depth of overbreak.

Figure 4.16 shows that spalling failure is likely to initiate ahead of the tunnel face. It should be noted that the LDP approach used here is only for schematic purposes and may not represent the actual conditions as it was mainly developed from shear-based failure criteria. Nevertheless, research on hard rock tunnelling has shown that considerable microseismic events could be monitored ahead of the tunnel face (i.e. damage initiation), with the notch development (i.e. spalling slabs) becoming visible at about 0.5-1 m from the face (Martin, 1997).

4.3.2.4. Case 4: Influence of Rock Block Size

Case 3 demonstrated that the different degree of fracturing at that right- and left-side hand walls of the tunnels mobilised different failure modes (stress-induced vs structural driven) during the tunnel face advancement when using the CWFS approach. This case investigates further the combined influence of rock block size and chosen constitutive law in relation to the observed failure mechanisms and predicted deformations. This sensitivity analysis was performed only for the blocks with RBS equal to 80% and for $Sh / Sv = 0.5$.

The effect of block size was examined using simplified jointed rock mass models in a controlled discontinuum modelling environment. In contrast to the stochastic DFN model introduced in the previous cases, two set of persistent and orthogonal discontinuities with dip angles of 45° were considered in this case. Block size was controlled by varying the joint spacing between 0.5 and 5m as shown in Table 4.4.

Table 4.4. UDEC model geometries with varying joint spacing.

Model No.	Joint Spacing (m)	Block Area (m ²)	Tunnel Diameter / Joint Spacing
1	5.0	25.0	1.0
2	2.5	6.25	2.0
3	1.0	1.0	5.0
4	0.5	0.25	10.0

The results of the simplified jointed models for the CWFS and E-B approaches are shown in Figure 4.17. It is again clear that the traditional modelling approaches underestimate the extent of damage regardless of the degree of blockiness in the rock mass. Although both models capture similar patterns of joint failure and there is a clear increasing joint slip/opening as spacing decreases, the disturbed zones in the CWFS approach are significantly larger and follow a shape fairly similar to the X-shaped shear

zones formed by the discontinuities. It is interesting to note that for the CWFS models the overall mode of failure changes as block size decreases. When joint spacing is large then the walls of the excavation experience a pure brittle spalling type of failure. However, when joint spacing decreases then the shearing of joints mobilises a shear type of failure mechanism in the blocks that resembles the shape of a “butterfly”. This is attributed to the fact that joint slip affects stress concentrations and allows the block material to pass from a brittle failure environment (i.e. the peak envelope in the DISL approach at low confinement) into a shear-based mechanism (i.e. the residual envelope in the DISL approach at high confinement).

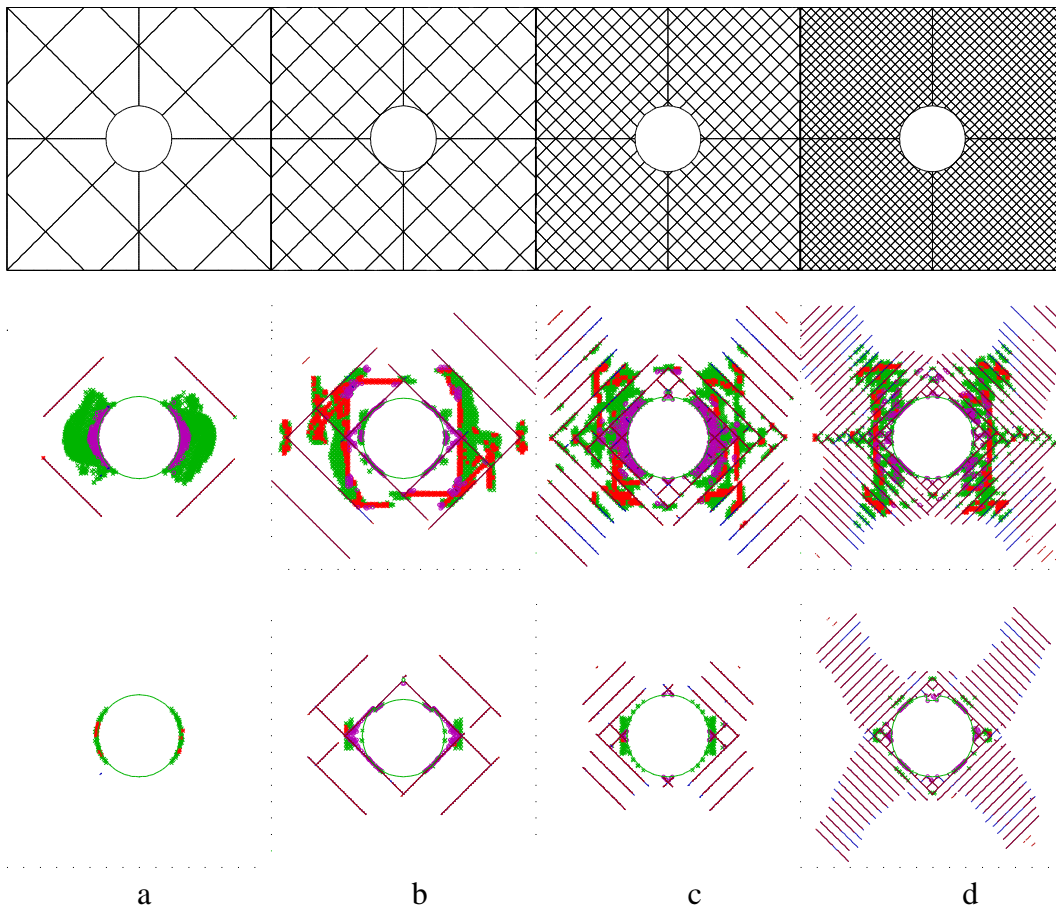


Figure 4.17. Predicted disturbance with varying joint spacing when using the CWFS (above) and E-B (below) models: a) 5 m; b) 2.5 m; c) 1 m; and d) 0.5 m.

4.3.2.5. Case 5: Influence of Modelling Approach

This case examines the combined effect of constitutive model selection and discontinuum modelling techniques in the behaviour of underground excavations hosted in massive to moderately jointed rock masses. The analysis employs a Grain-Based Modelling (GBM) approach to represent the rock blocks as a packing of deformable micro-blocks, called Voronoi elements. The mechanical behaviour of a GBM is controlled by the grain-to-grain interface micro-properties and the geometrical arrangement of the Voronoi blocks (i.e. size and size distribution). The advantage of using this approach is the explicit simulation of newly generated macro-fractures through the initiation, propagation and coalescence of micro-cracks.

Two different sizes of micro-blocks were generated around the circular excavation, as shown in Figure 4.18. Voronoi blocks within 2 m from the tunnel contour were specified to have an average edge length of 5 cm (i.e. equivalent to the size of a lab-scale sample), while the blocks in the outer zone were built with an average edge length of 30 cm. In some cases, due to mesh generation difficulties or in order to improve the computational runtimes, only the inner zone was included in the analysis.

In the current GBM scheme, the Voronoi blocks are assumed to behave elastically, while the contacts that separate them follow the Coulomb Slip with Residual strength (CSR) model (i.e. E-B) or a Cohesion-Loss and Friction-Hardening (CLFH) model. As a result, damage is confined only along the micro-contacts, and once the contact strength is exceeded either in shear or in tension, the bond between the grains breaks and a compression-induced, tensile or sliding crack is initiated. The conventional CSR model was adopted to simulate the elastic-brittle macro-behaviour of a rock block with UCS of 40 MPa for the properties given in Table 4.1. While the CLFH approach was used to represent the CWFS macro-behaviour of a rock block with UCS of 40 MPa and CI of 20 MPa for the properties given in Table 4.2.

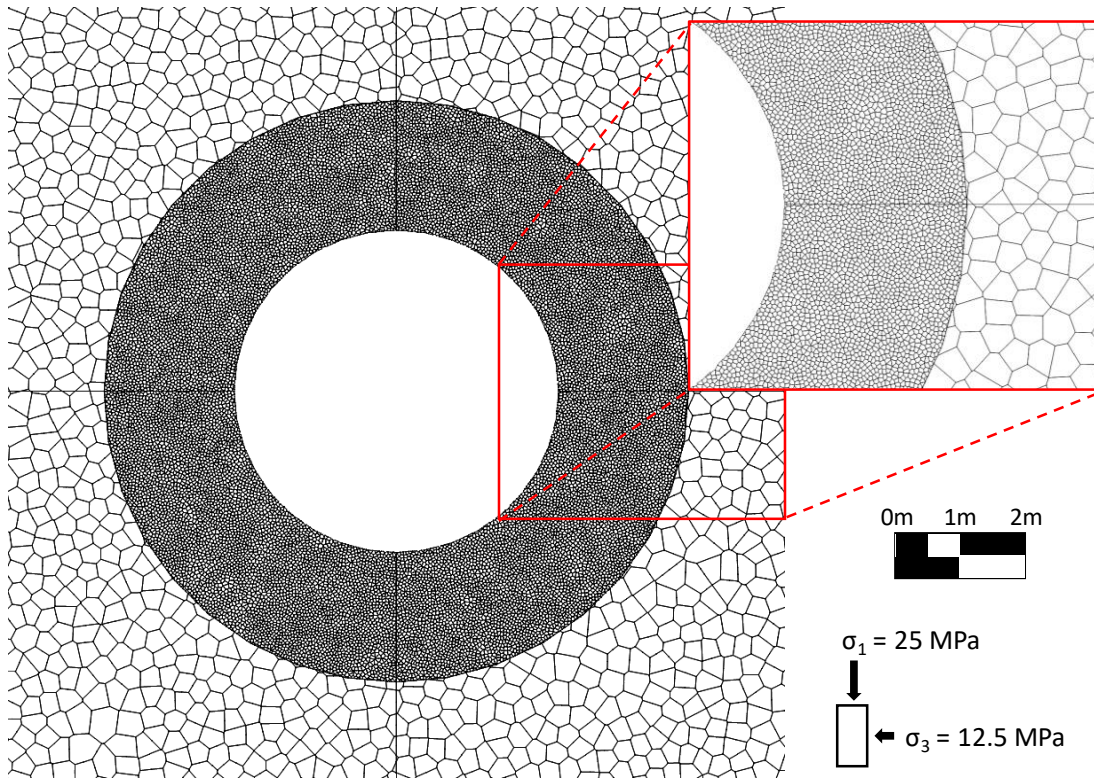


Figure 4.18. Voronoi block assemblage used for the tunnel-scale analysis.

Calibration of the Voronoi micro-properties against the block-scale macro-properties was first necessary before performing the tunnel-scale modelling. The calibration involved the simulation of large-scale UCS tests with size 1×2 m (Figure 4.19), in which the strength and stiffness values of the Voronoi contacts and elements were varied until obtaining the target block-scale properties. For the models using the CSR constitutive law, once the contact strength is exceeded either in shear or in tension, an elastic-brittle softening procedure is followed where the contact parameters decrease to a residual value. On the other hand, for the models using the CLFH approach the strain-dependent CWFS concept was adopted in which the peak and residual cohesive and frictional strengths are mobilised at the same stage. Table 4.5 lists the calibrated UDEC Voronoi micro-parameters for the CSR and CLFH models respectively.

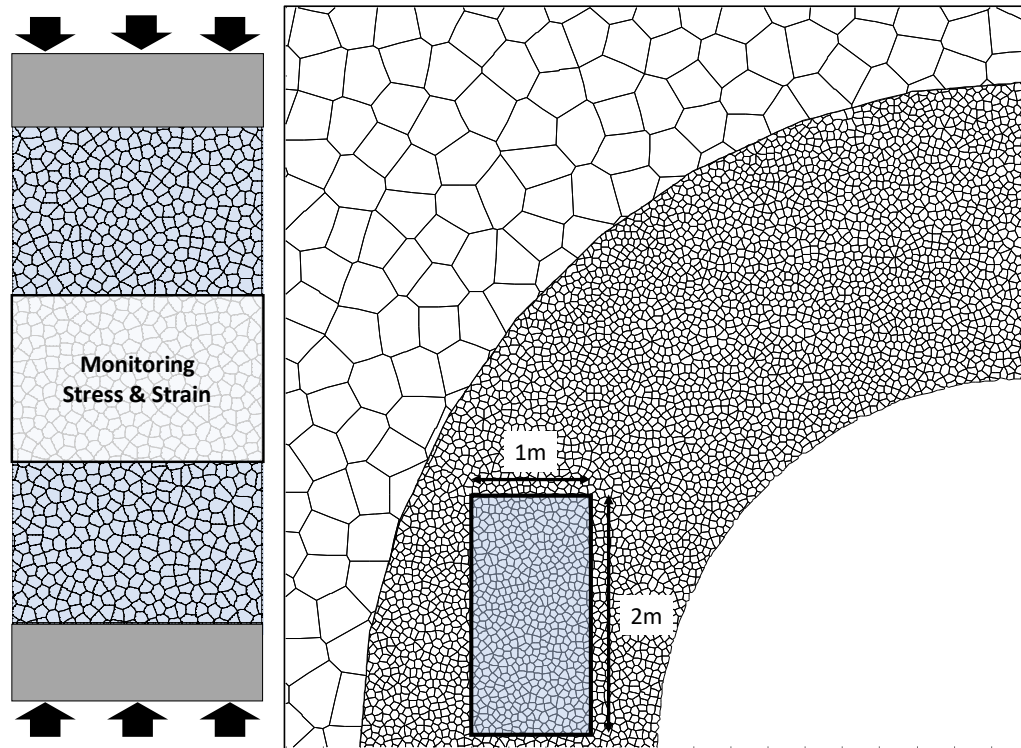


Figure 4.19. UDEC GBM used for the UCS testing calibration.

Table 4.5. Calibrated UDEC Voronoi micro-properties.

Target macro-mechanical behaviour				E-B (Table 4.1)	CWFS Table 4.2
Voronoi Grain Elastic Properties					
Young's Modulus	E_m	GPa	19		
Poisson's Ratio	ν_m	-	0.20		
Voronoi Contact Elastic Properties					
Normal Stiffness	k_n	GPa/m	21000		
Shear Stiffness	k_s	GPa/m	10500		
Voronoi Contact Strength Properties					
Voronoi micro-mechanical behaviour		-	-	CSR	CLFH
Peak	Cohesion	c_{mp}	MPa	7.9	7.5
	Friction Angle	ϕ_{mp}	°	52.3	19.0
	Dilation Angle	ψ_{mp}	°	0.0	18.0
	Tensile Strength	t_{mp}	MPa	3.3	2.0
Residual	Cohesion	c_{mr}	MPa	0.0	0.1
	Friction Angle	ϕ_{mr}	°	25.0	40.0
	Dilation Angle	ψ_{mr}	°	0.0	0.0
	Tensile Strength	t_{mr}	MPa	0.0	0.001

Figure 4.20 shows the comparison of the stress-strain curves and sample damage between the results of the models using the CSR and CLFH models respectively.

The stress-strain response of the sample using the CSR model shows an initial linear elastic trend up to the peak stress value of 40 MPa. Once the peak UCS is exceeded, the model exhibits a clear elastic-brittle behaviour and experiences a rapid loss of strength. The sample fails mainly due to axial splitting but as more damage is accumulated then the model captures the development of typical macroscopic shear fractures which form a double pyramid type of failure.

The calibration of the CLFH model was undertaken considering the CWFS properties listed in Table 4.2. Essentially the Voronoi defect matrix was bonded together with a shear strength equivalent to the CI threshold of 20 MPa. Typically, the CI level in GBMs is calibrated for lab-scale samples by targeting a non-linear response in the stress-strain curves at about 50% of the peak UCS. However, for a block-scale sample near the excavation that experiences spalling failure, then a more dramatic strength reduction (and non-linearity) is envisioned at the CI level due to the increased sample heterogeneity with scale. The derived stress-strain plot for the sample using the CLFH model revealed a distinctly different response compared to the CSR model. The model shows an initial linear elastic reaction up to the CI damage threshold level of 20 MPa, and then due to early extensional microcracking the stress-strain curves deviate from linearity and follow a strain hardening behaviour until the peak strength. Therefore, the model captures the anticipated in-situ strength for the rock blocks (i.e. CI damage level) at low confinements (i.e. near the excavation boundary) which represents the first portion of the tri-linear strength envelope in the DISL or CWFS approach. The onset of systematic damage in the CLFH model essentially reflects the disruption of material continuity and the loss of cohesion in between the different grain boundaries. Until reaching that point, friction plays only a minor role in the failure process but becomes active following the grain bond rupture or separation.

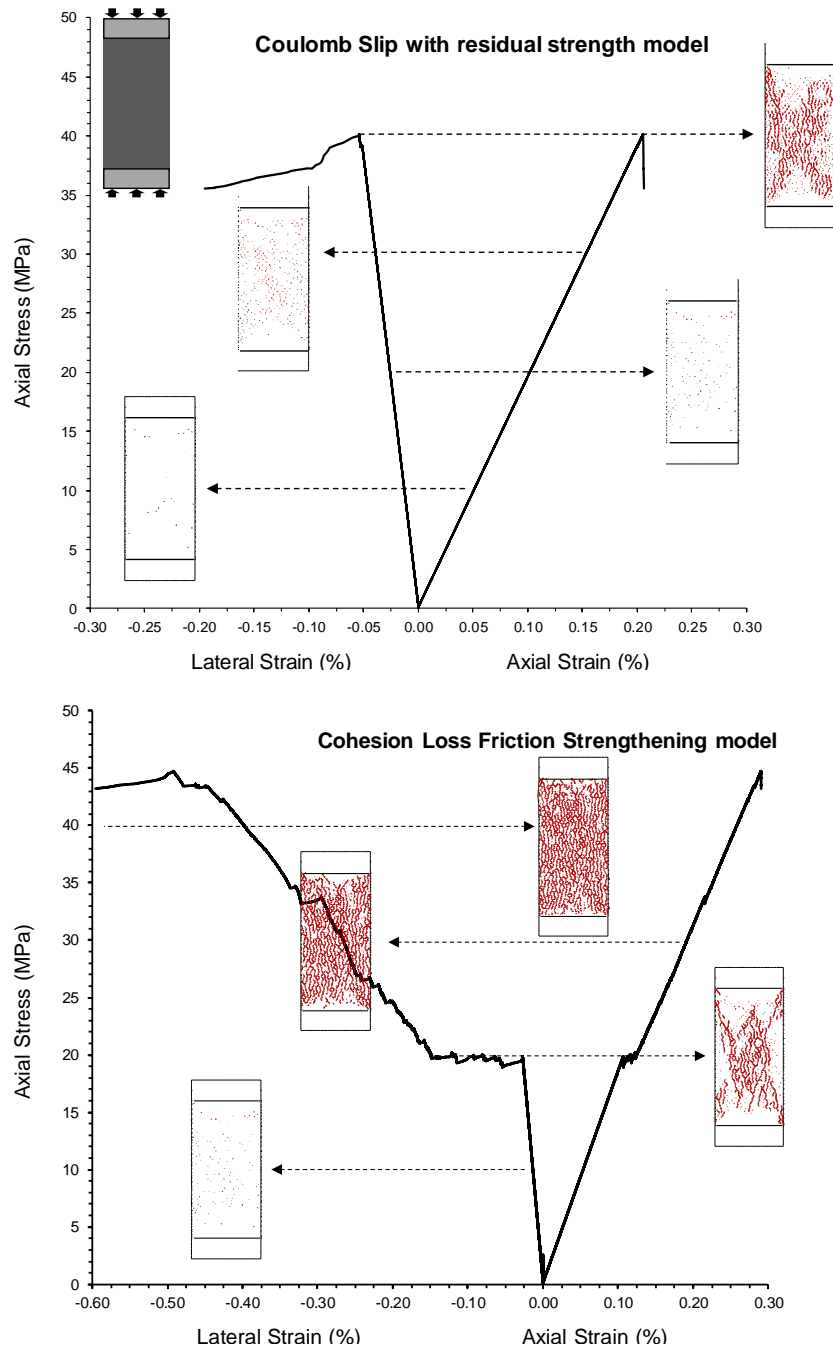


Figure 4.20. Stress-strain diagrams obtained from UCS tests using the a) Coulomb Slip with residual strength (CSR) model and b) Cohesion-Loss and Friction-Hardening (CLFH) model.

Following the initial Voronoi block calibration, tunnel-scale simulations were run to investigate the capabilities of the GBMs models in capturing the anticipated extent of damage when using the CSR and CLFH models.

Figure 4.21 presents a comparison between the DFN free models that use the continuum E-B and Voronoi CSR approaches. The Voronoi model shows good agreement with the continuum E-B model at 100% relaxation. Both approaches have captured a similar failure mechanism around the excavation and almost identical rock mass displacements. Although, the failed crack distribution in the Voronoi model revealed some damage at the shoulders of the tunnel, these individual cracks have not yet interacted with each other as the stress conditions at their tips have not yet allowed them to propagate in an unstable manner. Nevertheless, the Voronoi CSR model, as in the case of the continuum E-B model, underestimates the depth of the expected disturbance at the zone of maximum tangential stresses (i.e. the walls of the tunnel).

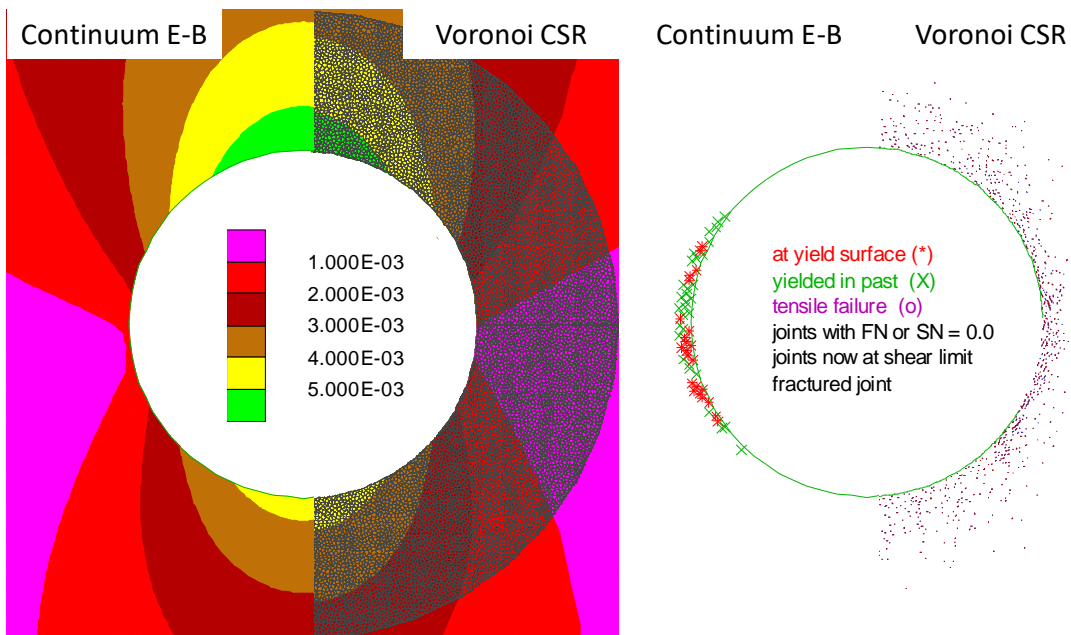


Figure 4.21. Comparison of predicted rock mass deformation and disturbance for the DFN free continuum E-B and Voronoi CSR models.

Figure 4.22 presents the development of damage for different relaxation stages for the DFN free models that use the continuum CWFS and Voronoi CLFH approaches. To obtain a reasonable agreement between the models, the peak friction angle of the CLFH model was reduced from 19 to 10°. The analysis showed that the Voronoi CLFH model provides good agreement with the damage predicted by the continuum CWFS at the roof and the side-walls of the tunnel. However, it is obvious that the CLFH model led to the concentration of more fractures at the upper and lower shoulders of the tunnel and a lesser lateral damage at the side-walls (i.e. the region of maximum compressive stress).

The results of the current study are in general agreement with findings from Shin (2010) who demonstrated that the UDEC Voronoi CLFH approach provides a better and more realistic representation for the extent of the EDZ in massive hard rocks in comparison with the conventional CSR model. However, in the absence of specific procedures on how to calibrate the micro-properties in the Voronoi CLFH approach, significant effort is required to calibrate tunnel-scale problems. Currently, the most systematic guidelines for GBM calibration are given by Kazerani and Zhao (2010) and Gao and Stead (2014) but both studies focus on the calibration of micro-properties by using the traditional E-B or E-P material laws.

It is also important to highlight that in UDEC, the strain-hardening model used to replicate the CWFS approach for the zone elements, allows for the mobilisation of residual and peak Mohr–Coulomb parameters at different plastic strain limits. However, in the CLFH constitutive model for the Voronoi contacts, the cohesion-loss and friction-hardening occurs simultaneously as the model is not allowing to prescribe variation of properties as a function of the plastic strain. The effect of this difference between the continuum and GBM techniques cannot be quantified from our results but it is generally accepted that friction needs to be activated only after a significant reduction of the cohesive component (Martin and Chandler, 1994).

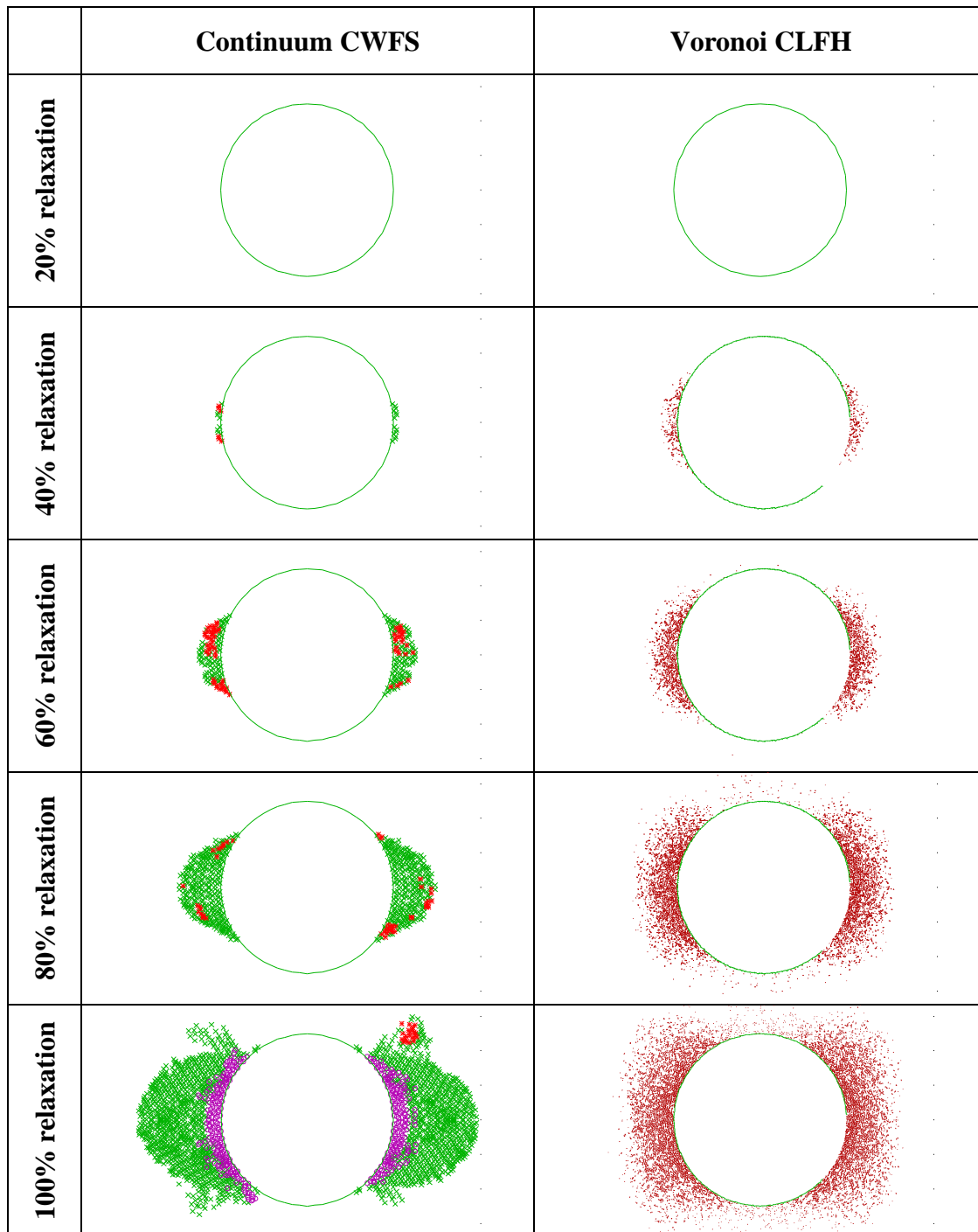


Figure 4.22. Comparison between the DFN-free continuum CWFS and Voronoi CLFH models for the progressive development of damage during tunnelling.

Although the simulated EDZ showed good agreement between the continuum CWFS and Voronoi CLFH models, the magnitude of displacement around the excavation is different. Figure 4.23 illustrates a coloured contour plot of displacement magnitude. The rock mass surrounding the tunnel in the Voronoi CLFH model appears to have attracted considerably reduced deformation. For the zones in the side-walls where the maximum compressive stress is expected, the continuum CWFS predicts more than 10 mm movement while the Voronoi CLFH model predicts less than 1 mm (i.e. 100% difference). In a similar fashion, the analyses results for the tensile regions in the roof and floor of the tunnel reveals differences up to 50% between the continuum CWFS (≈ 10 mm) and Voronoi CLFH models (≈ 5 mm).

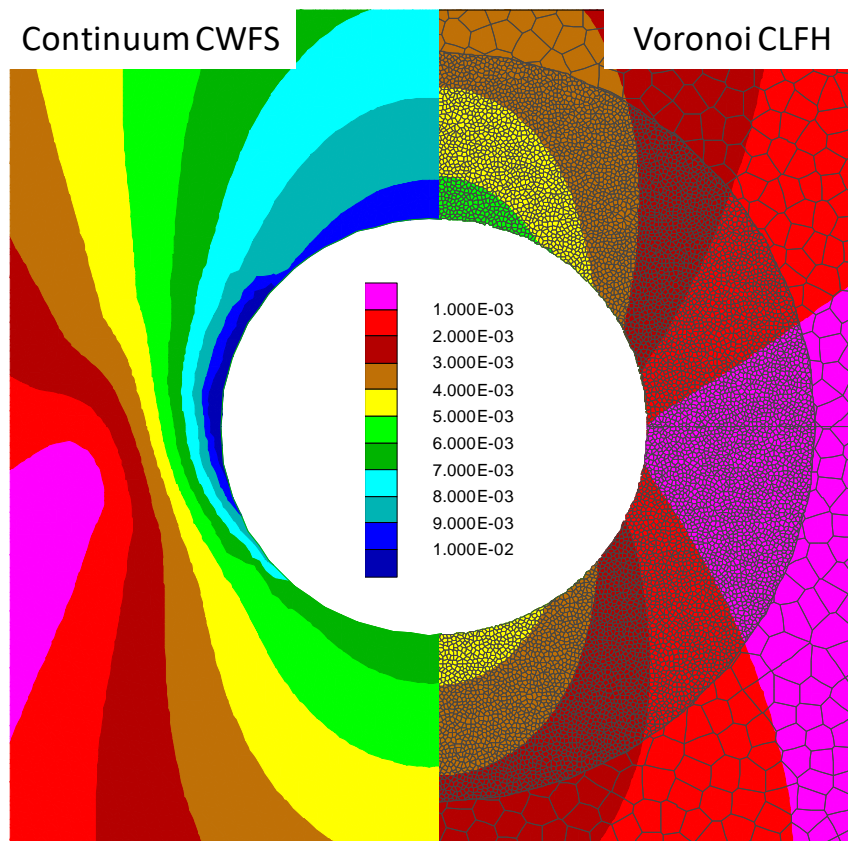


Figure 4.23. Predicted rock mass displacements for the DFN free continuum CWFS and Voronoi CLFH models.

The significant difference between the continuum CWFS and Voronoi CLFH models for the predicted rock mass closure led to further investigation of the condition of the rock mass around the excavation. Brittle fracturing and rock mass deformation are very sensitive to the stress state near the excavation boundaries. Figure 4.24 illustrates the tunnel-induced differential stresses at the stage of 100% relaxation. The continuum CWFS model captures the expected low confinement at the zone of maximum tangential stresses near the excavation side-walls and then stresses increase rapidly outside the spalling region. On the other hand, the inner low confining cell appears to be absent from the Voronoi CLFH model which predicts very high confining pressures around the tunnel. For the tunnel roof and floor, the continuum CWFS model predicts an increased deconfinement in the anticipated tensile region compared to the Voronoi CLFH model, which in turn releases a greater amount of rock mass deformation as was shown in Figure 4.23.

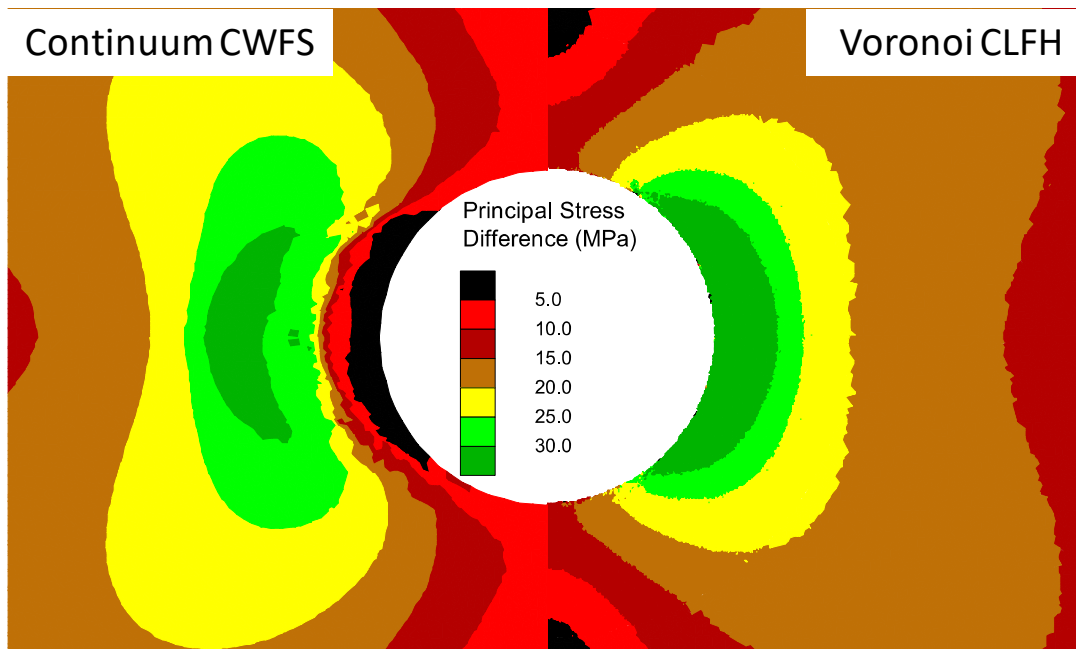


Figure 4.24. Principal stress difference around the tunnel at the stage of 100% relaxation for the DFN free continuum CWFS and Voronoi CLFH models.

The stress state at the side-wall and roof of the tunnel is further investigated by exporting the tunnelling-induced maximum and minimum stresses at the intermediate and final relaxation stages. Figure 4.25 presents with the black envelope the idealised linear elastic stress paths for the side-wall and roof of the circular excavation. The stresses on the boundary of the side-wall increase to the maximum level of $3\sigma_1 - \sigma_3$ and reduce at the roof to the minimum level of $3\sigma_3 - \sigma_1$. Also shown in Figure 4.25 are the predicted stress paths from the continuum CWFS (left-half) and Voronoi CLFH (right-half) models. From the stress paths in the tensile region (i.e. blue lines for the roof), both models appear to follow a similar behaviour with the linear elastic envelopes. In the case of the zone of maximum compression (i.e. red lines for the side-wall) it was evident that the Voronoi CLFH model essentially follows the path of an elastic material, while significant stress distribution is observed at the continuum CWFS model due to the CI threshold being exceeded.

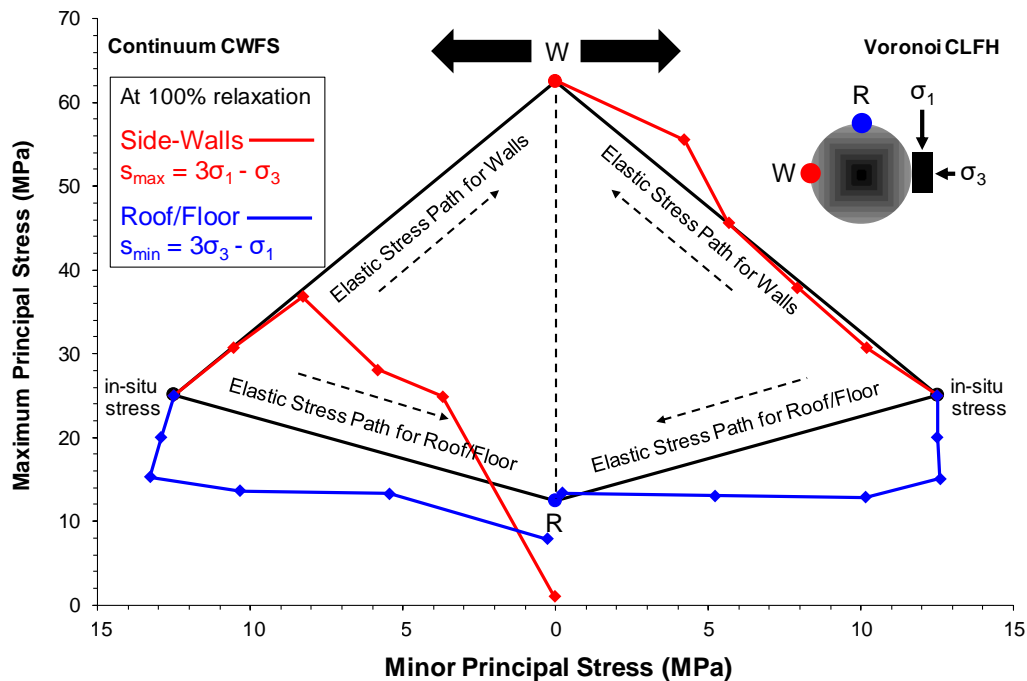
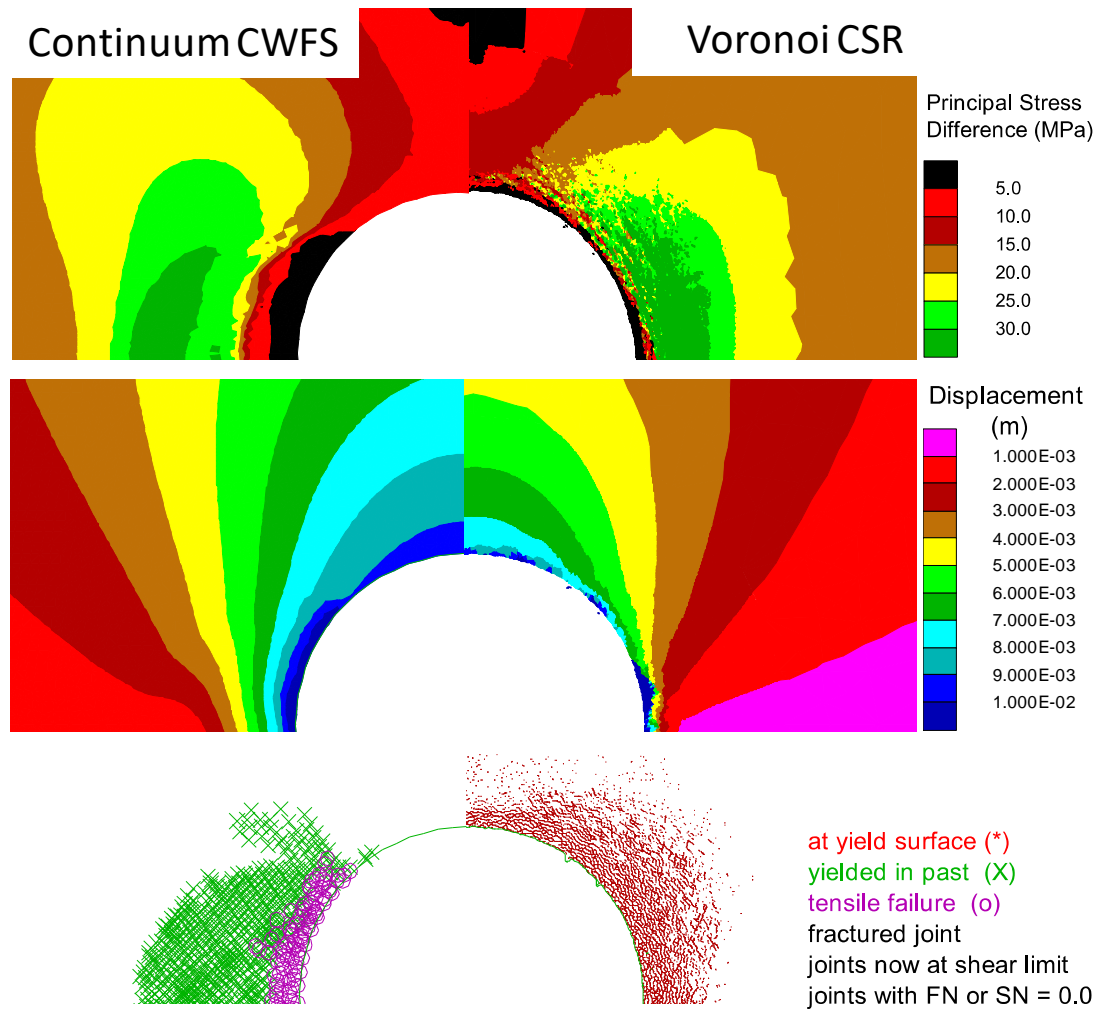


Figure 4.25. Tangential stress paths for the roof and side-walls of the circular tunnel: i) elastic and ii) predicted from the continuum CWFS and Voronoi CLFH models.

From Figure 4.25, it is evident that the micro-properties used for the Voronoi CLFH model have not triggered the anticipated weakening effect of a rock mass that experiences brittle failure near the excavation boundaries. It is therefore concluded that the calibrated CLFH properties shown in Figure 4.20 from the UCS tests, although have captured successfully the CI damage, need certain modifications to i) avoid the significant strength-hardening after the CI stress level; and ii) to capture the in-situ rock mass softening behaviour near the excavation boundaries. To replicate the redistribution of tangential stresses on the side-walls and the high deformation at the tunnel roof, a sensitivity analysis was performed by either altering the Voronoi contact properties and/or by employing different constitutive laws. Due to space limitations in the current paper, only two models are presented which appear to have approached the behaviour of the continuum CWFS model that was shown in the figures above.

In the first modelling attempt, the conventional Voronoi CSR model was used and the contacts properties were softened up to that level where the overall model response resembled the behaviour of the CWFS model. Figure 4.26 presents the results of this analysis together with the re-calibrated micro-properties. The predicted deformation is in reasonable agreement between the two models and as can be seen the shape and magnitude of the displacement contours at the circumference of the tunnel are similar. As can be seen from Figure 4.27, the Voronoi CSR model captured the fracturing of the rock mass parallel to the direction of loading at the region of maximum compressive stress (i.e. the side-walls). Due to this damage, a low confinement zone has been developed but its size is more than 50% smaller from the inner cell predicted by the CWFS model. Also, in the roof/wall of the tunnel, the Voronoi CSR model creates an increased deconfinement which in turn produces significant damage in the tensile region that is not in agreement with the results from the continuum CWFS model. From these results, it can be said that the calibration is regarded as being semi-satisfactory due to the partial agreement/disagreement between the two models.



Calibrated Voronoi CSR model against the behaviour of the Continuum CWFS				
Normal Stiffness		kn	GPa/m	16000
Shear Stiffness		ks	GPa/m	8000
Peak	Cohesion	c_{mp}	MPa	73.3
	Friction Angle	ϕ_{mp}	$^{\circ}$	28.3
	Dilation Angle	ψ_{mp}	$^{\circ}$	0.0
	Tensile Strength	t_{mp}	MPa	1.39
Residual	Cohesion	c_{mr}	MPa	0.0
	Friction Angle	ϕ_{mr}	$^{\circ}$	25.0
	Dilation Angle	ψ_{mr}	$^{\circ}$	0.0
	Tensile Strength	t_{mr}	MPa	0.0

Figure 4.26. Comparison between the DFN-free continuum CWFS and the re-calibrated Voronoi CSR models at the stage of 100% relaxation.

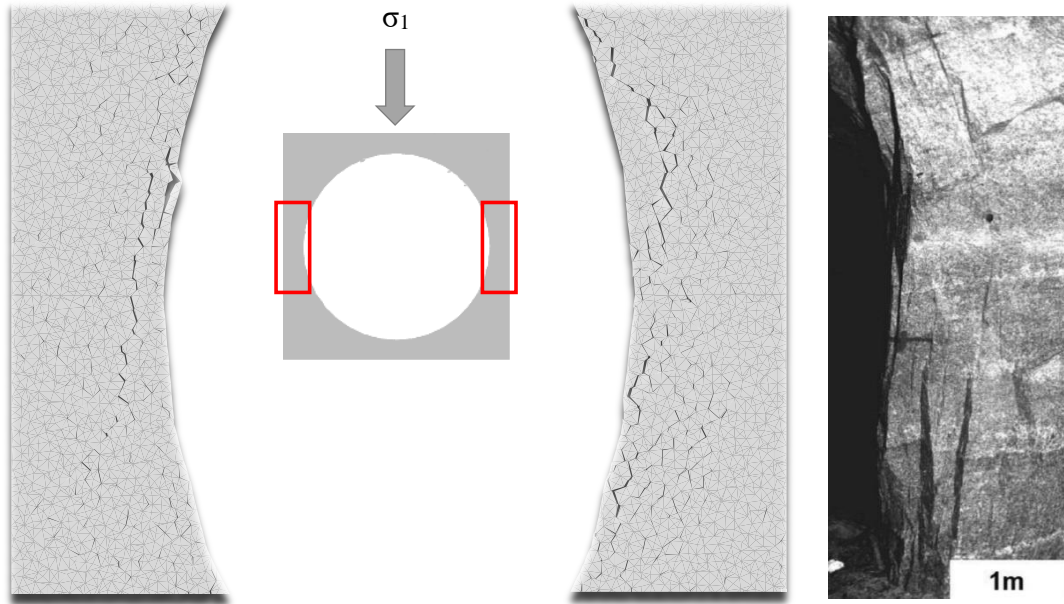
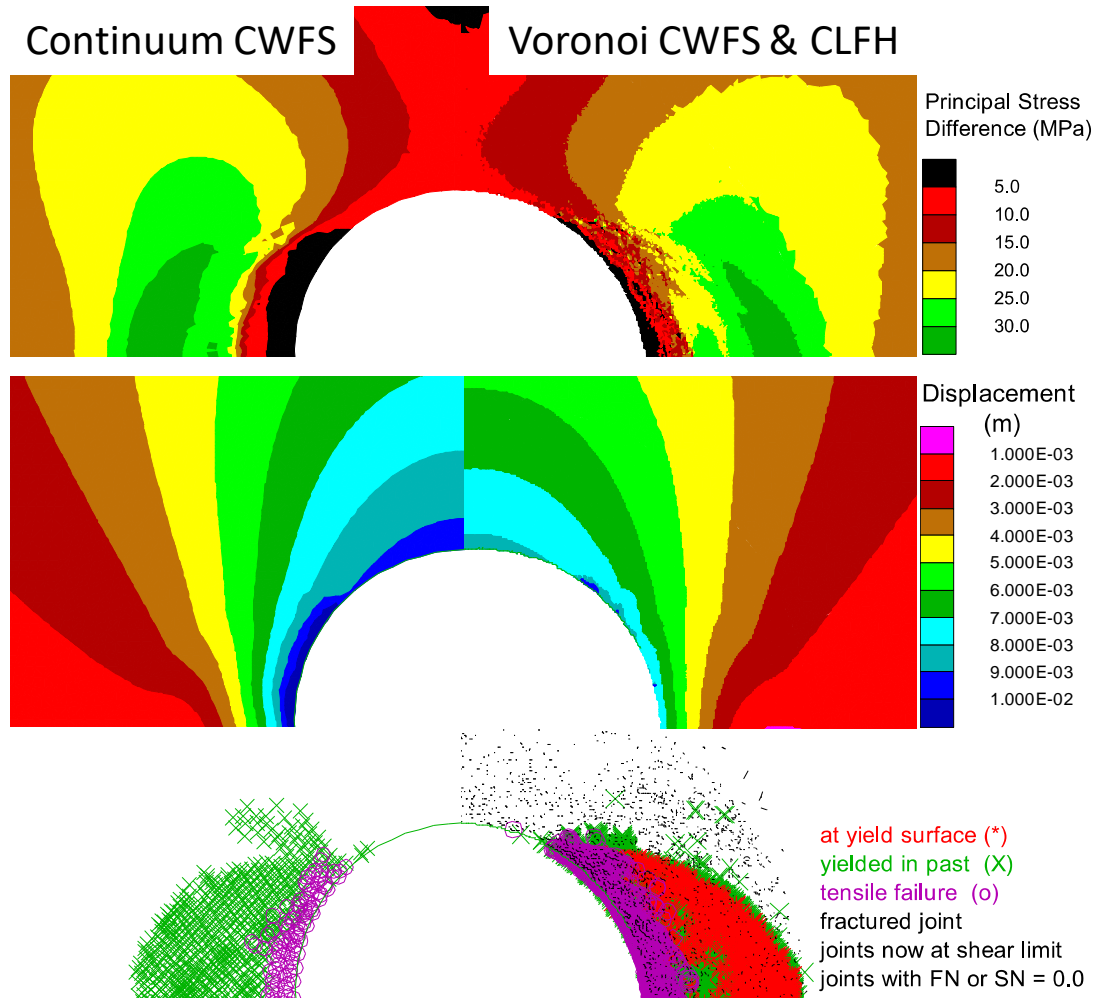


Figure 4.27. Predicted tensile fracturing at the side-walls of the excavation from the recalibrated Voronoi CSR model. The figure at the right presents an example from an excavation spalling damage reported by Diederichs et al. (2004).

In the second modelling attempt, a hybrid model was employed in which the Voronoi zone elements and contacts followed the CWFS and CLFH models respectively. Thus, the Voronoi zones in this analysis are not exhibiting anymore a linear elastic behaviour but potentially involve plastic deformations via the violation of the prescribed yield criterion (i.e. the CWFS). Figure 4.28 presents the predicted rock mass behaviour. As can be observed, the size of the low confinement zone, the predicted displacement and the damage in the tensile and compressive regions are in close agreement with the response of the rock mass from the continuum CWFS model. From these results, it can be said that the calibration is regarded as being satisfactory and it appears that the results from the hybrid CWFS & CLFH model are in much better agreement with the behaviour predicted by the CSR model. However, since this model involves more variables, the calibration process requires more effort in comparison with the traditional modelling approaches.



Calibrated hybrid Voronoi CWFS & CLFH model against the behaviour of the Continuum CWFS				Voronoi Contacts	Voronoi Zones
Peak	Cohesion	c_{mp}	MPa	6.0	7.5
	Friction Angle	ϕ_{mp}	°	17.0	18.9
	Dilation Angle	ψ_{mp}	°	17.6	17.6
	Tensile Strength	t_{mp}	MPa	2.0	2.47
Residual	Cohesion	c_{mr}	MPa	0.0	0.1
	Friction Angle	ϕ_{mr}	°	50.0	61.0
	Dilation Angle	ψ_{mr}	°	0.0	3.5
	Tensile Strength	t_{mr}	MPa	0.0	0.01

Figure 4.28. Comparison between the DFN-free continuum CWFS and the calibrated hybrid Voronoi CWFS & CLFH model at the stage of 100% relaxation.

Examining the stress paths at different locations behind the tunnel contour reveals that both models predict similar behaviours. Figure 4.29 indicates that at the side-wall, the hybrid CWFS & CLFH model (i.e. left-hand plot) shows a significant stress redistribution up to 1 m from the tunnel boundary while at the CSR model (i.e. right-hand plot) the spalling depth is 0.5 m. Essentially, both models have captured the fundamental processes of brittle damage near the excavation periphery which involve the initial build-up of high stresses and then the sudden deconfinement parallel to the direction of maximum loading, leading to macroscopic axial splitting. The stress paths for the tunnel roof are again similar between the two models with the exception of the 0.0 m measurement for the CSR model which overpredicts damage in the tensile region. In general, the stress paths from the hybrid model are in better agreement with the anticipated rock mass behaviour and failure mechanisms.

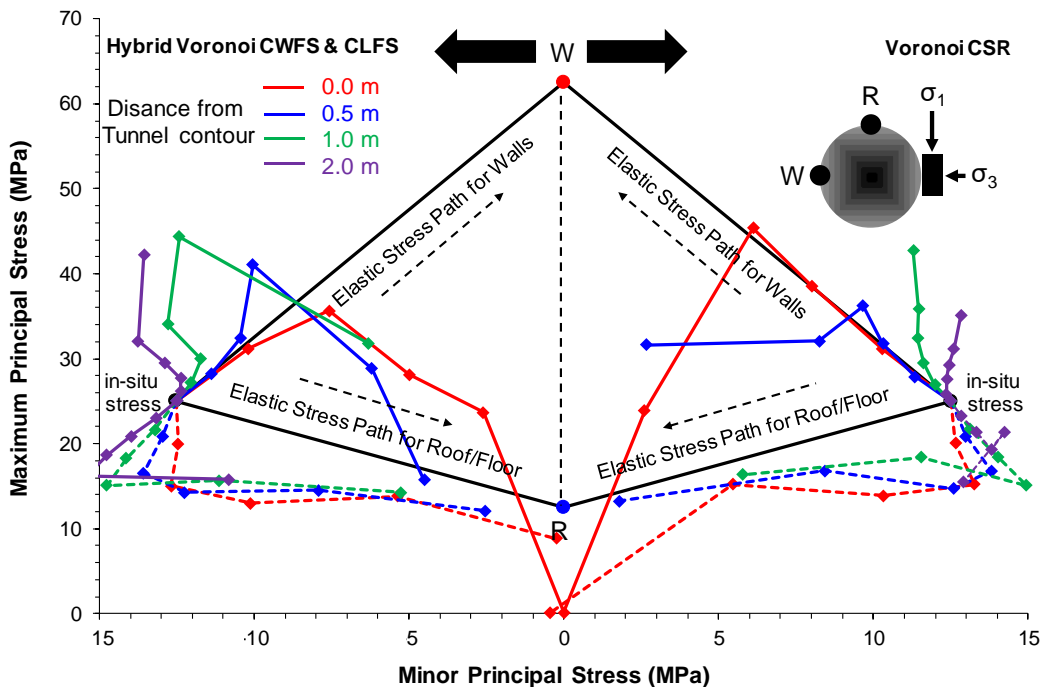


Figure 4.29. Tangential stress paths for the roof and side-walls of the circular tunnel: i) elastic and ii) predicted from the Voronoi CWFS & CLFS and CSR models.

The stress paths of the side-walls at 0.0 m from the Continuum CWFS and Voronoi models are re-plotted in Figure 4.30 together with the failure envelopes from the DISL approach. In both the Continuum CWFS and hybrid Voronoi CWFS & CLFS models, when the stress path reaches the CI threshold at 40% tunnelling relaxation then a local stress redistribution occurs causing brittle failure in the side-walls. Following this initial damage, the stress paths travel parallel to the CI envelope up to the stage of 80% relaxation when the rock loses all the internal capacity to maintain stresses due to extensile fracturing. The Voronoi CSR model behaves in a similar manner but the stress history suggests that the stress drop occurs at 60% relaxation and thus the rock is slightly stronger. While the initial Voronoi CLFH model is obviously elastic as it crosses the damage and spalling zones without any sign of weakening or relaxation.

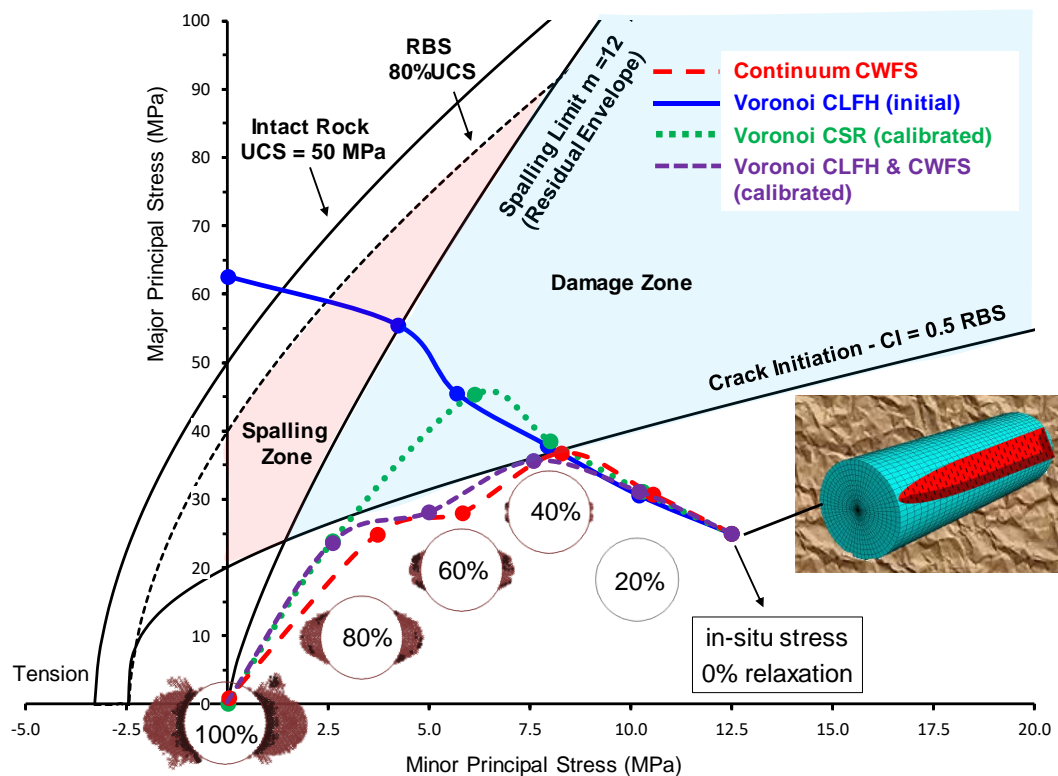


Figure 4.30. Stress paths for the tunnel side-wall from the continuum CWFS and Voronoi models plotted together with the tri-linear envelope of the DISL approach.

Following the simulation of the pseudo-continuum models, the analyses of the re-calibrated Voronoi models were repeated by embedding into the Voronoi skeleton the DFN described in the previous sections (Figure 4.31). The resulting synthetic rock mass is able to capture both the effect of pre-existing joints and the crack evolution processes within the intact rock material in between joints (i.e. the inter-block damage).

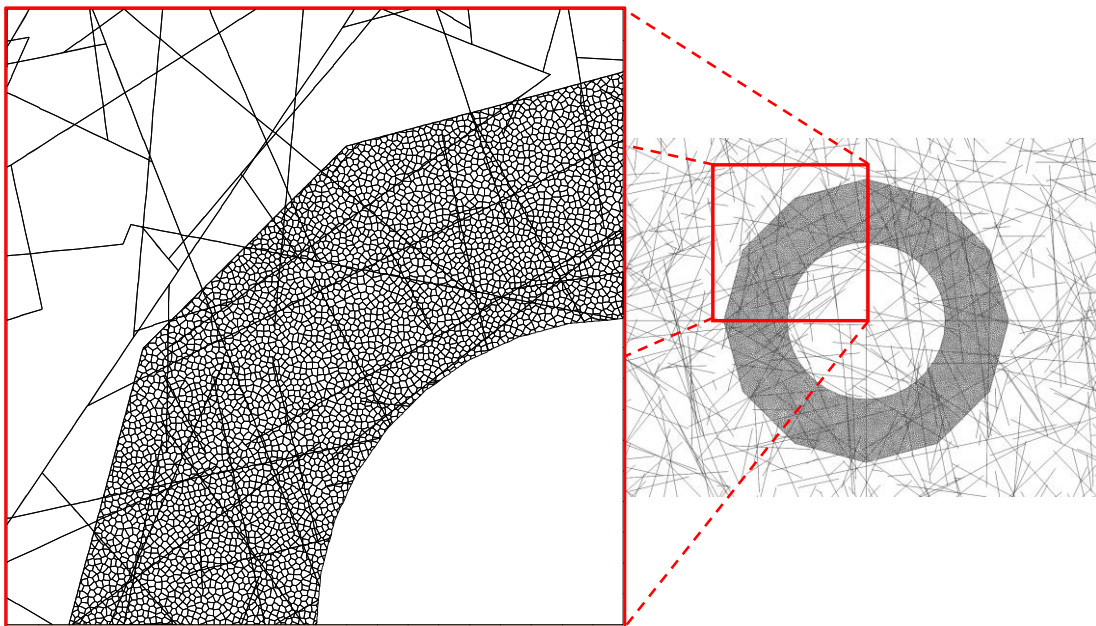


Figure 4.31. Synthetic Rock Mass geometry (i.e. Voronoi models & DFN).

The predicted disturbance for the Voronoi & DFN models for the CSR and CWFS & CLFH approaches are presented in Figure 4.32 and Figure 4.33 respectively, against the disturbance that was mobilised by the continuum CWFS & DFN model. As can be seen, up to the stage of 80% relaxation (i.e. 20% of the in-situ stresses have not yet released), the damage shape and extent for both the rock blocks and the discontinuities are in perfect agreement between the different approaches. However, at the stage of 100% relaxation, the blocks of the Voronoi model experiences a considerably reduced damage and the extent of the failed discontinuities is limited only within 2-3 m (i.e. one tunnel radius) from the tunnel periphery. On the other hand, the

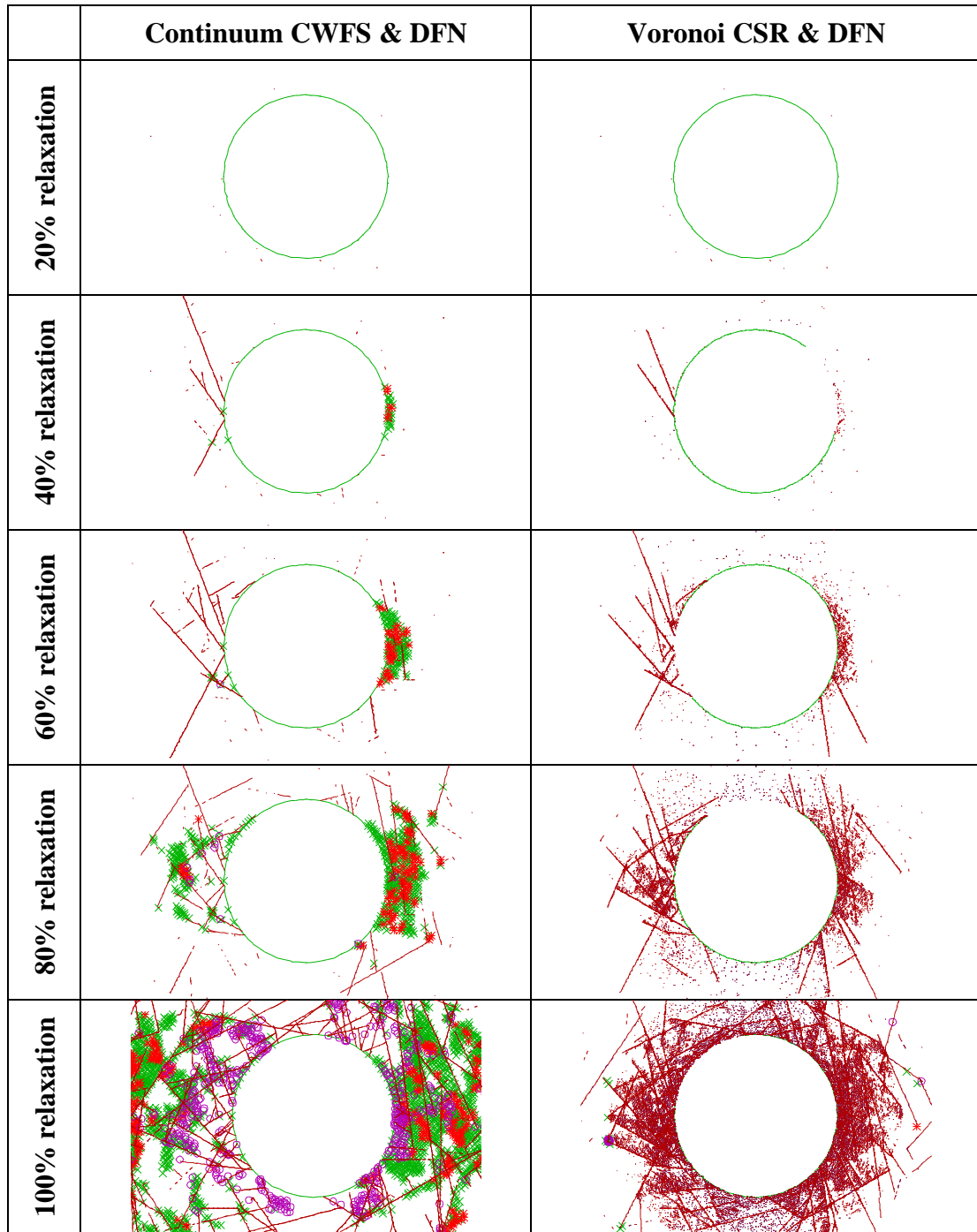


Figure 4.32. Comparison between the discontinuum CWFS and discontinuum Voronoi CSR models for the progressive development of damage.

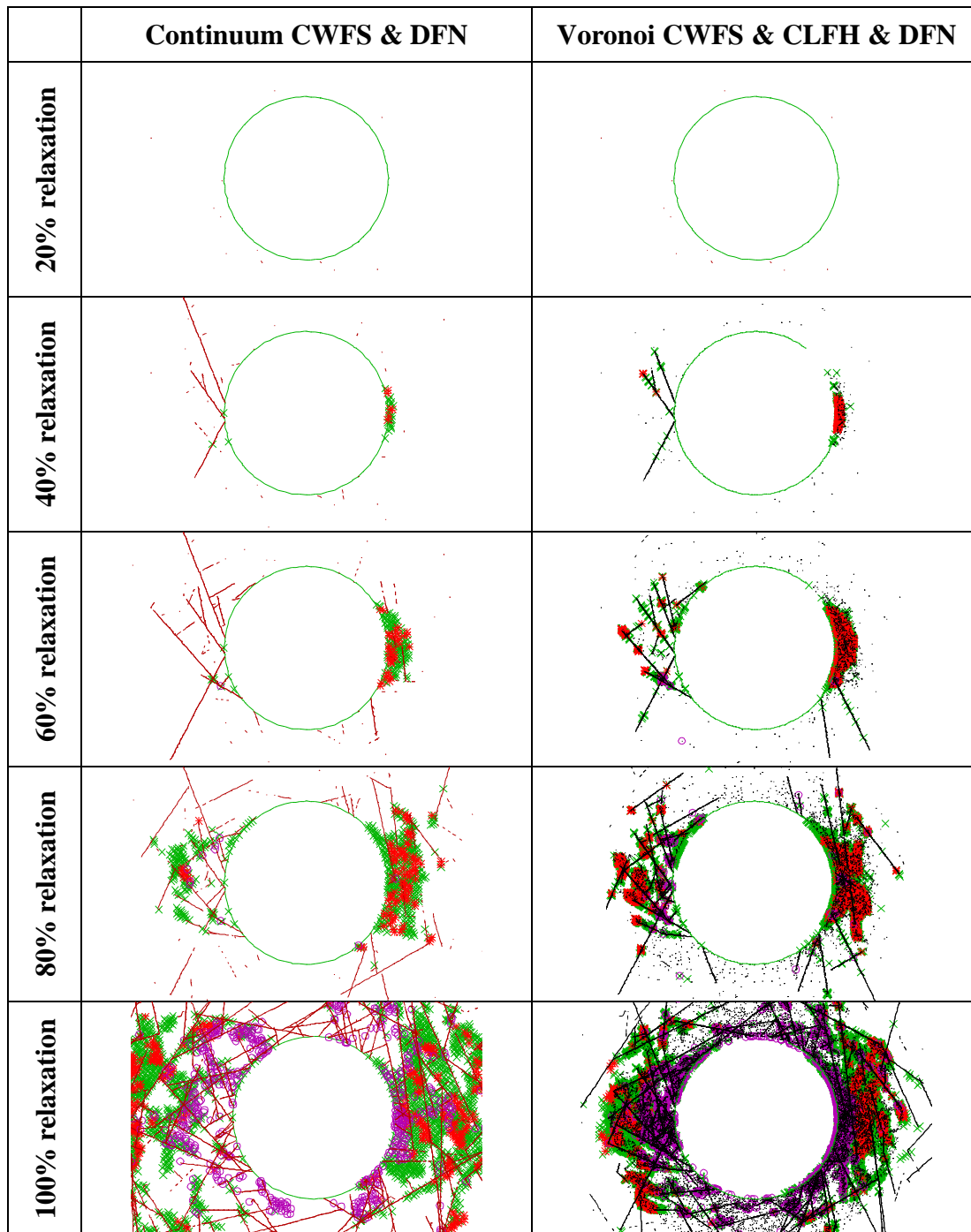


Figure 4.33. Comparison between the discontinuum CWFS and discontinuum Voronoi CWFS & CLFH models for the progressive development of damage.

the extent of damage in the continuum CWFS & DFN model has propagated more than one tunnel diameter (i.e. 5-6 m). Apart from the size of the EDZ, significant differences were also observed at the stress conditions around the excavation and at the magnitude of displacements. These comparisons for the stage of 100% relaxation are shown in Figure 4.34 and Figure 4.35. The continuum & DFN model shows displacements in the range of 10 to 30 mm while the tunnel closure from the Voronoi & DFN models is only between 5-15 mm. The size of the low confinement zone is predicted up to 0.5 m from the Voronoi & DFN models while the continuum & DFN model shows up to 2 m, with the shape of deconfinement mainly be driven by fractures striking parallel to the excavation periphery. In the continuum CWFS & DFN model the higher displacements and deconfinement are observed at rock blocks which are bounded by persistent (i.e. block-forming) fractures. Apparently, the significant mismatch between the behaviour of the two approaches (i.e. continuum blocks vs Voronoi blocks) is because the Voronoi block assemblage creates a well-interlocked rock mass structure that resists dramatic deconfinement away from the excavation and thus restricts the shear and/or opening of large-scale fractures only close to the tunnel boundaries.

In general, as the in-situ stress magnitudes increase with depth, the pre-existing discontinuities are expected to become clamped and the failure mechanisms are dominated by stress-induced slabbing type of failure rather than by structurally controlled block failures (Martin et al., 2001). The Voronoi & DFN models therefore provide a more realistic rock mass behaviour as blocks maintain their interlock at a distance behind the excavation and do not allow the block-forming fractures to relax. Alternatively, it was shown that when rock blocks in a discontinuum model are represented by an equivalent continuum material, then the rock mass surrounding the opening experiences a very aggressive relaxation at the stage of complete deconfinement, causing excessive kinematic freedom and an unrealistically large low confinement zone that overpredicts damage.

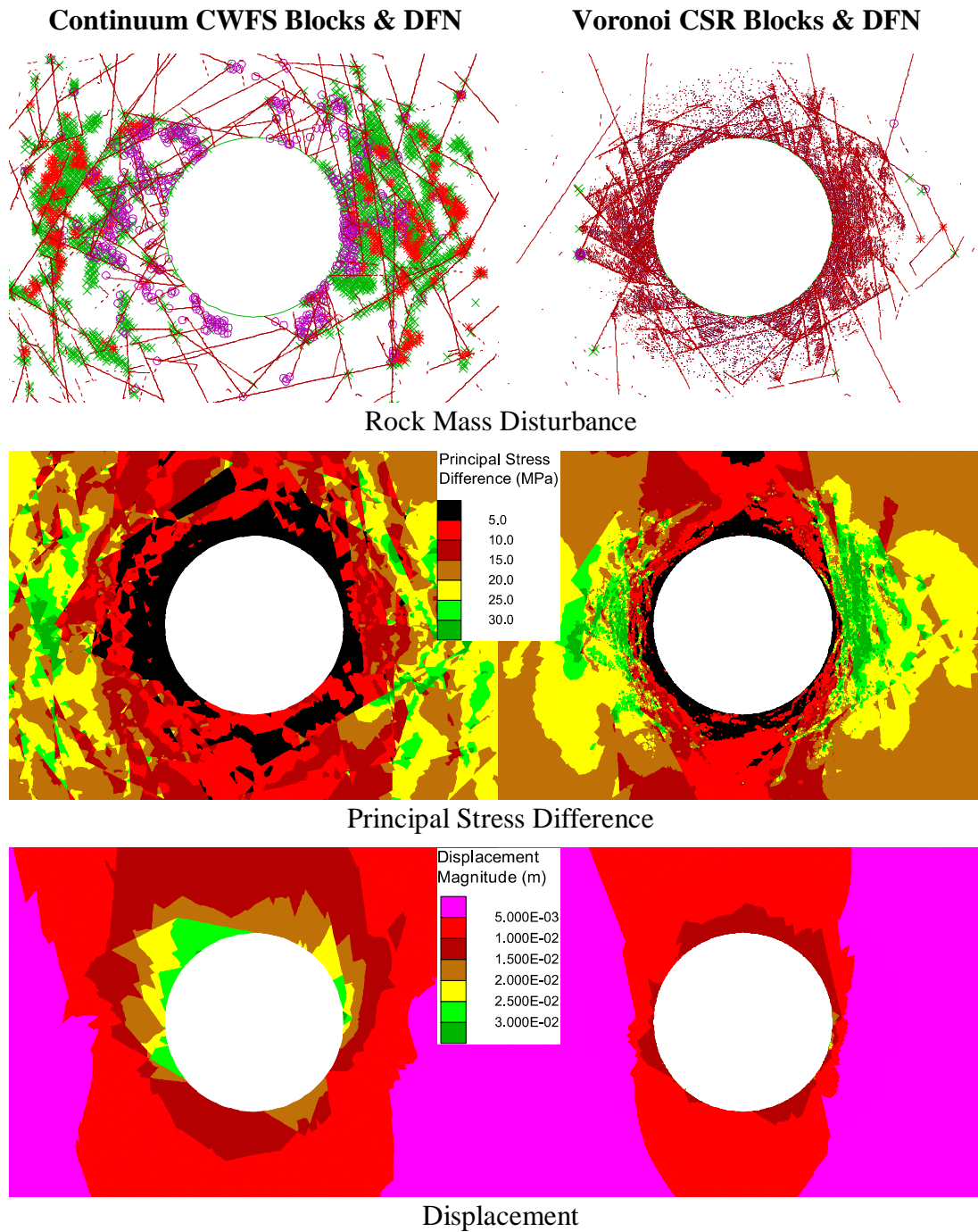


Figure 4.34. Comparison between the discontinuum CWFS and discontinuum Voronoi CSR models at the stage of 100% relaxation.

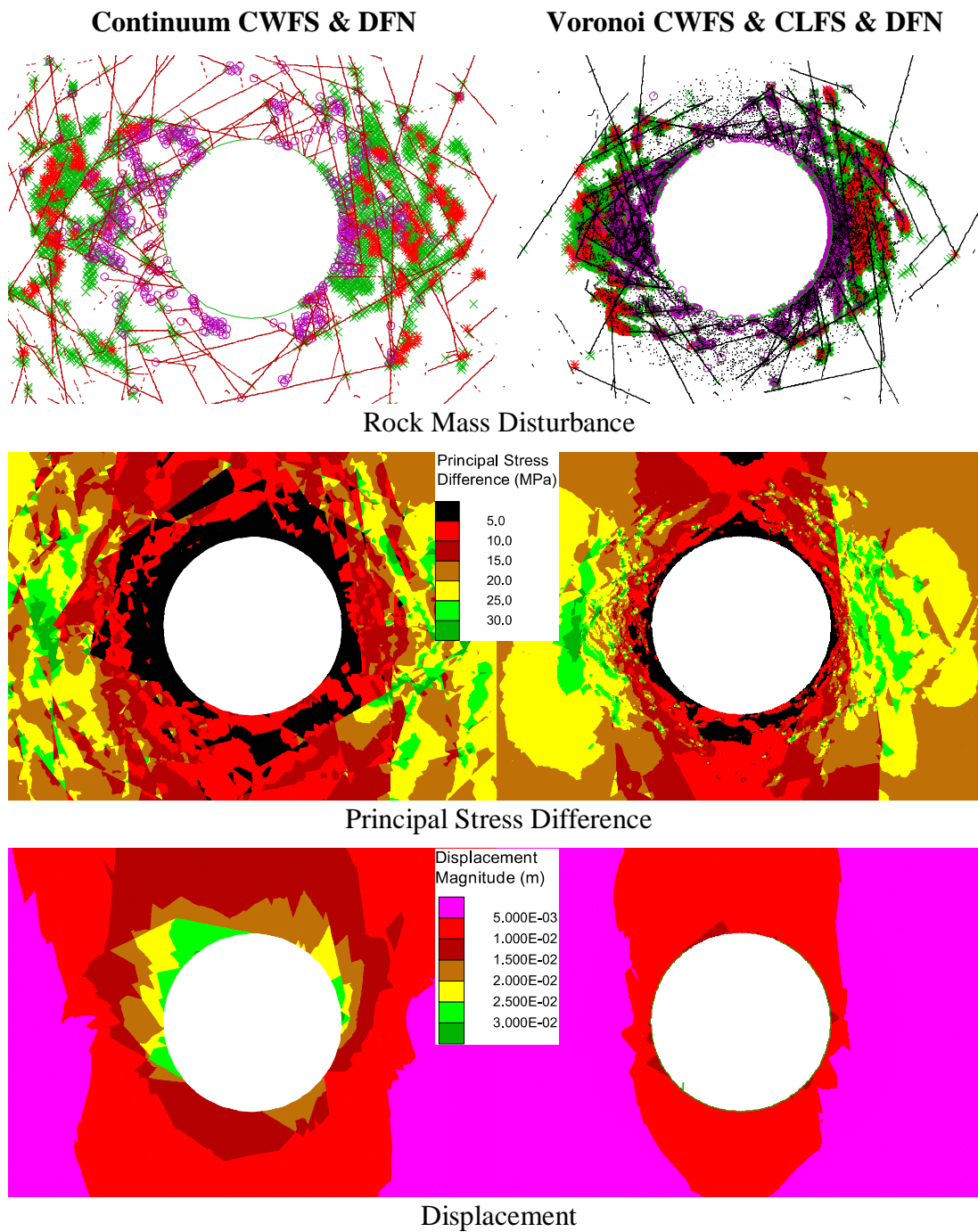


Figure 4.35. Comparison between the discontinuum CWFS and discontinuum Voronoi CWFS & CLFS models at the stage of 100% relaxation.

4.4. Summary and Conclusions

In moderately jointed and blocky rock masses, rock block strength is a significant factor controlling the rock mass behaviour and the response of the structural elements used as rock support and rock reinforcement. This paper outlined the available tools and theoretical background for estimating the properties of defected and non-defected rock blocks for use in discontinuum modelling. Special focus was given on the selection of appropriate constitutive relationships and discontinuum modelling techniques as traditional approaches do not well represent the actual in-situ strength of well-interlocked blocks near the excavation boundaries and fail to capture the anticipated failure mechanisms.

The mechanical behaviour of blocks containing micro and meso-scale defects is influenced significantly by the geometrical pattern and condition of such defects. However, the role of defects is typically neglected in rock engineering design or are mistakenly logged/mapped as large-scale joints, hence over-penalising in that way the rock mass strength (Jakubec, 2013).

The unconfined strength of rock blocks is challenging to define due to the limited availability of large-scale tests and the difficulties in testing representative lab scale rock samples (e.g. defected vs non-defected and disturbed vs non-disturbed). To overcome some of these problems, Stavrou et al. (2019) proposed an approach that provides RBS estimates considering the size of the sample and the in-situ condition of defects (i.e. intensity, persistence and strength) within blocks. However, further research is required to improve the proposed method as in its current form represents the results of two-dimensional analyses and thus provides lower bound estimates.

The strength of rock blocks under confined conditions is typically derived based on a combination of approaches which either reduce the measured lab-scale intact rock

strength or improve the estimated rock mass scale strength. While, in theory, the properties of blocks should lie in between that of the rock mass and the intact rock, several inaccuracies could arise as different lithologies are influenced by different scaling effects and/or variable degrees of heterogeneities and also the assigned block quality relies on the subjectiveness of the project engineer. Stavrou and Murphy (2018) proposed a block-scale GSI parameter, named the micro Geological Strength Index (mGSI), that can be used to describe the confined strength of rock blocks considering scale effects and material quality. The predicted RBS values when using the mGSI approach are in strong agreement with estimates from the traditional Hoek–Brown criterion and a quantification of the mGSI was presented in terms of specimen size and defect condition (i.e. intensity, persistence and strength). An important characteristic is the dramatic confined strength reduction with rather small mGSI reduction steps, which suggests that special care is needed for the selection of design mGSI values and that narrower mGSI ranges are deemed suitable for the characterisation of rock blocks to avoid the underestimation of strength.

Apart from the selected approaches for estimating the absolute strength magnitudes, another significant modelling aspect is the shape of the confined strength envelope in relation to the stress conditions nearby the excavation boundaries. It has long been recognised that the traditional linear or non-linear failure envelopes do not represent the in-situ strength of competent rock masses subjected to high stress conditions. In these cases, the envelope follows an S- or tri-linear shape to replicate the expected stress-induced fracturing in the low confining region adjacent the tunnel periphery, and the delayed mobilisation of friction following a significant loss of cohesion. With this approach, the in-situ strength of rock blocks at low confinement is controlled by the crack initiation threshold while at higher confining stresses the envelope makes a sharp transition and is controlled by the spalling limit and the crack

damage threshold. The modified brittle model can be established following the DISL approach proposed by Diederichs (2007) or the procedure described by Kaiser (2016).

Following the review for estimating the properties of defected and non-defected rock blocks, a series of continuum, discontinuum, Voronoi and Voronoi & discontinuum modelling cases were run in UDEC to study the influence of scaled block properties and modelling techniques on the behaviour of underground openings excavated in moderately jointed/blocky rock masses. All cases considered, a circular excavation at depth of 1000 m and a DFN was included in the discontinuum models to represent the fracturing pattern of a rock mass with a GSI of 60 ± 5 .

Case 1 considered three progressively reduced rock block UCS values to reflect the increased heterogeneity of blocks containing defects. To reduce the intact rock UCS from 80% to 20%, the mGSI in the Hoek–Brown equations had to be reduced from 96 to 71 and the material was assumed to follow an elastic-plastic behaviour. Significant differences were found between the models highlighting that block strength is an important factor in discontinuum modelling and that careful block characterisation is needed in selecting design mGSI values.

Case 2 presented a comparison between block models that use in the post-peak phase the elastic-plastic, elastic-brittle and strain-softening behaviour. For the analysed strength-stress ratios, it was found that the block post-peak properties have little influence in the overall rock mass response around the tunnel.

Case 3 investigated the differences in adopting the traditional Hoek–Brown/Mohr–Coulomb criterion and the modified the DISL/CWFS approach. The results revealed that the conventional model underestimated the EDZ and rock mass deformation because overestimates the in-situ strength of blocks. As expected, the CWFS model predicted a larger damage around the excavation, but the extent of disturbance appears to have been magnified by the presence of pre-existing fractures

causing local stress concentrations. By examining the damage evolution at different tunnelling relaxation stages, it was further confirmed that the CWFS model captures the progressive formation of a v-shaped notch type of failure due to the CI level been slowly exceeded, while the traditional model was unable to replicate the damage behaviour in a realistic manner. From this case it was shown that the DISL/CWFS concept plays an important role, not only when it is employed in continuum models but also when it is used to describe the brittle behaviour of continuum rock blocks in between joints in discontinuum models.

Case 4 examined the effect of adopting the CWFS approach and the conventional models, in rock masses with variable block sizes in relation to the excavation size. It was again confirmed that the traditional modelling approaches underestimate the extent of damage regardless of the degree of blockiness in the rock mass.

Case 5 investigated the combined influence of constitutive model selection and discontinuum modelling techniques. The analyses compared the results of models in which the blocks were simulated as an assemblage of Voronoi elements and as a continuum medium in between joints. For the micro-contacts that separate the Voronoi polygons, the CSR and CLFH models were used to study the capabilities of the micro-mechanical models in capturing the anticipated rock mass response. It was found that when the Voronoi micro-properties are properly calibrated, then the tunnel behaviour is in good agreement with continuum-based models. For the DFN-free models, the Voronoi CLFH approach provided a much better representation for the damage around the tunnel in comparison with the conventional CSR model. However, damage is only one aspect to check when assessing the stability state of the model. It was shown that calibrating the extent and shape of the EDZ in Voronoi models does not necessarily lead to correct displacement magnitudes and stress redistributions. Thus, the interpretation and calibration of a Voronoi model should be based on a combination of indicators which are the: i) pattern of failed zones and joints; ii) tunnel-induced stress

paths at different relaxation stages; and iii) rock mass deformations. From the calibration exercise it was also evident that significant effort is required to calibrate tunnel-scale Voronoi problems, and that future studies will benefit from the development of specific calibration steps for the Voronoi CLFH approach as current guidelines mainly focus on the traditional material laws. Regarding the Voronoi models in which the DFN was included in the analysis, significant differences were observed in comparison to the models in which the blocks are represented as a continuum material in between the fracture network. The results showed that the Voronoi models predicted a considerably reduced damage, stress relaxation and deformation around the opening. The Voronoi block assemblage is believed to provide a more realistic rock mass behaviour by creating a well-interlocked structure that allows the macro-scale discontinuities to slip/open only when material continuity has been disturbed by substantial fracturing.

The behaviour of the circular tunnel at depth revealed that block strength, constitutive relationships and modelling techniques are all very important factors in simulating the behaviour of underground openings. Hence, derivation of representative input parameters and selection of appropriate constitutive models are key for reliably simulating the behaviour of the discontinuum rock mass. The traditional failure criteria and modelling approaches do not well represent the behaviour of rock blocks and would likely lead to misleading observations. While the estimation of parameters for defected blocks and the calibration of numerical models are challenging tasks, the current study shows that if rock block strength is poorly characterised and/or if inappropriate modelling assumptions are used, meaningful understanding of the intrinsic stability (i.e. deformation, size of disturbance, failure modes) are lost and hence the predicted rock mass behaviour could bear little or no relationship with reality.

References

- Baecher, G. and Einstein, H. 1981. *Size effect in rock testing. Geophysical Research Letters*, 8(7), pp.671-674.
- Bandis, S.C., Sharp, J.C., Mackean, R.A. and Bacasis, E.A. 2011. Explicit Characterisation and Interactive Analysis for Engineering Design of Rock Caverns *In: Proceedings of the Joint Hong Kong Institute of Engineers – Hong Kong Institute of Planning Conference on Planning and Development of Underground Space.*, pp.133–142.
- Barton, N., Lien, R. and Lunde, J. 1974. Engineering classification of rock masses for the design of tunnel support. *Rock Mechanics*. 6(4), pp.189–236.
- Bewick, R.P., Kaiser, P.K. and Amann, F. 2019. Strength of massive to moderately jointed hard rock masses. *Journal of Rock Mechanics and Geotechnical Engineering*, 11(3), pp.562-575.
- Bieniawski, Z.T. 1989. *Engineering rock mass classifications: a complete manual for engineers and geologists in mining, civil, and petroleum engineering*. John Wiley & Sons.
- Carpinteri, A. 1994. Fractal nature of material microstructure and size effects on apparent mechanical properties. *Mechanics of Materials*. 18(2), pp.89–101.
- Carter, T.G., Diederichs, M.S. and Carvalho, J.L. 2008. Application of modified Hoek-Brown transition relationships for assessing strength and post yield behaviour at both ends of the rock competence scale. *Journal of the Southern African Institute of Mining and Metallurgy*. 108(6), pp.325–338.
- Day, J.J., Hutchinson, D.J. and Diederichs, M.S. 2012. A Critical Look At Geotechnical Classification For Rock Strength Estimation. *46th U.S. Rock*

Mechanics/Geomechanics Symposium., p.10.

- Dershowitz, W., Lee, G., Geier, J., Foxford, T., LaPointe, P. and Thomas, A. 2014. FracMan Version 7.4—Interactive Discrete Feature Data Analysis, Geometric Modeling, and Exploration Simulation: User Documentation.
- Diederichs, M.S. 2007. The 2003 Canadian Geotechnical Colloquium: Mechanistic interpretation and practical application of damage and spalling prediction criteria for deep tunnelling. *Canadian Geotechnical Journal*. 44(9), pp.1082–1116.
- Diederichs, M.S., Kaiser, P.K. and Eberhardt, E. 2004. Damage initiation and propagation in hard rock during tunnelling and the influence of near-face stress rotation. *International Journal of Rock Mechanics and Mining Sciences*. 41(5), pp.785–812.
- Diederichs, M.S., Carter, T. and Martin, C.D. 2010. Practical rock spall prediction in tunnels *In: Proceedings of ITA World tunnel congress.*, p.1e8.
- Einstein, H.H., Baecher, G.B. and Hirschfeld, R.C. 1970. The effect of size on strength of a brittle rock. *International Society of Rock Mechanics, Proceedings*. 1(1–19).
- Gao, F.Q. and Stead, D. 2014. The application of a modified Voronoi logic to brittle fracture modelling at the laboratory and field scale. *International Journal of Rock Mechanics and Mining Sciences*. 68, pp.1–14.
- Hajiabdolmajid, V., Kaiser, P.K. and Martin, C.D. 2002. Modelling brittle failure of rock. *International Journal of Rock Mechanics and Mining Sciences*. 39(6), pp.731–741.
- Hoek, E. 1994. Strength of rock and rock masses. *ISRM News Journal*. 2(2), pp.4–16.
- Hoek, E. and Bieniawski, Z.T. 1965. Brittle fracture propagation in rock under compression. *International Journal of Fracture Mechanics*. 1(3), pp.137–155.

- Hoek, E. and Brown, E.T. 1997. Practical estimates of rock mass strength. *International Journal of Rock Mechanics and Mining Sciences*. 34(8), pp.1165–1186.
- Hoek, E. and Brown, E.T. 2018. The Hoek–Brown failure criterion and GSI – 2018 edition. *Journal of Rock Mechanics and Geotechnical Engineering*, 11(3), pp.445-463.
- Hoek, E. and Brown, T. 1980a. Empirical strength criterion for rock masses. *Journal of Geotechnical and Geoenvironmental Engineering*. 106(ASCE 15715).
- Hoek, E. and Brown, T. 1980b. *Underground Excavations in Rock* [Online]. Taylor & Francis. Available from: <https://books.google.co.uk/books?id=XeGKeYa8d30C>.
- Hoek, E., Kaiser, P. and Bawden, W. 1995. *Support of Underground Excavation in Hard Rock*.
- Hunt, D.D. 1973. The influence of confining pressure on size effect.
- Itasca, U. 2014. Version 6.0. *Itasca Consulting Group Inc., Minneapolis, Minnesota*.
- Jakubec, J. 2013. Role of defects in rock mass classification. *Australian Centre for Geomechanics*. Ground Support 2013, pp.1–8.
- Jakubec, J., Board, M., Campbell, R., Pierce, M. and Zaro, D. 2012. Rock mass strength estimate—Chuquicamata case study *In: MassMin 2012*. Sudbury, Canada: Canadian Institute of Mining, Metallurgy and Petroleum (CIM).
- Kaiser, P.K. 2016. *Ground Support for Constructability of Deep Underground Excavations: Challenge of Managing Highly Stressed Ground in Civil and Mining Projects*. ITA/AITES.
- Kaiser, P.K., Amann, F. and Bewick, R.P. 2015. Overcoming challenges of rock mass characterization for underground construction in deep mines *In: 13th ISRM*

- International Congress of Rock Mechanics*. International Society for Rock Mechanics.
- Kaiser, P.K., Diederichs, M.S., Martin, C.D., Sharp, J. and Steiner, W. 2000. Underground works in hard rock tunnelling and mining *In: ISRM International Symposium*. International Society for Rock Mechanics and Rock Engineering.
- Kaiser, P.K. and Kim, B.-H. 2015. Characterization of strength of intact brittle rock considering confinement-dependent failure processes. *Rock Mechanics and Rock Engineering*. 48(1), pp.107–119.
- Kazerani, T. and Zhao, J. 2010. Micromechanical parameters in bonded particle method for modelling of brittle material failure. *International Journal for Numerical and Analytical Methods in Geomechanics*. 34(18), pp.1877–1895.
- Laubscher, D.H. and Jakubec, J. 2001. The MRMR rock mass classification for jointed rock masses. *Underground Mining Methods: Engineering Fundamentals and International Case Studies, WA Hustrulid and RL Bullock (eds) Society of Mining Metallurgy and Exploration, SMME.*, pp.475–481.
- Marinos, V. and Carter, T.G. 2018. Maintaining geological reality in application of GSI for design of engineering structures in rock. *Engineering geology*. 239, pp.282–297.
- Martin, C.D. 1997. Seventeenth Canadian geotechnical colloquium: the effect of cohesion loss and stress path on brittle rock strength. *Canadian Geotechnical Journal*. 34(5), pp.698–725.
- Martin, C.D. and Chandler, N.A. 1994. The progressive fracture of Lac du Bonnet granite *In: International Journal of Rock Mechanics and Mining Sciences & Geomechanics Abstracts*. Elsevier, pp.643–659.
- Martin, C.D., Kaiser, P.K. and Alcott, J.M. 1996. Predicting the depth of stress-induced

- failure around underground openings *In: Proc. 49th Canadian Geotechnical Conference.*, pp.105–114.
- Martin, C.D., Christiansson, R. and Söderhäll, J. 2001. *Rock stability considerations for siting and constructing a KBS-3 repository. Based on experiences from Aespoe HRL, AECL's URL, tunnelling and mining.* Swedish Nuclear Fuel and Waste Management Co.
- Martin, C.D., Kaiser, P.K. and Christiansson, R. 2003. Stress, instability and design of underground excavations. *International Journal of Rock Mechanics and Mining Sciences.* 40(7–8), pp.1027–1047.
- Martin, C.D., Kaiser, P.K. and McCreath, D.R. 1999. Hoek-Brown parameters for predicting the depth of brittle failure around tunnels. *Canadian Geotechnical Journal.* 36(1), pp.136–151.
- Oliveira, D. and Diederichs, M.S. 2017. Tunnel support for stress induced failures in Hawkesbury Sandstone. *Tunnelling and Underground Space Technology.* 64, pp.10–23.
- Pierce, M., Gaida, M. and DeGagne, D. 2009. Estimation of rock block strength *In: RockEng09 (Proceedings, 3rd CANUS Rock Mechanics Symposium, Toronto.*
- Schlotfeldt, P. and Carter, T.G. 2018. A new and unified approach to improved scalability and volumetric fracture intensity quantification for GSI and rockmass strength and deformability estimation. *International Journal of Rock Mechanics and Mining Sciences.* 110, pp.48–67.
- Shin, S.W. 2010. *Excavation disturbed zone in Lac du Bonnet granite.* Edmonton, Canada: University of Alberta.
- Singh, M.M. and Huck, P.J. 1972. Large scale triaxial tests on rock *In: The 14th US Symposium on Rock Mechanics (USRMS).* American Rock Mechanics

Association.

- Stavrou, A. and Murphy, W. 2018. Quantifying the effects of scale and heterogeneity on the confined strength of micro-defected rocks. *International Journal of Rock Mechanics and Mining Sciences*. 102, pp.131–143.
- Stavrou, A., Vazaios, I., Murphy, W. and Vlachopoulos, N. 2019. Refined Approaches for Estimating the Strength of Rock Blocks. *Geotechnical and Geological Engineering*.
- Tani, K. 2001. Scale effect on shear strength of sedimentary soft rocks observed in triaxial compression test (influence of potential joints) *In: 36th National Conference of the Japanese Geotechnical Society.*, pp.597–598.
- Vazaios, I., Farahmand, K., Vlachopoulos, N. and Diederichs, M.S. 2018. Effects of confinement on rock mass modulus: A synthetic rock mass modelling (SRM) study. *Journal of Rock Mechanics and Geotechnical Engineering*. 10(3), pp.436–456.
- Vazaios, I., Vlachopoulos, N. and Diederichs, M.S. 2017. Integration of lidar-based structural input and discrete fracture network generation for underground applications. *Geotechnical and Geological Engineering*. 35(5), pp.2227–2251.
- Vlachopoulos, N. and Diederichs, M.S. 2009. Improved longitudinal displacement profiles for convergence confinement analysis of deep tunnels. *Rock Mechanics and Rock Engineering*. 42(2), pp.131–146.
- Vlachopoulos, N. and Vazaios, I. 2018. The numerical simulation of hard rocks for tunnelling purposes at great depths: a comparison between the hybrid FDEM method and continuous techniques. *Advances in Civil Engineering*. 2018.
- Weibull, W. 1951. A statistical distribution function of wide applicability. *Journal of Applied Mechanics*. 18, pp.293–297.

Yoshinaka, R., Osada, M., Park, H., Sasaki, T. and Sasaki, K. 2008. Practical determination of mechanical design parameters of intact rock considering scale effect. *Engineering Geology*. 96(3–4), pp.173–186.

Chapter 5

5. Discussion and Conclusions

5.1. Thesis Summary

In this chapter a summary of the key findings from each chapter is presented. It is shown how the results of the work presented in earlier chapters form a coherent body of work that contributes from different angles knowledge on the mechanical behaviour of rock blocks and their potential contribution to the overall rock mass behaviour. Finally, recommendations for future work are also given in this chapter. Illustrations, diagrams and formulae shown in the previous chapters are not reproduced, neither are the detailed discussions. For specific topics the reader is referred to the relevant sections in Chapters 2, 3 and 4.

In Chapter 1, a literature review was presented outlining the different chapters within the relevant published work. It was identified that the behaviour of rock blocks is a significant factor controlling the rock mass behaviour around underground openings and the various rock-support interactions. The unconfined and confined properties of blocks are influenced by scale effects and the presence of micro- and meso-scale defects (Pierce et al., 2009). Such defects impact significantly on the mechanical behaviour of blocks and it is therefore critical in accounting for their weakening effects. However, due to the practical difficulties in testing large block

volumes and/or characterising the condition of the defects, it is challenging to define representative parameters for design. This challenge is made more complex by the difficulties in testing representative lab scale rock samples, as typically the specimens sent for testing are either from the relatively stronger parts of the core and/or influenced by planes of weakness and/or have been disturbed due to drilling/handling damage. In this context, Chapters 2 and 3 investigated, through a series of simulated laboratory tests, the combined impact of scale and material heterogeneity on the compressive strength of rock blocks. Despite the need of estimating representative block properties, Chapter 1 also contained the recognition that the selection of appropriate constitutive relationships in modelling is of equivalent importance as the traditional Hoek–Brown approaches are not an ideal method to represent the in-situ strength of competent rock masses subjected to high compressive stresses near the excavation boundaries. In such cases, the envelope follows an S- or tri-linear shape to replicate the lower in-situ strength in the low confining region adjacent the tunnel periphery and the expected extensile fracturing (Martin et al. 1999). The modified brittle model can be established following the Damage-Initiation and Spalling-Limit (DISL) approach proposed by Diederichs (2007) or the procedure described by Kaiser (2016). Typically, these modified envelopes are used in fracture-free continuum-based models, but relatively little modelling work has been undertaken to test the influence in adopting this approach in discontinuum modelling. In this respect, Chapter 4, described a series of tunnel-scale simulations, investigating the combined influence of scaled properties, constitutive relationships and modelling techniques on the behaviour of underground openings excavated in moderately jointed/blocky rock masses. Thus, the combined work of Chapters 2, 3 and 4 provides a procedure for estimating representative block properties during the ground investigation and interpretation phases, and then provides guidelines on how to use these properties within appropriate constitutive relationships and modelling techniques during the design and construction phases.

In Chapter 2, a numerical study was performed to develop a method for estimating the confined strength of rock blocks considering scale effects and in-situ heterogeneity (Stavrou and Murphy, 2018). Grain-Based Models (GBM) within UDEC were developed to simulate the results of lab- and block-scale compression tests. The properties of progressively larger in size and degrading in strength GBM samples were calibrated against the Yoshinaka et al. (2008) scaling relation. The results from the large-scale triaxial tests revealed a strong size/condition effect to the predicted confined peak strength values. The triaxial tests were performed over a limited range of confining stresses and it was shown that the strength of the samples with defects does not recover to the strength of defect free samples as confinement increases. This emphasises the importance of understanding the condition of blocks within the region of low confinement around an excavation, as failure would be driven by local heterogeneities at different scales. In terms of Mohr–Coulomb properties, cohesion was found to decrease with both increasing scale and degrading sample condition in a manner similar to the scale/condition dependant reduction of UCS, while the friction angle appeared relatively insensitive. This behaviour confirmed that cohesion plays a far more important role at low confinement which is linked to the concept of cohesion-loss and friction mobilisation. A scaling relationship was proposed that links the lab- and block-scale cohesion and sample size, given that the block UCS is known. The peak confined strength values were also fitted to the Hoek–Brown criterion and a new block-scale Geological Strength Index (GSI) parameter was introduced named micro GSI (mGSI) to express the elevated rock block disturbance with increasing scale and decreasing material quality. Both the proposed linear and non-linear approaches for predicting the confined strength of blocks were linked to the scaled block UCS. Thus, it was revealed that knowledge of the scale/condition related UCS reduction of rock blocks is key to characterise their behaviour under confined conditions. This conclusion from Chapter 2 led to the work presented in Chapter 3.

In Chapter 3, a series of simulated unconfined compressive tests were performed to develop a methodology for estimating the UCS of rock blocks considering the combined influence of scale and pre-existing defects (Stavrou et al., 2019). As part of the modelling process, micro-Discrete Fracture Networks (μ DFNs) were embedded into Grain-Based Models (GBMs) within UDEC to capture both the fracturing of the intact material and the effect of pre-existing defects. Following the initial calibration of a lab-scale intact (non-defected) rock sample, randomly distributed defects of increased frequency, persistence and strength were integrated in a series of progressively larger in size samples to generate synthetic rock block (SRB) models. The μ DFN geometries were generated using Fracman. Based on the numerical findings, guidelines for estimating the strength of defected rock blocks were proposed in an attempt to refine two existing empirical relationships given by Yoshinaka et al. (2008) and Laubscher and Jakubec (2001). The results from the scaling analysis were plotted as a function of the μ DFN P_{10} and P_{21} defect intensities and a progressive strength reduction was observed as defect frequency and persistence increase and defect strength decreases. A similar but lower magnitude reduction was also observed for the block Young's modulus. When the results for the UCS values were expressed as a function of the "Defect Intensity \times Persistence" (DIP) factor, strong clustering was observed which allowed us to standardise the data along specific strength reduction envelopes. Following the logic of the Laubscher and Jakubec (2001) approach, a set of diagrams were developed that express the rock block strength as function of sample size, defect intensity, defect persistence and defect strength. The block strength predictions from these diagrams should be considered as lower bound estimates due to the limitations of the UDEC two-dimension (2D) analyses. The use of the "Defect Intensity \times Persistence" or DIP factor is likely to be transferable to larger scales and rock mass classifications systems that currently consider only the blockiness of rock masses and not the effect of non-persistent discontinuities.

Chapter 4 provided a brief review on the available tools for estimating the scaled properties of rock blocks and described the commonly adopted constitutive relationships in rock engineering design. It was presented that the combination of the diagrams given in Chapter 3 for estimating the UCS of blocks with the mGSI-strength relationship given in Chapter 2, allowed the quantification of the mGSI in terms of specimen size, intensity and condition of defects. Thus, once the block strength has been estimated from these diagrams, then a mGSI value could be chosen from the relationship between mGSI and block UCS to estimate the block confined strength. However, the estimated confined strength from this relationship reflects shear type failure modes away from the excavation boundaries where confinement is high. For the region of low confinement adjacent the excavation, the confined strength should be expressed using the modified DISL approach to capture the low in-situ strength of the blocks and the expected spalling. Chapter 4 then focused on the influence of scaled block properties, appropriate constitutive relationships and modelling techniques via a series of tunnel-scale simulations. Block strength was shown to be an important factor in discontinuum modelling, affecting the extent of damage and rock mass deformations. It was highlighted that careful block characterisation is needed as rather small mGSI reduction steps lead to dramatic reductions in the strength of blocks. A comparison between the traditional Hoek–Brown and the modified DISL criteria for block represented as continuum media, revealed significant differences. The conventional approaches overestimated the in-situ strength and for that reason the size of the predicted damage and the magnitude of deformation were underestimated. In addition, the models did not capture the anticipated low confinement region near the excavation. On the other hand, the DISL approach matched the damage profile that was expected for the stress conditions investigated. Although, the DISL approach is typically employed in continuum-based numerical models, it was shown that it also plays an important role in discontinuum models for representing the behaviour of

continuum blocks in between joints. In Chapter 4 the influence of modelling techniques was also examined and models in which the blocks are simulated as a packing of Voronoi elements rather than being a rock governed by continuum mechanics. It is shown that significant effort is required to calibrate the Voronoi micro-properties for tunnel-scale problems. Regardless of the adopted Voronoi constitutive relationships, the results show that the Voronoi models predicted a considerably reduced damage, stress relaxation and deformation compared to the models that blocks simulated as continuum material. The Voronoi skeleton appeared to create a strongly-interlocked structure that fixed the pre-existing joints, minimising in this way the joint slip/opening and allowing the stress-induced slabbing type of failure to dominate the behaviour of the model before the activation of kinematic instabilities. This behaviour is believed to provide a more realistic behaviour for rock mass subjected in high stresses at depth. The significance of this observation from a geotechnical perspective is that the continuum approach is significantly more conservative, leading to potential costly over-engineering. Designers may wish to consider the computationally more expensive GBM approach, or to calibrate tunnel-scale models based on GBM models or to use 3D models to account for the stress confinement in the out-of-plane direction.

The conclusion from the combined work presented in Chapters 2, 3 and 4 is that the scaled block properties, constitutive relationships and modelling techniques are all very important factors which are strongly interrelated with each other when simulating the behaviour of underground openings in discontinuum models. Only when representative block properties and appropriate modelling approaches have been chosen can become possible to ensure the i) realistic simulation of the rock mass behaviour in terms of failure mechanisms, stress relaxation and deformation; ii) realistic prediction of rock-support interactions and the appropriate specification of support measures and excavation sequences; and iii) safe and cost-effective construction of civil and mining engineering projects.

5.2 Thesis Contribution

- Development of Grain-Based Models (GBMs) to simulate compression (unconfined and confined) and indirect tensile (Brazilian) tests.
- Proposal of linear (Mohr–Coulomb) and non-linear (Hoek–Brown) scaling relationships for predicting the confined strength of blocks considering scale effects and material heterogeneity (e.g. defect intensity, weathering).
- Introduction of a new block-scale Geological Strength Index (GSI) parameter, named micro GSI (mGSI), to express the rock block strength reduction with increasing scale and decreasing material quality.
- Development of Synthetic Rock Block (SRB) samples by integrating micro-discrete fracture networks (μ DFNs) into GBMs to simulate Unconfined Compressive Strength (UCS) tests.
- Investigation of the combined effect of defect geometry (i.e. intensity and persistence), defect strength and specimen size on the UCS of blocks.
- Refinement of existing empirical approaches for estimating the UCS of rock blocks as a function of a newly proposed “Defect Intensity \times Persistence” (DIP) factor, the strength of defects and the sample size.
- Quantification of the mGSI in terms of defect intensity and condition.
- Investigation of the influence of scaled block properties, constitutive relationships and modelling techniques on the behaviour of tunnel-scale continuum and discontinuum simulations.
- Verification that the conventional constitutive approaches overestimate the rock block in-situ strength and underestimate the disturbance and magnitude of deformation.
- Verification that the Synthetic Rock Mass (SRM) modelling technique captures a more realistic rock mass behaviour and failure modes.

5.3 Future Work

The quantified diagrams proposed for estimating the UCS of rock blocks were developed based on 2D plain-strain models in which the micro-defects are infinitely long in the out-of-plane direction. As a result, the analyses represent lower bound estimates and certain adjustments are required to improve the predicted block strengths. Future studies should focus on three-dimensional (3D) models to simulate the representative defect geometries and the available support due to the 3D confinement.

In addition to the peak strength of the defected blocks, future studies should also examine scale effects at the crack initiation and systematic damage thresholds. The influence of a confinement dependent block stiffness and the stiffness degradation due to damage are also important topics which typically are neglected in modelling.

The numerical investigations presented in Chapters 2, 3 and 4 were conducted assuming that the properties of blocks, joints and Voronoi elements are constant across the models in the different scenarios examined. However, variability in the grain, defect and block scale should be expected and as such future studies should focus in examining the influence of property variability by employing strength distributions along the zones and contacts of the blocks and/or micro-blocks.

The calibration of the UDEC tunnel-scale Voronoi models required significant effort. Currently, there are no available guidelines for calibrating the DISL approach when using Voronoi-elements and as such future research should focus in developing a procedure for prioritising the calibration of the peak and residual properties.

In the current UDEC version, the peak and residual properties of joints are activated simultaneously. Future modelling studies should also examine the influence of activating the cohesive and frictional strength properties at different plastic strain limits as cohesion is typically lost before the activation of the frictional strength.

References

- Diederichs, M.S. 2007. The 2003 Canadian Geotechnical Colloquium: Mechanistic interpretation and practical application of damage and spalling prediction criteria for deep tunnelling. *Canadian Geotechnical Journal*. 44(9), pp.1082–1116.
- Kaiser, P.K. 2016. *Ground Support for Constructability of Deep Underground Excavations: Challenge of Managing Highly Stressed Ground in Civil and Mining Projects*. ITA/AITES.
- Laubscher, D.H. and Jakubec, J., 2001. The MRMR rock mass classification for jointed rock masses. *Underground Mining Methods: Engineering Fundamentals and International Case Studies*, WA Hustrulid and RL Bullock (eds) Society of Mining Metallurgy and Exploration, SMME, pp.475-481.
- Martin, C.D., Kaiser, P.K. and McCreath, D.R. 1999. Hoek-Brown parameters for predicting the depth of brittle failure around tunnels. *Canadian Geotechnical Journal*. 36(1), pp.136–151.
- Pierce, M., Gaida, M. and DeGagne, D. 2009. Estimation of rock block strength *In: RockEng09 (Proceedings, 3rd CANUS Rock Mechanics Symposium, Toronto)*.
- Stavrou, A. and Murphy, W. 2018. Quantifying the effects of scale and heterogeneity on the confined strength of micro-defected rocks. *International Journal of Rock Mechanics and Mining Sciences*. 102, pp.131–143.
- Stavrou, A., Vazaios, I., Murphy, W. and Vlachopoulos, N. 2019. Refined Approaches for Estimating the Strength of Rock Blocks. *Geotechnical and Geological Engineering*.
- Yoshinaka, R., Osada, M., Park, H., Sasaki, T. and Sasaki, K. 2008. Practical determination of mechanical design parameters of intact rock considering scale effect. *Engineering Geology*. 96(3–4), pp.173–186.

Appendix A

Example of UDEC UCS test

```
; Author   : Anastasios Stavrou
; Title    : Uniaxial Compressive Test - 100x250mm
; Date     :
; Units    : Length: meter
;           Density: kg/m3
;           Force: N
;           Stress: Pa
; UDEC v.  : 6
```

```
-----
; Define Geometry
;-----
```

```
def setup ; define FISH function setup
; Constants for sample geometry
bl_x_le = -0.020 ; block left
bl_x_ri = 0.120 ; block right
bl_y_to = 0.280 ; block top
bl_y_bo = -0.030 ; block bottom
sa_x_le = 0.000 ; sample left
sa_x_ri = 0.100 ; sample right
sa_y_to = 0.250 ; sample height
sa_y_bo = 0.000 ; sample bottom
; Constants for voronoi generator
e_l = 0.005 ; average edge length - 5mm
i_n = 25 ; iteration number for size distribution - default n = 5
end
setup ; execute FISH function setup
```

```
new ; new UDEC simulation
round 0.00001 ; up to 1% of typical edge length - default 0.5
set ovtol 0.0005 ; default = 0.5*round
```

```
; Create block
block bl_x_le,bl_y_bo bl_x_le,bl_y_to bl_x_ri,bl_y_to bl_x_ri,bl_y_bo
```

```
; Create sample
crack bl_x_le,sa_y_to bl_x_ri,sa_y_to ID 11 ; create upper platen
crack bl_x_le,sa_y_bo bl_x_ri,sa_y_bo ID 11 ; create lower platen
crack sa_x_le,sa_y_bo sa_x_le,sa_y_to ; create left edge of sample
```

```

crack sa_x_ri,sa_y_bo sa_x_ri,sa_y_to ; create right edge of sample
del bl range bl_x_le,sa_x_le sa_y_bo,sa_y_to ; delete left side block
del bl range sa_x_ri,bl_x_ri sa_y_bo,sa_y_to ; delete right side block

; monitoring lines at the middle of the platens
crack bl_x_le,0.2650 bl_x_ri,0.2650 ID 22

; Define regions for later use
; region of rock sample
jregion id=1 sa_x_le,sa_y_bo sa_x_ri,sa_y_bo sa_x_ri,sa_y_to sa_x_le,sa_y_to
; regions of platens
jregion id=2 bl_x_le,sa_y_to bl_x_ri,sa_y_to bl_x_ri,bl_y_to bl_x_le,bl_y_to
jregion id=3 bl_x_le,bl_y_bo bl_x_ri,bl_y_bo bl_x_ri,sa_y_bo bl_x_le,sa_y_bo

; Create voronoi blocks
voronoi edge e_l iteration i_n range jreg 1

save geom.sav
;XXXXXXXXXXXXXXXXXXXXXXXXXXXXXXXXXXXXXXXXXXXXXXXXXXXXXXXXXXXXXXXXXXXXX

;-----
; Define DFN Geometries
;-----

crack 0.002 0.086 0.011 0.088 ID 99
crack 0.002 0.244 0.012 0.248 ID 99
crack 0.002 0.039 0.011 0.044 ID 99
crack 0.013 0.025 0.023 0.025 ID 99
crack 0.015 0.075 0.025 0.077 ID 99
crack 0.015 0.188 0.016 0.198 ID 99
crack 0.017 0.17 0.017 0.179 ID 99
crack 0.026 0.067 0.03 0.077 ID 99
crack 0.027 0.109 0.03 0.119 ID 99
crack 0.031 0.04 0.039 0.046 ID 99
crack 0.033 0.247 0.043 0.248 ID 99
crack 0.036 0.018 0.043 0.025 ID 99
crack 0.037 0.18 0.042 0.189 ID 99
crack 0.038 0.155 0.044 0.163 ID 99
crack 0.04 0.071 0.047 0.079 ID 99
crack 0.041 0.121 0.05 0.124 ID 99

```

```

crack 0.043 0.049 0.052 0.052 ID 99
crack 0.045 0.037 0.055 0.038 ID 99
crack 0.046 0.056 0.047 0.066 ID 99
crack 0.05 0.162 0.057 0.17 ID 99
crack 0.068 0.081 0.078 0.081 ID 99
crack 0.079 0.157 0.085 0.165 ID 99
crack 0.08 0.012 0.082 0.022 ID 99
crack 0.081 0.185 0.083 0.195 ID 99
crack 0.083 0.169 0.093 0.171 ID 99
crack 0.083 0.099 0.09 0.105 ID 99
crack 0.089 0.22 0.097 0.225 ID 99
crack 0.09 0.237 0.1 0.239 ID 99
; crack.....
; crack.....
; etc.....

save DFN_cracks.sav
;XXXXXXXXXXXXXXXXXXXXXXXXXXXXXXXXXXXXXXXXXXXXXXXXXXXXXXXXXXXXXXXXXXXXX

;-----
; Generate Finite Difference Mesh
;-----

gen edge 0.002   range jreg 1 ; zone sample
gen quad 0.01,0.01 range jreg 2 ; zone upper platen
gen quad 0.01,0.008 range jreg 3 ; zone lower platen

save zoning.sav
;XXXXXXXXXXXXXXXXXXXXXXXXXXXXXXXXXXXXXXXXXXXXXXXXXXXXXXXXXXXXXXXXXXXXX

;-----
; Define Material Properties
;-----

def rockprop ; define FISH function const
; voronoi block properties
bl_d = 2500 ; material density
y_mod = 26.0E9 ; elastic young's modulus
p_rat = 0.25 ; poisson's ratio
; calculate bulk and shear moduli

```

```

b_mod = y_mod/(3.0*(1.0-2.0 * p_rat)) ; elastic bulk modulus, K
s_mod = y_mod/(2.0*(1.0+p_rat)) ; elastic shear modulus, G

; voronoi contact properties
j_kn = 15600E9 ; contact normal stiffness
j_ks = 14040E9 ; contact shear stiffness
j_c = 11.3E6 ; contact cohesion
j_f = 47.5 ; contact friction angle
j_t = 3.3E6 ; contact tensile strength
j_rc = 0.0 ; contact residual cohesion
j_rf = 25.0 ; contact residual friction angle
j_rt = 0.0 ; contact residual tensile strength

; DFN crack properties
DFN_j_kn = 15600E9 ; joint normal stiffness
DFN_j_ks = 14040E9 ; joint shear stiffness
DFN_j_c = 0.0 ; joint cohesion
DFN_j_f = 45.0 ; joint friction angle
DFN_j_t = 0.0 ; joint tensile strength
DFN_j_rc = 0.0 ; joint residual cohesion
DFN_j_rf = 15.0 ; joint residual friction angle
DFN_j_rt = 0.0 ; joint residual tensile strength
;DFN_ap_init=30e-6 ; joint initial aperture
;DFN_ap_res=5e-6 ; joint residual aperture

ntab = 1
end
rockprop ; execute FISH function const

;-----
; Define Constitutive Models
;-----

; Apply elastic, isotropic block model
group zone 'voronoi blocks' range jreg 1
group zone 'platens' range jreg 2
group zone 'platens' range jreg 3
group joint 'DFN' range ID 99
zone model elastic density bl_d bulk b_mod shear s_mod range group 'voronoi
blocks'

```

```
zone model elastic density 7750 shear 80.0E9 bulk 160.0E9 range group 'platens'
```

```
; Apply Coulomb slip model with residual strength
; voronoi micro-cracks
prop jmat=1 jkn=j_kn jks=j_ks jcoh=j_c jfric=j_f jten=j_t
prop jmat=1 jrescoh=j_rc jrfric=j_rf jrten=j_rt
prop jmat=2 jkn=j_kn jks=j_ks jcoh=j_rc jfric=j_rf jten=j_rt
; with internal fracture flag
change jcons=5
; to be used for new contacts
set jcondf=5
set jmatdf=2
; sample/platen contact
prop jmat=3 jkn=j_kn jks=j_ks jcoh=1E10 jfric=0.01 jten=1E10
change jmat=3 range ID 11
; monitoring crack at the middle
prop jmat=4 jkn=j_kn jks=j_ks jcoh=1E10 jfric=50 jten=1E10
change jmat=4 range ID 22
```

```
; Apply Coulomb slip model with residual strength to DFN cracks
joint model residual jkn=DFN_j_kn jks=DFN_j_ks jfric=DFN_j_f jrfric=DFN_j_rf
jcoh=DFN_j_c jrcoh=DFN_j_rc jten=DFN_j_t jrten=DFN_j_rt range group 'DFN'
```

```
save props.sav
```

```
;XXXXXXXXXXXXXXXXXXXXXXXXXXXXXXXXXXXXXXXXXXXXXXXXXXXXXXXXXXXXXXXXXXXX
```

```
;-----
; Calculate Average Axial Stress and Axial Strain
;-----
```

```
; APPROACH No.1
; Calculate average axial stress along the contact top platen-sample
; Calculate the axial strain as the change in distance between the platens
```

```
def sigmav_1
sum_pl = 0.0
n_z_pl = 0.0
x_z_pl = 0.0
loop n (1,25)
x_z_pl = (sa_x_ri/25) * float(n)
```

```
iz = z_near(x_z_pl,sa_y_to)
sum_pl = sum_pl + z_syy(iz)
n_z_pl = n_z_pl + 1
endloop
sigmav_1 = - sum_pl/n_z_pl
end
```

```
def ax_str
ax_str = (gp_ydis(i_gb)-gp_ydis(i_gt))/(sa_y_to)
end
def set_lim
i_gt = gp_near(sa_x_ri/2,sa_y_to)
i_gb = gp_near(sa_x_ri/2,sa_y_bo)
end
set_lim
hist sigmav_1
hist ax_str
```

; APPROACH No.2

; Calculate average axial stress along a fictious "joint" at the middle of the top platen

```
def sigmav_2
whilestepping
sum_up=0.0
num_up=0.0
ic=contact_head
loop while ic # 0
if c_mat(ic) = 4 then
sum_up=sum_up+c_nforce(ic)
num_up=num_up+1
endif
ic=c_next(ic)
endloop
compress_up=sum_up
sigmav_2=compress_up/sa_x_ri
end
hist sigmav_2
```

; APPROACH No.3

; Calculate average axial stress at the middle one third of the sample

```
; Define Coordinates for Monitoring Lines
```

```
def mp_cr
```

```
p_y1 = (sa_y_to/3)*2
```

```
p_y2 = ((sa_y_to/3*2)+(sa_y_to/2))/2
```

```
p_y3 = (sa_y_to/2)
```

```
p_y4 = ((sa_y_to/2)+(sa_y_to/3))/2
```

```
p_y5 = (sa_y_to/3)
```

```
p_x1 = (sa_x_le)
```

```
p_x2 = (sa_x_ri/4)
```

```
p_x3 = (sa_x_ri/2)
```

```
p_x4 = (sa_x_ri/4)*3
```

```
p_x5 = (sa_x_ri)
```

```
end
```

```
mp_cr
```

```
def stress_strain
```

```
ntab = ntab + 1
```

```
; Axial Stress along Line1 level = p_y1
```

```
z_1L1 = z_near(p_x1,p_y1)
```

```
z_2L1 = z_near(p_x2,p_y1)
```

```
z_3L1 = z_near(p_x3,p_y1)
```

```
z_4L1 = z_near(p_x4,p_y1)
```

```
z_5L1 = z_near(p_x5,p_y1)
```

```
z_syy1L1 = z_syy(z_1L1)
```

```
z_syy2L1 = z_syy(z_2L1)
```

```
z_syy3L1 = z_syy(z_3L1)
```

```
z_syy4L1 = z_syy(z_4L1)
```

```
z_syy5L1 = z_syy(z_5L1)
```

```
; Axial Stress along Line 2 level = p_y2
```

```
z_1L2 = z_near(p_x1,p_y2)
```

```
z_2L2 = z_near(p_x2,p_y2)
```

```
z_3L2 = z_near(p_x3,p_y2)
```

```
z_4L2 = z_near(p_x4,p_y2)
```

```
z_5L2 = z_near(p_x5,p_y2)
```


$z_syy1L2 = z_syy(z_1L2)$
 $z_syy2L2 = z_syy(z_2L2)$
 $z_syy3L2 = z_syy(z_3L2)$
 $z_syy4L2 = z_syy(z_4L2)$
 $z_syy5L2 = z_syy(z_5L2)$

; Axial Stress along Line 3 level = p_y3

$z_1L3 = z_near(p_x1,p_y3)$
 $z_2L3 = z_near(p_x2,p_y3)$
 $z_3L3 = z_near(p_x3,p_y3)$
 $z_4L3 = z_near(p_x4,p_y3)$
 $z_5L3 = z_near(p_x5,p_y3)$

$z_syy1L3 = z_syy(z_1L3)$
 $z_syy2L3 = z_syy(z_2L3)$
 $z_syy3L3 = z_syy(z_3L3)$
 $z_syy4L3 = z_syy(z_4L3)$
 $z_syy5L3 = z_syy(z_5L3)$

; Axial Stress along Line 4 level = p_y4

$z_1L4 = z_near(p_x1,p_y4)$
 $z_2L4 = z_near(p_x2,p_y4)$
 $z_3L4 = z_near(p_x3,p_y4)$
 $z_4L4 = z_near(p_x4,p_y4)$
 $z_5L4 = z_near(p_x5,p_y4)$

$z_syy1L4 = z_syy(z_1L4)$
 $z_syy2L4 = z_syy(z_2L4)$
 $z_syy3L4 = z_syy(z_3L4)$
 $z_syy4L4 = z_syy(z_4L4)$
 $z_syy5L4 = z_syy(z_5L4)$

; Axial Stress along Line 5 level = p_y5

$z_1L5 = z_near(p_x1,p_y5)$
 $z_2L5 = z_near(p_x2,p_y5)$
 $z_3L5 = z_near(p_x3,p_y5)$
 $z_4L5 = z_near(p_x4,p_y5)$
 $z_5L5 = z_near(p_x5,p_y5)$

$z_syy1L5 = z_syy(z_1L5)$

```

z_syy2L5 = z_syy(z_2L5)
z_syy3L5 = z_syy(z_3L5)
z_syy4L5 = z_syy(z_4L5)
z_syy5L5 = z_syy(z_5L5)

```

```

z_syyL1 = z_syy1L1+z_syy2L1+z_syy3L1+z_syy4L1+z_syy5L1
z_syyL2 = z_syy1L2+z_syy2L2+z_syy3L2+z_syy4L2+z_syy5L2
z_syyL3 = z_syy1L3+z_syy2L3+z_syy3L3+z_syy4L3+z_syy5L3
z_syyL4 = z_syy1L4+z_syy2L4+z_syy3L4+z_syy4L4+z_syy5L4
z_syyL5 = z_syy1L5+z_syy2L5+z_syy3L5+z_syy4L5+z_syy5L5
tot_z_syy = z_syyL1+z_syyL2+z_syyL3+z_syyL4+z_syyL5

```

; Lateral Strain along Left side

```

gp_1L1 = gp_near(p_x1,p_y1)
gp_1L2 = gp_near(p_x1,p_y2)
gp_1L3 = gp_near(p_x1,p_y3)
gp_1L4 = gp_near(p_x1,p_y4)
gp_1L5 = gp_near(p_x1,p_y5)

```

```

x_disp1L = abs(gp_xdis(gp_1L1))
x_disp2L = abs(gp_xdis(gp_1L2))
x_disp3L = abs(gp_xdis(gp_1L3))
x_disp4L = abs(gp_xdis(gp_1L4))
x_disp5L = abs(gp_xdis(gp_1L5))

```

; Lateral Strain along Right side

```

gp_5L1 = gp_near(p_x5,p_y1)
gp_5L2 = gp_near(p_x5,p_y2)
gp_5L3 = gp_near(p_x5,p_y3)
gp_5L4 = gp_near(p_x5,p_y4)
gp_5L5 = gp_near(p_x5,p_y5)

```

```

x_disp1R = abs(gp_xdis(gp_5L1))
x_disp2R = abs(gp_xdis(gp_5L2))
x_disp3R = abs(gp_xdis(gp_5L3))
x_disp4R = abs(gp_xdis(gp_5L4))
x_disp5R = abs(gp_xdis(gp_5L5))

```

```

x_dispL = (x_disp1L+x_disp2L+x_disp3L+x_disp4L+x_disp5L)/5
x_dispR = (x_disp1R+x_disp2R+x_disp3R+x_disp4R+x_disp5R)/5

```

```
x_disp = (x_dispL+x_dispR)
```

```
sigmav_3 = - tot_z_syy / 25
```

```
lat_str = - x_disp / sa_x_ri
```

```
vol_str = ax_str + lat_str
```

```
; axial stress vs axial strain
```

```
xtable(1,ntab) = ax_str
```

```
ytable(1,ntab) = sigmav_1
```

```
xtable(2,ntab) = ax_str
```

```
ytable(2,ntab) = sigmav_2
```

```
xtable(3,ntab) = ax_str
```

```
ytable(3,ntab) = sigmav_3
```

```
; axial stress vs lateral
```

```
xtable(4,ntab) = lat_str
```

```
ytable(4,ntab) = sigmav_1
```

```
xtable(5,ntab) = lat_str
```

```
ytable(5,ntab) = sigmav_2
```

```
xtable(6,ntab) = lat_str
```

```
ytable(6,ntab) = sigmav_3
```

```
; volumetric_strain
```

```
xtable(7,ntab) = ax_str
```

```
ytable(7,ntab) = vol_str
```

```
end
```

```
stress_strain
```

```
table 1 (0,0)
```

```
table 2 (0,0)
```

```
table 3 (0,0)
```

```
table 4 (0,0)
```

```
table 5 (0,0)
```

```
table 6 (0,0)
```

```
table 7 (0,0)
```

```
hist sigmav_3
```

```
hist lat_str
```

```
hist vol_str
```



```
-----  
; Define Boundary Conditions  
-----  
  
; engage servo control  
call boucnr.fin  
call servo.fis  
; fix platen top and bottom sides at the x-direction  
bound xvel = 0 ra yr 0.278 0.282  
bound xvel = 0 ra yr -0.032 -0.028  
; apply load from top and bottom  
bound yvel = -0.01 ra yr 0.278 0.282  
bound yvel = 0.01 ra yr -0.032 -0.028  
  
save loading.sav  
;XXXXXXXXXXXXXXXXXXXXXXXXXXXXXXXXXXXXXXXXXXXXXXXXXXXXXXXXXXXXXXXXXXXX  
  
-----  
; Cycle 500000 - Monitor Every 100 Steps  
-----  
  
def supstep  
stress_strain  
if ns=0 then  
ns=5  
end_if  
command  
step ns  
print k  
end_command  
end  
def supsolve  
loop k (1,nsup)  
supstep  
end_loop  
end  
set high_unbal=2e3  
set low_unbal=9e1  
set high_vel= 0.02
```

```
set nsup=5000 ns=100 ; UDEC will cycle nsup*ns times
supsolve
```

```
save cycle1.sav
```

```
;XXXXXXXXXXXXXXXXXXXXXXXXXXXXXXXXXXXXXXXXXXXXXXXXXXXXXXXXXXXXXXXXXXXX
```

```
;-----
```

```
; Define servo-control FIS
```

```
;-----
```

```
; Fish function to adjust velocity such that
; unbalanced force is below high_unbal
; (and above low_unbal) to ensure small inertial effects.
```

```
def servo
```

```
  while_stepping
```

```
  v_factor = 0.0
```

```
  if unbal>high_unbal then
```

```
    v_factor = 0.975
```

```
  endif
```

```
  if unbal<low_unbal then
```

```
    v_factor = 1.025
```

```
  endif
```

```
  if v_factor # 0.0 then
```

```
; NOTE: outer boundary list is circular
```

```
  i_b = bou_head
```

```
  ib_n = 0
```

```
  loop while ib_n # bou_head
```

```
    ib_n = imem(i_b)
```

```
    if imem(i_b+$KBDY) = 4 then
```

```
      by_vel = fmem(i_b + $KBDAPY)
```

```
      by_vel = by_vel * v_factor
```

```
      if abs(by_vel) > high_vel then
```

```
        by_vel = sgn(by_vel)*high_vel
```

```
      end_if
```

```
      fmem(i_b + $KBDAPY) = by_vel
```

```
    end_if
```

```
    i_b = ib_n
```

```
  end_loop
```

```
end_if
```

```
end
```

Appendix B

Example of UDEC Tunnel-Scale Simulation


```
-----  
; Create DFN  
-----  
  
crack -9.4269477456 -105.455416745 -9.58346225611 -105.53093843 ID 99  
crack -9.58346225611 -105.53093843 -9.9999999731 -105.731926984 ID 99  
crack -9.34322520635 -109.948517388 -9.37884095601 -110.000000066 ID 99  
crack -9.34501098386 -109.802803105 -9.40641046047 -110.000000066 ID 99  
crack -9.23893428139 -110.000000066 -9.47893182478 -109.629962987 ID 99  
crack -9.47893182478 -109.629962987 -9.95834830693 -108.890785522 ID 99  
crack -9.71951514773 -109.941970891 -9.79171800903 -109.876489228 ID 99  
crack -9.79171800903 -109.876489228 -9.82560143165 -109.845759935 ID 99  
crack -9.82560143165 -109.845759935 -9.83755243115 -109.834921426 ID 99  
crack -9.83755243115 -109.834921426 -9.91940746001 -109.76068551 ID 99  
crack -9.82654378108 -108.851147956 -9.82778430275 -108.859348601 ID 99  
crack -9.82778430275 -108.859348601 -9.86180320672 -109.084239072 ID 99  
crack -9.86180320672 -109.084239072 -9.97492149762 -109.832047052 ID 99  
crack -9.97492149762 -109.832047052 -9.99565336398 -109.969094342 ID 99  
crack -9.9999999731 -109.991222447 -9.97709688834 -110.000000066 ID 99  
crack -9.4896851658 -110.000000066 -9.43957652162 -109.591849393 ID 99  
crack -9.43957652162 -109.591849393 -9.39581849344 -109.235432452 ID 99  
crack -9.39581849344 -109.235432452 -9.34532262675 -108.824122733 ID 99  
crack -9.34532262675 -108.824122733 -9.29576705686 -108.420489139 ID 99  
crack -7.85842171601 -108.712045497 -8.00820854596 -108.920848197 ID 99  
crack -8.00820854596 -108.920848197 -8.17929700307 -109.15934307 ID 99  
crack -8.17929700307 -109.15934307 -8.42763594083 -109.505523748 ID 99  
crack -8.42763594083 -109.505523748 -8.78235790424 -110.000000066 ID 99  
crack -9.9999999731 -108.300603217 -9.46364440314 -108.940944738 ID 99  
crack -9.46364440314 -108.940944738 -9.03660014562 -109.450780458 ID 99  
crack -9.03660014562 -109.450780458 -8.80824372462 -109.723408288 ID 99  
crack -9.24887524835 -109.487367219 -9.44379251182 -109.484111375 ID 99  
crack -9.44379251182 -109.484111375 -9.9999999731 -109.474821157 ID 99  
crack -9.10675627283 -104.816281385 -7.04229393891 -107.583634204 ID 99  
crack -9.9999999731 -106.392327255 -9.93172970704 -106.325162834 ID 99  
crack -9.93172970704 -106.325162834 -9.41171373903 -105.813569254 ID 99  
crack -7.78800228528 -104.728875345 -8.23187473706 -105.223666808 ID 99  
; crack.....  
; crack.....  
; etc.....
```

```

;-----
; Generate Finite Difference Mesh
;-----

gen edge 0.05 range annulus (0,-100) (2.5,3.0)
gen edge 0.25 range -10,10 -110,-90
gen edge 1.0

save zoning.sav
;XXXXXXXXXXXXXXXXXXXXXXXXXXXXXXXXXXXXXXXXXXXXXXXXXXXXXXXXXXXXXXXXXXXX

;-----
; Define Material Properties
;-----

def rockprop ; define FISH function const
; GBM properties
GBM_dens = 2500 ; material density
GBM_y_mod = 19.0E9 ; elastic young's modulus
GBM_p_rat = 0.20 ; poisson's ratio
GBM_b_mod = GBM_y_mod/(3.0*(1.0-2.0 * GBM_p_rat)) ; elastic bulk modulus,
K
GBM_s_mod = GBM_y_mod/(2.0*(1.0+GBM_p_rat)) ; elastic shear modulus, G
GBM_coh = 7.5E6 ; cohesion
GBM_fri = 18.9 ; friction angle
GBM_ten = 2.47E6 ; tensile strength
GBM_dil = 17.6 ; dilation angle

; DFN properties
DFN_j_kn = 15000E6 ; normal stiffness
DFN_j_ks = 1500E6 ; shear stiffness
DFN_j_c = 0.35E6 ; cohesion
DFN_j_f = 35 ; friction angle
DFN_j_t = 0.0 ; tensile strength
DFN_j_rc = 0.0 ; residual cohesion
DFN_j_rf = 25 ; residual friction angle
DFN_j_rt = 0.0 ; residual tensile strength

; GBM contact properties CWFS
GBM1_j_kn = 16000E9 ; contact normal stiffness

```

```

GBM1_j_ks = 8000E9 ; contact shear stiffness
GBM_j_c = 6.0E6 ; contact cohesion
GBM_j_f = 17.0 ; contact friction angle
GBM_j_t = 2.0E6 ; contact tensile strength
GBM_j_d = 17.6 ; contact dilation angle
GBM_j_rc = 0.0 ; contact residual cohesion
GBM_j_rf = 50.0 ; contact residual friction angle
GBM_j_rt = 0.00 ; contact residual tensile strength
GBM_j_rd = 0.001 ; contact shear displacement at zero dilation
;
GBM2_j_kn = 4000E9 ; contact normal stiffness
GBM2_j_ks = 2000E9 ; contact shear stiffness
;
ntab = 1
end
rockprop ; execute FISH function const

;-----
; Define Constitutive Models
;-----

;Glued Joints
joint model area jkn=DFN_j_kn jks=DFN_j_ks jfriction 89.0 jcohesion 1.0E9
jtension 1.0E9
joint model area jkn=DFN_j_kn jks=DFN_j_ks jfriction 89.0 jcohesion 1.0E9
jtension 1.0E9 range id 11
;new contact default
set jcondf joint model area jkn=DFN_j_kn jks=DFN_j_ks jfriction 30

; Apply Coulomb slip model with residual strength to DFN cracks
group joint 'DFN' range id 99
joint model residual jkn=DFN_j_kn jks=DFN_j_ks jfric=DFN_j_f jrfric=DFN_j_rf
jcoh=DFN_j_c jrcoh=DFN_j_rc jten=DFN_j_t jrten=DFN_j_rt range group 'DFN'
;new contact default
set jcondf joint model area jkn=DFN_j_kn jks=DFN_j_ks jfriction 30

; GBM - CWFS model
group zone 'GBM'

```

```

zone model ss dens GBM_dens bu GBM_b_mod sh GBM_s_mod coh GBM_coh fr
GBM_fri ten GBM_ten dil GBM_dil ctable 21 ftable 22 ttable 23 dtable 24 range
group 'GBM'
table 21 0,GBM_coh 0.002,0.1E6 ; cohesion
table 22 0,GBM_fri 0.004,61.0 ; friction angle
table 23 0,GBM_ten 0.002,0.01E6 ; tensile strength
table 24 0,GBM_dil 0.004,3.5 ; dilation angle

; GBM - Coulomb slip model with residual strength
prop jmat=1 jkn=GBM1_j_kn jks=GBM1_j_ks jcoh=GBM_j_c jfric=GBM_j_f
jten=GBM_j_t jdi=GBM_j_d
prop jmat=1 jrescoh=GBM_j_rc jrfric=GBM_j_rf jrten=GBM_j_rt zdi=GBM_j_rd
change jmat=1 range id 9

; GBM - Coulomb slip model with residual strength
prop jmat=2 jkn=GBM2_j_kn jks=GBM2_j_ks jcoh=GBM_j_c jfric=GBM_j_f
jten=GBM_j_t jdi=GBM_j_d
prop jmat=2 jrescoh=GBM_j_rc jrfric=GBM_j_rf jrten=GBM_j_rt zdi=GBM_j_rd
change jmat=2 range id 69

prop jmat=3 jkn=GBM2_j_kn jks=GBM2_j_ks jcoh=GBM_j_rc jfric=GBM_j_rf
jten=GBM_j_rt

; with internal fracture flag
change jcons=5
; to be used for new contacts
set jcondf=5
set jmatdf=3

save props.sav
;XXXXXXXXXXXXXXXXXXXXXXXXXXXXXXXXXXXXXXXXXXXXXXXXXXXXXXXXXXXXXXXXXXXXX

;-----
; Boundary Conditions
;-----

;overburden stress for 975m
bou stress 0 0 -24.375E6 ra -25.1 25.1 -75.1 -74.9

;sides

```

```

bou xvelocity 0 ra -25.1 -24.9 -125.1 -74.9
bou xvelocity 0 ra 24.9 25.1 -125.1 -74.9
;bottom
bou xvelocity 0 ra -25.1 25.1 -125.1 -124.9
bou yvelocity 0 ra -25.1 25.1 -125.1 -124.9

insitu stress -11.25E6,0.0,-22.5E6 ygrad 12500,0.0,25000 szz -11.25E6 zgrad
0.0,12500

set gravity 0.0 -10

save bou.sav
;XXXXXXXXXXXXXXXXXXXXXXXXXXXXXXXXXXXXXXXXXXXXXXXXXXXXXXXXXXXXXXXXXXXXX

;-----
; Initial Equilibrium
;-----

solve elastic ratio 1E-6

save initial.sav
;XXXXXXXXXXXXXXXXXXXXXXXXXXXXXXXXXXXXXXXXXXXXXXXXXXXXXXXXXXXXXXXXXXXXX

;-----
; Excavate Tunnel and Relax
;-----

reset disp jdisp vel

;Excavate Tunnel and find domain
delete range annulus (0,-100) (0.0,2.5)

;history for GRC
history ydisplace 0.0,-97.5
history ydisplace 0.0,-102.5
history xdisplace -2.5,-100
history xdisplace 2.5,-100

def find_dom ; find excavation
tun_dom=d_near(x_tun,y_tun)

```

```
end
set x_tun=0 y_tun=-100
find_dom

;Fix boundary condition at excavation periphery
boundary interior xvelocity 0 range domain tun_dom
boundary interior yvelocity 0 range domain tun_dom

call ZONK.FIS

def relaxation_factor
  old_factor = old_f_
  new_factor = new_f_
  initial_it=ini_it_
  last_it=last_it_
end
;
set old_f_=1.0
set new_f_=0.9
set ini_it_=1
set last_it_=10
relaxation_factor
;
def GRC_hist
;histories for GRC
  gi_ =gp_near(0.0,-97.5)
  disp_ci=gp_ydis(gi_)
  gii_ =gp_near(0.0,-102.5)
  disp_cii=gp_ydis(gii_)
  giii_ =gp_near(-2.5,-100)
  disp_ciii=gp_xdis(giii_)
  giv_ =gp_near(2.5,-100)
  disp_civ=gp_xdis(giv_)

command
  table 11 insert disp_ci,old_factor
  table 12 insert disp_cii,old_factor
  table 13 insert disp_ciii,old_factor
  table 14 insert disp_civ,old_factor
endcommand
```

```

end
GRC_hist

step 1
zonk
relax

;Free boundary condition at excavation periphery
boundary interior xfr range domain tun_dom
boundary interior yfr range domain tun_dom

solve ratio 1.0E-6

GRC_hist

save unsup.sav
; xxxxxxxxxxxxxxxxxxxxxxxxxxxxxxxxxxxxxxxxxxxxxxxxxxxxxxxxxxxxxxxxxxxxxxxxxxxxxxx

;-----
; Define ZONK.FIS
;-----

; fish function to:
; 1. retrieve reaction forces from boundary corner data,
; 2. change boundary type to force boundary
; 3. gradually reduce the reaction force

def zonk
; mark gridpoints that are on interior boundary
; and set to force boundary

ib=block_head ; start of block list
loop while ib #0 ; loop through all blocks
  igp=b_gp(ib) ; start of gridpoint list for block ib
  loop while igp # 0 ; loop through all gridpoints
    ibou=gp_bou(igp) ; index of boundary corner associated with gridpoint
    if(ibou) < 0 then ; if address is negative then it is interior
      ibou2=abs(ibou)
      if (imem(ibou2+2)) = 4 then
        imem(ibou2+2)= 1 ; force boundary
      endif
    endif
  endloop
endloop

```

```
        imem(ibou2+3)= 1 ; force boundary
        gp_extra(igp) = 1.0
    endif
    else
        gp_extra(igp) = 0.0
    endif
    igp=gp_next(igp) ; next gridpoint
endloop
ib= b_next(ib) ; next block in list
endloop
end

def reduce
ib=block_head ; start of block list
loop while ib #0 ; loop through all blocks
    igp=b_gp(ib) ; start of gridpoint list for block ib
    loop while igp # 0 ; loop through all gridpoints
        ibou=gp_bou(igp) ; index of boundary corner associated with gridpoint
        if(ibou) < 0 then ; if address is negative then it is interior
            ibou2=abs(ibou)
            if gp_extra(igp) > 0.0 then
                forcex=fmem(ibou2+4) ; get current total x-force
                forcey=fmem(ibou2+5) ; get current total y-force
                fmem(ibou2+4)= forcex * red_factor ;reduce reaction force
                fmem(ibou2+5)= forcey * red_factor ;reduce reaction force
            endif
        endif
        igp=gp_next(igp) ; next gridpoint
    endloop
    ib= b_next(ib) ; next block in list
endloop
end

def relax

loop i (initial_it,last_it)
    red_factor = new_factor/old_factor
    reduce
    command
        solve ratio 1.0E-5
```



```
endcommand

disp_ci=gp_ydis(gi_)
disp_cii=gp_ydis(gii_)
disp_ciii=gp_xdis(giii_)
disp_civ=gp_xdis(giv_)

if i<10 then
    command
        table 11 insert disp_ci,new_factor
        table 12 insert disp_cii,new_factor
        table 13 insert disp_ciii,new_factor
        table 14 insert disp_civ,new_factor
    endcommand
endif

relax_factor=string(new_factor)
name1='state'+relax_factor+'.sav'
command
    save name1
endcommand

old_factor = new_factor
new_factor = new_factor - 0.1

endloop

initial_it=last_it+1
last_it=10

end
```